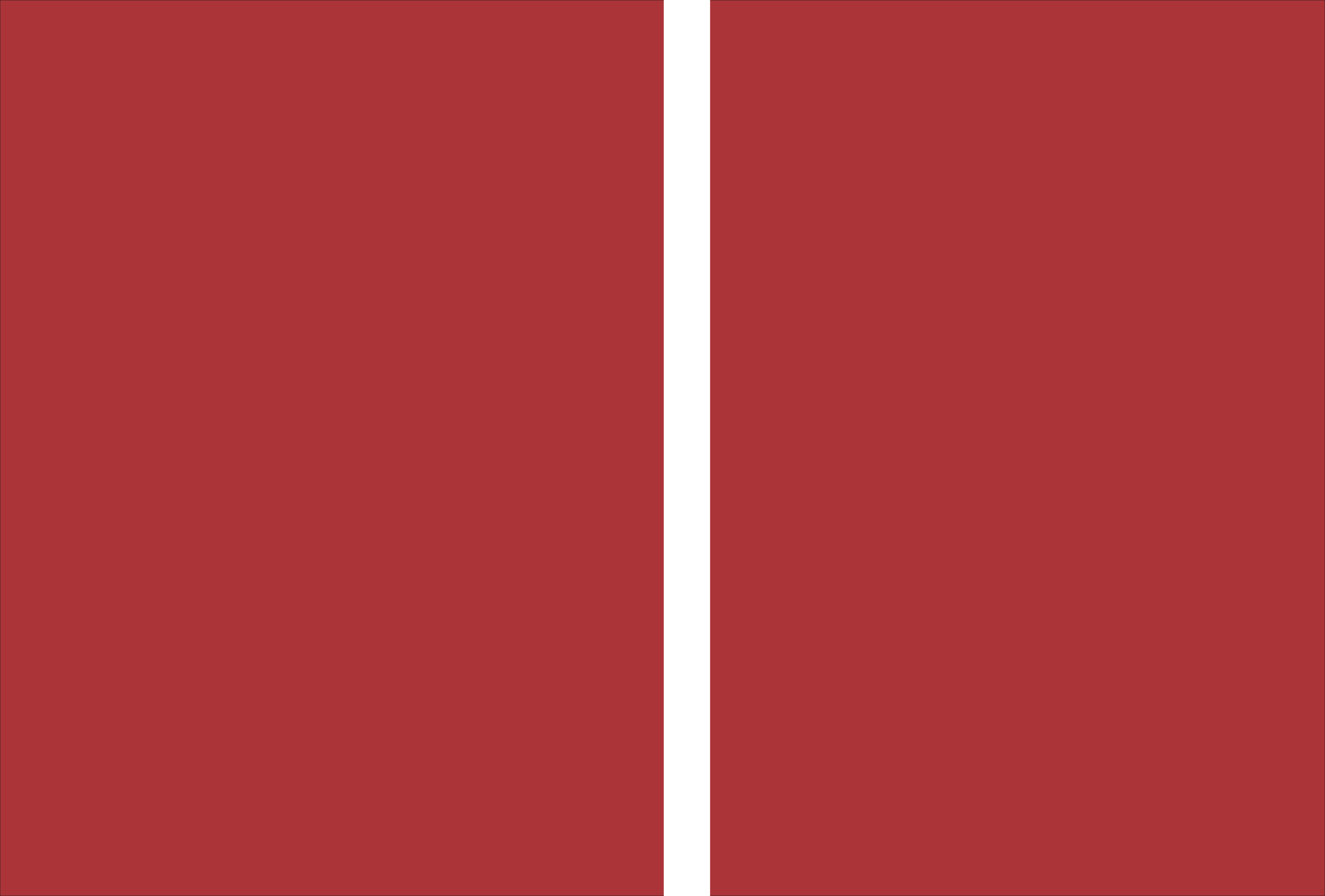


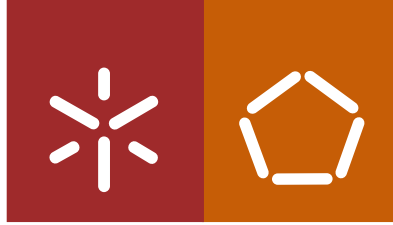


Universidade do Minho
Escola de Engenharia

Ana Patrícia Tavares Moreira

**Development of biosensor integrated into Dye
Sensitized Solar Cells for measuring cancer
biomarkers**





Universidade do Minho
Escola de Engenharia

Ana Patrícia Tavares Moreira

**Development of biosensor integrated into Dye
Sensitized Solar Cells for measuring cancer
biomarkers**

Tese de Doutoramento em Engenharia Biomédica

Trabalho efetuado sob a orientação da
Professora Doutora Goreti Sales
e da
Professora Doutora Graça Minas

DIREITOS DE AUTOR E CONDIÇÕES DE UTILIZAÇÃO DO TRABALHO POR TERCEIROS

Este é um trabalho académico que pode ser utilizado por terceiros desde que respeitadas as regras e boas práticas internacionalmente aceites, no que concerne aos direitos de autor e direitos conexos.

Assim, o presente trabalho pode ser utilizado nos termos previstos na licença abaixo indicada.

Caso o utilizador necessite de permissão para poder fazer um uso do trabalho em condições não previstas no licenciamento indicado, deverá contactar o autor, através do RepositóriUM da Universidade do Minho.



Atribuição-NãoComercial-Compartilha

CC BY-NC-SA

<https://creativecommons.org/licenses/by-nc-sa/4.0/>

Acknowledgments

I want to acknowledge my supervisors Prof. Goreti Sales and Prof. Graça Minas for their support, encouragement and guidance throughout this work. I would like to acknowledge Prof. Goreti for contributing with her scientific knowledge and teaching expertise and her enthusiasm for science. To Prof. Graça for her help and scientific knowledge during my PhD.

I would like to acknowledge all my colleagues in the Biomark group that in a direct or indirect way contributed to this work, especially Liliana Truta, Felismina Moreira and Gabriela Martins, and all others; my friends for their comprehension and support, especially for encouragement and friendship; my boyfriend Joao Ribeiro; and my family, my mother and my sister for being beside me in all moments of my life.

This work is funded by European Research Council is acknowledge for funding this work through the Starting Grant .3P's (GA 311086).



European Research Council
Established by the European Commission

STATEMENT OF INTEGRITY

I hereby declare having conducted this academic work with integrity. I confirm that I have not used plagiarism or any form of undue use of information or falsification of results along the process leading to its elaboration.

I further declare that I have fully acknowledged the Code of Ethical Conduct of the University of Minho.

Desenvolvimento de um biossensor integrado em células solares sensibilizadas por corante para medir biomarcadores de cancro

Os biomarcadores são biomoléculas presentes em tecidos ou fluidos corporais e desempenham um papel importante como ferramenta de diagnóstico em laboratórios clínicos e em hospitais, especialmente na área de oncologia. Estas biomoléculas podem ser associadas a doenças cancerígenas, possibilitam o diagnóstico e prognóstico destas doenças, bem como o acompanhamento e a sua evolução, face a um determinado tratamento.

A determinação desses biomarcadores deve ser, por isso, de baixo custo e rápida, com recurso a instrumentos pequenos e portáteis, de forma a permitir a sua utilização em programas de rastreio e em contexto clínico. Neste contexto, os biossensores representam um papel essencial, por serem tipicamente rápidos e baratos e permitirem um diagnóstico no ponto de cuidado médico. Apesar de existirem descritos na literatura vários biossensores dirigidos a biomarcadores de cancro, falta ainda um biossensor que apresente baixo custo e uma produção simples, com um reduzido número de requisitos. Estas características são fundamentais para a sua aplicação no rastreio do cancro.

Este trabalho propõe, por isso, a utilização de um material biomimético como elemento de bioreconhecimento para deteção de biomarcadores do cancro, material esse que atua como um anticorpo natural. Este material é sintético, barato e pode ser produzido para eventualmente qualquer molécula alvo, através de uma impressão molecular em estruturas poliméricas, com subsequente produção de polímeros molecularmente impressos (MIPs, do inglês *Molecularly-Imprinted Polymers*). A técnica eletroquímica é utilizada durante o desenvolvimento e a caracterização do MIP, por permitir procedimentos rápidos e de baixo custo, bem como a sua produção em suportes adequados do ponto de vista ambiental. O biossensor desenvolvido neste trabalho foi integrado, ainda, numa célula fotovoltaica, tendo em vista a produção de um novo sistema híbrido: um sistema elétrico que não necessite de uma fonte de energia elétrica. Essa célula fotovoltaica, uma célula solar sensibilizada por corante (DSSC, do inglês, *Dye Sensitized Solar Cell*), caracteriza-se pelo facto da energia gerada pelo sistema híbrido ser dependente da concentração de um biomarcador do cancro. Além disso, este sistema evoluiu no sentido de fornecer um sinal visível a qualquer utilizador, utilizando a sua interface com uma célula electrocrómica. Esta célula usou como material electrocrómico o poli(3,4-etilenodioxitiofeno) e um seu derivado, recebendo a energia gerada pelo dispositivo híbrido e convertendo-a numa dada cor. A intensidade desta cor é, também, dependente da concentração do biomarcador.

Em geral, este trabalho descreve a combinação altamente inovadora de diferentes técnicas (materiais sensores, células fotovoltaicas e electrocrómicas) para a produção de uma nova geração de dispositivos, dirigidos à deteção de biomarcadores do cancro. Esta combinação permitiu desenvolver sistemas simples e sem requisitos específicos, tornando-se apenas necessária a presença da amostra para gerar informação analítica.

Palavras-chave: Biossensor, cancro, célula electrocrómica, célula solar, impressão molecular.

Development of biosensor integrated into Dye Sensitized Solar Cells for measuring cancer biomarkers

Biomarkers are biomolecules present in tissues or body fluids that may be associated with cancer diseases. These biomolecules have shown an important role as diagnostic tools in clinical laboratories and hospitals, especially in oncology. Biomarkers may allow assessing cancer in an initial state of the disease, establishing an accurate prognosis, and following-up the progression of disease along the patient treatment.

The determination of these biomarkers should therefore be of low cost, also offering a fast response, with small and portable instruments, so that this may be of use in screening programs and point-of-care context. In this context, biosensors represent an essential role, due to their advantages as fast and cost-effective method in clinical diagnosis. Although there are several biosensors for determining cancer biomarkers reported in the literature, a biosensor that offers low cost and simple production features, with little requirements is still missing. These shall be very important in future wide screening programs in early cancer detection.

Thus, this work makes use of a biomimetic material as a biorecognition element for the detection of cancer biomarkers, acting like a natural antibody. This antibody-like material is synthetic, low cost and tailored on demand by molecularly-imprinted polymer (MIP) technology. Herein, electrochemical-based approaches were employed in its production, yielding a quick and low-cost procedure, as well as low cost supports. The biosensor developed herein is further integrated in a photovoltaic cell to generate a new hybrid sensing device that is self-powered. The photovoltaic cell was a dye sensitized solar cell (DSSC) and the electrical energy produced by the hybrid device depended on the concentration of cancer biomarker present. Moreover, this device also evolved to a self-signalling device, by coupling it to an electrochromic cell. This electrochromic cell consisted of a poly(3,4-ethylenedioxythiophene)-based electrochromic material and received the electrical energy generated by the hybrid system, converting it into a given colour. In this, the colour intensity was also concentration dependent.

Overall, this work describes the highly innovative combination of sensing material, and photovoltaic and electrochromic cells, to produce a new generation of self-powered and self-signalled devices devoted to cancer biomarker detection. This combination has zero-requirements, and only the sample shall be required to retrieve analytical data.

Keywords: Biosensor, Cancer, Electrochromic Cell, Molecular Imprinting, Solar Cell.

Index

Acknowledgments	iii
Resumo	v
Abstract	vi
Index	vii
Abbreviations and Symbols	xiii
List of Figures	xx
List of Tables	xxix
Chapter 1	32
1. Introduction	32
1.1. Motivation.....	32
1.2. Structure of this thesis.....	34
1.3. List of publications	36
1.3.1. Paper published in international scientific journal	36
1.3.2. Presentations made in scientific conferences.....	37
Chapter 2	39
2. Theoretical Concepts	39
2.1. Cancer Incidence.....	39
2.2. Cancer detection.....	41
2.3. Biosensors	44
2.3.1. Biorecognition element.....	45
2.3.2. Transduction approaches	52

2.3.3.	Electrochemical Biosensors for cancer biomarkers	62
2.4.	Photovoltaic cells	64
2.4.1.	Dye sensitized solar cell.....	64
2.4.2.	Photovoltaic characteristics of DSSC	66
2.5.	Electrochromic cell.....	69
2.5.1.	Set-up of an Electrochromic device.....	69
2.5.2.	Electrochromic material	71
Chapter 3	74
3.	Conductive Paper with Antibody-Like Film for Electrical Readings of Biomolecules	74
3.1.	Introduction	74
3.2.	Experimental section	75
3.2.1.	Apparatus	75
3.2.2.	Reagents	76
3.2.3.	Solutions	76
3.2.4.	Production of the conductive paper.....	76
3.2.5.	Surface analysis of the conductive paper.....	77
3.2.6.	Assembly of the antibody-like film.....	77
3.2.7.	Electrochemical assays	78
3.3.	Results and discussion	78
3.3.1.	Paper pre-treatment.....	79
3.3.2.	Turning the paper conductive	81
3.3.3.	Chemical/physical features of the conductive paper.....	84
3.3.4.	Assembly of the antibody-like material.....	87
3.3.5.	Rebinding to the antibody-like material.....	88
3.3.6.	<i>Optimization of the antibody-like assembly</i>	89
3.3.8.	Effect of monomer.....	91

3.3.9.	Application and reusability	95
3.4.	Conclusions	97
Chapter 4		99
4.	Novel electro-polymerized protein-imprinted materials using Eriochrome Black T: application to BSA sensing.....	99
4.1.	Introduction	99
4.2.	Experimental section	100
4.2.1.	Apparatus	100
4.2.2.	Reagents	100
4.2.3.	Solutions	101
4.2.4.	Electro-synthesis of biomimetic material.....	101
4.2.5.	Electrochemical assays	101
4.2.6.	Selectivity assays	102
4.3.	Results and Discussion	102
4.3.1.	Approach to produce the protein-imprinted film	102
4.3.2.	Optimization of relevant variables	104
4.3.3.	Electrochemical follow-up of the assembly	105
4.3.4.	Stability of the imprinted Poly(eriochrome black T)	107
4.3.5.	General analytical features.....	109
4.3.6.	Application of the biosensor	112
4.3.7.	Modifying the conductive support	113
4.3.7.1.	Electrochemical follow-up	113
4.3.8.	Re-evaluation of the Analytical Features	117
4.3.9.	Comparison to previously reported BSA sensors.....	119
4.4.	Conclusions.....	120
Chapter 5		122

5. Self-powered and self-signaled autonomous electrochemical biosensor applied to carcinoembryonic antigen determination.....	122
5.1. Introduction.....	122
5.2. Experimental section	123
5.2.1. Reagents and materials	123
5.2.2. Equipment	124
5.2.3. DSSC assembly and performance	125
5.2.4. Hybrid DSSC/biosensor	126
5.2.5. Electrochromic cell	128
5.3. Results and Discussion	129
5.3.1. Assembly of a suitable DSSC.....	129
5.3.2. Biosensing film production, characterization and rebinding features.....	133
5.3.3. Self-powered device	138
5.3.4. Self-powered and self-signalled device.....	142
5.3.5. Comparison to previously reported CEA sensors.....	144
5.4. Conclusions	145
Chapter 6	147
6. Photovoltaics, plasmonics, plastic antibodies and electrochromism combined for a novel generation of self-powered and self-signaled electrochemical biosensors.....	147
6.1. Introduction	147
6.2. Experimental section	148
6.2.1. Apparatus and materials	148
6.2.2. Reagents and solutions.....	149
6.2.3. Assembly of the counter electrode	149
6.2.4. Assembly of the imprinted film on the counter electrode.....	150
6.2.5. Rebinding assays on the imprinted film.	151

6.2.6.	Assembly of the photoanode electrode.....	151
6.2.7.	Assembly of the DSSC.....	152
6.2.8.	Assembly of the electrochromic cell.....	152
6.2.9.	Electrochemical assays.....	152
6.3.	Results and Discussion.....	153
6.3.1.	Assembly of biosensing element on the counter electrode.....	153
6.3.2.	Rebinding features of the imprinted film.....	157
6.3.3.	Integrating the imprinted film on the DSSC.....	160
6.3.4.	Enhancing the DSSC/biosensor efficiency.....	163
6.3.5.	Selectivity of DSSC/biosensor.....	166
6.3.6.	Inclusion of the self-signaling element.....	169
6.4.	Conclusions.....	171
Chapter 7.....		172
7.	Biosensors and photovoltaics merged in self-powered and self-signaled cable-free set-up.....	172
7.1.	Introduction.....	172
7.2.	Experimental section.....	173
7.2.1.	Apparatus.....	173
7.2.2.	Reagents and Solutions.....	173
7.2.3.	Set-up of DSSC.....	174
7.2.4.	Hybrid DSSC.....	177
7.2.5.	Electrochemical assays.....	178
7.3.	Results and Discussion.....	179
7.3.1.	Cr/Au films characterization.....	179
7.3.2.	Analytical performance of the WE/Gold.....	180
7.3.3.	Characterization of the WE/ITO electrode.....	184

7.3.4.	Electrochromic features of the EM	185
7.3.5.	Assembly of hybrid DSSC	186
7.4.	Conclusions.....	195
Chapter 8	197
8.	Conclusion and Future Work	197
8.1.	Conclusions.....	197
8.2.	Future Work.....	199
References	200
Appendix	220
I.	Conductive Paper with Antibody-Like Film for Electrical Readings of Biomolecules... ..	220
II.	Novel electro-polymerized protein-imprinted materials using Eriochrome Black T: application to BSA sensing.....	225
III.	Self-powered and self-signaled autonomous electrochemical biosensor applied to carcinoembryonic antigen determination.	233
IV.	Photovoltaics, plasmonics, plastic antibodies and electrochromism combined for a novel generation of self-powered and self-signalled electrochemical biosensors.....	235

Abbreviations and Symbols

Abbreviations

AA	- Acetic acid
AAC	- Acrylic acid
ACN	- Acetonitrile
AE	- Auxiliary electrode
AM	- Acrylamide
APBA	- 3-aminophenylboronic acid
ATR	- Smart Attenuated Total Reflectance
AuNPs	- Gold Nanoparticles
BAM	- N,N'-methylene-bisacrylamide
BSA	- Bovine Serum Albumin
CEA	- Carcinoembryonic Antigen
CA 15.3	- Carbohydrate Antigen 15-3
CA 125	- Carbohydrate Antigen 125
CE	- Counter Electrode
Crea	- Creatinine
CNTs	- Carbon nanotubes
CRT	- Carnitine
DSSC	- Dye Sensitized Solar Cell
DMF	- N,N-dimethylformamide

DTA	- Differential Thermal Analyzer
EBT	- Eriochrome Black T
EC	- Electrochromic Cell
EDC	- 1-ethyl-3-(3 dimethylaminopropyl)-carbodiimide
EDOT	- 3,4-ethylenedioxythiophene
EDS	- Energy Dispersive X-Ray
EIS	- Electrochemical Impedance Spectroscopy
EM	- Electrochromic Material
EP	- Electropolymerization
EtOH	- Ethanol
Fe₃O₄NPs	- Magnetic iron oxide nanoparticles
FRP	- Free Radical Polymerization
FTIR	- Fourier-Transform Infrared Spectroscopy
FTO	- Fluorine Tin Oxide
GHS	- Nanogold hollow microspheres
Glu	- Glucose
Hb	- Hemoglobin
HEPES	- 4-(2-hydroxyethyl)-1-piperazineethanesulfonic acid
HRP	- Horseradish peroxidase
HSL	- Hue, Saturation and Luminousness system
H₂SO₄	- Sulfuric Acid
HMII	- 1-Hexyl-3-methylimidazolium iodide
I_D	- Intensity D band
I_G	- Intensity G band

IgG	- Immunoglobulin G
ITO	- Indium Tin Oxide
KCl	- Potassium Chloride
K₃[Fe(CN)₆]	- Potassium Hexacyanoferrate III
K₄[Fe(CN)₆]	- Potassium Hexacyanoferrate II trihydrate
LED	- Light Emitting Diode
LiClO₄	- Lithium perchlorate
LiI	- Lithium iodide
LOD	- Detection Limit
LOQ	- Limit of quantification
MI	- Molecular Imprinting
MIP	- Molecularly-Imprinted Polymer
MNPs	- Magnetic nanoparticles
Mn₃O₄	- Manganous–manganic oxide
MPPy	- Molecularly-Imprinted Polypyrrole
MPTS	- Methacryloxy propyltrimethoxysilane.
MUDA	- 11-mercaptoundecanoic acid
Myo	- Myoglobin
MWCNTs	- Carbon nanotube, multi-walled
N719	-di-Tetrabutylammoniumcis-bis(isothiocyanato)bis(2,2'-bipyridyl-4,4'-dicarboxylato)ruthenium(II)
NaBH₄	- Sodium borohydride
NaClO₄	- Sodium Perchlorate
Na₂HPO₄	- Sodium phosphate dibasic dihydrate
NaH₂PO₄	- Sodium dihydrogen phosphate dihydrate

NHE	- Normal Hydrogen Electrode
NHS	- N-hydroxysuccinimide
NIP	- Non-imprinted Polymer
NPPy	- Non-imprinted Polypyrrole
NIR	- Near-Infrared
OAc	- Oxalic Acid
PANI	- Polyaniline
PB	- Phosphate Buffer
PBS	- Phosphate Buffer Saline
PEDOT	- Poly(3,4-ethylenedioxythiophene)
PET	- Poly(ethylene terephthalate)
POC	- Point-of-care
PPy	- Polypyrrole
Pth	- Polythiophene
PV	- Photovoltaic Cell
PVC	- Poly(vinyl chloride)
PVC-COOH	- Poly(vinyl chloride) carboxylated
PVD	- Physical vapor deposition
Py	- Pyrrole
RE	- Reference Electrode
SEM	- Scanning Electron Microscope
Si-SH	- 3-Mercaptopropylmethyldimethoxysilane
SNS-NH₂	- 4-[2,5-Di(thiophen-2-yl)-1H-pyrrol-1-yl]aniline
SPE	- Screen-Printed Electrode

Sulfo-LC-SPDP	-Sulfosuccinimidyl 6-(3'(2-pyridyldithio) propionamido) hexanoate
SWV	- Square wave Voltammetry
TBP	- 4- <i>tert</i> -Butylpyridine
TCO	- Transparent Conductive Oxide
TG	- Thermogravimetry
TiO₂	- Titanium Dioxide
WE	- Working Electrode
WHO	- World Health Organization

Symbols

ω	- Angular frequency
I_{pa}	- Anodic peak current
E_{pa}	- Anodic peak potential
A	- Area
I_{pc}	- Cathodic peak current
E_{pc}	- Cathodic peak potential
C_{bc}	- Conduction band
L	- Conductor length
C_{PE}	- Constant phase element
I	- Current
D	- Diffusion Coefficient of Species
C_{dl}	- Double Layer Capacitance

η	- Power conversion efficiency
N	- Exponent of the constant phase element
<i>FF</i>	- Fill Factor
<i>E_f</i>	- Final Potential
<i>Z''</i>	- Imaginary Component Impedance
<i>Z</i>	- Impedance
<i>E_i</i>	- Initial Potential
<i>I_s</i>	- Intensity of the incidence Light
<i>log</i>	- Logarithm
<i>Z₀</i>	- Magnitude of Impedance
<i>E₀</i>	- Maximum potential
<i>E_{min}</i>	- Minimum Potential
<i>n</i>	- Number of Electrons
<i>V_{oc}</i>	- Open circuit
<i>I_p</i>	- Peak Current
Φ	- Phase shift
<i>J-V</i>	- Photocurrent density-photovoltage
<i>E</i>	- Potential
ΔE	- Potential difference
<i>Z'</i>	- Real Component Impedance
<i>R</i>	- Resistance
<i>R_{ct}</i>	- Resistance of the charge transfer
<i>R_s</i>	- Resistance of the solution
ρ	- Resistivity

V	- Scan Rate
J_{sc}	- Short-Circuit Current density
I	- Specie
a_i	- Specie activity
c_i	- Specie concentration
E^\ominus	- Standard Electrode Potential
t	- Time
Δt	- Time-Interval
W	- Warburg diffusion element
Z_w	- Warburg Impedance

List of Figures

Figure 2.1 - Cancer incidence, expressing the (A) number of new cases in 2018, five Continents, all cancers, both sexes, all ages and (B) age-standardized incidence and mortality rates in 2018, worldwide, both sexes, all ages.	39
Figure 2.2 - Illustration of different Stages of Colorectal cancer.	40
Figure 2.3 - Cancer incidence, expressing the number of incident cases and death in 2018, worldwide, females, all ages.....	41
Figure 2.4 - Illustration of different kinds of cancer biomarkers.	42
Figure 2.5 - Schematic representation illustrating the main function and use (top) of a biosensor device, along with the device main elements (bottom).	45
Figure 2.6 - Steps of Molecular Imprinting Polymer synthesis: (1) Interaction between template and monomers; (2) polymerization and (3) template removal.	50
Figure 2.7 - Representative scheme of the principle of operation of a biosensor based on configuration of three electrodes: (A) biorecognition process; (B) monitoring process of resulting signal from interaction between the target molecule and the biorecognition element on transducer element; (C) results it displays in an electrochemical signal....	53
Figure 2.8 - Typical voltammogram for a reversible system, where I_{pa} is the Anodic peak current; I_{pc} is the Cathodic peak current; E_{pa} is the anodic peak potential and E_{pc} is the cathodic peak potential.	56
Figure 2.9 - Comparison of typical voltammogram obtained for (ir)reversibility systems.	57
Figure 2.10 - Nyquist plot that illustrates both real (Z') and imaginary (Z'') components of impedance at each ω . R_s : solution resistance; R_{ct} : charge transference resistance; ϕ : phase angle.	60
Figure 2.11 - Typical Bode diagram representing the impedance by (A) modulus ($\log(Z)$) and (B) phase ($\log(\phi)$) plots of an electrochemical system as function of the angular frequency (ω).	61

Figure 2.12 - Typical simplified <i>Randles</i> equivalent circuit. R_s : resistance of solution; R_{ct} : resistance of charge transfer; C_{dl} : double layer capacitance and Z_W : Warburg impedance.	62
Figure 2.13 - Schematic representation of a DSSC during the conversion of solar energy into electrical energy.....	65
Figure 2.14 - Schematic representation of the electron transfer reactions involved in the generation of energy in the DSSC. S represents the dye sensitizer; I^-/I_3^- is the redox mediator CB is the conduction band and VB is the valence band.....	67
Figure 2.15 - The current-voltage (A) and power-voltage (B) characteristics of DSSC.....	68
Figure 2.16 - Basic design of an electrochromic device, indicating transport of positive ions under the action of an electric field.	70
Figure 2.17 - The Periodic Table of the elements, referring to the transition metals whose oxides have well-documented electrochromism.	72
Figure 3.1 - Schematic representation of the production of the conductive paper and its sensitization by an antibody-like material.....	79
Figure 3.2 - Picture of hydrophilic (A) and hydrophobic paper (B) with a drop of a coloured aqueous solution on top for 0 (A_1/B_1) and 1 minute (A_2/B_2), and the subsequent contact angle of the hydrophobic paper (C).....	80
Figure 3.3 - FTIR spectra of several materials at different stages of the production of conductive paper.	81
Figure 3.4 - Thermogravimetric plot of conductive ink, pure graphite and pure PVC-COOH (A), with the corresponding differential data, DTG/DTA (Carbon in B) and PVC-COOH in C).....	83
Figure 3.5 - SEM images of graphite (1) and carbon ink (2) of increasing magnifications (A to C).....	84
Figure 3.6 - FTIR (A) and Raman (B) spectra of graphite powder and conductive paper. ...	85
Figure 3.7 - Raman spectra of the antibody-like film on conductive paper (A); and a direct comparison before and after calibration of the MI material of EDOT (B) or DBS (C). ...	89
Figure 3.8 - EIS data for CRT concentrations at the imprinting stage equal to (A) 1.00×10^{-2} mol/L or (B) 1.00×10^{-3} mol/ L (EDOT was the monomeric unit of the polymer), and the corresponding electrical circuit.	90

Figure 3.9 - EIS data of the assembly of the antibody-like material. A) sensory layer of DBS, B) sensory layer of EDOT.	91
Figure 3.10 - EIS spectra obtained by calibrating the imprinted paper-based devices. Imprinted DBS (A,C) and EDOT (B,D) based materials in HEPES buffer (A,B) and urine samples (C,D).	93
Figure 3.11 - Calibration curve of the imprinted paper-based devices. Imprinted DBS (A, C) and EDOT (B, D) based materials in HEPES buffer (A, B) and urine samples (C, D). Insets display the corresponding typical calibrations, including also the response of the control materials.	94
Figure 3.12 - Consecutive calibrations in serum solutions of the antibody-like polymeric sensors prepared with DBS (A) and EDOT (B) monomers.	96
Figure 4.1 - Schematic representation of the assembly of the BSA sensor. (A) oxidation of the carbon electrode area; (B) Electropolymerization of monomers in the presence of the protein; (C) template removal and (D) protein rebinding.....	103
Figure 4.2 - SWV (A) and EIS (B) data in the carbon SPE in $[\text{Fe}(\text{CN})_6]^{3-/4-}$ solution prepared in PBS buffer, pH 7.00, when assembling MIP (1) or NIP (2) materials, starting with the oxidation of the carbon electrodes, the electrical polymerization for assembling the imprinted or non-imprinted material and the template removal. Insets: the electrical circuit applied.	107
Figure 4.3 - Stability of the EIS readings after thermal treatment (A) and along time (B).	108
Figure 4.4 - Nyquist plots of MIP biosensors (A, B) and the corresponding calibrations (C, D), obtained after incubation of BSA standard solutions prepared in PBS buffer (A, C) or simulated serum (B, D), followed by EIS reading in standard in $[\text{Fe}(\text{CN})_6]^{3-/4-}$ solution prepares in the same medium. The response of the corresponding NIP films is also included.....	110
Figure 4.5 - The corresponding calibrations curves of the control material A) obtained after incubation of BSA standard solutions prepared in PBS buffer; B) simulated serum in $[\text{Fe}(\text{CN})_6]^{3-/4-}$ solution prepares in the same medium.....	111
Figure 4.6 - Calibration curves of the MIP and NIP BSA electrodes evaluated in simulated serum, and the standard derivation between the different electrodes.	113

Figure 4.7 - EIS (1) and SWV (2) data for the different stages of the assembly of the MIP-PEDOT (A) and NIP-PEDOT (B) biosensor using the redox probe $[\text{Fe}(\text{CN})_6]^{3-/4-}$ prepared in PBS buffer.	114
Figure 4.8 - Raman spectra of several films concerning the several stages of modification of the assembly the MIP-PEDOT on the carbon electrode. 1) and 2) are characteristic peaks of PEDOT.	115
Figure 4.9 - Nyquist plots of MIP-PEDOT biosensors (A, B) and the corresponding calibrations (C, D), obtained after incubation of BSA standard solutions prepared in PBS buffer (A, C) or simulated serum (B, D), followed by EIS reading in standard in $[\text{Fe}(\text{CN})_6]^{3-/4-}$ solution prepares in the same medium. The response of the corresponding NIP films is also included.	118
Figure 5.1 - Schematic representation of the several stages of the biosensing film assembly (A), its integration in the DSSC as the counter electrode to produce the hybrid device (B) and the interface of the external circuit with the electrochromic cell (C).	127
Figure 5.2 - Schematic representation of a conventional DSSC, combining counter electrode (FTO-glass and catalytic film) and photoanode (TiO_2 as semiconductor and suitable dye, hit by light), in liquid contact through an I^-/I_3^- electrolyte.	130
Figure 5.3 - Current values obtained for the oxidative scanning of an EDOT solution of 0.01 mol/L, prepared in 0.10 mol/L of KCl, using an FTO-glass support as working electrode, an Ag/AgCl as reference electrode and platinum as counter electrode. Inset: the picture of the resulting FTO-glass with <i>in-situ</i> generated PEDOT.	131
Figure 5.4 - Photocurrent density-photovoltage ($J-V$) and power conversion efficiency characteristic curves of the DSSCs using different counter electrodes, of Pt or PEDOT (A); using photoanodes with different areas (0.2 cm^2 or 0.7 cm^2) (B); and using CEs within the different stages of the production of the sensing film (C).	132
Figure 5.5 - Electrochemical CV (A) and EIS (B) data of the different steps (1) involved in the assembly of the sensing polymers, highlighting the results of the MPPy layer before and after template removal (2). Data corresponding to 5.00×10^{-3} mol/L $[\text{Fe}(\text{CN})_6]^{3-/4-}$ readings in PBS buffer, pH 7.40	135
Figure 5.6 - Raman spectra of the different materials followed along the assembly of the biosensing	136

Figure 5.7 - Typical Nyquist plots (A) of the MPPy film after consecutive incubations in increasing concentrations of CEA standard solution, and the corresponding calibration curves (B), also compared to the typical behaviour of the NIP.....	138
Figure 5.8 - Electrochemical CV (A) and EIS (B) data of the Mppy and NPPy materials after proteinase K treatment. Data obtained with a 5.00×10^{-3} mol/L $[\text{Fe}(\text{CN})_6]^{3-/4-}$ standard redox probe, prepared in PBS buffer, pH 7.40.	140
Figure 5.9 - Typical J - V and power conversion efficiency curves of the hybrid DSSC/Biosensing set-up against CEA increasing concentrations in ranging from 0.10 ng/mL to 100.0 $\mu\text{g/mL}$, prepared in acetate buffer solution (A) or in human urine from healthy individual, diluted 100 \times (B), and in the presence of an I^-/I_3^- redox electrolyte. Inset: typical calibration curves plotting the power conversion efficiency against log CEA increasing concentrations.....	141
Figure 5.10 - Coloured behaviour of the electrochromic material when evaluated under a working potential in the 3-electrodes system (A) and when interfaced in the external circuit of the hybrid device DSSC/biosensor (B), with the corresponding calibration (C), generated by plotting the colour coordinates of the HSL coloured space against the logarithm CEA concentration.....	143
Figure 6.1 - Schematic representation of the several stages of the hybrid/DSSC biosensor set-up with optical detection, namely the photoanode with plasmonic enhancement(A) and the biosensing counter electrode (C) combined in the DSSC cell (B), and their interface of the electrochromic cell (D.	150
Figure 6.2 - SEM images of FTO conductive glasses according to the different stages of their modification.....	154
Figure 6.3 - Raman spectra of modification of counter electrode after electropolymerization of PEDOT on the FTO glass.....	155
Figure 6.4 - Electrochemical EIS data of different steps involved in the construction of the different electrodes. (A) FTO glass with or without PEDOT. (B) MIP electrodes with or without CEA. (C) NIP electrodes with or without proteinase K treatment. Data corresponding to $5.00 \times 10^{-3} [\text{Fe}(\text{CN})_6]^{4/3-}$ readings in PB buffer, pH 7.00.	157
Figure 6.5 - Nyquist plots and the corresponding calibration curves (inset, as relative R_{ct} versus $\log[\text{CEA}]$) of the FTO/PEDOT/MIP electrode in a 3-eletrodes cell, with a	

5.00×10 ⁻³ [Fe(CN) ₆] ^{3-/4-} redox probe, prepared in PB buffer, pH 7.00, after incubation of increasing concentrations of CEA solutions prepared in buffer (A) or in diluted sample solution (B).....	158
Figure 6.6- Calibration curves corresponding to analytical performance of (A) FTO/PEDOT/MIP or (B) FTO/PEDOT/NIP electrodes, operating in a 3-electrodes cell, incubated previously in increasing concentrations of CEA standard solutions, prepared in PBS, in the presence of a 5.00×10 ⁻³ M [Fe(CN) ₆] ^{3-/4-} redox probe, prepared in PB buffer, pH 7.00.....	159
Figure 6.7 - Photocurrent density-photovoltage (<i>J-V</i>) and power conversion efficiency characteristic curves of DSSCs assembled (A) with different CEs (FTO/PEDOT, FTO/PEDOT/MIP-CEA or FTO/PEDOT/MIP) and a photoanode of TiO ₂ sensitized with N719; or assembled (B) with different photoanodes, with or without AuNPs, and a CE of FTO/PEDOT/MIP. Studies made with an electrolyte of I ⁻ /I ₃ ⁻	160
Figure 6.8 - Power curves and the corresponding calibration curves (inset, as relative η versus log[CEA]) of the FTO/PEDOT/MIP electrode in the DSSC set-up, after incubating increasing concentrations of CEA solutions, prepared in buffer (A) or in diluted sample solution (B). DSSC with a photoanode of TiO ₂ and an electrolyte of I ⁻ /I ₃ ⁻	162
Figure 6.9 - Power curves (A) of the FTO/PEDOT/MIP electrode in the DSSC set-up containing a photoanode with AuNPs, after incubation in increasing concentrations of CEA solutions, prepared in diluted urine sample solution, (B) the corresponding calibration plots as η' versus log[CEA], along with the colour generated by the electrochromic cell (C) and the corresponding saturation coordinate of the HSL colour system against log[CEA].....	164
Figure 6.10 - Power curves (A) of the FTO/PEDOT/NIP electrode in the DSSC set-up containing a photoanode with AuNPs, after incubation in increasing concentrations of CEA solutions and (B) the corresponding calibration plots as η' versus log[CEA], prepared in diluted sample solution.	165
Figure 6.11 - Percentage signal change when binary solutions are incubated in the sensing layer of the electrode and tested after in the DSSC/biosensor configuration. CEA 50 ng/mL; CA 125, 2.5 U/mL; CA 15.3, 1.6 U/mL; and urea 1.2 mg/mL.....	167

Figure 6.12 - Power curves of the FTO/PEDOT/MIP electrode in the DSSC set-up containing a photoanode with AuNPs, after incubation with (A) CEA; (B) CA 15.3 and (C) CA 125, prepared in buffer solution. (D) Selectivity study of DSSC/biosensor with single solutions of CEA and interfering species. CEA 50 ng/mL; CA 125, 2.5 U/mL; CA 15.3, 1.6 U/mL; and urea 1.2 mg/mL.....	168
Figure 6.13 - Selectivity study of DSSC/biosensor with single solutions of CEA and interfering species. CEA 50 ng/mL; CA 125, 2.5 U/mL; CA 15.3, 1.6 U/mL; and urea 1.2 mg/mL..	169
Figure 7.1 - Schematic representation of the several stages of the Hybrid DSSC set-up (B) with the photoanode (A) and biosensing film assembly back-side of DSSC/CE (C): eletropolymerization (1); Template Removal (2) and rebinding (3); combined in DSSC cell.....	174
Figure 7.2 - Photograph of the masks used during the deposition of (A) the Au and Cr films and (B) the ITO film on DSSC/CE.....	176
Figure 7.3 - Schematic representation of the design of the sensing system for the deposition process of (A) Au and ITO materials on DSSC/CE, and a (B) picture of the system after deposition on the back-side of DSSC/CE, indicating the location for MIP and EM deposition.	180
Figure 7.4 - A) Cyclic voltammogram of 3-electrode system with WE/Gold recorded of a solution of 5.00 mmol/L $[\text{Fe}(\text{CN})_6]^{3-/4-}$ prepared in an aqueous solution of KCl, at different scan rates, and B) the corresponding plots of the anodic/cathodic peak currents against the square root of the scan-rate.....	181
Figure 7.5 - Cyclic voltammogram data of the different steps involved in the assembly of MIP-CEA, using the 3-electrode system with a WE of Gold. Data corresponding to 5.00 mmol/L $[\text{Fe}(\text{CN})_6]^{3-/4-}$ readings in PB buffer, pH=7.00	183
Figure 7.6 - Raman spectra of the different materials followed along the assembly of the biosensing	184
Figure 7.7 – Picture (left) picture of 3 electrode system for EM (1) and MIP (2) deposition on the back-side of DSSC/CE and visible spectra (right) of the ITO film in glass.....	185
Figure 7.8 - Performance of the EM in electrochemical system with 3-electrode system.	186

Figure 7.9- Biosensing device integrated outside of DSSC produced by nano/microfabrication techniques, using PV measurement system. The resulting signal ($J-V$ and power conversion efficiency characteristic curves) is obtained from potentiostatic.....	187
Figure 7.10 - Photocurrent density-photovoltage ($J-V$) and power conversion efficiency characteristic curves of the DSSC with A) ITO glass and B) FTO glass on cathode.....	188
Figure 7.11 - Schematic representation A) DSSC/CE-WE, which the current flow across WE/Gold surface or B) DSSC/CE-AE, using an electrolyte as interfacial region between WE/Gold and AE. Current flow on Biosensor without A ₁) or with B ₂ electrolyte.	190
Figure 7.12 - $J-V$ and power conversion efficiency characteristic curves of hybrid DSSC assembled: WE/Gold; WE/Gold/MIP-CEA and WE/Gold/MIP using Biosensor reading: A) without or B) with electrolyte of 3.00 mol/L KCl on its surface.	191
Figure 7.13 - EIS data of hybrid DSSC using WE/Gold reading: (Blue colour) without or (Pink colour) with electrolyte of 3.00 mol/L KCl on its surface.	193
Figure 7.14 – $J-V$ and power conversion efficiency characteristic curves of hybrid DSSC with corresponding calibration curves (inset, as relative η . Versus $g_{og}[CEA]$) of the WE/Gold/MIP on hybrid DSSC, after incubation of increasing concentrations of CEA standard solutions, prepared in PB buffer. Biosensor reading: A) without or B) with electrolyte of 3.00 mol/L KCl on its surface.....	194
Figure I.1 - EIS data for different iron redox probe concentrations prepared in HEPES buffer.	221
Figure I.2 - Calibration curve obtained for a CRT sample. S corresponds to the slope of the experimental calibration; R_{ct} the charge transfer resistance of each spiked level; and $[k]$ the known concentration of carnitine present in the each level of spiked sample.	222
Figure I.3 - Calibration curve obtained for CRT in synthetic urine.....	223
Figure II.1 - Electropolymerization graph of EBT by CV in PBS buffer pH 7. (A) The electropolymerization graph of EBT at 100 mV/s, indicating anodic peaks (1 and 2) and cathodic peak (3); (B) Influence of protein presence during electropolymerization process.....	226

Figure II.2 - Nyquist plots for polymeric systems formed with different BSA concentrations, evaluated in $[\text{Fe}(\text{CN})_6]^{3-/4-}$ in PBS buffer pH 7. (A) 1.00×10^{-5} mol/L; (B) 1.00×10^{-6} mol/L; (C) 1.00×10^{-7} mol/L.	227
Figure II.3 - Nyquist plots of the same MIP film in $[\text{Fe}(\text{CN})_6]^{3-/4-}$ in PBS buffer pH 7.00, read after BSA incubation periods of (A) 15 min, (B) 20 min, or (C) 30 min, and the corresponding calibration curves (D).	228
Figure II.4 - Bode diagrams obtained at the assembly of MIP (1) and NIP (2) films on carbon supports, corresponding to readings in $[\text{Fe}(\text{CN})_6]^{3-/4-}$ solution, prepared in PBS buffer, pH 7.00.	229
Figure II.5 - Selectivity study of the BSA sensor.	231
Figure II.6 - Calibration curves of the MIP BSA sensor assembled directly on the carbon support or on a PEDOT film, prepared in simulated serum.	232
Figure III.1 - Scheme of Synthesis of SNS-NH ₂	233
Figure III.2 - ¹ H- NMR spectrum of SNS-NH ₂ in CDCl ₃	233
Figure III.3 - Performance of electrochromic material in electrochemical system with 3-electrodes and under the indicated working potential (against Ag/AgCl reference electrode).	234
Figure III.4 - Performance of electrochromic material when coupled with DSSC-PEDOT (DSSC Potential).	234
Figure IV.1 - SEM images and EDS analysis of photoanodes prepared with (A) TiO ₂ or (B) TiO ₂ with AuNPs, both sensitized with dye N719.	235
Figure IV.2 - EC performance representing MIP _(TiO₂) behavior against CEA increasing concentrations in the range of 0.10 ng/mL to 100.00 µg/mL in real urine from healthy individual, diluted 1000x.	236
Figure IV.3 - EC performance representing MIP _(TiO₂+NPs) behavior against CEA increasing concentrations in the range of 0.10 ng/mL to 100.00 µg/mL in real urine from healthy individual, diluted 1000x.	236

List of Tables

Table 2.1 - Cancer biomarkers currently used in clinical practice.	43
Table 2.2 - Previous immunosensors reported in the literature for CEA.	47
Table 2.3 - Previous works reporting MIP-based biosensors with electrochemical transducer for CEA and CRT detection.....	63
Table 2.4 - Electrochromism observed in conducting polymer.	73
Table 3.1 - Analytical data extracted from the collected Raman spectra of the several materials.	86
Table 4.1 - Analytical data extracted from the collected Raman spectra of the several materials.	116
Table 4.2 - Previous works reporting molecularly-imprinted polymers for BSA detection.	120
Table 5.1 - Photovoltaic parameters of DSSCs based on Pt and PEDOT counter electrodes, using different photoanodes areas (0.2 cm ² , 0.7 cm ² , and 1.4 cm ²).....	133
Table 5.2 - Raman intensity and Raman shift of typical peaks observed in the Raman spectra of different materials (Peaks 1 to 4 signalled in Figure 5.6).....	137
Table 5.3 - Photovoltaic data obtained with the hybrid DSCC/biosensor device, at the different stages of the biosensing film assembly, obtained for a photoanode area of 0.7 cm ²	139
Table 5.4 - Previous works reporting MIP materials for CEA detection in the literature.	144
Table 6.1 - Photovoltaic features of DSSCs assembled with photoanodes containing or not AuNPs and a CE of FTO/PEDOT/MIP.....	163
Table 7.1 - Photovoltaic-parameters of DSSCs based on different CEs.	189

Table 7.2 - Photovoltaic-data obtained with the hybrid DSSC, at the different states of biosensing film assembly on DSSC/CE/biosensing, obtained with reading of DSSC/CE-WE.	191
Table 7.3 - Photovoltaic-data obtained with the hybrid DSSC, at the different states of biosensing film assembly on DSSC/CE/biosensing, obtained with reading of DSSC/CE-AE.	192
Table I.1 - Further bioanalytical Parameters.....	224
Table II.1 - Circuit report of plot fitted to experimental data using equivalent circuit.	230

To my lovely grandmother Rosa and grandfather Manuel
and
to my mother for the encouragement and love in all moments of my life.

1. Introduction

1.1. Motivation

Early detection of cancer diseases can increase the effectiveness of treatment and consequently increase the survival rate of patients. In the case of cancer diseases treatment, it is important an early diagnosis, because, according to the World Cancer Report 2018, published by the World Health Organization, these illnesses cause many deaths worldwide. The most common causes of cancer death are lung, prostate, colorectal and breast cancer diseases [1]

The diagnosis of cancer is often made by using conventional imaging techniques, as X-ray, computed tomography, resonance and ultrasound, but biochemical methods, as cytometry or biopsy, may also be employed [2-5]. Overall, these methods present high cost, take time and may be at the borderline between life and death, while requiring significant economic/human resources [6]. Moreover, a biopsy is an invasive approach that must be avoided and none of the conventional approaches is available in point-of-care (POC) analysis, which is today the main tool for an early detection.

In general, POC testing allows performing the clinical analysis near the doctor, thereby providing the required information in time to carry out a more accurate and earlier diagnosis. POC testing can also ensure more accurate data by avoiding analyte changes during sample transport/storage, caused by delayed release of analytes (e.g., release of K^+ from red blood cells during refrigerated storage), by continued metabolism (e.g., decrease in glucose/pH and increase in lactate from active red blood cells under hypoxic conditions), and by protein/peptide degradation in whole blood [7, 8]. The devices involved in POC testing should be portable, small, easy to use and carry, and inexpensive [9, 10].

The combination of biological molecules as biorecognition element with compact apparatus (for signal reading) is today the closer approach meeting POC requirements. These devices, also known as biosensors, have emerged several years ago to reproduce biological reactions on a suitable support. In general, biosensors use biological molecules as biorecognition element, in direct contact with a transducer of optical, mass, magnetic or electrical nature [11-13]. The main objective of the biorecognition element is to provide the sensor the ability to interact with the target analyte and distinguish it from other species that may be present in the sample.

So far, some biosensors have been developed to monitor cancer diseases in POC [14, 15]. However, most of these present some economic and/or social limitations. The most common biosensors published for this purpose are immunosensors [16-18], where the biorecognition element is an antibody and their mode of operation is inspired by the immune system [19, 20]. Natural antibodies are very expensive materials with little stability, leading to high cost devices with short lifetimes. Moreover, these biosensors require a dedicated energy source that may hamper the portability, as these are always linked to transducing and measuring apparatus.

Thus, this project aims to develop novel devices for screening cancer biomarkers in POC, with the purpose of reducing the requirements of existing biosensors and improve early detection. Only biomarkers present in biological fluids and relevant to cancer diseases were considered herein. Carcinoembryonic Antigen (CEA) and carnitine (CRT) were selected for this purpose. The biorecognition elements used to selectively detect these biomarkers were of synthetic nature, employing molecular Imprinting (MI) technology. The molecularly-Imprinted Polymer (MIP) materials were further interfaced as a counter electrode (CE) in a Dye Sensitized Solar Cell (DSSC), to ensure the production of a self-powered hybrid system. Finally, self-signaling was ensured by coupling to this hybrid system an electrochromic cell (EC). Overall, it was possible to produce a self-powered and self-signaled device to monitor cancer biomarkers in POC applications.

1.2. Structure of this thesis

This thesis reports the sequential development of an innovative biosensor for cancer biomarker detection with self-powered and self-signalling features. It is organized in eight chapters.

The present chapter, **Chapter 1** gives the motivation of the developed work along to thesis and describes its structure and framework, listing also the publications and presentations associated with this PhD.

Chapter 2 introduce a brief literature review about theoretical contextualization, essential for the different stages of the research: cancer biomarkers, main components of biosensors as biorecognition elements and transducers, highlighting those with greater relevance to the present research work. Thus, it addresses specifically the biomarkers: CEA and CRT, which are associated with colorectal and ovarian cancer diseases, respectively. Moreover, a general concept about transducers used for target monitoring, as well as photovoltaic cell (PV) and EC used to create the autonomous device is shown in this chapter.

The following chapters from 3 to 7, report development, characterization, applications of electrochemical assays of biosensors, using poly(3,4-ethylenedioxythiophene) (PEDOT), not only as biomimetic material, but also as conductive material on the transducer support. As conventional DSSCs employ conductive polymers as catalytic materials in their CE, the idea would be to develop a biosensor based on a MIP film also produced from these materials.

Chapter 3 shows a biosensor for potential cancer biomarker, CRT, tailored on a novel and inexpensive support to prepare the use electrical transduction. The support uses cellulose paper as substrate, made hydrophobic with solid wax and covered by a home-made conductive ink having graphite as core material. The recognition material consisted of an antibody-like receptor film for CRT, tailored on this support and prepared by electrically sustained polymerization of 3,4-ethylenedioxythiophene (EDOT) or dodecylbenzenesulfonic acid (DBS). The performance of the biosensor for screening CRT was successfully achieved by electrochemical measurements and the film displayed high sensitivity/selectivity for rebinding CRT. Although PEDOT is widely used as a catalytic material in DSSC, herein it also

demonstrated to be a good biomimetic material for biomolecule screening applications in POC.

Although low limit of detection (LOD) and good sensitivity features were obtained by the previous biosensing devices, additional studies were made in **Chapter 4** towards the direction of an interface between the biosensor and the PV, also yielding improved analytical features. For this purpose, two different catalytic materials in the CEs of DSSCs were tested as support to assemble the MIP. This included carbon and the conducting polymer PEDOT. The two approaches used Bovine Serum Albumin (BSA) as model target protein, instead of the typical protein cancer biomarker due to its high cost. The polymeric material acted as a plastic antibody for BSA and was obtained through a bulk imprinting strategy, by electropolymerizing Eriochrome Black T (EBT). EBT was never employed before to produce a polymeric protein imprinted material.

In **Chapter 5**, a new approach is studied to integrate the biosensor inside the PV coupled to an EC. Polypyrrol (PPy) is widely used as catalytic material in DSSC and it is also employed as a biomimetic material in biosensors. Therefore, the CE of the DSSC was modified with an antibody-like film by polymerizing pyrrole (Py) for CEA detection. This approach was expected to lead to a good stability and performance of the biosensor inside the DSSC. PEDOT was selected as electrocatalyst element for the CE material, tested on conductive glass and compared with a carbon-based material, as explored in the previous chapter. Firstly, the biosensing film is optimized and evaluated in a conventional 3-electrodes electrochemical system (the working electrode (WE) the auxiliary electrode (AE) and the reference electrode (RE)). Then, it is integrated inside the DSSC and evaluated by monitoring several photovoltaic parameters, as power conversion efficiency (η), short-circuit current density (J_{SC}) and fill factor (FF). Finally, this biosensing device is coupled to the EC and the corresponding analytical response evaluated by the monitoring its colour in the presence of different concentrations of CEA, in order to provide semi-quantitative data. The corresponding colour coordinates were also extracted and manipulated to address a quantitative information.

The sensitivity of this biosensing device is improved further in **Chapter 6** by employing plasmonic nanostructures on the photoanode of the DSSC to improve the cell efficiency, and by adding EDOT into the MIP film to improve the conductivity features of the CE. Gold

nanoparticles (AuNPs) were used as plasmonic nanostructures in the DSSC, and their effect was monitored by preparing photoanodes without these materials. The biorecognition element used herein was made by the electropolymerization of Py, as in the previous work, but this time EDOT was also added into it. Once again, PEDOT was used as the cathode support for the DSSC; the same biomarker (CEA) was selected as target; and the coloured readout was made by the same EC and approach.

Chapter 7 describes a new approach to simplify the design of the autonomous device and the handling of biosensor under POC context. In chapters 5 and 6, the analysis of the sample requires opening and closing the PV in subsequent readings of CEA, which may turnout time-consuming. Herein, an electrical circuit was designed to allow the production of both MIP and EC on the backside of a conductive glass by nano/microfabrication approaches using sputtering technique. The geometries of the sensing areas were inspired in the commercial 3-electrodes systems. Suitable electrical connections were made to ensure a suitable connection between the three parts of the system, the PV, the MIP and the EC. The electrical connection of the biosensor is produced by deposition of Gold (Au) material and the electrochemical/optical parameters were considered to evaluate its performance. The target biomarker selected in this work was CEA.

Chapter 8 summarizes the main results obtained along the several works described in this thesis and presents the future perspectives for this research work.

1.3. List of publications

1.3.1. Paper published in international scientific journal

- (1)** Felismina T.C. Moreira, Ana P. Moreira-Tavares, M. Goreti F. Sales. Sol-gel-based Biosensing Applied to Medicinal Science. *Current Topics in Medicinal Chemistry*, 15(3), 245-255, 2015.
- (2)** Ana P.M. Tavares, Nádia S. Ferreira, Liliana A.A.N.A Truta, M. Goreti F. Sales, Conductive Paper with Antibody-Like Film for Electrical Readings of Biomolecules. *Scientific Reports* 6, Article number 26132, 13, 2016.

- (3) Nádia S. Ferreira, Ana P.T. Moreira, M.H.M. de Sá, M. Goreti F. Sales. New electrochemically-derived plastic antibody on a simple conductive paper support for protein detection: Application to BSA. *Sensors & Actuators B*, 243, 1127-1136, 2017.
- (4) Ana P.M. Tavares, M. Goreti F. Sales. Novel electro-polymerized protein-imprinted materials using Eriochrome Black T: application to BSA sensing. *Electrochimica Acta*, 262, 214-225, 2018.
- (5) Ana P.M. Tavares, Liliana A.A.N.A Truta, Felismina T.C. Moreira, G. Minas, M. Goreti F. Sales. Photovoltaic, plasmonics, plastic antibodies and electrochromism combined for a novel generation of self-powered and self-signalled electrochemical biomimetic sensors. *Biosensors and Bioelectronics*, 137, 72-81, 2019.
- (6) Ana P.M. Tavares, Liliana A.A.N.A Truta, Felismina T.C. Moreira, Liliana P.T. Carneiro, M. Goreti F. Sales. Self-powered and self-signalled autonomous electrochemical biosensor applied to carcinoembryonic antigen determination. *Biosensors and Bioelectronics*, 140, 111320, 2019.

1.3.2. Presentations made in scientific conferences

- (1) Ana P.M. Tavares, Nádia S. Ferreira, Liliana A.A.N.A. Truta, M. Goreti F. Sales. A new biomimetic sensor for detecting carnitine, a potential biomarker in ovarian cancer. Poster J6 1st ASPIC International Congress, Fundação Calouste Gulbenkian, Lisboa, 25-26 November 2014.
- (2) Ana P.M. Tavares, M. Goreti F. Sales. Synthesis of an antibody-like material for the detection of Albumin. Poster 2, Graduate Student Symposium on Molecular Imprinting, Medway School of Pharmacy, Kent, 27-28 August, 2015.

- (3)** Nádia S. Ferreira, Ana P.M. Tavares, M. Goreti F. Sales. New modified electrochemical conductive paper support for BSA detection. Poster 8, Graduate Student Symposium on Molecular Imprinting, Medway School of Pharmacy, Kent, 27-28 August, 2015.
- (4)** Carolina Hora, Liliana A.A.N.A. Truta, Ana P.M. Tavares, Manuela F. Frasco, Ana M. Piloto, M. Goreti F. Sales Integrating biosensors in photovoltaic cells: the 3P's project. Poster 27, iBEM – International Biomedical Engineering Meeting, Biblioteca Almeida Garrett, Porto, 21 of March 2016.
- (5)** Ana P.M. Tavares, M. Goreti F. Sales. A novel Antibody -like material assembled on novel screen -printed electrodes for screening CEA Cancer Biomarker. Poster P2.306, Biosensors 2016, Svenska Massan, Gothenburg, Sweden. Congress 25-27 May 2016.
- (6)** Carolina Hora, Ana P.M. Tavares, Adélio Mendes, M. Goreti F. Sales. A novel Biomimetic material integrated in a conductive polymer powered by a dye-sensitized solar cell. Oral O17, Biosensors 2016, Svenska Massan, Gothenburg, Sweden. Congress 25-27 May 2016.
- (7)** Ana. P.M. Tavares, Carolina Hora, M. Goreti F. Sales. A novel Antibody-like material assembled on novel device for detection CEA cancer biomarker. Oral O26, Graduate Student Symposium on Molecular Imprinting, Medway School of Pharmacy, Kent, 27-28 de Agosto 2015.
- (8)** Ana P.M. Tavares, P.J. Sousa, Carolina Hora, G. Minas, Goreti Sales. Biosensors and photovoltaics merged: towards a self-sustained device. Oral B17, EMN Meeting on Biomaterials 2017, Milan, Italy. Congress 15-18 August 2017.

2. Theoretical Concepts

2.1. Cancer Incidence

Cancer is the uncontrolled growth of cells, which often invades the surrounding tissue. This growth can spread to any part of the body through the blood and lymph systems [21]. According to World Health Organization (WHO), 18.1 million new cases and 9.6 million death in 2018 were associated with cancer and it is estimated that cancer is the second leading cause of death in the world [22]. The most recent data of GLOBOCAN, 2018, revealed that the higher levels of cancer cases are in Asia (48.1 %), followed by Europe (23.5 %) and North America (13.2%). The other continents presented registries lower to 8%, as seen in **Figure 2.1-A)** [22].

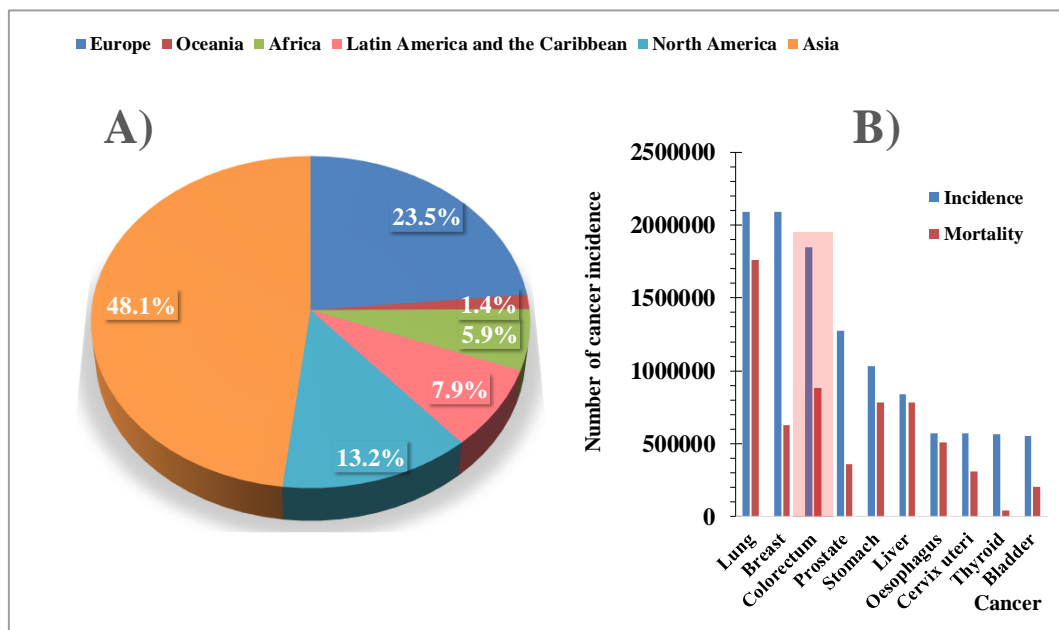


Figure 2.1 - Cancer incidence, expressing the **(A)** number of new cases in 2018, five Continents, all cancers, both sexes, all ages and **(B)** age-standardized incidence and mortality rates in 2018, worldwide, both sexes, all ages.

Among the most diagnosed types of cancer, colorectal appears in the third position, corresponding to 10.2 % of the total cases, with one of the highest mortality rates (9.2 %) in the world [23-25] (**Figure 2.1**). In 2018, 1.8 million of new colorectal cancer cases were estimated and 881000 deaths in worldwide. Colorectal cancer (**Figure 2.2**) is one of the most affected by the current lifestyle adopted by our societies. It is estimated that 75 % or more of colorectal cancer incidence is attributed to the high consumption of red/processed meats, and fast food, coupled with the low intake of vegetables and fruits. Moreover, smoking, drinking alcoholic beverages, along with obesity and/or diabetes II have been also correlated with colorectal cancer [22, 26-28]. Overall, improving this scenario requires early diagnosis, as this increases the chances for a successful treatment of this disease.

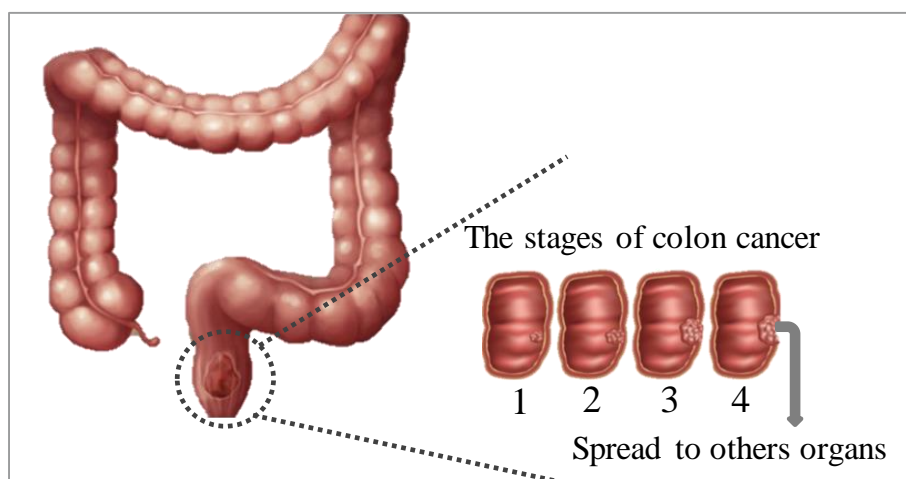


Figure 2.2 - Illustration of different Stages of Colorectal cancer.

There are some biomarkers employed in the detection of colorectal cancer, being CEA the most common among these. CEA is an important tumor marker and it has been employed in the diagnosis of over 90 % colorectal cancer [29, 30]. It is also used as a marker to follow-up disease progression/regression [31].

Another cancer disease that presents a high number of cases and death is ovarian cancer. According to WHO in 2018, ovarian cancer was the 8th most diagnosed cancer among women, presenting 295 414 new cases (corresponding to 3.4 %) and 184 799 (corresponding to 4.4 %) cancer deaths (Figure 2.3) [32].

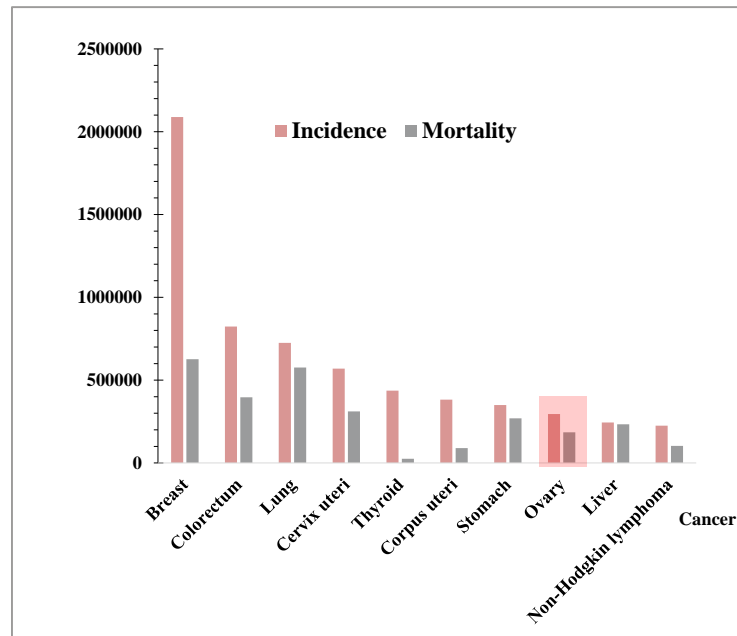


Figure 2.3 - Cancer incidence, expressing the number of incident cases and death in 2018, worldwide, females, all ages.

This cancer is considered one of the deadliest gynecologic cancer and it is usually diagnosed at an advanced stage [33, 34]. However, when ovarian cancer is found in its early stages, the treatment is more effective, and patient has more chance to survive. So, it is necessary an early detection by screening of specific biomarker.

Some studies have identified a biogenic quaternary amine, more specifically the CRT, in the normal ovary and transformed in primary and metastatic ovarian cancer [33, 35, 36]. Thus, this metabolite has been identified as potential biomarker of ovarian cancer.

2.2. Cancer detection

Macroscopic imaging techniques are at the core of the conventional methods for detecting cancer diseases and include tomography, magnetic resonance imaging and ultrasound. These techniques provide anatomical information without tissue invasiveness, determining the location and extension of the lesion caused by the tumor [2, 3, 5]. Nevertheless, these techniques have some drawbacks, considering the low sensitivity in identifying cancer at an

early stage, the high operator-dependency, the high expensive, the time consuming procedures and the inability to operate outside proper facilities. In addition, the results obtained can induce a false negative values in cancer screening [4, 6, 37].

After imaging screening, the confirmation of the disease is established by means of a tissue biopsy. Biopsy is a surgical procedure guided by an imaging technique that allows collecting directly cells/tissues from the tumor, which must be observed later by a pathologist later to establish a more accurate diagnosis. In essence, biopsies are invasive procedures that cause a great discomfort to the patient [38]. Moreover, these may not lead to a reliable result, because the sample taken for analysis may not represent the overall tissue malignancy. In addition, the result of the analysis is not promptly available, delaying the initiation of the treatment, whenever it is necessary.

In general, cancer is difficult to detect in its initial stage, using the conventional imaging and visual inspection methods, due to the absence of visible morphological alterations in the tissues. Striving to understand more about cancer, researchers have found in the past decades that cancer installation and progression is related to biochemical changes that also occur in circulating fluids. These biochemicals are commonly known as cancer biomarkers [39-41].

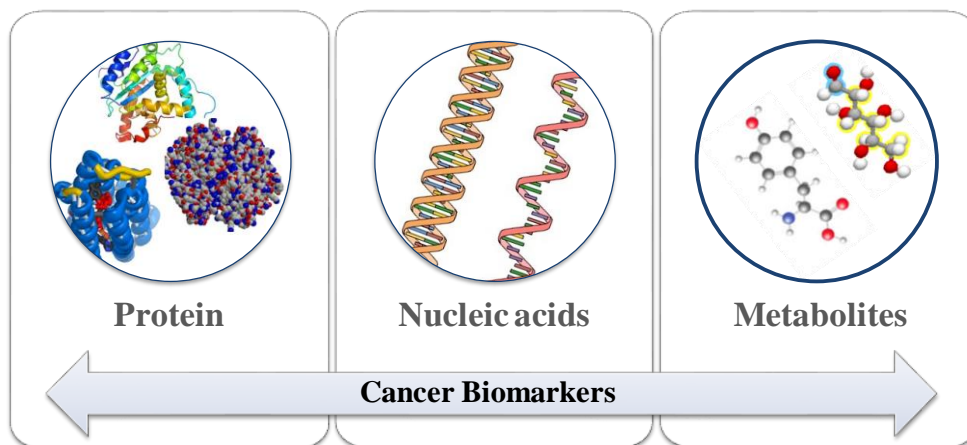


Figure 2.4 - Illustration of different kinds of cancer biomarkers.

Typically, a biomarker is a biomolecule that is produced by the body and that signals a specific biological event. Thus, a cancer biomarker is defined as a biomolecule that is produced

by the body in response to cancer cells growth. Cancer biomarkers include proteins, nucleic acids, metabolites, and other biochemicals (**Figure 2.4**) found in biological fluids or in tissues with a certain concentration range. A cancer biomarker must be a quantifiable biological parameter that is measured and evaluated as an indicator of the presence of an abnormal condition based on their physiological levels [39, 41, 42]. This makes cancer biomarkers a very important tool for diagnosing and monitoring cancer installation, response to treatment or eventual cancer recurrence [14, 42].

In general, as cancer biomarkers are present in biological fluids as blood, urine or saliva, their determination may be established quickly in POC, in an earlier stage of the disease [39, 40]. However, a single biomarker does not have the full power to produce an accurate information, and a panel of biomarkers becomes necessary for this purpose. Currently, there are several biomarkers used in clinical practice for cancer detection (**table 2.1**).

The most relevant cancer biomarkers for the purposes of this work are CEA and CRT, which highlight among the many cancer biomarkers currently emerging in the literature [39, 40]. Overall, these offer new promises for monitoring cancer events in an earlier stage, although clinical validation may still miss in some of these [33, 35, 36].

Table 2.1 - Cancer biomarkers currently used in clinical practice.

Biomarker	Cancer	Levels in cancer	Ref.
Prostate specific antigen (PSA)	Prostate cancer	> 4.00 ng/mL	[43-46]
CEA	Colorectal cancer	> 10 ng/mL	[47-49]
CA 125	Ovarian cancer	> 35 U/mL	[50-53]
CA 19-9	Pancreatic cancer	> 37 U/mL	[54-57]
CA 15-3	Breast cancer	> 30 U/mL	[58-60]

CRT, also known as 3-hydroxy-4-*N,N,N*-trimethylaminobutyric acid, is a biogenic quaternary amine, playing an essential role in the transport of long-chain fatty acids into the mitochondrial matrix [61]. Besides its important role in cellular metabolism and energy production, CRT also displays antioxidant properties, protecting cells from oxidative stress conditions related to several diseases [62-64]. In 2011, Fong and co-authors identified CRT as a metabolite present in normal ovary and increased in primary and metastatic ovarian cancer [33]. This way CRT might be considered a potential biomarker of ovarian cancer. Normally, CRT metabolite is presented a normal physiological value between 1-5 μM in human plasma [33, 65].

CEA is a glycosylated protein with 180-200 kDa molecular weight, with an isoelectric point of ~ 4.7 . It is expressed in normal mucosal cell and overexpressed in most adenocarcinomas, especially in colorectal [66-68]. Normally, the detection of CEA is done in serum samples, presenting a normal physiological value between 2.5 ng/mL and 5 ng/mL, in non-smokers and smokers, respectively [47, 49, 69, 70]. The increase in serum CEA concentration is directly proportional with the colorectal cancer stage.

Overall, these biomarkers are monitored in liquid biopsies (biologic fluids), which facilitates the collection of the patient sample. Moreover, these are an interesting choice for establishing wide screening programs and applications in POC context [71]

2.3. Biosensors

In the last decades, biosensors have become an essential tool in the field of medicine, especially in cancer diagnosis [15, 72-74]. Typically, biosensors are small and cheap devices, being easy to use as analytical tools and providing a quick response, on site, with a low sample volume, which are relevant features to be applied on wide cancer disease screening programs [6, 75, 76].

A biosensor is a device that combines a biological component with a physical transducer. The biological component is immobilized on a support and responsible for interacting with a given target analyte, which is further converted by the transducer into a measurable signal

(Figure 2.5) [11, 73]. In general, a biosensor estimates the level of biomarker present in a biological sample by producing a signal that is associated with its concentration.

Biosensors can be classified according to the mechanism that confers the specificity of the analytical response, or the mode of signal transduction, as explained in the following sections [12, 77].

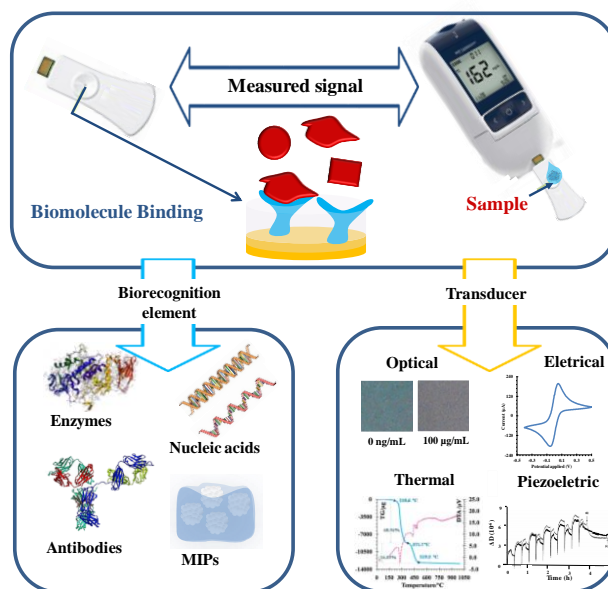


Figure 2.5 - Schematic representation illustrating the main function and use (top) of a biosensor device, along with the device main elements (bottom).

2.3.1. Biorecognition element

The biological recognition plays crucial role in the sensitivity and specificity of the sensor device since it is responsible for distinguishing the specific biomolecule from interfering molecules present in a biological sample. This includes use of proteins (antibodies, enzymes, membrane receptors, etc.) and nucleic acids (DNA, RNA, aptamers, etc.), among others [12, 15, 73]. Yet, other biosensing recognition elements comprise non-naturally occurring compounds, such as synthetic biomimetic materials. In general, biosensors based in biological elements have been classified into DNA biosensors, enzymatic sensors, or immunosensors [77, 78].

In general, when nucleic acids are used as biorecognition element, the recognition process occurs through base pairing interactions between the target sequence and its complementary

sequence, which is related to tumor specific genetic sequences and immobilized on the transducer [79]. Thus, the target analyte is also a nucleic acid, and its detection is made typically with great specificity and affinity [80, 81]. There are also specific nucleic acid sequences that may be designed to capture a given compound, which is not a nucleic acid itself. These are named aptamers and undergo a very expensive and complex process to be successfully designed. Moreover, nucleic acid sequencing is, also, quite expensive [82].

Meanwhile, enzymatic sensors use an enzyme as bioreceptor material, which recognizes a given biomolecule and then reacts with it, to promote a change in the signal of the transducer. Despite the high selectivity and sensitivity of the enzymatic sensors [83, 84], enzymes are expensive biological materials that may change their catalytic action with several variables, including temperature and the surrounding medium. Thus, their reliable operation in a biosensing device is restricted to specific conditions [72, 85], leading to short lifetime devices that need to be stored properly.

Typically, immunosensors use an antibody as biorecognition element, for which its operation is based in antibody/antigen interactions. Such interactions are monitored under conditions that decrease non-specific interactions, thereby conferring a good selectivity to the biosensor response [19, 77, 86-88].

As an example of the relevance of immunosensors, **table 2.2** lists the immunosensors reported in the literature for CEA, highlighting the different detection modes and the main analytical features of the reported device. Almost all methods are capable to interact with samples lower than the normal physiologic level (2.5 - 5 ng/mL) with LODs values varying from 1.5 pg/mL to 3.00 ng/mL, except the works reported in [89, 90]. Additionally, these immunosensors also presented differences in terms of wideness of the concentration response range. Piezoelectric-based detection is linked to the higher LODs observed. Moreover, analytical performance of immunosensors can be improved when nanostructured materials are introduced into the sensing element [91-94], being able to achieve concentrations of 4.90 pg/mL. There are also some immunosensors using enzymes-linked markers to provide a better sensitivity [86, 88, 95-99], and achieving concentrations below 1.5 pg/mL and wide linear response. Overall, antibodies used in biosensors offer great advantage in terms of specificity and selectivity, but also hinder major final goals, like cost,

stability, durability and robustness of the final device. An alternative to natural antibodies consists in the fabrication of biomimetic materials, aiming at replacing these by synthetic analogues.

Table 2.2 - Previous immunosensors reported in the literature for CEA.

Biorecognition Element	Material support	Immunosensor assembly	LOD	Linear response	Ref.
HRP-labelled anti-CEA	Carbon fiber	anti-CEA was immobilized on carbon fiber microelectrodes modified with AuNPs and functionalized with protein A	5.0 pg/mL	0.01-160 ng/mL	[88]
Anti-CEA	Quartz crystal	Anti-CEA modified by Sulfo-LC-SPDP was immobilized onto surface of the gold membrane placed on quartz crystal.	1.50 µg/mL	1.5-30 µg/mL	[89]
Anti-CEA	Quartz crystal	Anti-CEA was immobilized onto gold previously deposited on quartz crystal and functionalized with Protein A.	66.7 ng/mL	66.7-466.7 ng/mL	[90]
Anti-CEA	Pt	Anti-CEA was immobilized on Pt electrode modified with Au and PANI nanocomposites and graphene quantum dots.	0.01 ng/mL	0.5 to 1000 ng/mL	[91]

HRP: horseradish peroxidase; GHS: nanogold hollow microspheres; AuNPs: gold nanoparticles; Sulfo-LC-SPDP: sulfosuccinimidyl 6-(3'(2-pyridyldithio) propionamido) hexanoate; Mo: molybdenum; Mn₃O₄: manganous–manganic oxide; Fe₃O₄NPs: magnetic iron oxide nanoparticles; MUDA: 11-mercaptoundecanoic acid; EDS: 1-ethyl-3-(3 dimethylaminopropyl)-carbodiimide; NHS: N-hydroxysuccinimide; MWCNTs: Carbon nanotube, multi-walled.

Table 2.2 - Previous immunosensors reported in the literature for CEA. (cont.).

Biorecognition Element	Material support	Immunosensor assembly	LOD	Linear response	Ref.
Anti-CEA	Glassy carbon	anti-CEA was immobilized on glassy carbon electrode modified with polythion and AuNPs using BSA as blocking	0.055 ng/mL	0.1 -120 ng/mL	[92]
Anti-CEA	ITO	Anti-CEA was immobilized onto ITO glass modified with a nanocomposite containing MWCNTs, chitosan and Mo-doped Mn ₃ O ₄	4.90 pg/mL	0.1-125 ng/mL	[93]
HRP-labelled anti-CEA	Glassy carbon	HRP-anti-CEA was immobilized onto glassy carbon electrode modified with Prussian blue and a functionalized chitosan membrane with AuNPs and Fe ₃ O ₄ NPs using glutaraldehyde as a crosslinker	10 pg/mL	0.1–220 ng/ mL	[95]
HRP-labelled anti-CEA	Glassy carbon	poly(o-phenylenediamine) nanospheres modified with HRP-labelled anti-CEA was immobilized on glassy carbon electrode using glutaraldehyde as a crosslinker.	3.2 pg/mL	1.0–60 ng/mL	[96]

HRP: horseradish peroxidase; GHS: nanogold hollow microspheres; AuNPs: gold nanoparticles; Sulfo-LC-SPDP: sulfosuccinimidyl 6-(3'(2-pyridyldithio) propionamido) hexanoate; Mo: molybdenum; Mn₃O₄: manganous–manganic oxide; Fe₃O₄NPs: magnetic iron oxide nanoparticles; MUDA: 11-mercaptoundecanoic acid; EDS: 1-ethyl-3-(3 dimethylaminopropyl)-carbodiimide; NHS: N-hydroxysuccinimide; MWCNTs: Carbon nanotube, multi-walled.

Table 2.2 - Previous immunosensors reported in the literature for CEA (cont.).

Biorecognition Element	Material support	Immunosensor assembly	LOD	Linear response	Ref.
HRP-labelled anti-CEA	Graphite	CEA was immobilized on screen-printed electrode modified with toluidine blue and chitosan.	0.19 ng/mL	0.50-31.3 ng/mL	[99]
Anti-CEA	Gold	anti-CEA was immobilized on gold electrode modified with dithiol	0.20 ng/mL	0-200 ng/mL	[100]
Anti-CEA	FTO	Anti-CEA was immobilized with a mixture of EDC/NHS on FTO functionalized with APTES and blocked with BSA.	0.043 ng/mL	0.25-1.5 ng/mL	[101]
Anti-CEA	Gold	Anti-CEA was immobilized with a mixture of EDC/NHS onto gold sensor functionalized with MUDA and blocked with BSA.	3.00 ng/mL	3.00-400 ng/mL	[102]
HRP-GHS labelled anti-CEA	Gold	Anti-CEA was immobilized on gold electrode modified with thionine and functionalized AuNPs with protein A	<1.50 pg/mL	0.01-200 ng/mL	[103]

HRP: horseradish peroxidase; GHS: nanogold hollow microspheres; AuNPs: gold nanoparticles; Sulfo-LC-SPDP: sulfosuccinimidyl 6-(3'(2-pyridyldithio) propionamido) hexanoate; Mo: molybdenum; Mn₃O₄: manganous–manganic oxide; Fe₃O₄NPs: magnetic iron oxide nanoparticles; MUDA: 11-mercaptoundecanoic acid; EDS: 1-ethyl-3-(3-dimethylaminopropyl)-carbodiimide; NHS: N-hydroxysuccinimide; MWCNTs: Carbon nanotube, multi-walled.

Biomimetic materials for antibodies are artificial receptors that display similar properties to those of the natural receptors. These materials consist in tailor-made artificial receptors that bind target analytes in similar way to antibodies, by displaying molecular recognition phenomena of high affinity and selectivity. MI technology is one approach to the production of these biomimetic materials [104, 105]. MI consists in imprinting a specific biomolecule as a template in a three-dimensional rigid structure (**Figure 2.6**). In this process, there are three main steps: complexation **(1)**, polymerization **(2)** and extraction **(3)**. The first step allows the functional monomers to become either strongly linked or interacted with the template molecule, forming a complex (template/monomers). In the polymerization stage, the monomers in this complex are polymerized along with other monomers, generating a rigid polymeric matrix. Finally, the template is removed from the polymeric network, generating vacant imprinted cavities [106, 107].

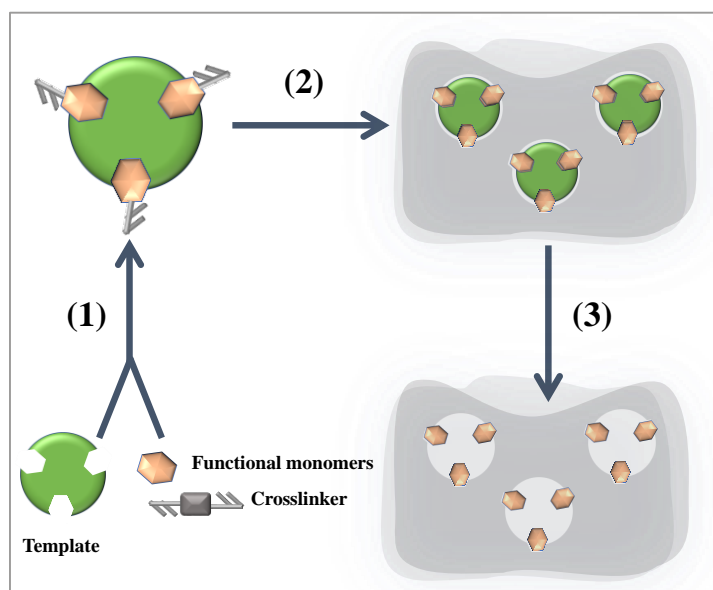


Figure 2.6 - Steps of Molecular Imprinting Polymer synthesis: **(1)** Interaction between template and monomers; **(2)** polymerization and **(3)** template removal.

In general, MIPs can recognize and bind different molecules with similar affinity and specificity to their biological counterparts [108]. Furthermore, assays relying on MIPs offer several advantages, because these materials may be easily tailored with a suitable selectivity

for the target molecule, while offering greater stability than natural antibodies. Furthermore, these are inexpensive, may be reusable and have a low response time for fast screening in biological samples [109-111].

MIPs are typically obtained by free radical polymerization carried out in bulk conditions. The general procedure involves functional and cross-linking monomers that are organized around a template (to be imprinted) and copolymerize next with other monomeric/cross-linking units, after the action of an initiator, to form a cross-linked polymeric structure [106, 112]. The typical monomers used for this purpose are vinyl-based with common functionalities. In a given polymer, monomers with different chemical functions may be employed.

Bulk polymerizations usually take place above 50 °C, under a nitrogen atmosphere and in the presence of a porogenic solvent. These are suitable conditions to imprint small molecular weight molecules (~200-1200 Da), such as antibiotics or amino acids, but unsuitable to imprint proteins (as many cancer biomarkers). As far as possible, the 3D structure of the protein must be preserved under the polymerization reaction, meaning that water-based conditions are required, with pH values close to their natural environment and taking place at a maximum temperature of 42 °C. Yet, the typical initiators have low water solubility. Moreover, the large size of the proteins hinders first their extraction from the polymeric matrix, and later their rebinding [107].

An alternative approach to produce a MIP material with different polymerization conditions is the electropolymerization. In electropolymerization, MIPs are synthesized by applying an electrical stimulus, using mostly phenyl-derived monomers, in aqueous solutions, thereby allowing preserving the natural conformation of the proteins. In addition, electrosynthesis allows creating several nanometer thick polymer films, presenting the advantage of a fine control over polymeric growth around the protein. Compared to traditional polymerization, this one does not require a chemical initiator to trigger the polymerization and the MIP growth occurs directly on the transducer surface. Furthermore, electropolymerization presents other advantages such as fast production and the ability to use few microliters to generate the MIP surface by means of three-electrode systems [107, 112]

There are some works in the literature devoted to cancer biomarkers making use of MIP approaches coupled to electrical polymerization [113, 114]. In these, the electrochemical

detection is mostly employed, as the application of an electrical stimulus demands the presence of electrochemical systems. The advantages of electropolymerization coupled to the previous experience in the field of MIP materials contributed to select a MIP biorecognition element for CRT and CEA assembled by electropolymerization. Typically, there are several transduction approaches that may be employed, but electrochemical is the natural detection system as the assembly of the biorecognition element already requires a three-electrode set-up.

2.3.2. Transduction approaches

The transducer is the element of the biosensor that is responsible for converting the physico-chemical changes produced by the interaction between the biomolecule of interest and biorecognition element into a measurable signal. According to the basic principles of signal transduction, a biosensor can be divided into several types of transducers: thermometric, piezoelectric, optical, and electrochemical [11-13].

The thermometric biosensor is based on heat of reactions caused by the interaction between specific a biomolecule and the biorecognition element, which induces thermal changes and subsequent signal variations [13]. Biosensors with piezoelectric transducers measure the mass change during same interaction, which induces a change in the resonator frequency of the piezoelectric transducer. Optical biosensors are based on a detectable light change on the photodetector transducer that change upon biomolecule/biorecognition element interaction [115]. Finally, electrochemical biosensors monitor this interaction by following the electrical signal after subjecting the chemical system into a specific electrical condition [116].

Among the several transduction schemes, electrochemical transducing offers rapid quantitative information with only small amounts of analyte. The required equipment is of low cost and allows miniaturization, enabling portability and field analysis [116, 117]. Besides, it can provide valuable information about stoichiometry and equilibrium constants, mass transfer processes, velocity and behavior of reactions (reversible, *quasi*-reversible and irreversible) [9].

There are several electroanalytical techniques that may be used, from which the most traditional ones are potentiometry, conductometry, and amperometry [13, 118]. The approaches typically involved in obtaining quantitative data in biosensors include electrochemical impedance spectroscopy (EIS), cyclic voltammetry (CV) or square wave voltammetry (SWV). All these are simple and inexpensive, providing selective readings with low concentrations and low sample volumes [119]. Their single requirement is an electrical energy source.

In general, the electrochemical performance is normally evaluated by a three-electrode cell, in contact with a standard redox probe. The electrodes considered herein are WE, RE (Ag/AgCl) and AE (platinum) (**Figure 2.7**). The performance of the biosensor with increasing concentrations of target biomarker is also obtained by following an electrical signal of interest. This procedure is typically known as calibration curve.

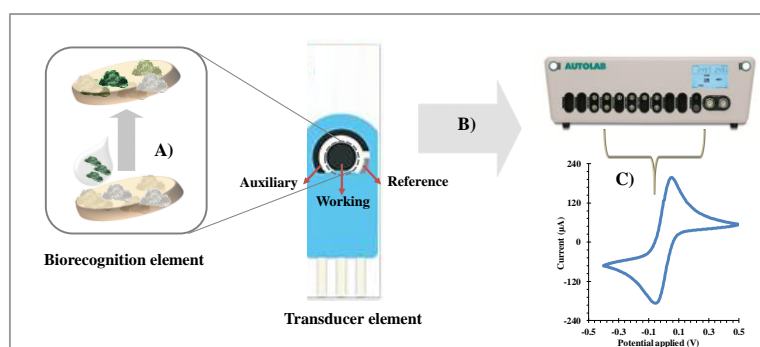


Figure 2.7 - Representative scheme of the principle of operation of a biosensor based on configuration of three electrodes: **(A)** biorecognition process; **(B)** monitoring process of resulting signal from interaction between the target molecule and the biorecognition element on transducer element; **(C)** results it displays in an electrochemical signal.

The electrochemical technique depends on the Ohm's law (**equation 1**) and it is defined by resistance (R) in terms of ratio between electric potential (E) and current (I).

$$R = \frac{E}{I} \quad \text{equation (1)}$$

2.3.2.1. Cyclic voltammetry

CV is the most common, simple and fast electroanalytical technique for acquiring both qualitative and quantitative information about any electroactive species involved in electrochemical reactions. This technique has proven to be very useful in obtaining information about fairly complicated electrode reactions [120]. It consists in applying a potential at a steady scan rate (the rate of change of potential with time, $v = \Delta E / \Delta t$) on the WE, leading to oxidation/reduction reactions of the electroactive species present. Thus, the CV plot measures the resulting electrical current at the WE surface against the applied potential, which is controlled by the RE [121]. When an electrochemical reaction occurs, it can lead to mass transfer of the electroactive species from the solution to the electrode surface, by convection, migration or diffusion. The general shape of the observed voltammogram depends on the reversibility of the redox couple on the electrode surface. According to redox couple features, these can be subdivided in reversible, quasi-reversible and irreversible [121].

Theoretical foundations report that the electrochemical reversibility of a redox couple provides kinetic information on the reaction rate of the redox couple, and it should be fast enough to keep the electron transfer process in equilibrium, expressed by the *Nernst* equation (equation 2).

$$E = E^{\ominus} + 2.303 \frac{RT}{nF} \log\left(\frac{Ox}{Red}\right) \quad \text{equation (2)}$$

In **equation 2**, E is the potential of an electrochemical cell, E^{\ominus} the standard electrode potential, measured against the normal hydrogen electrode (NHE) and the relative activities of the oxidized (*Ox*) and reduced (*Red*) analyte in the system at equilibrium. In the *Nernst* equation, F is the Faraday's constant (96485 C.mol⁻¹), R is the universal gas constant (8.314 J.mol⁻¹), n is the number of electrons and T is the temperature.

The first theoretical analysis of the wave shape for a reversible system was achieved by *Randles* and *Sevcik* [121]. The *Randles-Sevcik* equation (**equation 3**) allows obtaining the peak current (I_p).

$$I_p = -2.69 \times 10^5 n^{\frac{3}{2}} A D^{\frac{1}{2}} C \nu^{\frac{1}{2}} \quad \text{equation (3)}$$

In **equation 3**, n is the number of electrons involved in the reaction, A is the electrode surface area (cm^2), D is the diffusion coefficient of the species (cm^2/s), C is the bulk concentration of the species (mol/dm^3), ν is the scan rate (V/s), and I_p is the peak current.

In a reversible reaction, the total amount of oxidized species at the anodic peak will be equal to the amount of species reduced at the cathodic peak [121, 122]. Thus, one can summarize all the information in a diagnosis for linear scanning and CV at 25°C of reversible reactions:

- linearity between I_p and $\nu^{\frac{1}{2}}$;
- E_p independent from ν ;
- $\Delta E = E_{pa} - E_{pc} = 57.0/n$ mV;
- $|I_{pa}/I_{pc}| = 1$.

The typical response of such reversible redox process may be seen in **Figure 2.8**.

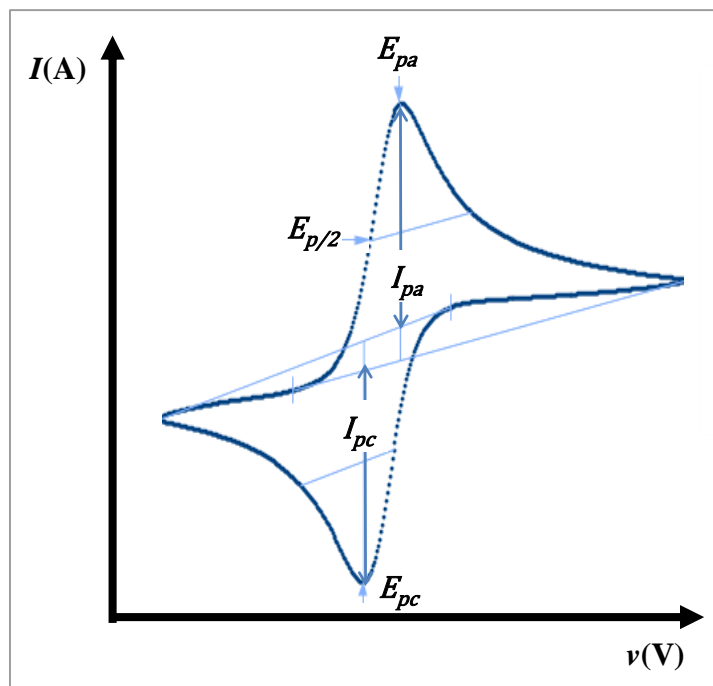


Figure 2.8- Typical voltammogram for a reversible system, where I_{pa} is the Anodic peak current; I_{pc} is the Cathodic peak current; E_{pa} is the anodic peak potential and E_{pc} is the cathodic peak potential.

If one of the above conditions is missing, the system cannot be considered reversible, and should be considered as *quasi*-reversible or irreversible, depending on the extension of the irreversibility.

In irreversible processes the electron transfer kinetics is very slow-moving compared to the timescale of the sweep. In this type of reaction, the value of the cathodic peak current is described by the following **equation 4**.

$$I_p = -2.99 \times 10^5 n(\alpha_c n')^{\frac{1}{2}} A D_0^{\frac{1}{2}} C v^{\frac{1}{2}} \quad \text{equation (4)}$$

In **equation 4**, α_c is the cathodic charge transfer coefficient and n' is the number of electrodes transferred in the rate-limiting step.

However, the electrode processes are not always fast (reversible systems) or very slow (irreversible systems), and sometimes one must consider the whole voltammogram characteristics. This is the case of a *quasi-reversible* behavior, in which the kinetics of the oxidation and reduction reactions must be considered simultaneously. Overall, the extent of irreversibility increases with increased scan rate, while at the same time a decrease in the current of the peak relative to the reversible case and a separation between the anodic and cathodic peak are evidenced, as shown in **Figure 2.9**.

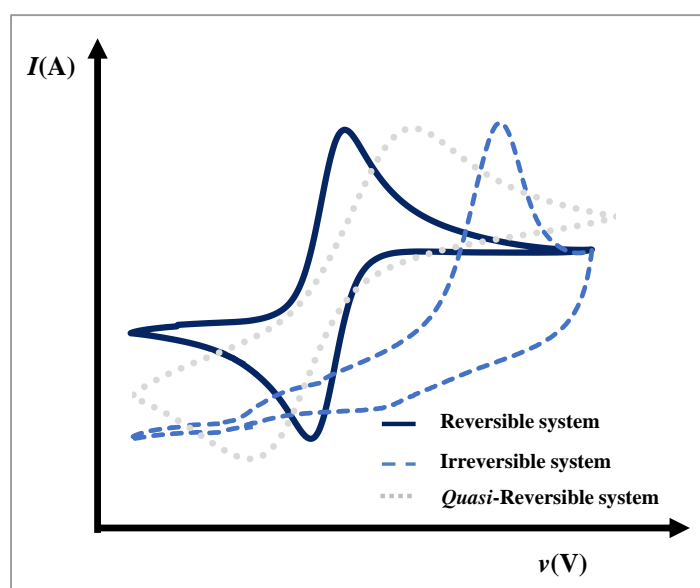


Figure 2.9 - Comparison of typical voltammogram obtained for (ir)reversibility systems.

2.3.2.2. *Electrochemical impedance spectroscopy*

EIS consists in the induction of a small disturbance of the sinusoidal signal on the WE. Under this condition, the electrochemical system under study is affected and gives the subsequent response of the system at a frequency range. The response to the applied disturbance can generate a signal with different phase and amplitude. This measurement of the difference between phase and amplitude allows the analysis of the electrode process in relation to diffusion, double layer and other contributions [121].

In general, EIS evaluates the variations of the electrical transfer charges from the redox system that occur on the surface WE along each modification step. This technique is used for characterizing resistance, corresponding to the ability of a circuit to resist the flow of current. In turn, the impedance (Z) value depends of the voltage-time function $E(t)$ and the current-time function $I(t)$ and it is calculated by the following **equation 5**.

$$Z = \frac{E(t)}{I(t)} \quad \text{equation (5)}$$

In which, $E(t)$ represents a sinusoidal voltage, defined as **equation 6**,

$$E(t) = E_0 \sin(\omega t) \quad \text{equation (6)}$$

E_0 is a maximum potential and ω consists in the angular frequency ($\omega = 2\pi f$), expressed in rad/s of the electrical circuit that combines resistances and capacitances, which can adequately represent the electrochemical cell. When E is applied in the electrochemical cell, the response is expressed by the intensity of I (**equation 7**).

$$I(t) = I_0 \sin(\omega t + \phi) \quad \text{equation (7)}$$

The electrical response of impedance is defined as the proportionally factor between the applied potential perturbation and current response, in which it is calculated by using an expression analogous to the *Ohm's* law as follows, in **equation 8**.

$$Z = Z_0 \frac{\sin(\omega t)}{\sin(\omega t + \phi)} \quad \text{equation (8)}$$

Where the (Z) is characterized by the magnitude ($|Z|$) and phase angle (ϕ). The expression for Z is composed by a real (plotted on the X -axis) and an imaginary part (plotted on the Y -axis). In the Nyquist plot, the impedance can be represented as a vector of length $|Z|$, while the angle between this vector and the X -axis, generally called as a phase angle, is defined as $\phi = \tan^{-1} (-Z''/Z')$. Then, by applying *Eulers* relationship given by **equation 9**.

$$e^{i\phi} = \cos(\phi) + i \sin(\phi) \quad \text{equation (9)}$$

It is possible to express the impedance as a complex function, where i is the imaginary number defined as $i = (-1)^{1/2}$, and therefore the potential response is defined by **equation 10**.

$$\text{Re}(Z) = Z' = |Z| \cos(\phi) \quad \text{equation (10)}$$

In the same way, the current response is defined as **equation 11**.

$$\text{Im}(Z) = Z'' = |Z| \sin(\phi) \quad \text{equation (11)}$$

Thus, the impedance can be represented as a complex number (**equation 12**).

$$Z = |Z| (\cos(\phi) + i \sin(\phi)) \quad \text{equation (12)}$$

The above discussion showed that Impedance measures the resistance to the electrical current flow of the electrochemical cell over a wide frequency range. This measurement can be evaluated by two different ways: *Nyquist* and *Bode* plots.

Nyquist plot allows evaluating the changes on the conductive surface through of solution resistance (R_s) and charge transfer resistance (R_{ct}) values. These values can be determined by a semicircle, as a represented in **Figure 2.10**, where it is characteristic of a simple equivalent electrical circuit with a single time constant (t), even though EIS plots often contain several semicircles.

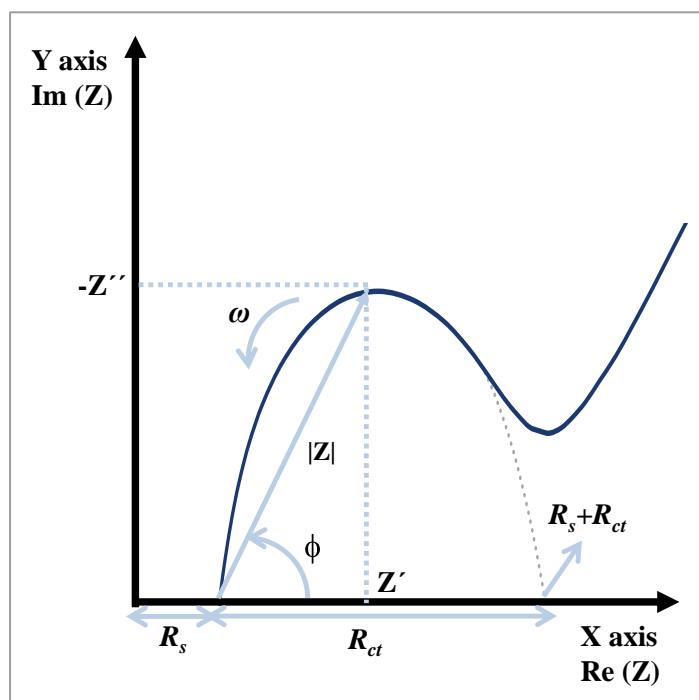


Figure 2.10 - Nyquist plot that illustrates both real (Z') and imaginary (Z'') components of impedance at each ω . R_s : solution resistance; R_{ct} : charge transference resistance; ϕ : phase angle.

Although *Nyquist* plots give a fast overview of the EIS data to produce qualitative interpretations, *Bode* plots offer a more complete way of presenting the impedance data. These involve plots with the frequency on the X-axis (logarithm scale (\log)) and both the absolute values of the impedance and the phase angle on the Y-axis (logarithm scale (\log)).

The *Bode* plots are represented by Bode modulus (**Figure 2.11-A**) and *Bode* phase (**Figure 2.11-B**), using $\log(|Z|)$ and $\log(\phi)$, respectively, as a function of $\log(\omega)$. The *Bode* phase is associated with the double layer capacitance (C_{dl}) of the electrochemical cell [121, 123].

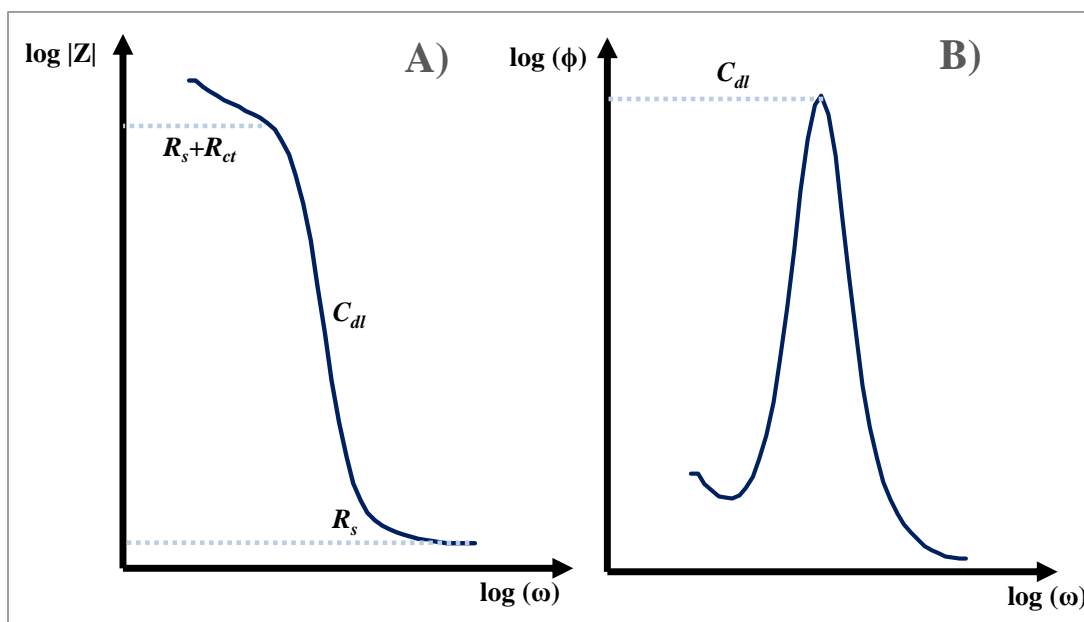


Figure 2.11 - Typical Bode diagram representing the impedance by (A) modulus ($\log(|Z|)$) and (B) phase ($\log(\phi)$) plots of an electrochemical system as function of the angular frequency (ω).

From these, it is possible to define equivalent electrical circuit models and process models by developing mathematical methods based on the kinetics of the involved reactions. The models are used to experimental data in order to estimate the parameters that can be described, interpreted and fitted the impedance data adequately [121]. The *Randles* equivalent circuit is one of the simplest and most common equivalent circuit models. This circuit combines the R_s , with the double layer capacitance (C_{dl}), R_{ct} and the Warburg impedance (Z_W) [124], as suggested in **Figure 2.12**. R_s is the solution resistance between WE and RE and depends on the ionic concentration. The application of the electric field is related to two processes, R_{ct} , that is related to current flow (electron transfer) produced by redox

reactions at the interface electrode surface/solution, and C_{dl} , which stores charges coming from the interface between electrode and solution. Finally, the Z_W is related to diffusion of the electroactive species from the solution to the interface [120, 125, 126].

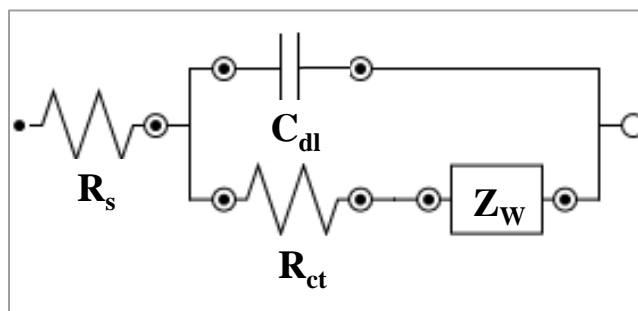


Figure 2.12 - Typical simplified *Randles* equivalent circuit. R_s : resistance of solution; R_{ct} : resistance of charge transfer; C_{dl} : double layer capacitance and Z_W : Warburg impedance.

Overall, EIS is a powerful technique for monitoring the electrical resistance changes of a system on the electrode surface, arising from a given chemical modification. Thus, this electrochemical method could be a highly sensitive tool in the field of biosensors during the immobilization of the biological element on the transducer surface and biorecognition processes.

2.3.3. Electrochemical Biosensors for cancer biomarkers

As mentioned before, an electrochemical biosensor converts the effect of the interaction between a specific biomolecule and a biorecognition element into an electrical signal that is proportional to the concentration of this biomolecule [127]. Although it remains a challenge, the development of electrochemical biosensors targeting cancer biomarkers has received much attention from the scientific community due to their high sensitivity, simplicity, fast response and low cost [113, 114, 128, 129]. In general, electrochemical transduction leads to wider linear ranges of response and lower LODs in biosensors, when comparing to other transduction schemes [116, 130].

Electrochemical sensing has also used MIP materials as biorecognition elements, as exploring different electrochemical detection techniques for cancer biomarker sensing, such

as CV, EIS, SWV, differential pulse voltammetry (DPV) and potentiometry [113, 114, 128, 130-133]. A brief list of these works targeting CEA and CRT biomarkers is shown in **table 2.3**, highlighting transducer component and the main analytical features.

Table 2.3 - Previous works reporting MIP-based biosensors with electrochemical transducer for CEA and CRT detection.

Biomarker	Transduction	LOD	Linear response	Ref
CEA	CV, EIS, SWV	—	0.05 – 1.25 pg/mL	[113]
	EIS	2 ng/mL	0.0025 – 1.5 µg/mL	[131]
	DPV	<0.26 pg/mL	0.001 – 1000 ng/mL	[132]
CRT	Potentiometry	12.90 µg/mL	16.12 – 161.2 µg/mL	[134]
	Potentiometry	0.57 µg/mL	0.71 – 16.12 µg/mL	[135]
	EIS	0.0347 ng/mL	0.161 ng/mL – 16.1 µg/mL	[136]

Overall, MIP-based biosensors published throughout years showed that there are few devices using MIP biorecognition elements for CEA and CRT. Yet, these devices confirmed the high analytical potential of the electrochemical detection combined with MIP materials, leading to low LODs and wide linear ranges, within the concentration range of clinical interest.

Yet, electrochemical sensing remains with a single requirement, which is the need for electrical energy. In turn, medical diagnosis should be of easy access, anywhere in the world. Thus, a new possibility may arise when a renewable energy source, such as a PV, is coupled to electrochemical sensing.

2.4. Photovoltaic cells

PV cells are devices that allow converting the energy of sunlight into electricity by using a phenomenon called the PV effect. This phenomenon occurs in semiconducting materials that are able to absorb photons from light, which subsequently excite electrons these into an electrical circuit, which generates voltage/current in solar cells [137, 138]. In general, PV cells may represent a sustainable energy source, because these may replace other non-renewable sources of energy, such as fossil fuel and nuclear energy.

There are different types of PV cells, some of these with industrial maturity, such as the well-known crystalline silicon cells [118, 119]. This type of cell uses silicon-based materials as semiconducting material. Silicon is employed in monocrystalline and polycrystalline PV cells, depending of its molecular structure. The crystalline structure of silicon affects electrically efficient of the PV cell, in particular, with monocrystalline cell being more efficient than polycrystalline ones [138]. Currently, more than 85 % of the electric current produced by solar energy is based on silicon-based PVs [139], but the production of this type of cells presents high costs. In addition, the search for silicon can lead to its scarcity in the market, predicting increased costs. Thus, in the last decades, researchers have been looking for alternatives to conventional silicon cells. DSSC, also known as *Grätzel* cells, have emerged in this context and attracted much attention along the last two decades, due to their low cost, easy manufacture and high η [140, 141].

2.4.1. Dye sensitized solar cell

The DSSC is composed by two electrodes, an anode (photoanode) and a cathode, as shown in **Figure 2.13**. These electrodes are made from a glass coated with a transparent conductive oxide (TCO). The main TCOs used in this type of solar cells are indium tin Oxide (ITO) and fluorine tin oxide (FTO). This last one shows better PV efficiency, low resistivity and stable temperature, when compared to ITO, and for this reason it is the most used TCO in DSSCs [142].

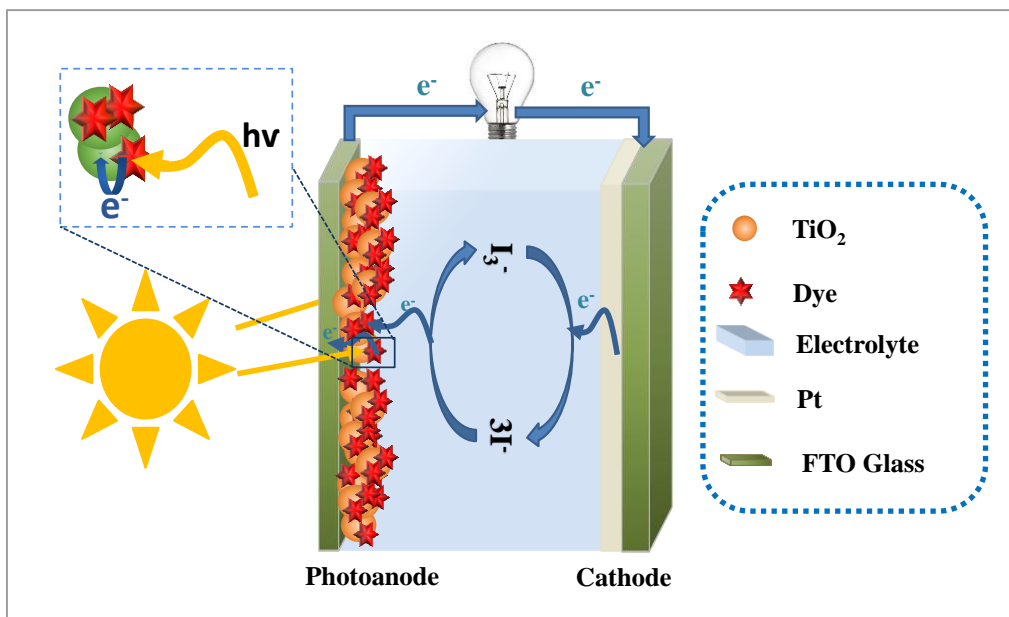


Figure 2.13- Schematic representation of a DSSC during the conversion of solar energy into electrical energy.

The photoanode is composed by a semiconductor material and a photosensitizer. Semiconductors such as niobium oxides [143], zinc [144], tin [145] have been tested in the DSSCs. However, Titanium dioxide (TiO_2) lead to DSSC of higher efficiency, when compared to the previous materials. Thus, the most used semiconductor is TiO_2 (more specifically in the anatase phase), which is deposited on FTO. The most widely and simplest method used for TiO_2 deposition on the substrate is the *Doctor-Blade* method [146-148]. In this, a rod or a glass slide is used to spread the amount of TiO_2 paste on the glass. In addition to the *Doctor-Blade* technique, there are other TiO_2 deposition methods, such as the sol-gel synthesis, thermal synthesis, vapor deposition, electrodeposition, and oxidation of Ti using oxidants or under anodizing, among others [149, 150]. However, these require specific equipment and become more expensive than the one using the *Doctor-Blade* approach [148]. The TiO_2 film deposited on the FTO is porous, which gives the photoanode a high surface area.

The TiO_2 film is then sensitized by adsorption of a dye monolayer, which allows the absorption of light [139, 151, 152]. In general, the immobilized sensitizer absorbs a photon to reach an excited state and this photoexcitation of the sensitizer transfers electrons from the dye onto the conduction band of the oxide (TiO_2). The injected electrons flow through the semiconductor network and reach the cathode via electron migration through the external

load, being used after to reduce the triiodide species to iodide species. The redox system is responsible for the regeneration of dye molecule [139].

The cathode electrode is conventionally composed by a transparent conductive glass, such as FTO, modified with a catalyst material. This catalyst material is responsible to accelerate the reaction, otherwise it would be too slow [153]. There are many materials currently used for this purpose. These include carbon nanostructures (graphite [153], graphene [154], carbon nanotubes [153], among others) or platinum (Pt) materials. [153, 155]. The most widely used material is Pt, due to its strong catalytic activity to reduce I_3^- , good conductivity and chemical stability [156, 157]. Since the materials used in CE may be compatible with the MIP biorecognition element [158], it would be interesting to use the electrode as support material for the biosensor assembly.

2.4.2. Photovoltaic characteristics of DSSC

In DSSCs, the electrical energy is generated through light absorbed by an organic dye (sensitizer) that is anchored to the surface of a semiconductor. The mechanism of this PV cell is based on the photo-electrochemical processes, which is carry out by relative kinetic rates of several charge transfer steps. In detail, the sunlight that hits the photoanode of the DSSC **(1)** causes a photo-excitation of the sensitizer and the dye molecules get excited from their ground state (S) to a higher energy state (S^*); the excited electrons are then injected into the conduction band of the semiconductor **(2)**. The dye molecule is regenerated by redox system **(3)**, which in turn is regenerated at the cathode via electrons arriving from the photoanode through the external circuit **(4)**, as represented in **Figure 2.14**.

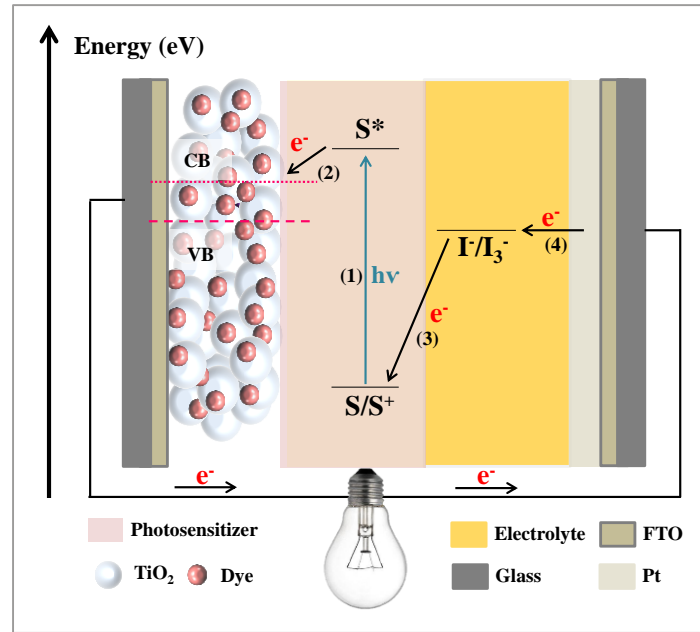


Figure 2.14- Schematic representation of the electron transfer reactions involved in the generation of energy in the DSSC. S represents the dye sensitizer; I^-/I_3^- is the redox mediator CB is the conduction band and VB is the valence band.

In general, the electron transfer dynamics within the DSSC influence the performance of the solar cell, which is evaluated by photocurrent density-voltage (J - V) curves [159-161]. The power conversion efficiency (η) of the DSSC is extracted from this measurement, and relates short-circuit current density (J_{sc}), fill factor (FF), open-circuit potential (V_{oc}), and the intensity of incident light (I_s), as shown in **equation 13**.

$$\eta = \frac{J_{sc} \times V_{oc} \times FF}{I_s} \quad \text{equation (13)}$$

In turn, FF is defined as ratio of actual power to that obtained from its J_{sc} and V_{oc} , as indicated in **equation 14**.

$$FF = \frac{P_{max}}{V_{oc} \times J_{sc}} = \frac{V_{max} \times I_{max}}{V_{oc} \times J_{sc}} \quad \text{equation (14)}$$

Where V_{max} and I_{max} are voltage and current density at which the maximum power output can be obtained during DSSC measurement, under incident light. The V_{oc} is the potential difference generated by the DSSC under illumination, between the redox couple (I^-/I_3^-) and the band gap of TiO_2 .

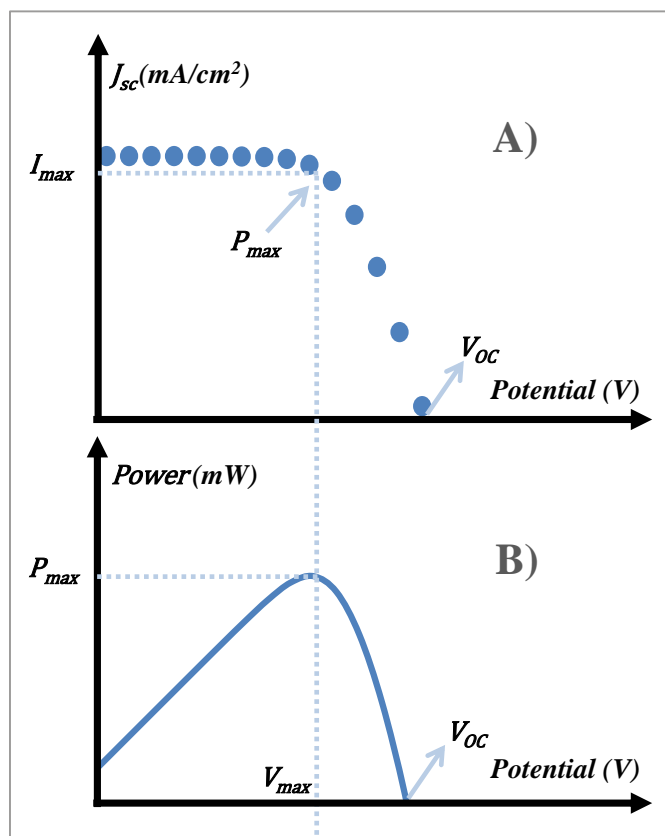


Figure 2.15- The current-voltage (A) and power-voltage (B) characteristics of DSSC.

Currently, the BioMark sensor research group demonstrated that a PV may operate as the electrical reading box of an electrochemical biosensor. Two works are published with this new approach, one relying on an immunosensor [162] and the other on a MIP material [163]. These materials were integrated in the CE of the DSSC. However, the electrical autonomy was not reached by these approaches, because an external computer remains necessary to analyze and interpret the data. To generate a fully autonomous device, the current produced by the

system may feed another cell that converts electrical energy into an optical change. This is the case of an EC element.

2.5. Electrochromic cell

An EC controls the optical properties (transmission, absorption, reflectance and/or emittance) in a continual but reversible manner upon voltage application. This is also called electrochromism, from which the term “electro” signals the applied electrical stimulus and “chromism” signals the change in the optical property of a given material [164-166]. In essence, chromic properties may further occur in response to diverse environmental stimulus, such as light irradiation (photochromism) [167, 168] and heat (thermochromic) [169, 170], but electrochromism is the single effect of interest to this work [171-174], as the PV cell is generating electrical current.

As PVs, EC operate under a given set-up and include specific electrochromic materials (EMs), displaying electrochromic properties, which are relevant in the context of this thesis. These features are described next.

2.5.1. Set-up of an Electrochromic device

In general, an EC consists of an electrochromic film and an ion storage film that are separated by a layer of an electrolyte (ionic conduction layer), all sandwiched between two transparent and conductive supports, as illustrated in **Figure 2.16** [169, 175].

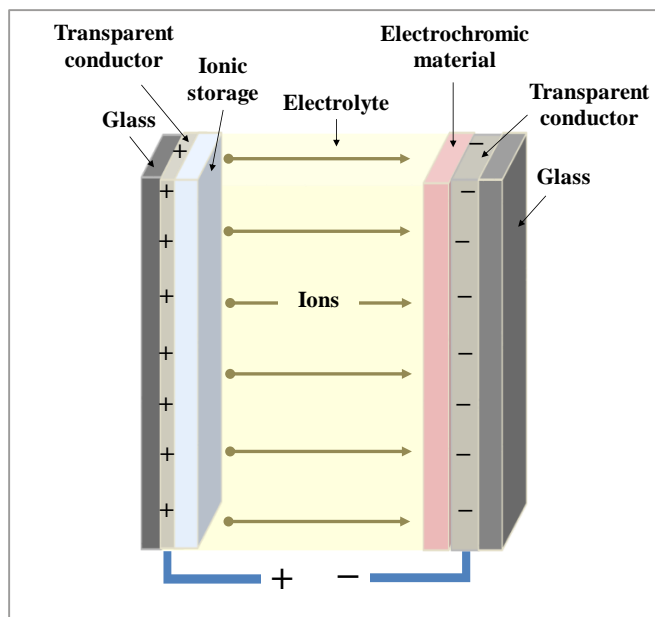


Figure 2.16 - Basic design of an electrochromic device, indicating transport of positive ions under the action of an electric field.

The transparent and conductive supports are, respectively, requisites for the perception of the electrochromic event and for the application of an external stimulus. In general, EC use ITO glass for this purpose [176, 177], from which one contains the electrochromic film. When a voltage is applied between the conductive supports, an electric field is formed and ions from the ionic conduction layer (electrolyte) are moved into the electrochromic film. Simultaneously, the electrons of the external circuit are injected (extracted) from the ITO glass and lead to an electron transfer within the electrochromic film, switching its optical properties between their oxidized and reduced stage.

The ionic conduction layer is a material with electrical conduction properties, containing free ions. The function of the electrolyte is to provide an electrical contact between two electrodes, creating a pathway for the ions to be ejected and reacted into the EM. The ions present in the electrolyte should offer high mobility and ability to be intercalated or extracted from the electrochromic layer. The ions H^+ , Li^+ , Na^+ and K^+ are at the top of this selection, being the most used ones in EC. The electrolyte can be either in liquid, gel or solid form. The most used form for electrolyte is solid, due to its chemical and physical properties. This kind of electrolyte is good insulator for open-circuit condition and presents a good chemical and

electrochemical stability, while the liquid electrolytes has sealing issues that can cause an electrolyte leakage, contributing to low electrochemical stability [169, 176, 177].

The ion storage layer is an important component in EC, because it allows improving the optical transmittance, reflectance, and adsorption properties and the switching speed of the EC display. Yet, the EC can be fabricated without an ion storage material, using only ITO as CE [178].

2.5.2. Electrochromic material

The EM displays electrochromic properties, which enable changing its optical features upon the application of an electrical stimulus. Typically, this change in optical features is reversible, being induced by the application of an electrical current or potential difference to electrochemical redox reactions [164, 174, 175, 179]. Thus, the material changes its colour generating different absorption bands in the visible region of the spectra (400-800 nm), upon switching chemical species between two redox states. In a typical example, EM that change their colour alter the electron states of the molecules, due to an external stimulus [174].

The selection of EM is based in some criteria: high-coloration efficiency (density of injected/ejected charge into the EM, necessary to induce its colour change); fast switching time (time needed for the electrochromic material to switch during redox process); large number of coloration with application of a few volts (different redox states lead the EM to exhibit several colours); good stability (stable redox process) and memory effect in open circuit (ability of the material to retain its colour upon removing the electrical stimulus) [164, 179, 180]. Nowadays, research on EMs is focused more in their optical properties in the visible/Near-infrared (NIR) spectral regions, for technology applications [179, 181, 182]. According to their composition, these materials can be classified as inorganic or organic EM.

Most of the inorganic EM are oxides of transition metals, where the tungsten trioxide is one of the most used in EC [183-185]. **Figure 2.18** shows the transition metals whose oxides have well-documented electrochromism in the literature.

The figure shows a standard periodic table of elements. A yellow rectangular box is drawn around the transition metal block, which includes elements from Scandium (Sc) to Cadmium (Cd) in the first row of transition metals, and from Rutherfordium (Rf) to Oganesson (Og) in the subsequent rows. The text "Electrochromic oxides" is placed to the right of this box. Below the periodic table, there are ten colored boxes representing different categories of elements: Alkali Metal (red), Alkaline Earth (orange), Transition Metal (yellow), Basic Metal (green), Metalloid (light blue), Nonmetal (blue), Halogen (purple), Noble Gas (pink), Lanthanide (light purple), and Actinide (dark purple).

Figure 2.17 - The Periodic Table of the elements, referring to the transition metals whose oxides have well-documented electrochromism.

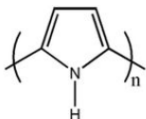
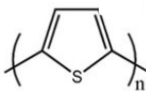
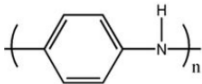
In general, the EM based on metal oxides can be divided into cathodic coloration materials (coloration in the reduced state) and anodic coloration materials (coloration in the oxidized state). These oxides are usually deposited by several techniques as sputtering, chemical vapor deposition, electrodeposition anodization, sol-gel process, etc. [164]. Thus, the method of preparation becomes more expensive and difficult to handle, due to the need for highly specialized equipment and qualified personnel. Slow switching times and limited number of colours over a wide range of potentials are also other disadvantages presented by these materials [177, 186]. For these reasons, organic materials have been widely used in electrochromic applications [164].

As opposed to inorganic EM, organic EM are not as stable but offer the advantages of high coloration efficiency, presenting large number of colours and fast switching time. Many organic substances show electrochromism and have been classified by viologens, phthalocyanines, and conducting polymers [164]. Among these, conducting polymers have been the most employed for electrochromic applications, due to their easy production and

structural modification, contributing to diverse colours with high contrast. Moreover, the switching optical properties occurs with few applied volts and needs low electrical power.

In general, organic EM are composed by monomers with aromatic compound that after polymerization lead to electronically conducting polymers. The most studied conducting polymers include PPy, polyaniline (PANI) and polythiophene (PTh) and their derivatives as PEDOT (**table 2.4**) [164, 187].

Table 2.4 - Electrochromism observed in conducting polymer.

Polymer	Structure	Coloration	
		Oxidized state (doped)	Reduced state (undoped)
PPy		Blue/Grey	Yellow/Green
Pth		Blue	Red
PANI		Green/Blue	Yellow

Electrochromism in conducting polymers is related to the doping/undoping process (insertion/extraction of ions through the polymer), which leads to a modification of polymer electronic structure (alteration of the band gap) and causes colour changes. Thereby, the energy gap between the valence band and the conduction band determines the optical properties of these materials [164, 179, 188].

Considering the low cost and easy fabrication features, EC based on organic conductive polymers may be used as display element to transduce the analytical response of an autonomous biosensor that merges MIP materials and PVs. Thus, the following chapters report the new approaches taken for the development of such biosensors.

3. Conductive Paper with Antibody-Like Film for Electrical Readings of Biomolecules

3.1. Introduction

In general, electrochemical biosensors may be designed on different supports, mostly plastic, as Polyethylene terephthalate (PET) or Polyvinyl chloride (PVC), and ceramics [189]. Although these materials work well on biosensors for POC applications, plastic-based ones are less robust and cheaper than ceramic-based devices. But an extended worldwide use of such biosensors with synthetic and non-biodegradable support materials pose environmental concerns. A truly worldwide application of POC devices requires replacing such materials by a naturally-derived compounds, provided that this natural compound confers proper electrical and mechanical stability features to the final POC device.

Cellulose paper as substrate is one of several possibilities in this context, offering the advantages of being readily available. This was tested herein by assembling on it a MIP material for CRT, considering CRT an emerging biomarker in ovarian cancer that may be determined in urine [190]. So far, most of the analytical methods described to determine CRT [191-193], miss portability features and the ones nearing it do not combine disposable supports and stable biorecognition materials, which are essential conditions to promote worldwide POC applications in early screening of ovarian cancer. Thus, novel electrochemical biosensors using renewable supports are also needed.

Thus, this work described the construction of a novel, disposable, stable and low-cost device, with an antibody-like film assembled on paper-based conductive supports. For this purpose, a regular paper is made hydrophobic and covered by a conductive ink. A critical point in assembling an electrochemical device is the ink, for which carbon-based conductive inks are

the most common ones. Carbon inks consist of graphite particles together with other ingredients that are responsible for the dispersion and adhesion in support [194-196]. Thus, a homemade conductive ink based on carbon materials was optimized regarding its adhesion, conductivity, and thermal stability. The Doctor-Blade technique was used for this purpose. The MIP material was assembled directly on the paper-based conductive support by an electrically-sustained polymerization of EDOT or dodecylbenzenesulfonic acid (DBS). The biomimetic surfaces so obtained were evaluated by electrochemical techniques and surface analysis, displaying successful features to be applied to the analysis of biological samples.

3.2. Experimental section

3.2.1. Apparatus

Polymeric film assemblies and electrochemical measurements were made in a potentiostat/galvanostat equipment from Metrohm, Autolab, PGSTAT302N, computer controlled by NOVA software. A cellulose paper support (3.3×1.0 cm) made conductive with conductive ink was used as WE; a Pt wire as CE; and a double-junction Ag/AgCl as RE.

The thermal behaviour of conductive ink was evaluated in the thermogravimetry analysis (TG)/differential thermal analyzer (DTA) Exstar TG/DTA 7200. The resistivity of the ink was measured by Fluke 175 True RMS multimeter. A Sonorex digitec sonicator, Bandelin, was used to promote the dissolution of the solids and homogeneity of the reacting solutions.

Fourier-transform infrared spectroscopy (FTIR) surface analysis of solid materials was made in a Nicolet iS10 spectrometer from Thermo Scientific coupled to a Smart Attenuated Total Reflectance (ATR) sampling accessory of germanium contact crystal, also from Nicolet. Raman analysis was performed using Thermo Scientific DXR Raman equipment coupled to confocal microscopy with 50× lenses (dark field/bright field) and 532 laser. The digital image of the contact angle was acquired by a digital camera Samsung PL150.

3.2.2. Reagents

All chemicals were of analytical grade and ultrapure Milli-Q laboratory grade water (conductivity $< 0.1 \mu\text{S}\cdot\text{cm}^{-1}$) was employed. Cellulose paper was obtained from Fanoia. Graphite powder, Phosphate Buffered Saline (PBS) tablets, EDOT, 4-(2-hydroxyethyl)-1-piperazineethanesulfonic acid (HEPES) and oxalic acid dehydrate (OAc) were purchased to Sigma-Aldrich; DBS to Acros Organics; N,N-dimethylformamide (DMF) to VWR; Poly(vinylchloride) carboxylated (PVC-COOH) to Fluka; Potassium Hexacyanoferrate III ($\text{K}_3[\text{Fe}(\text{CN})_6]$) and potassium hexacyanoferrate II trihydrate ($\text{K}_4[\text{Fe}(\text{CN})_6]$) to Riedel-de-Haën; CRT hydrochloride, and potassium chloride (KCl) to Merck; and sulfuric Acid (H_2SO_4) to Scharlau. Urea was obtained from Fagron, Creatinine (Crea) to Fluka, magnesium chloride to Riedel-de-Haën, calcium chloride to Purified, sodium dihydrogen phosphate (NaH_2PO_4) to Scharlau, potassium sulphate and sodium chloride to Panreac, ammonium chloride to Merck and BSA to Sigma.

3.2.3. Solutions

Stock standard solutions of CRT were prepared with a concentration of 1.0×10^{-3} mol/L, prepared in 1.0×10^{-2} mol/L HEPES buffer, pH 7.00. Less concentrated solutions (calibrating standards) were prepared by accurate dilution of the previous solution in the same buffer. Potentiostatic electropolymerization was made in solutions of 0.01 mol/L EDOT or 0.10 mol/L DBS, prepared in 0.10 mol/L KCl as supporting electrolyte in water. Electrochemical assays were performed in a solution containing 2.50×10^{-3} mol/L $\text{K}_3[\text{Fe}(\text{CN})_6]$ and 2.50×10^{-3} mol/L $\text{K}_4[\text{Fe}(\text{CN})_6]$ ($[\text{Fe}(\text{CN})_6]^{3-/4-}$), prepared in PBS buffer, pH 7.00.

3.2.4. Production of the conductive paper

The WE was constructed by cutting small pieces of cellulose paper (1.50×1.00 mm). Each piece was hydrophobized with wax, by heating up to 95°C , for 3 hours. The paper was cooled to room temperature (~ 20 min). The external surface of the waxed paper was then made conductive by applying the conductive ink by the *Doctor Blade* technique. The ink was

prepared simply by mixing graphite powder doped with 15% PVC-COOH in DMF. The ink casted on the paper was dried at 55°C, for 1h.

The thermal behaviour of conductive ink was monitored by TG analysis in the temperature range 35 – 1000 °C, for a heating rate of 5 °C/min, in a nitrogen atmosphere of 200 mL/min. Similar experiments were made with control materials, graphite powder and PVC-COOH, making use of the same experimental conditions.

3.2.5. Surface analysis of the conductive paper

The contact angle of the resulting conductive paper was measured for a drop of a pink dye solution placed on it. A digital image captured by a camera allowed measuring the interior angle formed on the surface, making use of the tangent line to the drop interface at the apparent intersection of all three interfaces. The PowerPoint program of Windows was used for to obtain the contact line and also find the corresponding interior angle.

FTIR analysis of the conductive paper was made directly on the ATR accessory. All spectra were collected under room temperature/humidity control after background correction. The number of scans was 32 for each samples and background. X-axis represented wavenumber, ranging 4000-600 cm^{-1} , and Y-axis % transmittance. Raman analysis was conducted after focusing the material on the optical microscope with a 50× lens. The spectra were collected with 8 mW power and 50 μm pinhole aperture. Automatic fluorescence and photoblinking corrections were made.

3.2.6. Assembly of the antibody-like film

Before use, the carbon surface of the conductive paper was subjected to an electrochemical oxidation, by imposing 5 successive cycles, in 0.50 mol/L of H_2SO_4 , from -0.20 to +1.50 V, at a scan-rate of 50 mV/s. Antibody-like films were prepared by eletropolymerization of EDOT or DBS, made by chronoamperometry (+0.90 V for 240 s), in a solution containing 1.00×10^{-3} mol/L CRT (template), 1.00×10^{-1} mol/L KCl (supporting electrolyte) and 1.00×10^{-2} mol/L EDOT or 1.0×10^{-1} mol/L mol/L DBS . After polymerization, the template was removed by incubation of

the films (on the conductive paper) in 0.50 mol/L OAc, for 1h. Control materials were prepared in parallel, by excluding the template from the procedure.

3.2.7. Electrochemical assays

CV experiments were conducted in HEPES buffer, pH 7.00, in 2.50×10^{-3} mol/L $[\text{Fe}(\text{CN})_6]^{3-/4-}$. The potential was scanned from -1.00 and +1.00 V at a scan rate of 50 mV/s, and with 10 crossing points (5 successive cycles). EIS measurements were conducted in the same redox couple $[\text{Fe}(\text{CN})_6]^{3-/4-}$ at a standard potential of 0.22 V, for 50 frequency values from 0.01–1000 Hz and a sinusoidal potential peak-to-peak amplitude of 0.01 V. The impedance data was fitted to a suitable electrochemical circuit using the ANOVA software.

The response of each WE to increasing concentrations of CRT was evaluated by incubating the electrode for a fixed period of time, in concentration values ranging from 1.00×10^{-8} to 5.00×10^{-3} mol/L. These solutions were prepared in 1.00×10^{-2} mol/L of HEPES, pH 7.00. This incubation period was followed by CV and/or EIS readings made in the previously indicated conditions. Selectivity studies were performed by electrochemical assays with $\text{K}_3[\text{Fe}(\text{CN})_6]$ and $\text{K}_4[\text{Fe}(\text{CN})_6]$ in the same buffer, after incubating the sensing layer in spiked urine samples. The initial urine sample solution was adjusted to 1.00×10^{-8} mol/L, and then this concentration was increased up to a maximum value of 5.00×10^{-3} mol/L.

The analytical application was tested in real samples (urine, diluted 1:10 in HEPES buffer). This was done by calibrating the electrodes in solutions with blank urine and analyzed after real samples spiked with known amounts of CRT. Different electrodes were used for the calibration and sample analysis procedure, for which the electrical output signal was always considered relative to blank (buffer signal prior to the incubation with the first standard).

3.3. Results and discussion

The production of a conductive paper involved two different stages (**Figure 3.1**). The first one considered a pre-treatment of the paper to turn cellulose supports hydrophobic and the

second one producing a suitable homemade conductive ink to cover such hydrophobic support. Only after this stage the antibody-like film was assembled on the material, as described later.

3.3.1. Paper pre-treatment

Cellulose is a biodegradable and renewable resource of well-known hydrophilic features[197], absorbing rapidly any drop of an aqueous solution placed on its surface (as shown in **Figure 3.1-A**). But the use of paper as support for electrical readings does not allow the existence of interactions between water molecules and the β -(1 \rightarrow 4)-glucose polymeric structure, because these interactions interfere with the electrical properties of the resulting surface. To avoid such interactions, the paper was made hydrophobic by covering the cellulose fibers with a fat compound. Wax was selected for this purpose, because it becomes liquid after moderate heating and may interpenetrate all cellulose fibers with high efficiency. Once cooled to room temperature, the oily compound became solid and remained on its position, covering all cellulose fibers and yielding a paper/wax matrix.

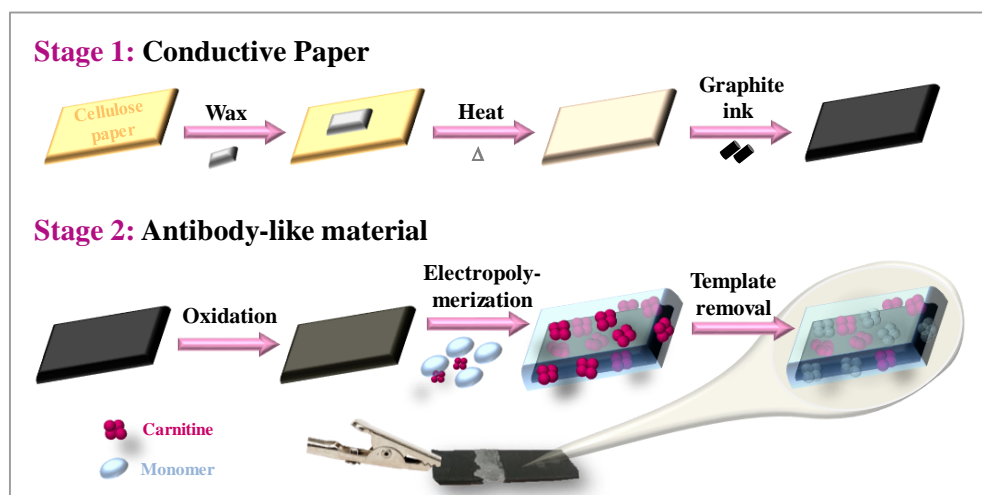


Figure 3.1 - Schematic representation of the production of the conductive paper and its sensitization by an antibody-like material.

In this work, each piece of paper was placed individually inside an oven, with specific amounts of wax on top of it, and heated for specific periods of time and temperature ranges. The best condition was found by monitoring the water-resistant properties of the final conductive paper inside the measuring buffer solution. Overall, an amount of 55 g wax per 56 mm³ piece of paper gave rise to a paper/wax matrix that repelled water, as observed on **Figure 3.1-B**. The aqueous solution was no longer absorbed on the paper and remained at the surface.

The hydrophobic pattern and the wettability of the wax paper were evaluated by contact angle measurements [198]. Contact angles reflected how strongly the liquid and the solid molecules interact with each other; when the molecules of an aqueous solution are weakly attached to the molecules at a solid surface, a drop of that solution will remain on its surface and the contact angle formed by it will depend on the extension of such attractive/repealing forces[199]. In general, angle values above 90° confirm the hydrophobic character of a given surface, with poor wetting properties and poor adhesiveness to liquid substances. In the present study, the water drop on the paper/wax presented a contact angle of 98° (**Figure 3.2-C**), thereby confirming its hydrophobic character and its possible application in electrical transduction systems.

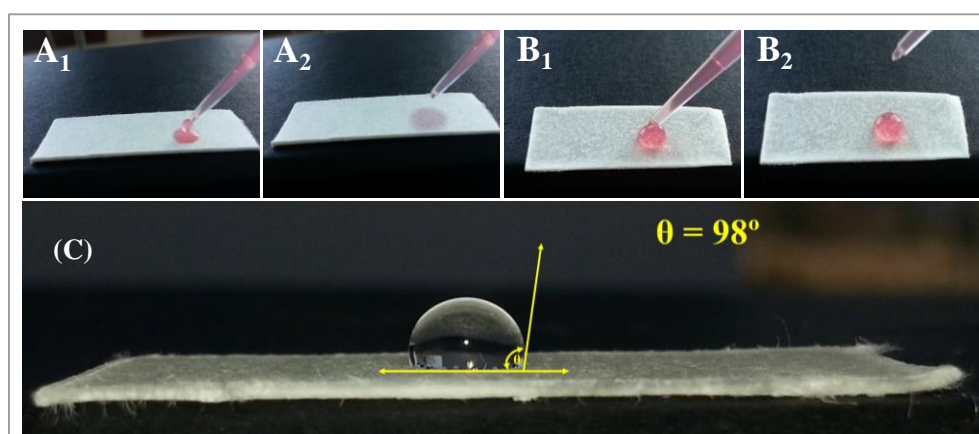


Figure 3.2 - Picture of hydrophilic (**A**) and hydrophobic paper (**B**) with a drop of a coloured aqueous solution on top for 0 (**A₁/B₁**) and 1 minute (**A₂/B₂**), and the subsequent contact angle of the hydrophobic paper (**C**).

The presence of wax within the cellulose fibers was also confirmed by FTIR studies (Figure 3.3). As expected, the cellulose paper showed a broad band centered at 3342.41 cm^{-1} , corresponding to the O–H stretch, and a peak at 1161.18 cm^{-1} , characteristic of the C–O stretch, both bonds intensely present at the glucose sub-units of cellulose. The wax spectra evidenced the C–H stretch typical of alkane compounds at 2849.18 and 2917.09 cm^{-1} and a small intensity peak at 721.79 cm^{-1} , corresponding to consecutive $-\text{CH}_2-$ groups characteristically present in paraffin. The FTIR spectra combined all the previous peaks, thereby confirming the successful inclusion of wax among the cellulose fibres.

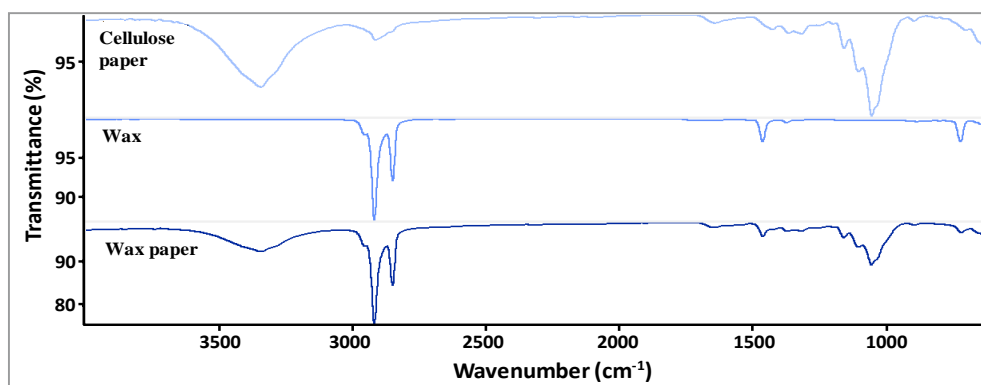


Figure 3.3 - FTIR spectra of several materials at different stages of the production of conductive paper.

3.3.2. Turning the paper conductive

A carbon-based ink made of graphite was prepared to confer electron conduction properties to the wax/paper support. Graphite has good electrical features, being readily available at a low cost.

It can also improve the accumulation of a target molecule at the electrode surface by electrochemical adsorption from any solution [200]. PVC-COOH was selected as polymeric support of the graphitic structures dispersed through the final ink. Thus, co-dissolution of graphite and PVC-COOH was tried out with different solvents. The best compromise between the viscosity of the ink solution and stability/conductivity of the final material was obtained by using DMF solutions. Since PVC-COOH is a non-conductive material, it is expected to increase the *Ohmic* resistance of the final ink and therefore its quantity should be set to a

minimum value. On the contrary, the adhesion of the ink to the wax-paper support would be improved by increasing the concentration of PVC-COOH. Thus, ink solutions were prepared with varying amounts of PVC-COOH: 5, 15, 20, 25 and 30%. The corresponding solutions were applied by following the doctor Blade technique and the papers let dry in an oven for 1 hour.

The resulting ink-paper resistance ranged 1.00–1.70; 0.90–1.50; 0.8–2.00; 7.00–11.00; and 2.00–28.00 k Ω , respectively. These values were obtained by measuring the final resistance at several spots within each paper and in different papers produced in the same way. In general, and as expected, the conductivity values increased with the decreasing amount of PVC-COOH. Ink solutions with 5% polymer gave rise to conductive wax papers of low conductivity values, but the final surface was heterogeneous, and the graphitic structures peeled out easily from the surface by physical contact. Above 20 % PVC-COOH, the dry ink was very stable against external damage, but displayed poor conductivity.

So, the final ink was prepared with 85 % graphite and 15 % PVC-COOH, co-dissolved in DMF. The thermal stability features of this ink (after drying) were evaluated by measuring mass loss curves (TG) and their first derivatives (DTG and DTA) compared to control materials, up to 1000 $^{\circ}$ C. The resulting thermogram is shown in **Figure 3.4-A**. It displays the behaviour of single graphite and PVC-COOH under thermal decomposition and their combined action when mixed to produce a conductive ink. The most significant decomposition observed accounted mostly the presence of PVC-COOH, starting at 218.60 $^{\circ}$ C, and ending at 519.50 $^{\circ}$ C. Ink mass losses up to 488.60 $^{\circ}$ C (**Figure 3.4-B**) were in good agreement with the % of PCV-COOH present in the ink. The total % ink mass loss was 12.73 %, which corresponded to 85 % of its initial mass (15%), while pure PVC-COOH had mass losses of 88%, up to 520 $^{\circ}$ C (**Figure 3.4-C**). These results suggested that no chemical interaction was established between the two ink ingredients. An additional ink mass loss of 3.37 % was observed before 1000 $^{\circ}$ C, which corresponded to mass losses occurring similarly in pure graphite. The results also showed that the ink was thermally stable up to 200 $^{\circ}$ C. Additional discussion regarding thermal analysis data is presented in the **Appendix I.1**.

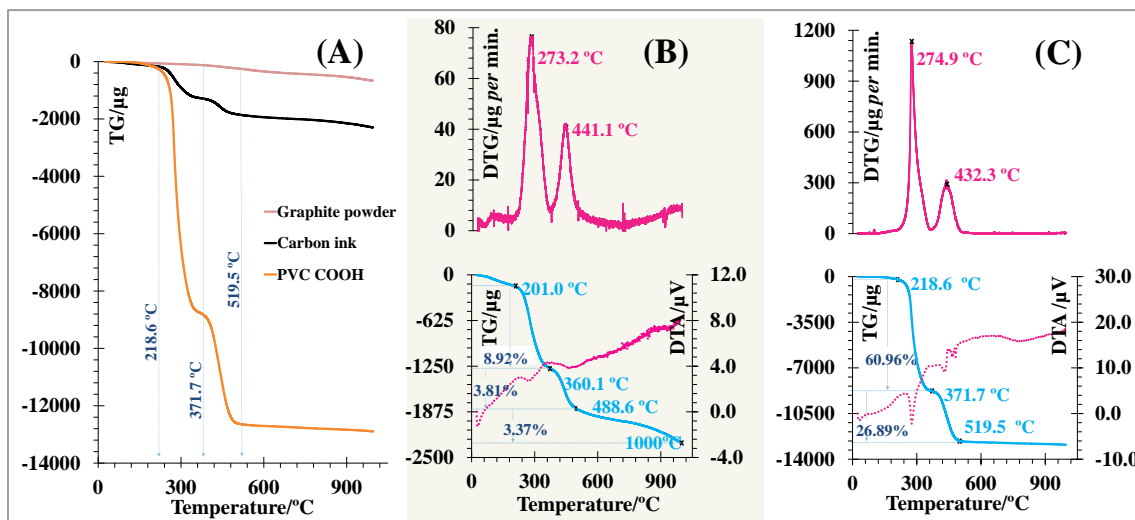


Figure 3.4 - Thermogravimetric plot of conductive ink, pure graphite and pure PVC-COOH (A), with the corresponding differential data, DTG/DTA (Carbon in B) and PVC-COOH in C).

The morphology of the final carbon ink was examined by Scanning Electron Microscope (SEM) (Figure 3.5), comparing the morphologic changes occurring from the original graphite material. The images have shown that graphite powder (Figure 3.5-A) is clearly different from the conductive ink. In greater magnification, it was possible to see that the particles of graphite (Appendix I.2) had several compact layers of graphene sheets, in contrast to the carbon ink, where these sheets were extensively separated, suggesting an effective exfoliation of the graphene. Energy Dispersive X-Ray Spectroscopy (EDS) analysis also indicated an increasing in the oxygen content when the ink was prepared (compared to the original graphite material), thereby confirming the existence of an oxidative process along the ink preparation.

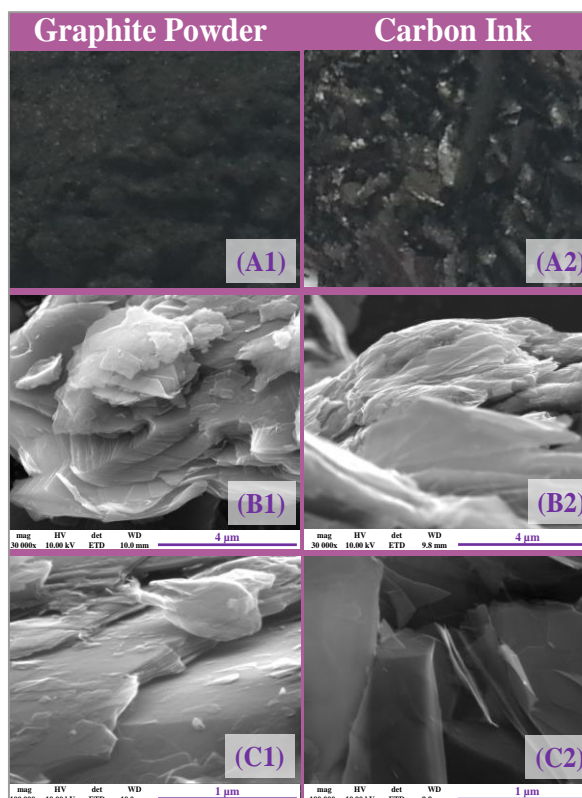


Figure 3.5 - SEM images of graphite (1) and carbon ink (2) of increasing magnifications (A to C).

3.3.3. Chemical/physical features of the conductive paper

The conductive paper was resistant to mechanical pressure by finger scratching after ink dry. No leaching of graphite particles was evidenced. The resulting electrodes were also left in water with a coloured hydrophilic dye, remaining stable for several days.

The FTIR spectra confirmed the presence of graphite at the outer surface of the conductive paper (**Figure 3.6-A**) and its subsequent blocking effect to the FTIR incident light source. Cellulose stretching was not evidenced in this, because the graphitic carbon did not allow incident radiation to permeate deeply into the paper. The increased intensity of C–H stretching bands evidenced the presence of the PVC polymer within the graphite-matrix.

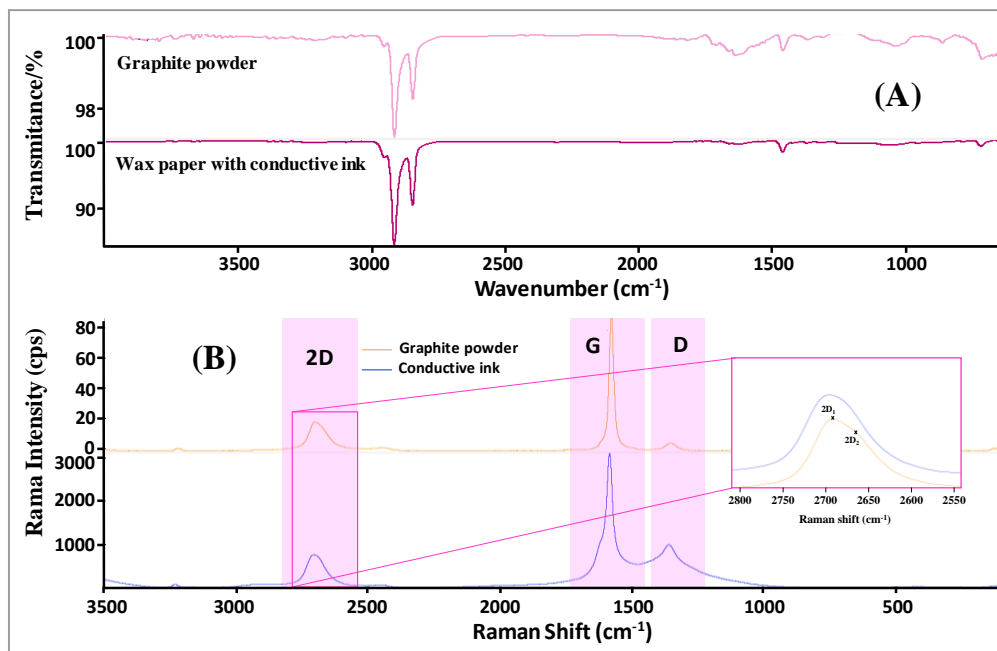


Figure 3.6 - FTIR (A) and Raman (B) spectra of graphite powder and conductive paper.

The Raman spectra of the conductive paper evidenced the three peaks occurring typically in graphite-based materials. These are known as G, D and 2D peaks [201]. The G peak expressed the C–C stretching of the first order scattering of sp^2 carbon hybridization and corresponded to the in-plane vibrational mode at E_{2g} phonons at Brillouin zone centre; the D band originated from a hybridized vibrational mode associated to the double resonance excitation of phonons close to the K point in the Brillouin zone, $\sim 1330\text{ cm}^{-1}$, containing a certain fraction of sp^3 hybridized carbons that indicated the presence of disorder or defect in the carbon material; the 2D peak [202] originated from a second-order process, involving two inter-valley phonons near the K point, and was of higher intensity than in graphite. The exact Raman shift and intensity values are indicated in **table 3.1**. Compared to graphite powder, the D band of the conductive paper was of higher intensity, revealing greater disorder in the conductive ink structure. The 2D in the Raman spectra of graphite was represented by two components $2D_1$ and $2D_2$ [201], both more intense than D peak. In contrast, the conductive ink had a single, sharp 2D peak and it was less intense than D peak; according to similarities found in the Raman spectra available in the literature [203], the main component of such ink may be reduced exfoliated graphene oxide (**Figure 3.6-B**).

Table 3.1 - Analytical data extracted from the collected Raman spectra of the several materials.

Material	Monomer	CRT*	Raman intensity			Raman Shift			Peak ratio	
			2D Peak	G Peak	D Peak	2D Peak	G Peak	D Peak	I _D /I _G	I _{2D} /I _G
Graphite powder	—	—	19.68	91.64	5.22	2693.58	1565.83	1337.9	0.06	0.215
Conductive paper	—	—	780.59	3184.93	1017.78	2697.00	1572.84	1347.0	0.32	0.245
Antibody-like	EDOT	—	258.09	780.70	256.31	2696.58	1574.52	1347.6	0.33	0.331
	EDOT	5×10 ⁻³	1062.73	3862.63	1493.69	2698.72	1575.73	1347.9	0.39	0.275
	DBS	—	1528.25	4085.84	1034.29	2711.64	1579.64	1349.2	0.25	0.374
	DBS	5×10 ⁻³	940.13	2606.84	722.85	2710.73	1578.40	1348.6	0.28	0.361

*Calibration of the material with CRT, up to a concentration of 5.0×10⁻³ mol/L.

The formation of sp³ C-H bonds as well as the breaking of the translational symmetric of sp² C=C, lead to defect in hydrogenated carbon material [202, 204]. The D band is often referred to as the disorder band or the defect band, which can be used as a measured of the quality of the carbons structures after modification process of them by the analysis of the intensity ratio between the D band (I_D) and G band (I_G) (I_D/I_G), i.e., it is used for quantifying the defect density in carbon material. The intensity ratio extracted from **table 3.1** indicated significant disorder, arising from structural defects. The I_D/I_G ratios of the graphite powder and ink were respectively 0.057 and 0.319 cps, reflecting the increase in structural disorder and the occurrence of the evolution of the graphite to graphene. Consequently, this graphene presented more defects than graphite powder. Overall, the obtained Raman spectra indicated that the ink become a graphene-based material, after being submitted to the previously mentioned conditions.

The electrochemical features of the carbon-ink/paper were evaluated by EIS measurements, making use of [Fe(CN)₆]^{3-/4-}, solutions with different concentrations prepared in 1.00×10⁻² mol/L PBS buffer.

The obtained data was shown as Nyquist plots (**Appendix I.2**), where R_{ct} corresponded to the diameter of the observed semicircle. In general, lower R_{ct} indicated quicker electron transfer rates with decreasing *Ohmic* resistance at the receptor surface. As expected, increasing concentrations of the redox probe yielded lower R_{ct} values. According to the obtained results, an intermediate concentration of 2.50×10^{-3} mol/L of iron probe was selected to proceed with the subsequent electrochemical measurements. This concentration ensured sensitive readings of EIS, thereby favouring the sensitive detection of opposite events, such as electrical blocking or increased conductivity.

3.3.4. Assembly of the antibody-like material

The antibody-like surfaces were assembled on conductive paper as shown in **Figure 3.1**. First, the conductive ink was oxidized with H_2SO_4 to remove unwanted-species hindering the electron transfer rate of the WE. This procedure yielded an increased number of hydroxyl (-OH), epoxide (-O-) and carboxyl groups (-COOH), thus leading to an increased negative polarity at the electrode surface that could improve the subsequent electrochemical polymerization processes[205]. The imprinting stage consisted of the electrochemical polymerization of a suitable monomer, in an aqueous solution containing supporting electrolyte (KCl, 0.10 mol/L) and the molecule to be imprinted (CRT). And finally, the imprinted sites were obtained once the template was removed, and these sites should be able to rebind again to another molecule of CRT. The imprinting effect upon the response of the paper-based electrodes was assessed by control materials, prepared similarly but without CRT.

EDOT and DBS were selected as monomers. The electrochemical polymerization of EDOT is well-known, yielding conductive, biocompatible and stable polymers [206]. On the contrary, the electrochemical polymerization of DBS has not been reported yet. DBS is typically employed as an anionic surfactant along with other monomers [207, 208], but its structure includes an aromatic ring strongly active towards electrophilic reagents, making its cationic polymerization possible under suitable electrical stimulus. Thus, the possibility of using DBS as regular monomer in electropolymerization to produce a polymeric film was tested herein.

The D/G peak ratio of the conductive paper (0.32) increased up to 0.33 in EDOT-based films but decreased to 0.25 in DBS films, whereas the 2D/G peak ratio (0.25) increased both in EDOT

(0.33) and DBS based films (0.37). The Raman shifts were also displaced in all peaks for both EDOT and DBS films; the larger Raman shift differences were observed for DBS films, with stronger evidence for 2D and G peaks.

After polymerizing EDOT or DBS on the conductive ink, the peak intensity ratio I_D/I_G changed in both imprinted materials (EDOT films increased to 0.328 cps, and DBS ones decreased to 0.25 cps), thereby confirming the occurrence of the electrically-induced polymerization. The Raman shifts of D, G and 2D peaks also increased (+9.12, +7.01, and +3.42 cm^{-1} , respectively), thereby confirming the polymer formation. These overall changes may also point out that the imprinted DBS polymer showed less disordered structural organization.

3.3.5. Rebinding to the antibody-like material

The chemical modifications of the surface morphology, occurring after the imprinting stage, were characterized by Raman spectroscopy. The corresponding data is indicated in **table 3.1**. As expected, the obtained spectra presented the typical G, D and 2D peaks observed in the conductive paper (**Figure 3.7**), regardless the monomer employed. But relative intensities of D/G and 2D/G peaks varied.

The adsorption of CRT to the antibody-like films was confirmed by Raman analysis of the films that had been calibrated with CRT standard solutions, with a concentration up to 5.0×10^{-3} mol/L. In the calibrated antibody-like EDOT film, all peaks shifted to higher values (D, +0.26 cm^{-1} ; G, +1.21 cm^{-1} ; and 2D, +2.14 cm^{-1}). Although the absolute Raman intensity increased significantly in the overall spectra, the peak intensity ratio I_D/I_G increased by 0.06 cps and the ratio I_{2D}/I_G decreased by -0.056. The calibrated antibody-like DBS film showed an opposite behaviour. The presence of CRT within the DBS-polymer matrix yielded Raman negative shifts in D (-0.61 cm^{-1}), G (-1.24 cm^{-1}) and 2D (-0.91 cm^{-1}) peaks. The overall Raman spectra showed lower intensity, but the changes in peak ratio were consistent with the EDOT-observed behaviour: I_D/I_G increased by 0.02 cps and I_{2D}/I_G decreased by -0.01.

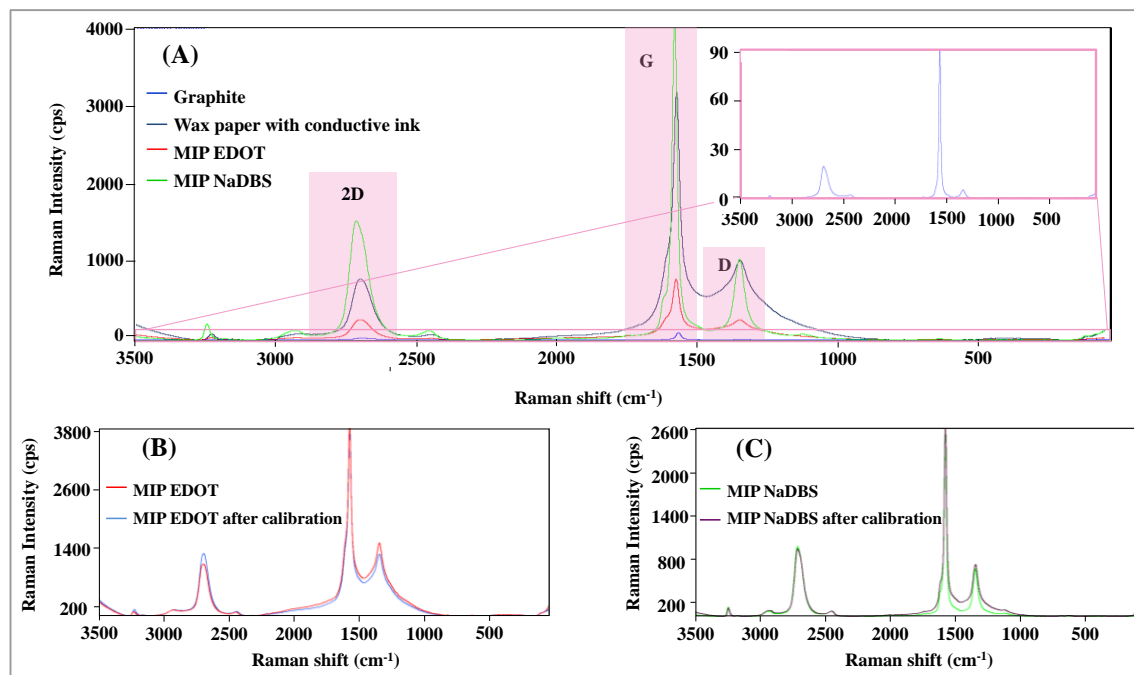


Figure 3.7 - Raman spectra of the antibody-like film on conductive paper **(A)**; and a direct comparison before and after calibration of the MI material of EDOT **(B)** or DBS **(C)**.

Overall, these results suggested that CRT remained within the imprinted material after calibration, both in EDOT and DBS polymers. A higher amount of CRT was expected to be present in EDOT-based material due to the higher changes in Raman peak intensity ratio observed for this polymer.

3.3.6. Optimization of the antibody-like assembly

The effect of the relevant variables at the assembly of an antibody-like film was checked by EIS. The electrical resistance was analyzed by *Nyquist* plots, showing the frequency of the response of the electrode when in contact with any electrolyte. It also indicates the R_{ct} at the electrode surface which is given by the semicircle diameter [209].

When the sensing layer at the electrodes was chemically modified, the typical charge transfer behaviour of the overall surface changed, thereby confirming the existence of such modifications. The typical charge transfer behaviour is evaluated with a well-known redox probe, such as $[\text{Fe}(\text{CN})_6]^{3-/4-}$.

3.3.7. CRT concentration at the imprinting stage

The number of effective rebinding positions for CRT depends of the number of CRT molecules entrapped within the imprinted polymer, but such number cannot be as high as to interfere with the polymer growth. This makes the concentration of CRT at the imprinting stage a critical variable. In this work, the imprinted layer was produced by using two different CRT concentrations: 1.00×10^{-3} and 1.00×10^{-2} mol/L. Lower concentrations were not tested as the number of template molecules to be imprinted would decrease a lot when compared to the number of monomeric species present.

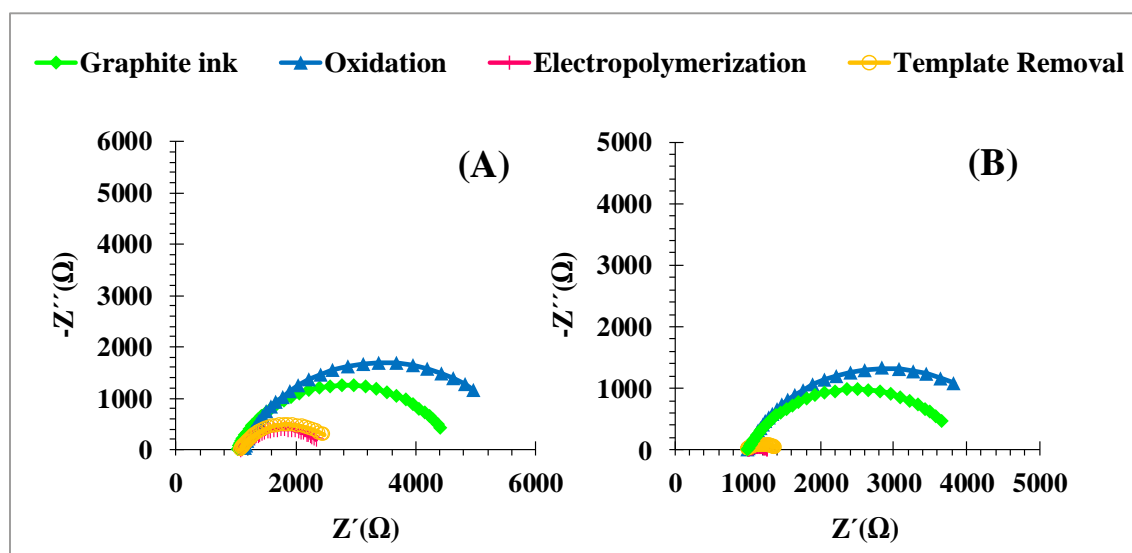


Figure 3.8 - EIS data for CRT concentrations at the imprinting stage equal to (A) 1.00×10^{-2} mol/L or (B) 1.00×10^{-3} mol/L (EDOT was the monomeric unit of the polymer), and the corresponding electrical circuit.

The results obtained for EDOT monomer are shown in **Figure 3.8**, plotting normalized values for the carbon-ink stage. The correction factor used for this purpose was calculated against the R_{ct} value of the conductive ink. In both concentrations of CRT tested, it was clear that the presence of polymeric EDOT (PEDOT) contributed to decrease the R_{ct} value of the sensing layer. This was attributed to the fact that PEDOT holds conductive properties, thereby increasing the conductivity features of the surface. This effect was less evident for higher

concentrations of CRT because the presence of a high number of these species hindered the polymerization of EDOT, yielding a more resistive material. The removal of CRT molecules located at the surface of the polymer was made by OAc (for 1h), yielding a slight increase of the overall R_{ct} . Overall, considering that a biosensor of low resistivity is expected to lead to a higher sensitivity, the concentration of 1.00×10^{-3} mol /L of CRT was selected for further experiments.

3.3.8. Effect of monomer

The electrical features of the sensory surface changed significantly with the selected monomer (EDOT or DBS). It is important to highlight at this point that the C_{PE} in the electrical circuit is the constant phase element, which can behave as resistance if $n=0$, capacitance when $n=1$ or Z_W if $n=0.5$ [124]. In the case of an imprinted DBS polymeric layer, the C_{PE} value changed between 109.25 and 390.09 μF and in EDOT polymer changed from 114.52 to 215.79 μF . Thus, in both cases this element behaved as capacitance, because $n \sim 1$. The equivalent circuit shown in **Figure 3.9** was used to analyze the Nyquist plots after each surface modification step at the biosensor fabrication with DBS (**Figure 3.9-A**) or EDOT (**Figure 3.9-B**).

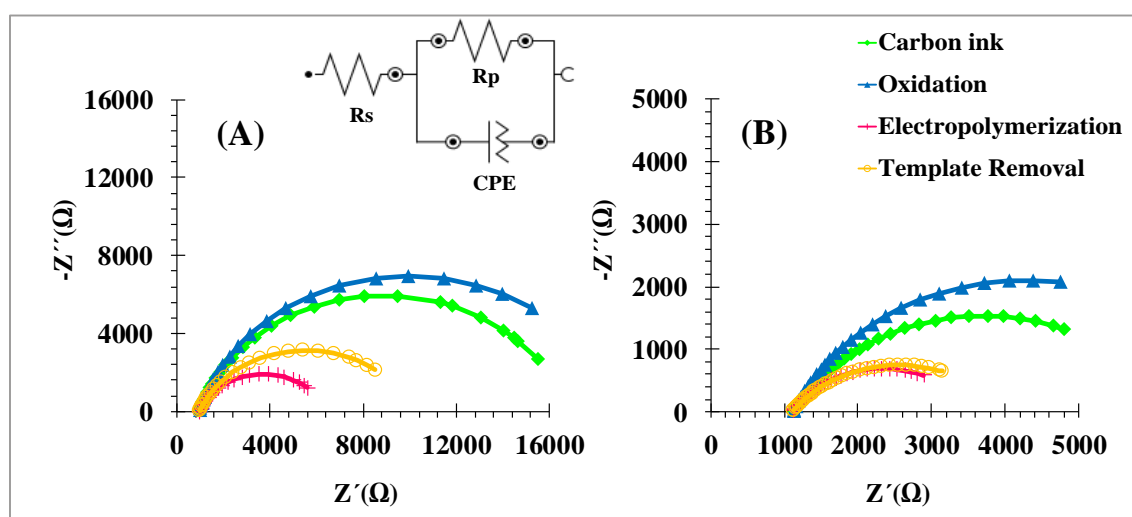


Figure 3.9 - EIS data of the assembly of the antibody-like material. **A)** sensory layer of DBS, **B)** sensory layer of EDOT.

In both cases, the electrolyte resistance corresponded to 2.50×10^{-3} mol/L of $[\text{Fe}(\text{CN})_6]^{3-/4-}$. The R_s values ranged 0.98–1.82 k Ω in DBS sensing layers and 1.11–1.37 k Ω in EDOT sensing materials. Overall, EIS measurements showed that both polymers displayed conductive features, because the original impedance decreased after electrochemical polymerization of EDOT or DBS by chronoamperometry. In addition, and comparing to EDOT sensing films, the DBS-imprinted film yielded higher decrease in resistance (meaning better electrical features) and the subsequent CRT removal promoted a higher resistance change (meaning that a higher number of rebinding positions for CRT are available, and thus better analytical features may be expected).

Overall electrical performance. The sensors were calibrated by incubating the antibody-like surface in solutions of increasing concentrations of CRT, for 30 minutes, and reading subsequently the EIS electrical features of the resulting surface. The corresponding *Nyquist* plots are shown in **Figure 3.10**, obtained in 2.50×10^{-3} mol/L $[\text{Fe}(\text{CN})_6]^{3-/4-}$ redox probe, and at a standard potential of 0.24 V for imprinted EDOT and 0.22 V for imprinted DBS, with a number of frequencies equal to 50 and an amplitude of 0.01V in both cases. The frequency range was 0.01-1000 Hz.

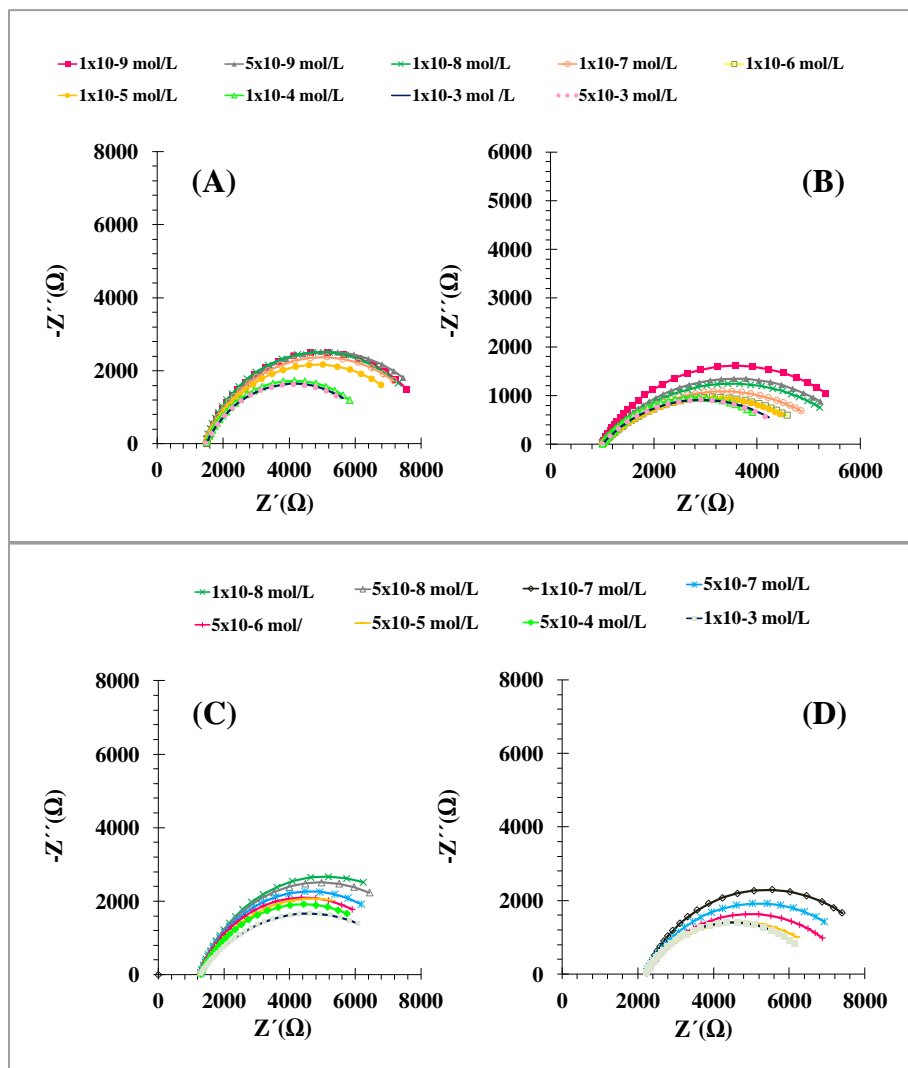


Figure 3.10 - EIS spectra obtained by calibrating the imprinted paper-based devices. Imprinted DBS (A,C) and EDOT (B,D) based materials in HEPES buffer (A,B) and urine samples (C,D).

Overall, the R_{ct} values decreased with increasing concentration of CRT. This suggested that the negative redox probe was attracted to the sensory layer when CRT was present, due to their opposite charges. In turn, this also evidenced that CRT was bound to the sensing polymeric films. **Figure 3.10** also shows at the inset the calibration curves plotting R_{ct} against log of CRT concentration, for both active and control materials. In general, polymeric films tailored with imprinted positions displayed a linear behaviour for increasing CRT amounts, in contrast to the response of control materials that was mostly random.

In buffer solutions, the imprinted DBS material responded with a linear trend from 1.00×10^{-8} mol/L to 1.00×10^{-3} mol/L, as $R_{ct} = -450.12 \times \log [\text{CRT}] + 3943.40$, with a regression correlation coefficient of 0.9984 (**Figure 3.10-A**). The imprinted EDOT responded similarly, having an $R_{ct} = -302.59 \times \log [\text{CRT}] + 2602.50$, and a regression correlation coefficient of 0.9979; the LOD was $< 1.0 \times 10^{-9}$ mol/L and the linear response was up to 1.00×10^{-4} mol/L. All control materials displayed random and uncontrolled behaviour.

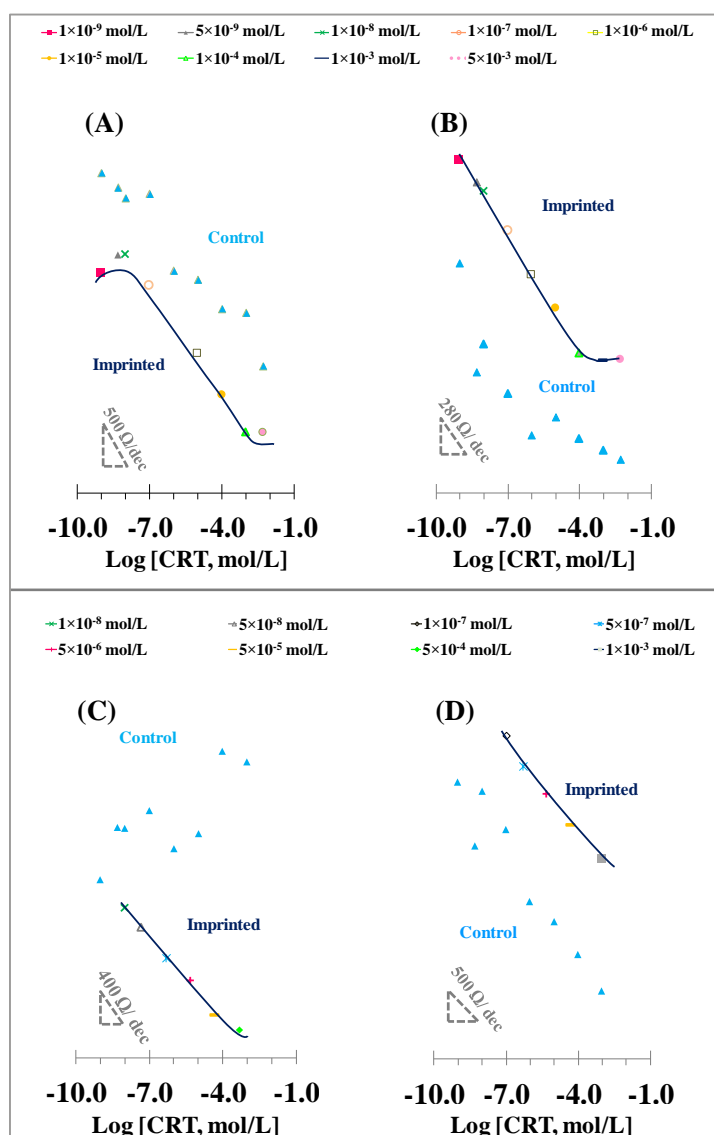


Figure 3.11 - Calibration curve of the imprinted paper-based devices. Imprinted DBS (**A, C**) and EDOT (**B, D**) based materials in HEPES buffer (**A, B**) and urine samples (**C, D**). Insets display the corresponding typical calibrations, including also the response of the control materials.

The selectivity of the sensory layers for CRT was tested by calibrating the paper-based sensors in real urine samples from healthy volunteer, diluted 10× in HEPES buffer. In general, the resulting EIS calibration curves for DBS (**Figure 3.11-C**) and EDOT (**Figure 3.11-D**) sensing materials showed good analytical features. The calibration curve of imprinted DBS (**Figure 3.11-C**) showed a linear dependence on $\log[\text{CRT}]$ from 1.00×10^{-8} to 5.00×10^{-4} mol/L, with a slope of $-376.01 \Omega/\text{decade}$. The calibrations of imprinted EDOT layer displayed linear behaviour from 1.00×10^{-7} to 1.00×10^{-3} mol/L, with a slope of $-452.40 \Omega/\text{decade}$. Control materials showed once again a random behaviour, thereby confirming that the response was mainly controlled by the rebinding of CRT to its imprinted positions on the polymeric matrix.

Overall, no interference from co-existing species present in real urine is expected to exist in the analysis of real samples, suggesting that these sensors would be capable of providing selective and specific readings of CRT in real samples.

The real urine already have CRT. For this reason, it was necessary to estimate the concentration of CRT in real urine by using the Gran's method for multiple standard addition. The CRT present in urine was $0.06 \mu\text{mol/L}$ (or 0.097 ng/mL) (**Appendix I.3**). Moreover, it was tested to calibration the paper-based sensors in synthetic urine with a best sensor (MIP DBS) to comparing with a real urine (**Appendix I.4**). The results show that calibration of the sensor under synthetic urine displays similar behaviour to that of the real urine.

3.3.9. Application and reusability

Spiked urine samples were analyzed by the previously described sensors, after calibrating these in negative urine samples (no CRT). The relative error of imprinted DBS ranged 3.90 to 6.50 %, with an average relative standard derivation of 1.10 %. For imprinted EDOT material, the relative error ranged from 9.10 to 15.40 %, with an average relative standard derivation of 3.30 %. These results indicated that both materials displayed good accuracy and precision, being DBS-based paper sensors the ones providing better relative errors.

The reason for such good analytical performance is perhaps a consequence of the very similar EIS data obtained in consecutive calibrations of the same sensor (**Figure 3.12**).

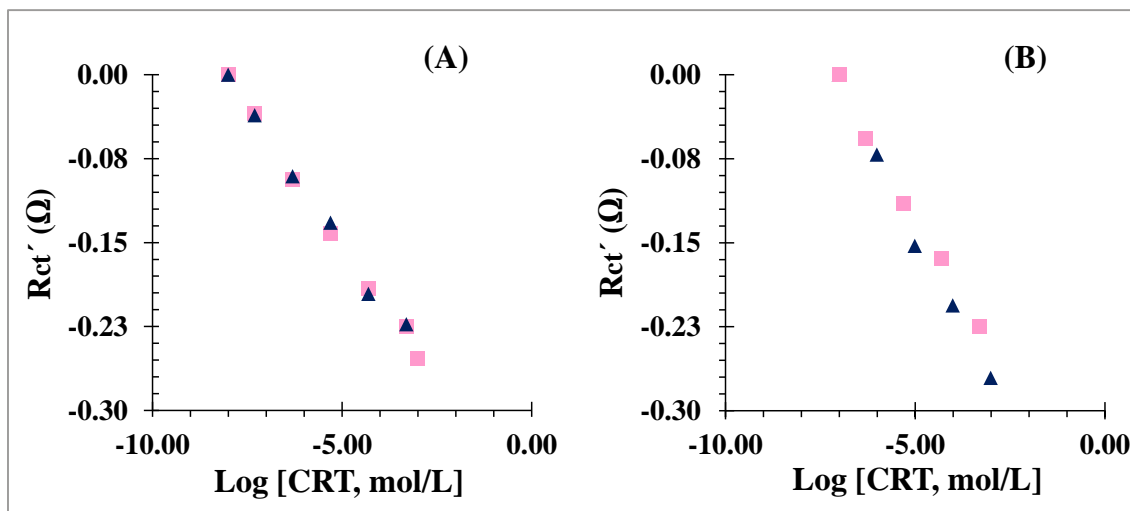


Figure 3.12 - Consecutive calibrations in serum solutions of the antibody-like polymeric sensors prepared with DBS **(A)** and EDOT **(B)** monomers.

The fact that consecutive calibrations yielded very similar features, pointed out the possibility of reusing such sensors. But not many calibrations could be made consecutively. This meant that CRT was standing on the surface and hindering the possibility of recovering the original signal. So, the CRT sensory layers were tested for an electrochemical cleaning, carried out by performing consecutive CV assays in HEPES buffer. These assays were made between -0.20 V and $+1$ V, at a potential scan-rate of 0.05 V/s with a number of crossings 10 (5 successive cycles). The efficiency of this cleaning process was tested by EIS, in the same redox couple $[\text{Fe}(\text{CN})_6]^{3-/4-}$, at a standard potential of 0.22 V, and using a number of frequencies equal to 50 scans and a sinusoidal potential peak-to-peak with amplitude 0.01 V, in the $0.01\text{Hz} - 1000$ Hz frequency range.

It was very interesting to observe that the results showed that both antibody-like films had better features in terms R_{ct} after electrochemical cleaning. The DBS based sensor presented a slope increase of ~ 70 Ω/decade (~ 20 %) and the LOD was lower than 1.00×10^{-8} mol/L; the most surprising results were those obtained with EDOT films, yielding slopes of ~ 450 Ω/decade (80 % higher), for a LOD lower than 1.00×10^{-7} mol/L, saturating the electrical response by 1.00×10^{-3} mol/L CRT.

In general, the electrochemical cleaning ensured not only reusability but also improved the observed analytical features. These features remained stable after 3 consecutive procedures of alternated calibration and cleaning and valid for more than a month.

3.4. Conclusions

The use of low-cost wax to make the paper hydrophobic was simple and effective, regarding the electrical requirements behind electrochemical sensing. The conductive ink proposed was prepared by quick and low-cost procedures, displaying excellent conductivity, thermal stability and good adhesion to the cellulose support. The tailoring of an antibody-like film for CRT was successfully achieved by simple electrochemical procedures and the film displayed high sensitivity/selectivity for rebinding CRT, even in complex matrix composition such as urine samples. The low LOD obtained also allows its practical application to the analysis of biological fluids. Moreover, LODs of these biosensors are better, when compare to other commercial methods. The coupled enzyme assays in L-CRT assay kits (from Sigma-Aldrich) have typical sensitivities of 1.60 ng/mL (colorimetric) or of 0.16 ng/mL (fluorimetric) CRT. ELISA KITS display in turn common sensitivities of 0.078 ng/mL. In this work is therefore of better sensitivity than the previous ones. MIP EDOT and MIP NaDBS showed LOD of 0.044 ng/mL and 0.0038 ng/mL, respectively. These sensors also display a wide concentration of linear response range. Despite the low cost and simplicity of preparation, the paper-based electrodes can be reused by several times before discard.

Overall, the simple construction, low cost and reusability suggest that these electrodes could have commercial viability for screening CRT or other molecules in POC. In addition, the application of the conductive ink proposed herein for the first time may be extended to prepare conductive films on different supports (such as glass, ceramics, or PET). Also, the present methodology shows to be dynamic, with further evolution perspectives and possibilities, in order to have a method suitable to be applicable in the context of the clinical analysis routine.

Considering the results obtained, it would be interesting to compare the performance of the biosensor, based on MI technique, on top of supports with different conductive materials, such as AuNPs, carbon nanostructures or conductive polymers. As these nanomaterials have exceptional electrical characteristics, they may further favor the response of the biosensors, increasing their sensitivity and LOD.

Moreover, it is important to test new electropolymerizable monomers, aiming to tailor new MIP materials that may display improved features to produce biosensors for cancer biomarkers. This is a new field of research, as within time MIP materials have evolved mostly around the same monomers.

4. Novel electro-polymerized protein-imprinted materials using Eriochrome Black T: application to BSA sensing

4.1. Introduction

Overall, the use of electropolymerization in protein imprinting is a relevant approach to produce suitable biosensors for POC. It requires however the selection of suitable monomers that may undergo electro-oxidation or electro-reduction under specific electrochemical parameters, if the target protein remains stable under the electrochemical conditions selected. Usually, most processes described in the literature involve electro-oxidation polymerizations and the oxidation of aromatic compounds. Monomers used for the purpose of small molecule imprinting include EDOT [210], Py [211], aniline [119], phenol [212], aminophenol [213] and phenylenodiamine [214]. In turn, monomers as o-aminophenol [213] and aniline boronic acid [215] have been employed for protein imprinting in electrically generated polymers [216, 217]. Thus, it is easy to conclude that the selection of monomers for electropolymerization is rather limited and that each monomer used so far holds a limited number of functionalities, which in turn may limit the electrostatic recognition of the protein upon rebinding.

Thus, this work aims to introduce a novel monomer that displays proper features for electropolymerization and its application in protein imprinting. The monomer selected for this purpose is EBT. EBT has been used to generate polymers by an electrical stimulus, [218] [219], [220] but never with the purpose of molecular imprinting. Herein, EBT may lead to the production of excellent complementary rebinding sites because it has different chemical functions within the same structure (nitro, sulfonic and hydroxyl), which may interact easily with proteins, also containing a wide diversity of functionalities.

Moreover, this new polymeric material is electropolymerized on a carbon surface, thereby yielding a low-cost support. This carbon support was also modified with PEDOT prior to the MIP synthesis, aiming to prepare a compatible support for operating a biosensor inside a PV.

BSA was selected as model target protein for this new biosensor with a poly(EBT) imprinted biorecognition element assembled on a carbon/PEDOT support. It is a low cost protein, with similarities with the Human serum albumin [221-223] that is involved in many physiological processes, including the regulation of blood osmotic pressure and pH [224].

4.2. Experimental section

4.2.1. Apparatus

A Metrohm Autolab potentiostat/galvanostat Autolab PGSTAT302N computerized electrochemical instrument, controlled by dedicated NOVA software was employed in all electrochemical measurements, including construction and analytical evaluation stages. Screen Printed electrodes (SPEs) of carbon ink were purchased from DROPSSENS, DRP-C110, with a WE of carbon with 4 mm diameter, a CE of the same material and a silver pseudo-reference (RE). All electrochemical measurements of the SPEs were made connecting these to a switch box interface, also from DROPSSENS. The chemical modification of electrode surface was confirmed by Raman from *Thermo Scientific DXR Raman* coupled to a confocal microscope.

4.2.2. Reagents

Ultrapure Milli-Q water was employed in all experiments, and chemicals were pro-analysis, used without further purification. $K_3[Fe(CN)_6]$ and $K_4[Fe(CN)_6]$ was produced by Riedel-de-Häen. PBS tablets, Myoglobin (Myo), Glucose (Glu), BSA, Hemoglobin (Hb) and Immunoglobulin G, (IgG) EDOT were purchased from Sigma-Aldrich. Crea was obtained from Fluka and H_2SO_4 from Scharlau. EBT was purchased from Biochem.

4.2.3. Solutions

Stock standard solutions of BSA for the calibration curve were prepared in 1.00×10^{-2} mol/L PBS buffer with pH 7.40 (obtained by dissolution of the commercial tablets, as indicated in the label). Less concentrated BSA standard solutions were needed to calibrate the biosensor and were prepared by accurate dilution of the stock solution in PBS buffer. Electrochemical measurements used a solution containing 5.00×10^{-3} mol/L $K_3[Fe(CN)_6]$ and 5.00×10^{-3} mol/L $K_4[Fe(CN)_6]$, also prepared in PBS buffer. The modification of the WE required a 0.50 mol/L H_2SO_4 solution, prepared in water, and 1.00×10^{-3} mol/L EBT, prepared in the same PBS buffer.

Simulated serum was prepared with the same concentrations as in real serum and used without dilution. Its composition was 0.85 g/L of Glu, 9.00×10^{-3} g/L of Crea and 4.30×10^{-5} g/L of Myo. Interfering globulin solutions were prepared in PBS buffer. Their composition was 1.20×10^{-2} g/L Hb or 0.7×10^{-3} g/L IgG.

4.2.4. Electro-synthesis of biomimetic material

The WE of the SPE was first cleaned by oxidation with H_2SO_4 by CV, under a potential range of -0.20 V and +1.50 V, for 5 cycles, with a v of 0.05 V/s. The protein-imprinted film was synthesized on the previously cleaned surface by eletropolymerizing a 1.00×10^{-3} mol/L solution of EBT prepared in PBS buffer, and containing 1.00×10^{-4} mol/L BSA. Polymerization was achieved by CV, between -0.45 V and +0.90 V, under a scan rate of 0.10 V/s, for 4 cycles. Finally, the imprinted BSA was extracted from the surface with PBS, pH 7.00, and under CV cycling, from -0.30 V to +0.80 V, with a scan rate of 0.10 V/s for 25 cycles.

Control SPEs were produced by synthesising non-imprinted polymer (NIP) films, using a similar approach but where the protein was missing.

4.2.5. Electrochemical assays

CV measurements were performed in the standard redox probe solution, containing 5.00×10^{-5} mol/L in $K_3[Fe(CN)_6]$ and in $K_4[Fe(CN)_6]$, prepared in PBS buffer. In CV assays, the potential was scanned from -0.30 to +0.70 V, at a scan rate of $0.05 \text{ V} \cdot \text{s}^{-1}$, along 2 successive CV

cycles. EIS measurements were conducted in the same redox couple $[\text{Fe}(\text{CN})_6]^{3-/4-}$, at a standard potential of 0.12 V (± 0.01 V) with 50 scans of frequencies, and a sinusoidal potential peak-to-peak with amplitude 0.01 V in the 0.01 Hz–100000 Hz frequency range. SWV analysis was performed roughly in the same condition as CV; the potential was scanned from -0.10 to +0.80 V.

4.2.6. Selectivity assays

Selectivity studies required the preparation of synthetic serum sample and its spiking with BSA. The concentrations of BSA selected for this purpose ranged between the concentrations applied to calibration curves having PBS buffer as background medium (1.00×10^{-7} – 1.00×10^{-5} mol/L). The simulated serum was prepared with 2.50×10^{-9} mol/L Myo concentration, Glu (4.72×10^{-6} mol/L) and Crea (7.96×10^{-5} mol/L), also in PBS buffer pH 7.40. These concentrations values have been selected according to their relative concentrations to BSA in biological serum samples.

4.3. Results and Discussion

4.3.1. Approach to produce the protein-imprinted film

A carbon-WE acts as support of the MIP-film. This electrode was first cleaned/oxidized and after subject to electropolymerization in a solution containing EBT and a known amount of BSA. The overall process is presented in **Figure 4.1**.

The cleaning stage of the electrode consisted on promoting the electrochemical oxidation of all materials standing at the carbon area. This was achieved by consecutive CV cycling in a solution of H_2SO_4 . This procedure oxidizes the impurities standing at the carbon electrode area, thereby improving their solubility in aqueous solution and allowing their lixiviation from the electrode surface. Thus, this oxidation stage enhanced the electron transfer capability of each blank carbon electrode and contributed for a higher reproducibility among the different commercial units of SPEs [225].

The imprinting stage was performed simply by covering the three-electrode system of the SPEs with a solution of EBT and BSA, and imposing CV conditions capable of yielding the formation of a thin-film of poly(EBT). These CV conditions selected are in agreement with the oxidation potential of EBT in a PBS solution. As shown in **Appendix II.1-A**, there are two oxidation potentials of EBT and one reduction potential. Under consecutive CVs, an EBT solution lead to the formation of a polymeric film. The collected data indicated that this polymer had non-conductive features, because its current decreased as the polymer was growing. On the other hand, the polymer was not highly isolating, as its current drop was moderate. No electrochemical alteration of BSA was evidenced under the same CV conditions, suggesting that BSA was chemically stable by the moment the polymer was growing.

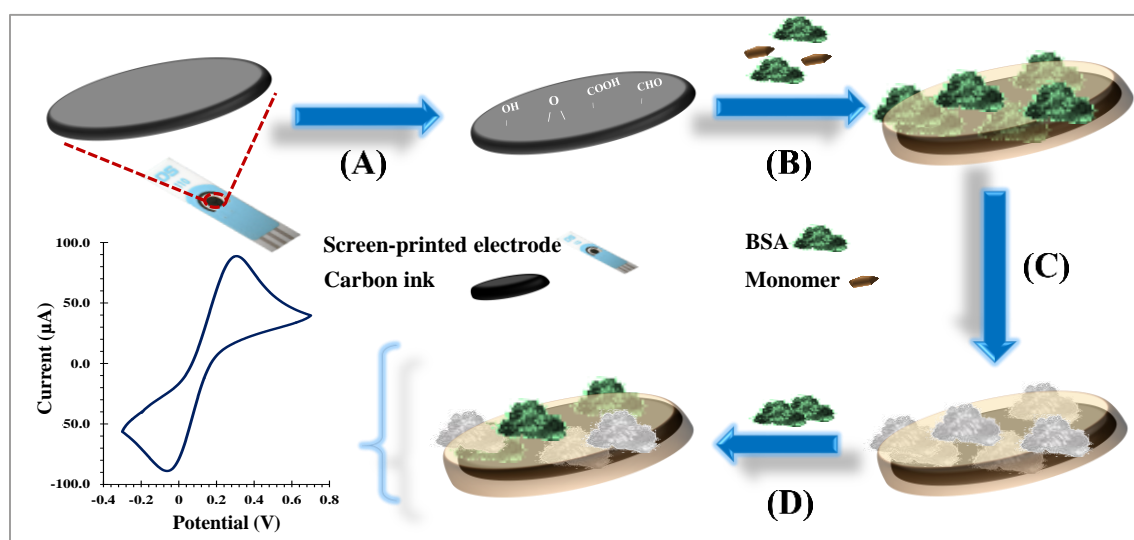


Figure 4.1 - Schematic representation of the assembly of the BSA sensor. **(A)** oxidation of the carbon electrode area; **(B)** Electropolymerization of monomers in the presence of the protein; **(C)** template removal and **(D)** protein rebinding.

The subsequent protein removal was achieved also by consecutive CV cycles, using only a PBS buffer. This treatment is expected to remove adsorbed compounds at the surface, also facilitating the exit of the protein exposed towards the outer surface of the polymer. A biosensor with a NIP thin-film was also produced in parallel (**Appendix II.1-B**) following the procedure employed in the production of the MIP film but without involving the protein. In this case, the imprinting stage involved a solution containing only EBT.

4.3.2. Optimization of relevant variables

The variables tested in the assembly of the protein-imprinted film were the concentration of the protein at the imprinting stage and the time given for the protein incubation. The concentration of BSA as varied between 1.00×10^{-7} mol/L and 1.00×10^{-5} mol/L, for a fixed concentration of EBT, always equal to 1.00×10^{-3} mol/L. The time given for the protein incubation was varied between 15 and 30 minutes.

The change in BSA concentration was evaluated by EIS, monitoring the resistance to R_{ct} of a redox standard system on a conductive surface. Herein, EIS data was plotted as *Nyquist* plots (**Appendix II.2**) and followed the R_{ct} changes occurring at that surface after each stage of chemical modification. Overall, the electropolymerization increased the R_{ct} of the previously oxidized carbon surface. The magnitude of such increase was higher for higher concentrations of protein. As BSA is not a conductive material, when it becomes entrapped within the polymer matrix it contributes for a further increase in the R_{ct} . The subsequent protein removal also indicated that BSA would be leaving the surface by decreasing the value of R_{ct} . This decrease was more intense up to concentrations of 1.00×10^{-5} mol/L BSA, suggesting the formation of a higher number of binding sites under this concentration, which was consistent with the higher number of BSA molecules per polymer formation. For higher concentrations of BSA the exit of the protein became limited, as the R_{ct} increased (instead of decreasing, as expected); it seemed that BSA adsorbed onto the MIP surface firmly, thereby limiting the access to other BSA molecules for rebinding. Considering these results, the concentration of BSA selected in this study was 1.00×10^{-5} mol/L of BSA at the imprinting stage.

The time of incubation of BSA at the rebinding period was 15, 20 or 30 min at room temperature, for complete calibrations with 7 standard BSA solutions, ranging from 5.00×10^{-7} and 1.00×10^{-5} mol/L. These results were also followed by EIS and were consistent with the previous studies, revealing a R_{ct} increase after BSA incubation (**Appendix II.3**). It was also observed that the longer is the incubation of BSA, the greater is the R_{ct} . This observation revealed time as variable that strongly affected the sensitivity of the biosensor. The calibration with 15 minutes incubation periods presented a linear response ranging from 5.00×10^{-7} mol/L to 1.00×10^{-5} mol/L and a slope $360.3 \Omega/\text{decade}$; the 20 minutes incubation showed a higher

slope, equal to 641.0 Ω /decade, for the same linear range; the 30 min incubation presented a slope 1137 Ω /decade for a linear response between 5.00×10^{-7} mol/L and 5.00×10^{-6} mol/L. Although, the incubation of 30 min had the best sensitivity when compared with other time conditions, the R_{ct} change saturated earlier, narrowing the concentration range of linear response. Thus, an intermedium time of incubation of 20 min was selected, offering intermedium conditions of slope and linear range of concentration.

4.3.3. Electrochemical follow-up of the assembly

All stages of the SPE modification leading to the production of a protein-imprinted sensor were followed by EIS and SWV. The data obtained is presented in **Figure 4.2**. The *Bode* plots corresponding to the *Nyquist* plots presented are also shown in **Appendix II.4**; the *Bode* phase expressed the capacitance of the electrochemical cell [121, 123]. The double layer capacitance of each step (**Appendix II.4-B**) was calculated from the frequency at the maximum of the semicircle present in the *Nyquist* plot.

In the *Bode* plots, the oxidized carbon showed ϕ values of 35.89° and 30.71° for MIP and NIP electrodes, at 2 Hz of frequency, respectively. This accounted the usual variability of the commercial devices, but readings in relative values leads to consistent and repeatable evaluations. Then, the MIP material shifted from 35.89° to 51.07° in ϕ , coupled with a frequency shift (1.43 Hz) after electropolymerization, and the angle decreased back to 48.30° and its frequency was 1.57 Hz after template removal. In turn, the NIP material increased around 10° ($\phi = 40.44^\circ$) with a frequency of 1.57 Hz after eletropolymerization, and showed no frequency shift after template removal, although coupled to a decrease in ϕ . Overall, the fact that after protein removal the frequency shifted only in the MIP film (and not in the NIP films) and the ϕ of MIP and NIP are in the same frequency, suggested that the protein molecules used as template successfully exited the polymeric film. Moreover, the *Bode* modulus reflected the solution resistance R_s , which consisted in the resistance between RE and WEs, mediated by the redox probe, and the R_{ct} . All modification stages showed approximately the same R_s , of $\sim 2.54 \Omega$, but the R_{ct} increased after the electropolymerization, both in MIP (from 3.27 Ω to 3.70 Ω) and NIP (from 30.71 Ω to 40.44 Ω) films. After template removal, the R_{ct} of the MIP decreased $\sim 0.12 \Omega$, while the NIP decreased $\sim 0.07 \Omega$.

In the *Nyquist* plots (**Figure 4.2-B**), the values for R_s and R_{ct} were determined by the semicircle. The *Randles* equivalent circuit was used herein because it was the model that best fitted the behaviour of biosensor along the different stages of its assembly, which all elements present error below to 7 % (**Appendix II.4**). This circuit combined the R_s , with the C_{PE} , the R_{ct} and the W . Overall, the MIP films showed that the R_{ct} of electropolymerization of EBT in MIP increased 2890 Ω (up to 4180 Ω) and then decreased by 1090 Ω (down to 3090 Ω) after template removal (**Figure 4.2-B₁**). This observation accounted the fact that the protein and the polymer act as non-conductive materials. In turn, the NIP had an R_{ct} increase of only 704 Ω after polymerization and an additional 190 Ω (but little) increase after template removal (**Figure 4.2-B₂**). The small R_{ct} increase in the NIP polymerization stage reflected the absence of the protein among the polymeric matrix, while the little increase in the template removal stage reflected the reorganization/stabilization of the polymeric surface just formed.

In the SWV assays (**Figure 4.2-A**), the corresponding data was evaluated in terms of peak current, which changed inversely to the R_{ct} values recorded previously. After MIP polymerization, the peak current decreased from 42.2 μA to 31.1 μA and the peak position shifted from 0.32 V to 0.43 V; the template removal yielded intermedium features, with a current increase up to 34.10 μA and a peak shift to 0.40 V (**Figure 4.2-A₁**). The SWV analysis of NIP showed a lower current after polymerization, followed by a slight current increase in the template removal stage (**Figure 4.2-A₂**). Overall, the SWV data was consistent with the EIS data.

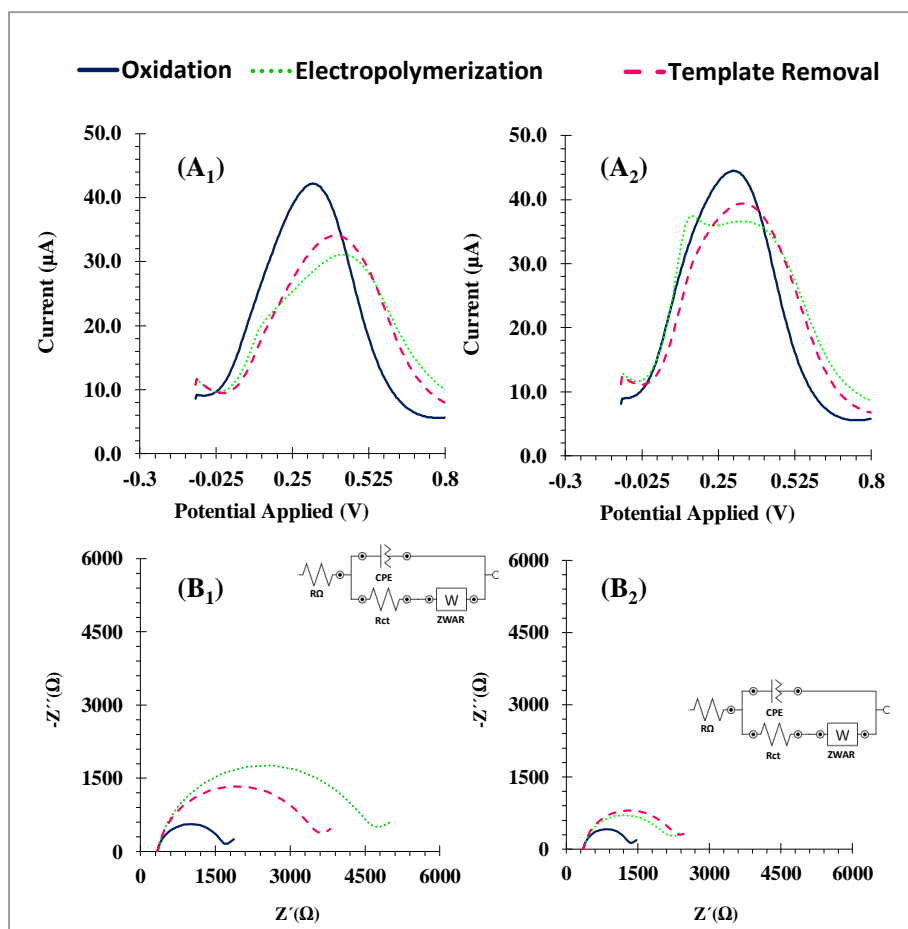


Figure 4.2 - SWV (A) and EIS (B) data in the carbon SPE in $[\text{Fe}(\text{CN})_6]^{3-/4-}$ solution prepared in PBS buffer, pH 7.00, when assembling MIP (1) or NIP (2) materials, starting with the oxidation of the carbon electrodes, the electrical polymerization for assembling the imprinted or non-imprinted material and the template removal.

Insets: the electrical circuit applied.

In general, all electrical data used to follow-up the assembly of the biosensor was consistent with a successful polymer formation and the efficient template removal. The stability of the polymer formed is an additional feature that deserves attention considering the possible commercial use of such devices and was studied next.

4.3.4. Stability of the imprinted Poly(eriochrome black T)

A biosensor shall present good stability features to provide precise and accurate measures along its storage and allow its subsequent commercialization. For this purpose, the thermal

stability of the materials was evaluated, and the signals presented by the biosensor were followed daily for a given period, by EIS (**Figure 4.3-B**).

The MIP-EBT polymer was evaluated daily with an iron redox probe within 8 days of its construction always kept under cold storage. Results of the electrochemical analysis showed that the signal variations ranged 0.24 – 7.07 %, with an average relative standard deviation of 3.07 % (corresponding to triplicate measurements). Longer periods were not evaluated as the biosensors are expected to have a single use, while these assays checked the stability under consecutive measures within ~1 week (not occurring under commercial use). Overall, these results suggest that the biosensor will offer enough stability for a possible commercialization under proper packaging, also allowing stable measurements at least for 8 days after opening the (commercial) package.

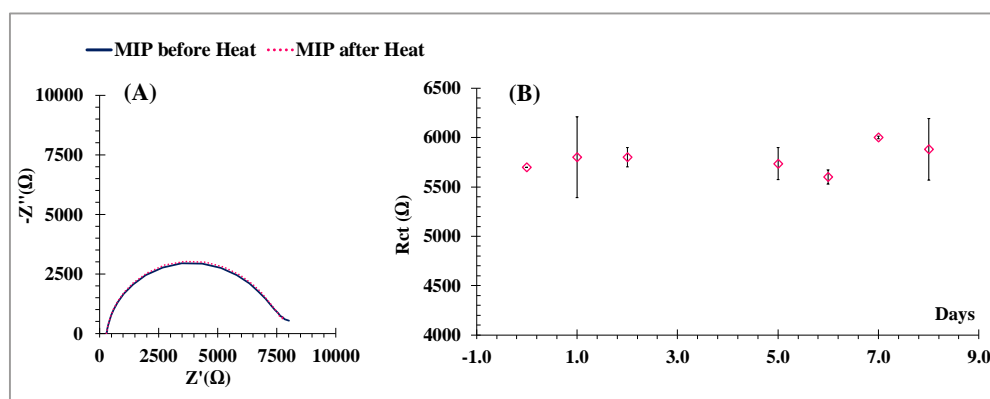


Figure 4.3 - Stability of the EIS readings after thermal treatment (A) and along time (B).

The thermal stability was also evaluated, as it may infer about its long-term stability under normal ambient conditions. In this test, the blank signal of the biosensor was recorded; then the biosensor was subject to a constant temperature of 45 °C for 2h30min (**Figure 4.3-A**) and let stand until room temperature was reached; finally, its blank signal was measured again. The MIP film had an R_{ct} of ~7120 Ω before heat treatment, and its R_{ct} varied ~10 Ω after heat treatment. Overall, the results obtained support the long-term stability of the device.

4.3.5. General analytical features

4.3.5.1. Calibration curves in buffer

EIS calibration curves were obtained first by incubating increasing concentrations of BSA standard solutions, ranging from 1.00×10^{-7} mol/L to 1.00×10^{-5} mol/L and prepared in PBS buffer. After each incubation, the *Nyquist* plot was obtained for a solution of 5.0×10^{-3} mol/L $[\text{Fe}(\text{CN})_6]^{3-/4-}$, prepared in PBS buffer, pH 7.00, at a standard potential of $0.12 \text{ V} \pm 0.02 \text{ V}$. This procedure applied to MIP and NIP films.

The data so obtained indicated a R_{ct} increase for increasing concentrations of BSA (**Figure 4.4-A**), accounting the presence of a non-conductive biomolecule bound to the sensing film. The resulting calibration curves so obtained plotted R_{ct} against \log of BSA concentration (**Figure 4.4-C**). In the MIP biosensor, a linear regression of $R_{ct} = 644.28 \log [\text{BSA}] + 7504.8$ was obtained, with a squared correlation coefficient of 0.9966, from 5.00×10^{-7} mol/L to 1.00×10^{-5} mol/L. The data obtained with the corresponding NIP films and in the same concentration range corresponded to smaller slope ($555.6 \text{ } \Omega/\text{decade}$) and a low squared correlation coefficient of 0.8097. Thus, the NIP film displayed an uncontrolled BSA rebinding profile, justified by the existence of nonspecific binding at the sensing surface (**Figure 4.5**).

Overall, the slope of the MIP was 16 % higher than that of the NIP. The linear response of the NIP was unacceptable for quantitative application purposes, in contrast to that of the MIP, where the linear response offered small differences between the experimental data points and the linear regression established. These results suggest that the rebinding positions of BSA generated among the polymeric matrix are dominating the analytical response. In turn, non-specific binding positions exist in smaller extent (as expressed by the NIP response) but generate an uncontrolled rebinding behaviour (as expressed by the very small correlation coefficient).

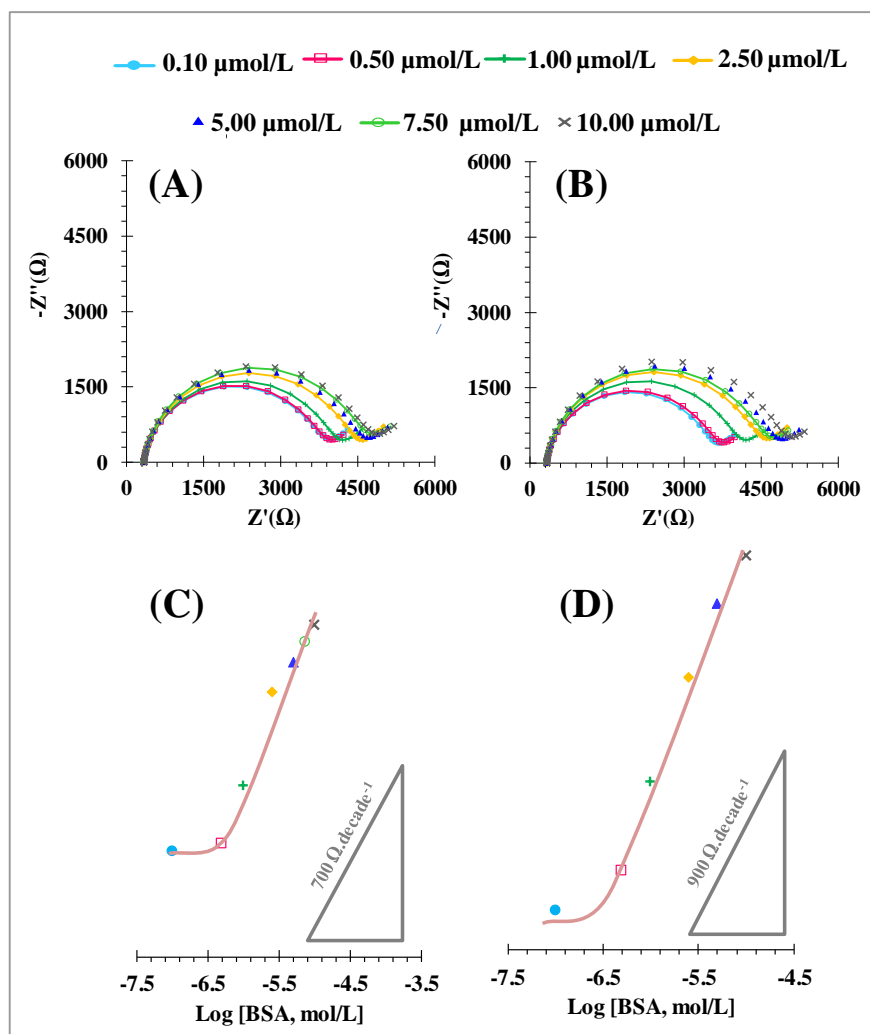


Figure 4.4 - Nyquist plots of MIP biosensors (A, B) and the corresponding calibrations (C, D), obtained after incubation of BSA standard solutions prepared in PBS buffer (A, C) or simulated serum (B, D), followed by EIS reading in standard in $[\text{Fe}(\text{CN})_6]^{3-/4-}$ solution prepares in the same medium. The response of the corresponding NIP films is also included.

4.3.5.2. Calibration curves in simulated serum

In a second stage, the background medium used for calibration was like serum. Considering that HSA would be a major component in serum, the use of blank serum this purpose was not possible. Instead, other ions that could coexist with BSA in real serum samples and are likely to interfere were used, considering their relative levels in biological fluids. The calibrating solutions were then prepared in a solution containing Crea, Glu and Myo in the same concentrations as expected in human serum (to allow determinations in samples without

dilution). The BSA concentrations changed from 1.00×10^{-7} to 1.00×10^{-5} mol/L (as in calibrations with standards in PBS buffer). Accordingly, EIS measurements were performed in 5.0×10^{-3} mol/L of $K_3[Fe(CN)_6]/K_4[Fe(CN)_6]$, prepared in the same background serum (**Figure 4.4-B**).

As in buffer, the R_{ct} increased for increasing BSA concentrations (**Figure 4.4-B**) and the resulting calibration curves plotted R_{ct} against log of BSA concentration (**Figure 4.4-D**). The MIP biosensor displayed a slope of $935.30 \Omega/\text{decade}$, with a squared correlation coefficient of 0.9904, from 5.00×10^{-7} to 1.00×10^{-5} mol/L. In the same concentration range, the NIP biosensor showed lower slope ($834.10 \Omega/\text{decade}$) and a poor squared correlation coefficient comparing with MIP (0.9392) (**Figure 4.5-B**). The LOD of the MIP biosensor was 4.51×10^{-7} mol/L.

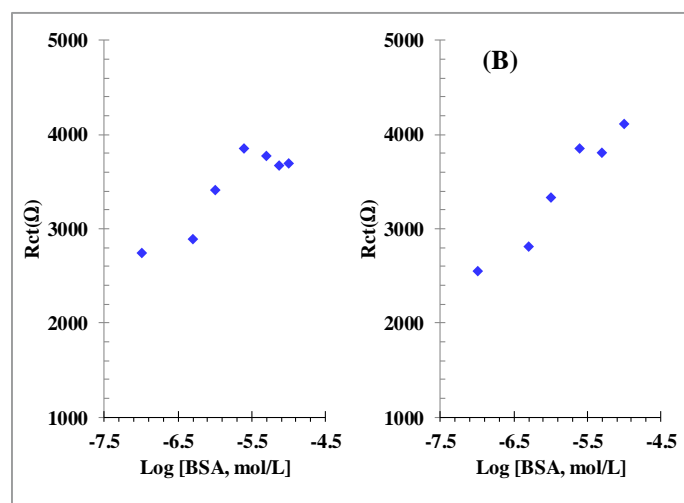


Figure 4.5 - The corresponding calibrations curves of the control material **A**) obtained after incubation of BSA standard solutions prepared in PBS buffer; **B**) simulated serum in $[Fe(CN)_6]^{3-/4-}$ solution prepares in the same medium.

Overall, the slope of the MIP was higher (12 %) than that of the NIP and the linear response was of a much superior quality, suggesting higher precision and reproducibility of the analytical data. Moreover, the use of simulated serum instead of buffer contributed to a 45 % slope increase. The higher ionic strength of the simulated serum, when compared to the PBS buffer is the probable cause for this result.

4.3.5.3. Selectivity

The selectivity test evaluated the effect of chemical compounds present in biological fluids. This was achieved by a competing test between BSA (in 4.00×10^{-6} mol/L) and other biomolecule present in human serum. The interfering species selected for this purpose, were the same selected to simulate the serum sample: Crea, Glu, and Myo. The incubation of the binary solutions (BSA + interfering species) was set 20 min, the same period used in the calibration procedure, and compared to that of a single BSA solution. The results obtained in **Appendix II.5** indicated a low binding of ability of Crea (4.45 %), Glu (3.82 %), Myo (7.64 %), Hb (11.4%) and IgG (-2.62%) revealing the good selectivity features of the MIP film.

Overall, the BSA dominated the analytical response, even in the presence of very high concentrations of other competing molecules. These results are consistent with the fact that the rebinding positions are controlling the analytical response. In fact, Myo is a small protein that would fit the huge cavities linked to BSA rebinding and it was unable to change significantly the response promoted by BSA.

4.3.6. Application of the biosensor

Simulated serum samples were analysed next. First, a MIP electrode was prepared and calibrated. Then, spiked simulated serum samples were tested in another sensor, just as a calibration is done. The concentrations of these spiked samples were calculated by means of the calibration curve of the first electrode. As different electrodes are involved in this process, only relative values are considered. In general, the experimental errors linked to the known amount of BSA present ranged from -6.60 to +15.4 % with an average relative standard derivation of ± 1.94 %. The response of the corresponding NIP is also evaluated, following the same procedures. The experimental errors obtained for the NIP were much higher than for the MIP, ranging -14.4 and -77.9% (**Figure 4.6**). Considering that this study was made in serum, it also suggested that the MIP was more selective than NIP.

Overall, it seemed clear that the MIP sensor is more selective and reproducible than the NIP, indicating a good accuracy and precision of the obtained MIP data.

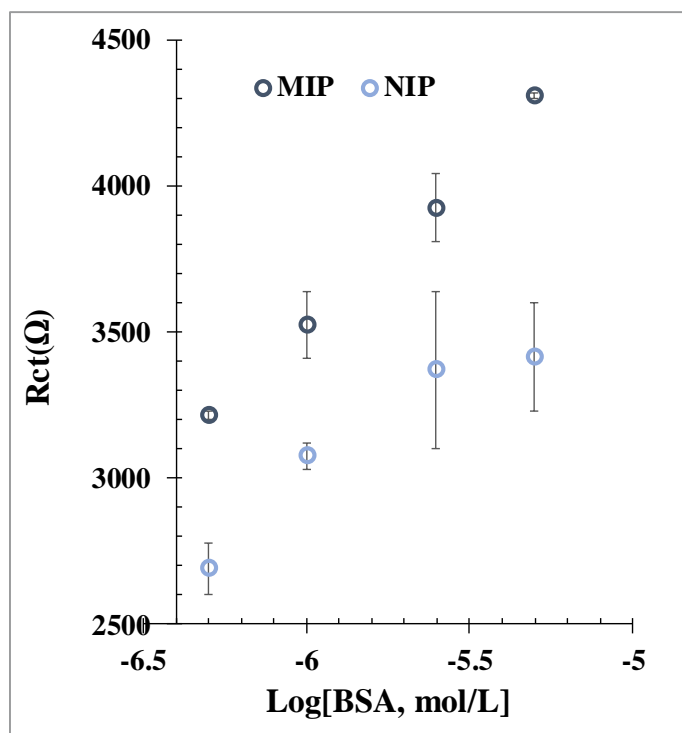


Figure 4.6 - Calibration curves of the MIP and NIP BSA electrodes evaluated in simulated serum, and the standard deviation between the different electrodes.

4.3.7. Modifying the conductive support

The ability of given MIP biosensor to distinguish BSA from other co-existing compounds is directly linked to the polymer surface interacting directly with the sample, but the sensitivity by which this discrimination is evidenced depends on the nature of the signal and the materials involved. Herein, as the signal is of electrical nature, we launched the hypothesis that the use of a highly conductive polymer could improve the sensitivity of the analytical response, i.e., the relative R_{ct} change between consecutive concentrations. For this purpose, PEDOT was electrodeposited on the carbon-WE. PEDOT exhibits high conductivity and is among the most stable conducting polymers currently available [226].

4.3.7.1. Electrochemical follow-up

The EIS data involved in the construction of the PEDOT modified sensor is presented in **Figure 4.7-A₁** and **Figure 4.7-B₁**. The PEDOT layer was obtained by electropolymerization of

EDOT, and this resulted in a significant decrease of the R_{ct} recorded in the Nyquist plots. The R_{ct} increased again after the formation of the PEPT/BSA (305.7 Ω , **Figure 4.7-A₁**) and PEPT (130.0 Ω , **Figure 4.7-B₁**) films, corresponding to MIP and NIP biosensors. The subsequent template removal step decreased again the R_{ct} ; this decrease was more significant in the MIP than in the NIP control, thereby confirming the exit of the protein from the polymeric matrix.

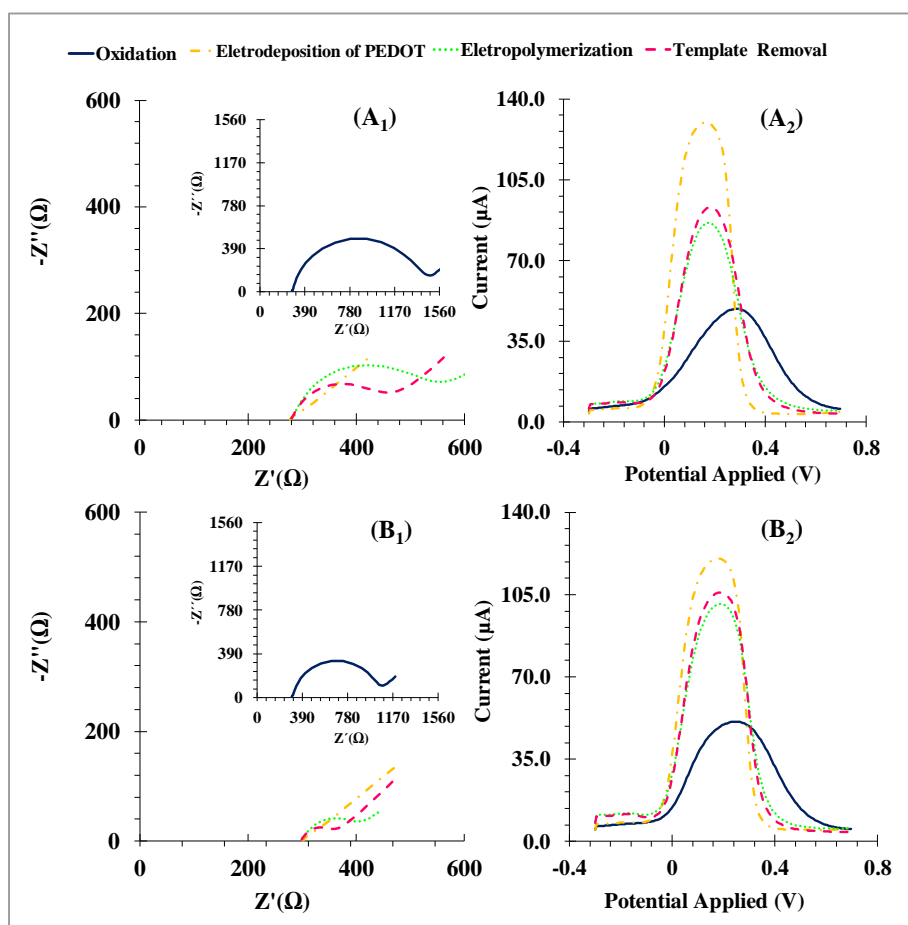


Figure 4.7 - EIS (**1**) and SWV (**2**) data for the different stages of the assembly of the MIP-PEDOT (**A**) and NIP-PEDOT (**B**) biosensor using the redox probe $[\text{Fe}(\text{CN})_6]^{3-/4-}$ prepared in PBS buffer.

Accordingly, the SWV data (**Figure 4.7-A₂** and **Figure 4.7-B₂**) was consistent with the previous EIS data. The PEDOT electropolymerization step increased the current of the oxidized carbon (6.68 μA in the MIP and 4.83 μA in the NIP), respectively, decreasing again after the electropolymerization step of PEPT. Such decrease was more evident in the MIP, confirming the presence of BSA within the polymeric matrix. The template removal caused a current

increase, which was smaller in the NIP. In addition, a peak potential shift was observed, but only in the MIP film (of -5.04 mV), which confirmed again the exit of the protein.

4.3.7.2. Raman spectroscopy follow-up

The Raman spectra of the WE was recorded for the several stages of electrode modification. The obtained spectra are shown in **Figure 4.8**, and evidenced three peaks occurring typically in carbon materials, located at 1370, 1580 and 2700 cm^{-1} Raman shift. These are known as G, D and 2D peaks, respectively. The G peak represented the bond-stretching vibrations of sp^2 hybridization carbon atoms, expressing the C=C stretching; the D peak expressed the vibrations of the carbon atoms of dangling bonds or sp^3 hybridized of carbon atoms, indicating the presence of disordered and/or defected in the carbon [201, 202]. The 2D peak represented the second order of the D band, involving a two-phonons lattice vibrational process, without the presence of any kind of disorder or defects [227].

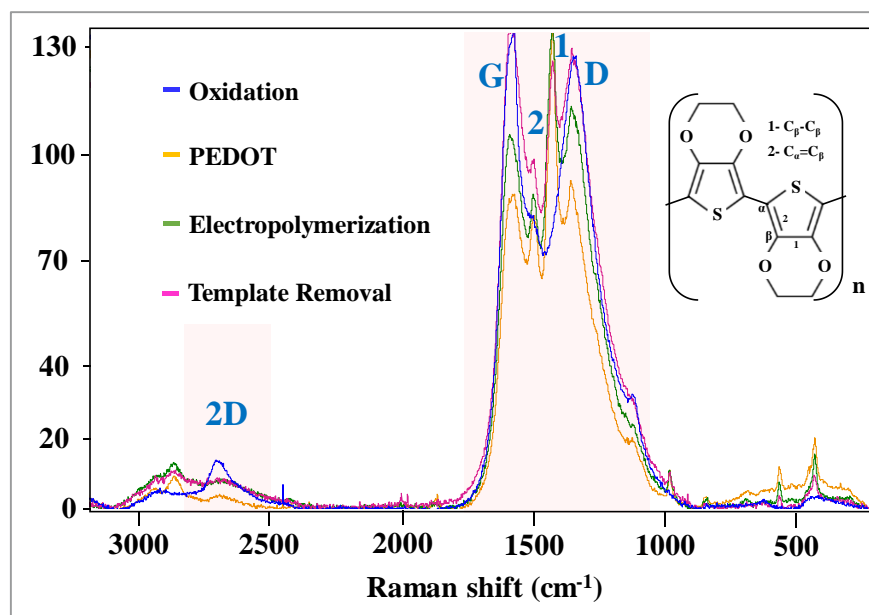


Figure 4.8 - Raman spectra of several films concerning the several stages of modification of the assembly the MIP-PEDOT on the carbon electrode. **1)** and **2)** are characteristic peaks of PEDOT.

The intensity ratio of I_D/I_G peaks is often used to quantify the defect density of the carbon material and was used herein to check the occurrence of a given chemical modification (**table 4.1**). The oxidized carbon was the starting material and yielded an I_D/I_G ratio of 0.94. When EDOT was electropolymerized on top, this ratio increased to 1.04. This signalled the C_{β} - C_{β} stretching in the PEDOT matrix and was coupled by a D peak shift to higher frequencies (from 1352.9 to 1366.8 cm^{-1}) and a G peak shift to lower frequencies (from 1583.4 to 1580.4 cm^{-1}) [228]. Two additional peaks appeared at this stage: **(1)** one at 1434.3 cm^{-1} , the strongest one, and probably assigned to $C_{\alpha}=C_{\beta}$ ($-O$) symmetric stretching vibration; **(2)** and at 1504.9 cm^{-1} assigned to the C=C stretching. Overall, the changes occurring at the Raman spectra upon EDOT electropolymerization confirmed the presence of PEDOT on top of the carbon electrode.

Table 4.1 - Analytical data extracted from the collected Raman spectra of the several materials.

Material	Raman intensity				Raman Shift				Peak ratio	
	1	2	G Peak	D Peak	1	2	G Peak	D Peak	I_D/I_G	I_1/I_2
Oxidized carbon	—	—	135.29	127.55	—	—	1583.41	1352.90	0.94	—
PEDOT	232.09	141.03	151.34	157.88	1434.32	1504.91	1580.41	1366.80	1.04	1.64
Electrical polymerization	164.00	106.87	127.30	136.62	1434.93	1509.28	1597.95	1364.00	1.07	1.53
Template Removal	155.83	121.50	168.06	160.34	1434.36	1504.80	1587.78	1361.17	0.95	1.28

The addition of a polymeric imprinted layer on the PEDOT is expected to contribute to disorder the sp^2 carbon system, thereby leading to an I_D/I_G ratio increase. This was confirmed by a moderate ratio increase, from 1.04 to 1.07. Considering that the PEDOT film yielded two additional peaks, the ratio between these peaks (I_1/I_2) was also evaluated; the intensity ratio decreased from 1.64 to 1.53, thereby also confirming that the PEDOT layer had been modified. Moreover, the 2 peaks had a Raman shift (from 1504.91 to 1509.28 cm^{-1}) as well as the G peak (from 1580.41 to 1597.95 cm^{-1}), thereby also confirming the successful modification of the PEDOT layer.

The template removal stage was in general consistent with the previous observations. The I_D/I_G ratio decreased (from 1.07 to 0.95), as well as the I_1/I_2 ratio (from 1.53 to 1.28). The 2 peaks had a Raman shift (from 1509.30 to 1504.80 cm^{-1}) as well as the G peak (from 1597.90 to 1587.80 cm^{-1}), thereby also confirming the successful protein exit.

Overall, Raman spectra confirmed the successful chemical modification of the sensing surface. The usefulness of such modification was evaluated next by checking the resulting analytical features.

4.3.8. Re-evaluation of the Analytical Features

To assess the effect of the PEDOT film under the PEBT imprinted layer on the performance of the BSA biosensor, the analytical features of this novel biosensor were also evaluated. This was done by calibration curves and selectivity studies, employing a similar approach to that reported for the biosensors without PEDOT. The obtained EIS data and the corresponding calibration curves results are present in **Figure 4.9**.

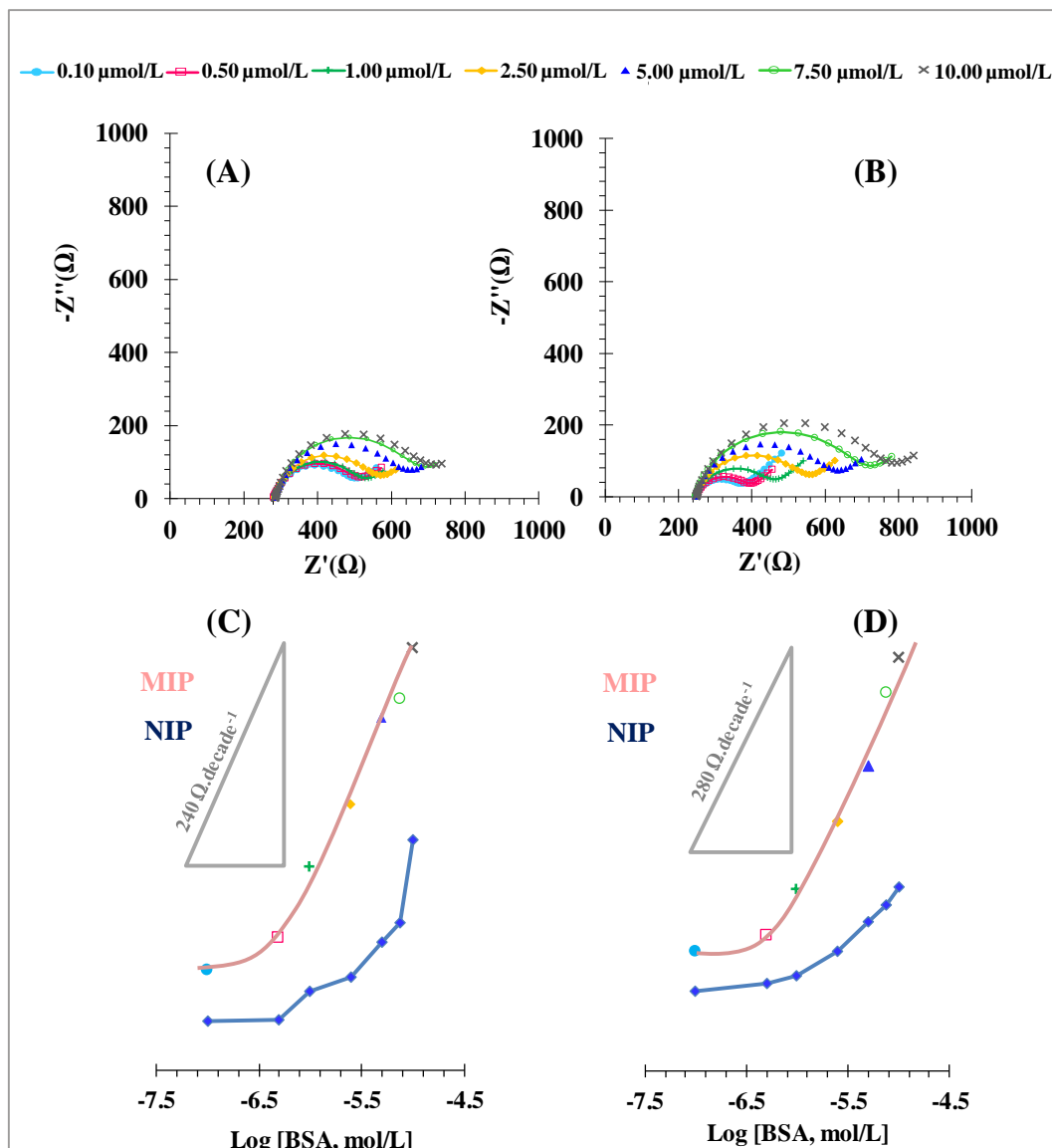


Figure 4.9 - Nyquist plots of MIP-PEDOT biosensors (**A, B**) and the corresponding calibrations (**C, D**), obtained after incubation of BSA standard solutions prepared in PBS buffer (**A, C**) or simulated serum (**B, D**), followed by EIS reading in standard in $[\text{Fe}(\text{CN})_6]^{3-/4-}$ solution prepares in the same medium. The response of the corresponding NIP films is also included.

4.3.8.1. Calibrations in PBS buffer

In PBS buffer solutions (**Figure 4.9A-C**), the MIP displayed a linear trend from 5.00×10^{-7} to 1.00×10^{-5} mol/L, fitting the equation $R_{ct} = 257.6 \times \log [\text{BSA}] + 1951.6$, with a squared correlation coefficient of 0.9896. In the same concentration range, the NIP material showed a much lower slope ($91.27 \text{ } \Omega/\text{decade}$, corresponding to only 35 % of the MIP slope)

and an unacceptable squared correlation coefficient (0.7281). These results indicated clearly that the non-specific response became negligible and that the sensitivity improved, only by placing a PEDOT film under the sensing polymeric layer. Although the absolute R_{ct} values seemed smaller than in the biosensor without PEDOT, its relative changes between consecutive concentrations were higher. This revealed and revealed an increased sensitivity, which was expected to lead to an increased accuracy.

4.3.8.2. Calibrations in simulated serum

In simulated serum conditions, a linear response was observed from 5.00×10^{-7} to 1.00×10^{-5} mol/L, with a slope of $285.4 \Omega/\text{decade}$ (**Figure 4.9-B**), and a squared correlation coefficient of 0.9859 (**Figure 4.9-D**). The LOD and limit of quantification (LOQ) of the MIP were 4.93×10^{-7} mol/L and 5.00×10^{-7} mol/L, respectively, like the ones presented. As reported before, the NIP presented lower slope and poorer regression correlation coefficient than the MIP; the slope was $69.60 \Omega/\text{decade}$ (39 % slope than that of the MIP) and the squared correlation coefficient was 0.866.

Overall, the relative R_{ct} changes increased from 0.31 to 2.69, when PEDOT was added to the carbon support before producing the MIP film of PEDOT on TOP (**Appendix II.6**). Thus, this tremendous sensitivity increase was clearly assigned to the presence of a conductive material under the antibody-like film. This fact seems to be related with positive charges that PEDOT has along polymeric structure [229], which it allows to electrostatic interaction between BSA (negative charged) and polymer.

4.3.9. Comparison to previously reported BSA sensors

MIP for BSA detection published throughout the years are listed in **table 4.2**. Comparing all these sensors, the surface to which the imprinted MIP is attached are very different, as well as the kind of monomers employed and the type of polymerization. However, these sensors present nanostructure materials with huge conductivity features and it seems to be related with reach very low LOD. In this work, it was possible to observe that the sensitivity of MIP had a significant increase after introduction the high conductive material, PEDOT, confirming the influence of nanostructured materials at the sensing element. Despite of the LOD of the

present sensor to be high, it shows LOD similar or better than some biosensors present in literature. This work also offers enough detection capability to real samples analysis, along with lower cost material and higher construction simplicity than all other concurring works. In addition, the proposed work fits well the disposable requirements in biological analysis in POC in terms of cost.

Table 4.2 - Previous works reporting molecularly-imprinted polymers for BSA detection.

Transducer	Support	MIP materials	LOD (mg/mL)	Linear response (mg/mL)	Ref
Optical	MPTS-modified ZnO particles	Surface grafting with AM, MAA and BAM	0.2	0.8–2.0	[230]
Optical	Hydrogel	Hydrogel with AM and BAM	3.2	3.2–5.7	[231]
Optical	Cr and Au layers	EP of APBA	0.02	0.02–0.8	[50]
Piezoelectrical	Au	FRP of MAA, AAC, and VPL	10	10-100	[232]
Electrical	CNTs decorated with MNPs	EP of Py	2.8×10^{-8}	1×10^{-7} to 1×10^{-1}	[233]

AM: Acrylamide; MAA: methacrylic acid; BAM: N,N'-methylene-bisacrylamide; APBA: 3-aminophenylboronic acid; AAC: acrylic acid; VPL: vinylpyrrolidone; Py: pyrrol; EP: Electropolymerization; FRP: Free Radical Polymerization; CNTs: Carbon nanotubes; MNPs: magnetic nanoparticles; MPTS: methacryloxy propyltrimethoxysilane.

4.4. Conclusions

EBT was applied successfully as monomer in the preparation of protein-MIP films by electropolymerization, having a protein as molecular target. The obtained polymeric films assembled on a carbon support displayed good rebinding features for BSA, offering also suitable thermal and long-term stability, and exceptional reproducibility within time.

The test of the biosensor for increasing BSA concentrations revealed good sensitivity/selectivity features, over a wide concentration range and ability to discriminate BSA

among other compounds. The calibration in simulated serum was more sensitive than that in PBS buffer. However, the inclusion of a highly conductive film before assembling the MIP layer (represented herein by PEDOT) lead to a significant increase upon the relative signal variations. The control materials (NIP) showed random or uncontrolled signal variations. This confirmed that the MIP response was mainly controlled by the specific rebinding sites tailored at the imprinting stage.

Overall, the biosensor presented herein displayed strong simplicity in designing, short measuring time, good analytical performance within the biological levels of BSA, and good selectivity against other possible interfering proteins. Moreover, these results confirmed that the introduction of a PEDOT film in the transducer is beneficial in terms of analytical output. This may be a relevant interface feature when trying to include the biosensor inside the PV.

5. Self-powered and self-signaled autonomous electrochemical biosensor applied to carcinoembryonic antigen determination

5.1. Introduction

Biosensors based on electrochemical transduction are amongst the most popular devices in biochemical sensing [234]. The current technology behind electrochemical biosensors has been further improved by generating a self-powered device with electrical autonomy features. To this end, a renewable electrical power source, DSSC, [141, 235] was merged with a biosensing unit targeting cancer biomarkers [162, 163]. A DSSC is a simple PV, inspired on the photosynthesis of plants and invented a long time ago by O'Regan & Grätzel [141]. It combines CE and WE in contact through an electrolyte redox system that ensures closing the electrical circuit and restoring the dye that was oxidized by light incidence [162, 235].

In the self-powered biosensor approach, the CE of the DSSC was modified with a biorecognition element to which a target biomarker would bind, turning the operation of the photovoltaic dependent from the concentration of that biomarker. This approach was tested successfully by using both natural [162] or plastic [163] antibodies as biorecognition elements to a target cancer biomarker. Yet, this self-powered device remained electrically dependent as the electrical output was being measured by a potentiostat.

Aiming to confer full autonomy to the device, a new signalling/transducing element was required. As a newly disruptive approach, never tested before, an EC was interfaced in the DSSC/biosensor hybrid set-up. The EC generates a colour that shall also be concentration dependent [164, 187]. As a single DSSC generates under normal condition ~ 0.7 V, and the EC may be of single use, organic materials were selected in this work, most specifically PEDOT.

As proof-of-concept, the self-powered and self-signalled device was designed to determine CEA. Herein, the sensing area of the device consisted in a MIP layer to recognize CEA assembled on a suitable CE support. The MIP layer was formed simply by electropolymerizing Py monomers in the presence of CEA. In turn, the selection of a suitable CE was critical. Typically, Pt is the preferred material, accounting its great electrocatalyst features, but it is too expensive and prohibits the production of a low cost device [235, 236]. In alternative, carbon materials or conductive polymers have been proven successful CEs in DSSCs. PEDOT in particular shows good conductivity, high transparency, remarkable stability, and low cost when compared to Pt [235, 237], as has been selected herein. Thus, the MIP film was assembled on a CE of a PEDOT layer on FTO glass.

Thus, the hybrid DSSC/biosensor was set-up with a traditional photoanode of TiO₂ with a ruthenium-based dye, an FTO/PEDOT CE containing an imprinted PPy film for CEA on top, and an I⁻/I₃⁻ redox-based electrolyte. The EC was interfaced in the external electrical circuit. This cell consisted of a PEDOT-based EM, a semi-solid electrolyte and an FTO-conductive glass. The overall set-up was optimized regarding the main critical aspects and tested in the analysis of real samples.

5.2. Experimental section

5.2.1. Reagents and materials

All chemicals were of analytical grade and water was deionized or ultrapure Milli-Q laboratory grade. The following chemicals were used: Acetic acid glacial (AA, 100 % p.a.), (Analar Normapur); acetonitrile (ACN, CH₃CN, 99.9 %) and NaH₂PO₄ (Scharlau); PBS (Amresco); CEA from human fluids, (EastCoast Bio); ethanol absolute (EtOH, ≥ 99.9 %), (Panreac); hexachloroplatinic (IV) acid hexahydrate (H₂PtCl₆·6H₂O, ~40% Pt for synthesis) and KCl (Merck); 1-hexyl-3-methylimidazolium iodide (HMII, C₁₀H₁₉IN₂, 98%) and EDOT, 97 % (Alfa Aesar); I₂, K₃[Fe(CN)₆], K₄[Fe(CN)₆], Na₂HPO₄ and Sodium acetate (Riedel-de-Häen); lithium iodide (LiI, anhydrous, beads, ~10 mesh, 99.999% trace metals basis), di-tetrabutylammonium cis-bis(isothiocyanato) bis(2,2'-bipyridyl-4,4'-dicarboxylato) ruthenium(II) (N719 dye) and TiO₂

(IV), anatase nanopowder (TiO_2 , 99.7 % trace metals basis, < 25nm), *p*-phenylenediamine and chloroform (Sigma-Aldrich); 4-*tert*-butylpyridine (TBP, $\text{C}_9\text{H}_{13}\text{N}$, >96.0 %), anhydrous toluene, anhydrous dichloromethane, 1,4-*bis*-2-thienylbutane-1,4-dione and Py (TCI). The conductive glass substrates used throughout had a conductive film of fluoride-doped tin oxide (FTO, sheet resistance 13.0 Ω/sq), and were acquired to Sigma-Aldrich. The electrolyte used in EC was a commercial Nafion solution, 20 wt.% (contains alcohols) from QUINTECH.

5.2.2. Equipment

All electrochemical measurements were made in a potentiostat/galvanostat, Autolab PGSTAT302N, from Metrohm, equipped with a Frequency Response Analysis (FRA) module, interfaced to computer and controlled by NOVA 1.9 software. DSSC measurements were made in the same equipment, coupled to a LED driver accessory, also from Metrohm. EIS was performed in a frequency range 0.1-100000 Hz. The J - V response of the solar cell was obtained using PV measurement system, under 100 mW/cm^2 , having a LED driver operating with 450 mA output warm white LED. The cell area was fixed at 0.6 cm^2 . Sintering was made in a Nabertherm GmbH P330 oven.

Solid materials were characterized by Raman spectrometry, using a DXR Raman spectroscope from Thermo Scientific, equipped with a confocal microscope. The Raman spectra was collected with a 785 nm excitation laser, in the Raman shift from 47 to 3300 cm^{-1} , for 0.5 mW power in combination with a 50 \times objective magnification for focus and collection of Raman-scattered light. The confocal aperture was set to 50 μm slit.

The digital image of the EM was acquired by a digital camera Sony A6000. The colour coordinates of images was obtained by the HSL colour system (Hue, Saturation and Luminousness of the HSL space) and measured by using the Paint program of Window.

5.2.3. DSSC assembly and performance

5.2.3.1. Counter electrode preparation

The DSSC was assembled in a conventional configuration (**Figure 5.2**), for which two different CEs were prepared. These were Pt or PEDOT based, always assembled on FTO/glass as support. First, the FTO area was cleaned by successive ultra-sonication in acetone followed by EtOH and deionized water washing. The active area of the electrode was defined after by applying an insulating film by spin-coating (1700 rpm/20 s) on a circle of 1.00 cm diameter. The subsequent removal of this circle granted an exposed FTO glass area of 1.00 cm diameter. A silver ink painted in one of the edges granted good electrical contact to this electrode.

The active area of the FTO glass was after covered by Pt or a PEDOT film. For the Pt coverage on top of FTO glass, a Pt salt was dissolved in EtOH and deposited by spin coating at 2000 rpm for 20s. Then, this glass was annealed in the oven at 450 °C for 15 min, resulting in the CE of Pt (Pt CE) [238]. In the PEDOT CE, this conductive polymer was produced *in-situ* by electropolymerization under a 3-electrode cell (FTO glass acting as WE, AgCl/Ag as RE and Pt as CE). The cell was submerged in a solution of 0.01 mol/L of EDOT prepared in aqueous KCl (0.10 mol/L), and was subject to a potential of 1.10 V during 15 s. It was then washed with ACN to remove exceeding material.

5.2.3.2. Photoanode preparation

The FTO glass substrate was ultrasonically cleaning in EtOH for 15 minutes, followed by 15 minutes in deionized water, and a drying stage in N₂ atmosphere. In parallel, a homogeneous suspension of 6.0 g of TiO₂ anatase nanopowder in 8.0 mL of EtOH absolute, 1.0 mL of AA and in 1.0 mL of ultrapure water, was prepared. This suspension was stirred for 1 h, at room temperature and the resulting paste casted on the clean FTO coated glass, via doctor blade method. Different photoanodes were produced for this purpose, having distinct geometries and areas: rectangular form with an area of 1.40 cm², and circular forms with areas of 0.70 and 0.20 cm².

The photoanodes were then annealed at 450 °C for 30 min to activate the electronic conduction, cooled down to 80 °C and immersed in a dye solution (5.0×10⁻⁴ mol/L of N719 in EtOH) for 18 h, at room temperature, in the dark [162, 235, 239-241]. After dye adsorption,

the photoanode was removed from the solution, cleaned with EtOH to remove non-adsorbed dye, and dried at room temperature [162, 235].

5.2.3.3. *Assembly and Performance*

The photoanode and the CE were placed face-to-face, in a sandwich configuration, with a spacer in-between and an I^-/I_3^- electrolyte in the middle to close the electrical circuit. The electrolyte solution contained 0.05 M of I_2 , 0.1 M of LiI, 0.6 M of HMII and 0.5 M of TBP, dispersed in ACN. The cell was sealed with a scotch magic tape (thickness 0.06 mm), acting also as a spacer layer between the two electrodes.

The performance of the DSSC was evaluated under a white LED illumination with 100 mW/cm² irradiation. The $J-V$ features of the cells were recorded in the potentiostat/galvanostat and used to calculate relevant photovoltaic data (overall η ; V_{OC} ; J_{SC} ; and FF).

5.2.4. Hybrid DSSC/biosensor

The glass-FTO electrodes were cleaned with EtOH following by acetone and water during 20 minutes in each washing inside of sonicator, to remove impurities. In order to enhance the electrocatalytic properties of the glass-FTO electrodes a PEDOT film were electrosynthesized on its surface **(1)**. Subsequently, the imprinted sensor **(Figure 5.1)** was assembled on glass-FTO/PEDOT surface **(2)** by CV cycling (10 cycles) in a solution containing Py (50×10^{-3} mol/L in PBS buffer) and CEA (0.25 ng/mL). CV scans ranged between -0.20 and +0.90 V, with a scan rate of 50 mV/s.

5.2.4.1. *CEA-biosensing film*

The biosensing film **(Figure 5.1-A)** was obtained by tailoring a MIP layer of Py (MPPy) on the FTO/PEDOT glass electrodes described in section 2.3.1. This was made by electropolymerizing by CV (10 cycles) a Py (5.0×10^{-2} mol/L, in PBS buffer) solution with CEA (0.25 ng/mL), in the 3-electrode cell. The 3-electrode cell was the same used to prepare the PEDOT film. CV scans ranged -0.2 to +0.9 V, at a scan-rate of 50 mV/s.

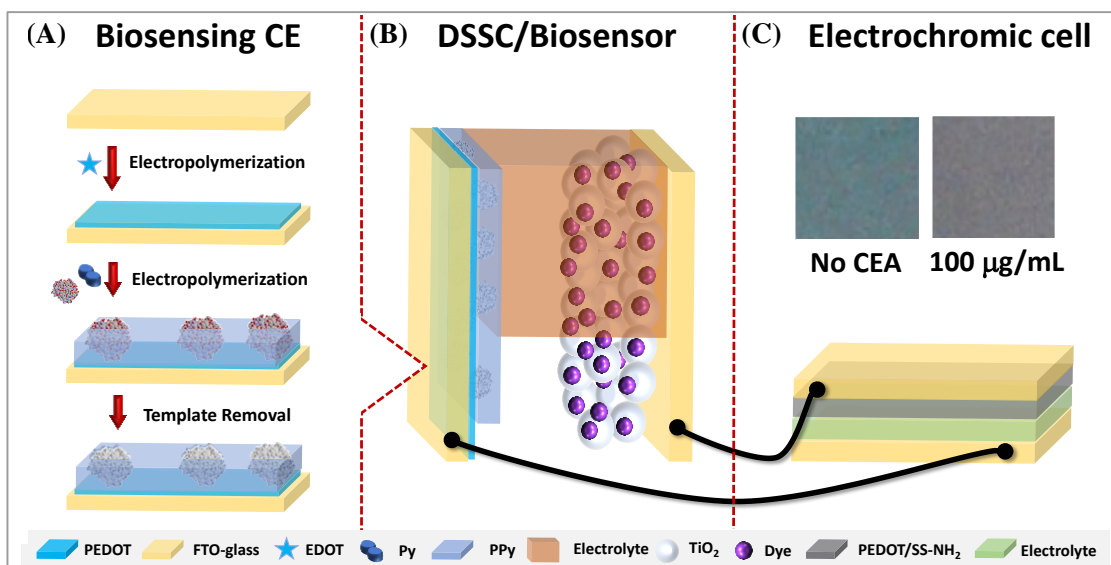


Figure 5.1 - Schematic representation of the several stages of the biosensing film assembly (A), its integration in the DSSC as the counter electrode to produce the hybrid device (B) and the interface of the external circuit with the electrochromic cell (C).

The resulting electrode (FTO/PEDOT/CEA-MPPy) was intensively washed with buffer and incubated for 5 hours in proteinase K (500 µg/mL), prepared in PBS buffer, pH 7.40), in the dark, in order to remove the protein template. The final imprinted material (FTO/PEDOT/MPPy) was then rinsed with PBS buffer, to remove peptide fragments and adsorbed proteinase K, and finally rinsed with MQ water. Non-imprinted materials (FTO/PEDOT/NPPy) were produced in parallel using exactly the same procedure, but excluding CEA from it. All these steps were evaluated by electrochemical techniques against an iron redox probe of 5.00×10^{-3} mol/L, prepared in acetate buffer.

5.2.4.2. CEA rebinding and electrochemical performance

The rebinding of CEA was made by incubating buffer, standard solutions or samples in the MPPy area for a given period. Calibrations started by incubating the CEA standard solution of lower concentration in the sensory surface of the electrode, for 15 minutes (the same time as with the buffer solution), followed by a washing step with buffer. CEA concentrations ranged from 0.1 ng/mL to 100 µg/mL, prepared in acetate buffer, pH 6.00.

After rebinding, the biosensing electrode was combined in a 3-electrodes system to monitor the EIS data changes of a standard iron redox probe. The data reported herein corresponded to a minimum of 3 independent evaluations. Assembly of the hybrid system and performance

The set-up of the hybrid device was like the regular DSSC, but the biosensing electrode replaced the normal CE (**Figure 5.1-B**). This set-up was made only after incubating the CEA standard solutions or samples in the biosensing film. The performance of the resulting DSSC was evaluated by monitoring EIS and J - V data.

5.2.5. Electrochromic cell

5.2.5.1. *Electrochromic material*

The EM was a PEDOT-based film placed on an FTO-glass support. This film was obtained by electropolymerizing EDOT, but in the presence of a derivative that would improve the colour change through potential variations. The derivative was 4-[2,5-Di(thiophen-2-yl)-1H-pyrrol-1-yl]aniline (SNS-NH₂), synthesised by adapting a literature procedure [242]. For this purpose, a solution of AA (1.5 mL) was added dropwise to a mixture of 1,4-*bis*-2-thienylbutane-1,4-dione (0.002 mol) and *p*-phenylenediamine (0.005 mol) in anhydrous toluene (25 mL), until a pH of 4 was reached. The resulting mixture was refluxed for 24h, under nitrogen, and the product formation followed by TLC. The final product was obtained by flash chromatography with dichloromethane (yield of 69%), followed by thin layer chromatography (TLC). Its chemical structure is shown in **Appendix III.1**, which was also confirmed by ¹H-RMN studies of the obtained product (**Appendix III.2**).

The EM was then generated on the FTO-glass support by electropolymerization of EDOT in the presence of SNS-NH₂. A solution of 2.50×10^{-4} mol/L SNS-NH₂ and 0.10 mol/L EDOT dissolved in 0.10 mol/L lithium perchlorate (LiClO₄)/0.1 mol/L sodium perchlorate (NaClO₄) prepared in ACN was used for this purpose, subject to single CV scanning, between 0.0 V and 1.30 V, at 0.05 V/s of scan rate. The resulting electrochromic features were evaluated using 0.10 mol/L of KCl as supporting electrolyte, by applying constant external potentials on a 3-electrodes set-up.

5.2.5.2. Cell set-up

The EC was set-up by sandwiching face-to-face the FTO-glass with the EM and another clean FTO-glass, with a polymeric electrolyte (Nafion®) in-between (**Figure 5.1-C**).

5.2.5.3. Interface in the hybrid DSSC/biosensor

The EC was interfaced in the external circuit linking the photoanode to the CE acting as biosensing film (**Figure 5.1B-C**). It was previously applied to a condition of 0.0 V, forcing the EM to its neutral state. Under working operation, a white LED hits the hybrid DSSC/biosensor, thereby generating current that crosses the EC and promotes its colour change.

5.3. Results and Discussion

5.3.1. Assembly of a suitable DSSC

A typical DSSC combines CE and photoanode, in electrical contact through a liquid redox I^-/I_3^- electrolyte solution, as shown in **Figure 5.2**. The traditional photoanode contains TiO_2 as semiconductor and a suitable dye adsorbed into it; the dye absorbs light and the excited electrons are injected into the conduction band of the semiconductor. The CE is expected to receive the electrons arriving from the photoanode through the external circuit and use these to reduce the redox electrolyte, which in turn would give these back to the dye, regenerating it. As the CE would be the support for the biosensor assembly, it was critical to find-out a compatible structure with both systems (biosensing and DSSC).

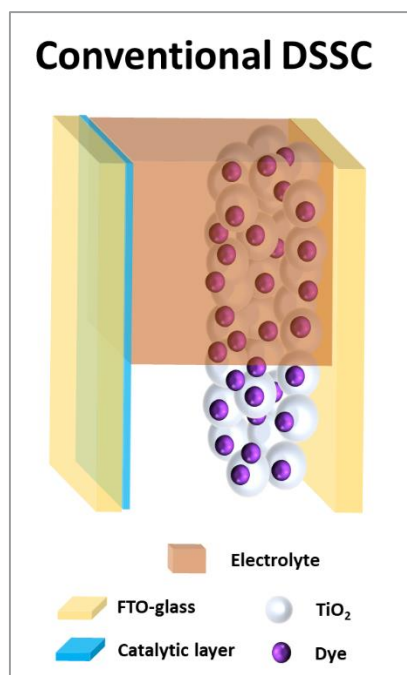


Figure 5.2 - Schematic representation of a conventional DSSC, combining counter electrode (FTO-glass and catalytic film) and photoanode (TiO₂ as semiconductor and suitable dye, hit by light), in liquid contact through an I⁻/I₃⁻ electrolyte.

5.3.1.1. Counter electrode

Two CEs were prepared and compared herein: the traditional Pt material and a PEDOT layer. The Pt CE was prepared by spin coating deposition, followed by reduction of Pt salt at high temperature to form Pt. The PEDOT CE was obtained by chronoamperometry, selecting a potential capable of generating a polymeric structure for a period of 15 s. A potential of +1.10 V was selected, considering that potentials higher than the oxidation peak (**Figure 5.3**) could result in electrochemical degradation, losing properties like conductivity and electroactivity, charge storage ability and poor adhesion to the substrate [243].

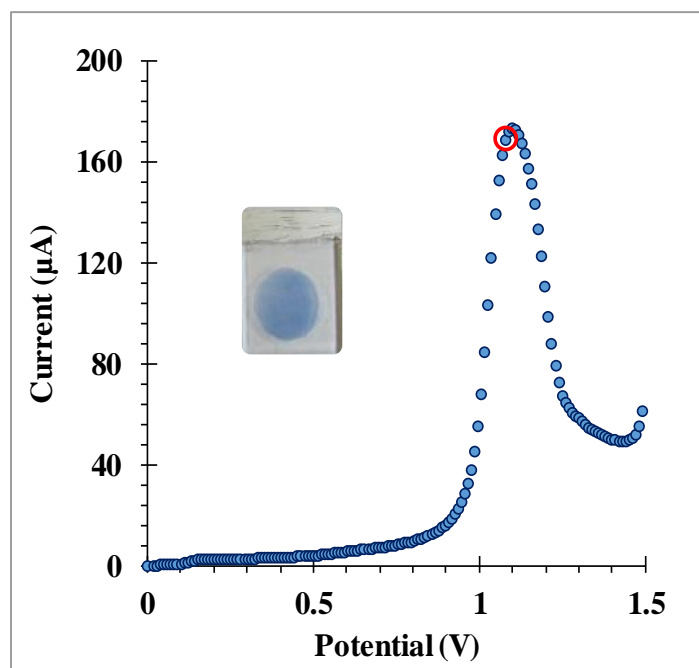


Figure 5.3 - Current values obtained for the oxidative scanning of an EDOT solution of 0.01 mol/L, prepared in 0.10 mol/L of KCl, using an FTO-glass support as working electrode, an Ag/AgCl as reference electrode and platinum as counter electrode. Inset: the picture of the resulting FTO-glass with *in-situ* generated PEDOT.

Figure 5.4-A shows the $J-V$ and η curves obtained for the DSSCs with different CEs (Pt and PEDOT), using the same photoanode and electrolyte. The main photovoltaic parameters were determined from these curves and are summarized in **table 5.1**. Comparing the PEDOT, the Pt CE yielded an increase of 11.1% in η value, and consequently an increment in the overall DSSC parameters: 2.1% V_{oc} , 5.9% in J_{sc} , and 3.4% in FF . Yet, a η of DSSC cells with PEDOT CE was also significant, equal to 10.36% due to the good conductivity and stability of this polymer, while reducing significantly the production cost of the final DSSCs [235, 237]. Thus, the PEDOT CE was selected in subsequent studies.

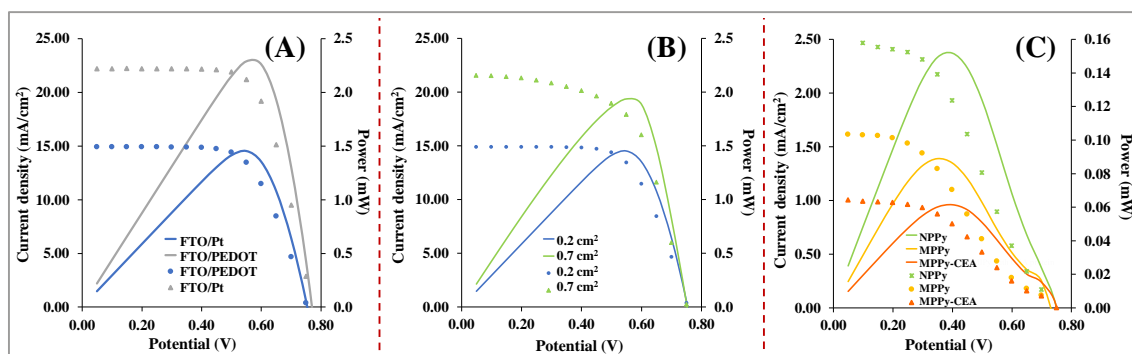


Figure 5.4 - Photocurrent density-photovoltage ($J-V$) and power conversion efficiency characteristic curves of the DSSCs using different counter electrodes, of Pt or PEDOT **(A)**; using photoanodes with different areas (0.2 cm^2 or 0.7 cm^2) **(B)**; and using CEs within the different stages of the production of the sensing film **(C)**.

5.3.1.2. Photoanode

The overall area of the photoanode was considered critical, as studies in the literature linked the efficiency of DSSCs to the photoanode area [244]. Moreover, it was of utmost importance to generate enough power to trigger the signalling device, more than to have a highly efficient cell, in which a small area would be efficiently used but producing little power.

Thus, different areas of photoanodes with a cell containing a PEDOT CE were studied for this purpose: 0.2 cm^2 or 0.70 cm^2 . The $J-V$ and η curves so obtained are represented in **Figure 5.4-B**, and the corresponding photovoltaic parameters (V_{oc} , FF , J_{sc} and η) shown in **table 5.2**. Overall, the photoanode area of 0.2 cm^2 yielded the higher η (10.4%) and higher areas of 0.7 cm^2 yielded lower η values (3.5%). Consistently, the J_{sc} densities decreased in 13.3 mA/cm^2 for 0.7 cm^2 , when compared to the DSSC-PEDOT cells with 0.2 cm^2 of photoanode area (20.9 mA/cm^2). Likewise, the V_{oc} -values decreased with higher photoanodes areas, from 754.1 mV to 752.3 mV (0.7 cm^2). In addition, the FF values, representing the photogenerated carriers able to extract out of the photovoltaic device [245], also decreased with the increasing of area ($\sim 7.7\%$).

Table 5.1 - Photovoltaic parameters of DSSCs based on Pt and PEDOT counter electrodes, using different photoanodes areas (0.2 cm², 0.7 cm², and 1.4 cm²).

Counter electrodes	Photoanode area (cm ²)	V_{oc} (mV)	J_{sc} (mA/cm ²)	FF (%)	η (%)
Pt	0.2	769.9 ± 7.7	22.19 ± 0.14	68.2 ± 0.8	11.65 ± 0.15
PEDOT	0.2	754.1 ± 12.6	20.85 ± 0.27	65.9 ± 0.7	10.36 ± 0.17
PEDOT	0.7	752.3 ± 10.5	7.55 ± 0.05	60.8 ± 0.6	3.45 ± 0.04

V_{oc} : open-circuit voltage; J_{sc} : short-circuit current density; FF : fill factor; η : power conversion efficiency.

Thus, it was clear that the area of the photoanode affected the performance of DSSC cell, as it related to variables affecting the electron transport per unit area and, also, electron recombination [244, 245]. Yet, the absolute power generated by the 0.7 cm² electrode was significantly higher than that produced by the 0.2 cm² photoanode (**Figure 5.4-B**). Therefore, it was more likely that the photoanode with larger area would generate enough current to trigger a colour change in the EC, thereby allowing a colour change perceptible to naked eye. So, this electrode was selected for further studies.

5.3.2. Biosensing film production, characterization and rebinding features

5.3.2.1. Assembly of the film

The assembly of the MIP film was made in several stages, as shown in **Figure 5.1-A**, having in mind that it would act as the CE of a DSSC. So, the imprinting was made in the FTO-glass with PEDOT (FTO/PEDOT) by forming a PPy film containing entrapped CEA (FTO/PEDOT/CEA-MPPy), followed by the removal of CEA from this polymeric network (FTO/PEDOT/MPPy) by means of enzymatic action. This was made in parallel with a control non-imprinted film (FTO/PEDOT/NPPy).

5.3.2.2. Electrochemical follow-up

All stages of the biosensing film assembly were followed by CV in the presence of a standard iron redox probe. The starting material was FTO-glass, which was a conductive support with

little ability to catalyse the oxidation or reduction of the redox probe, as reflected in the large potential peak-to-peak separation obtained in the CV assays shown in **Figure 5.5-A**. The subsequent polymerization of the PEDOT on this FTO-glass surface was confirmed by a significant decrease of the observed peak-to-peak separation, as expected for this conductive polymer.

The imprinting stage consisted in the *bulk* electropolymerization of the Py in the presence of the target analyte, CEA, made by CV (**Figure 5.5**). The resulting polymeric layer was confirmed by a significant reduction in the net current (**Figure 5.5-A₁**), due to the low electron transfer ability of PPy prepared in acetate buffer, pH 6. After the template removal with proteinase K, the oxidation/reduction peaks became more evident, thus supporting the availability of large pores that would enhance the electron transfer and favour the oxidation/reduction of the standard probe and thereby the exit of the protein from the imprinted layer.

In general, the electropolymerization of Py was similar in the presence (MPPy) and in the absence (NPPy) of CEA, considering the CV data (**Figure 5.5**), with the current increasing continuously in subsequent cycles. The non-imprinted film (FTO/PEDOT/NPPy) showed higher peak currents when compared to the MPPy film (FTO/PEDOT/MPPy) after template removal (**Figure 5.5-A₂**). This behaviour was linked to the typical capacitive current of PPy. However, the faradaic process become slower because the peak separation of the oxidation and reduction peak is higher than in the imprinted sensor. One hypothesis supporting this behaviour was the compactness of the NPPy film when compared to the increased porosity of the MPPy film out coming from presence of CEA molecules when the polymeric network was being formed and their subsequent removal.

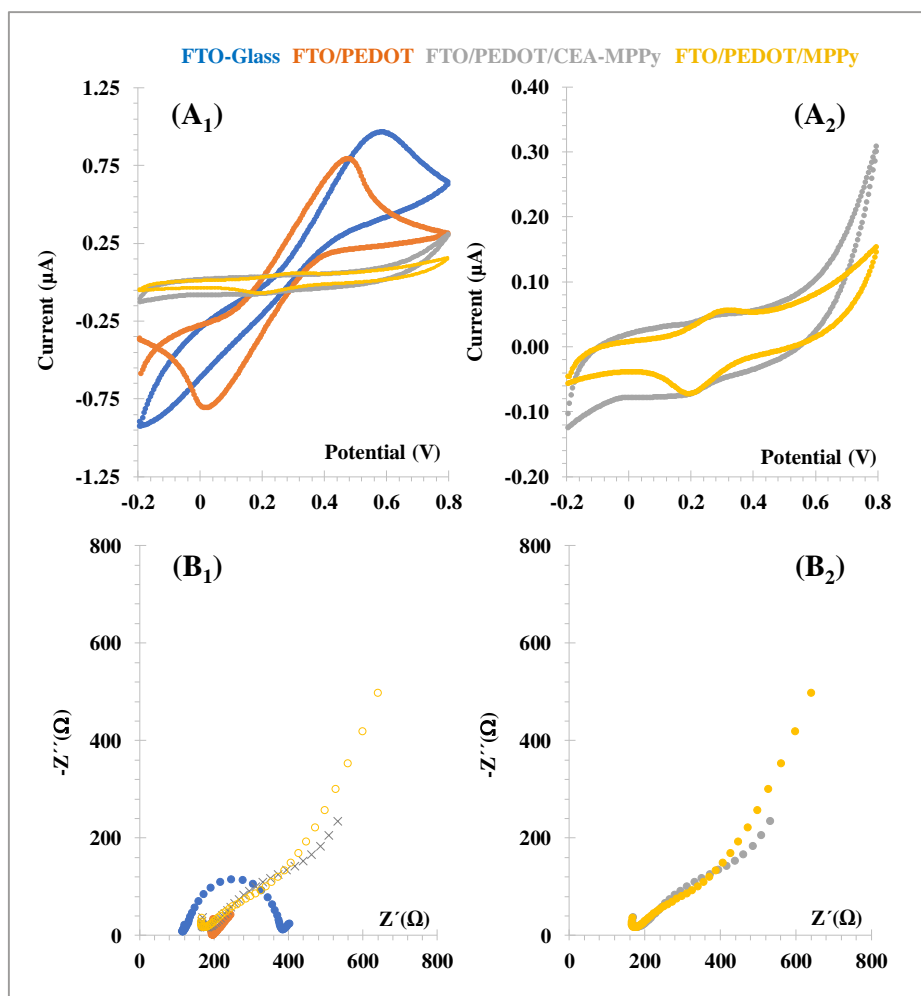


Figure 5.5 - Electrochemical CV (A) and EIS (B) data of the different steps (1) involved in the assembly of the sensing polymers, highlighting the results of the MPPy layer before and after template removal (2). Data corresponding to 5.00×10^{-3} mol/L $[\text{Fe}(\text{CN})_6]^{3-/4-}$ readings in PBS buffer, pH 7.40

EIS assays were also performed along all stages (Figure 5.5-B) and were consistent with the CV data. The FTO-glass exhibited an evident R_{ct} and, as expected, the presence of PEDOT eliminated it [246]. The formation of a PPy film on the FTO/PEDOT layer recovered some R_{ct} , supporting the fact that the MPPy film decreased the electroactive surface area, thereby hindering the electron transfer. After template removal, a more capacitive behaviour was observed, related to the presence of the rebinding cavities. The EIS data also showed higher R_{ct} in the NPPy, when compared to the MPPy (Figure 5.5), supported by the slower faradaic process observed in this film; the lower porosity of the NPPy would hinder the diffusion of redox active species, thereby increasing R_{ct} .

5.3.2.3. Raman spectroscopy follow up

To be sure that the several stages of electrode modification were effective, the different stages of the film assembly were analysed by Raman spectroscopy (**Figure 5.6**). The presence of PEDOT was clearly evidenced by the strongest intensity peak at 1455.7 cm^{-1} , probably assigned to $C_{\alpha}=C_{\beta}$ (-O) symmetric stretching vibration [247, 248]. Other characteristic peaks of PEDOT were also found: the peak at 988.44 cm^{-1} was assigned to the oxyethylene ring deformation; 1366.4 cm^{-1} to the $C_{\beta}-C_{\beta}$ stretching; 1493.6 cm^{-1} to asymmetric C=C stretching; and 1537.9 cm^{-1} to $C_{\alpha}=C_{\beta}$ asymmetric vibration [228]. Overall, the Raman spectrum confirmed the presence of PEDOT on top of the FTO-glass electrode.

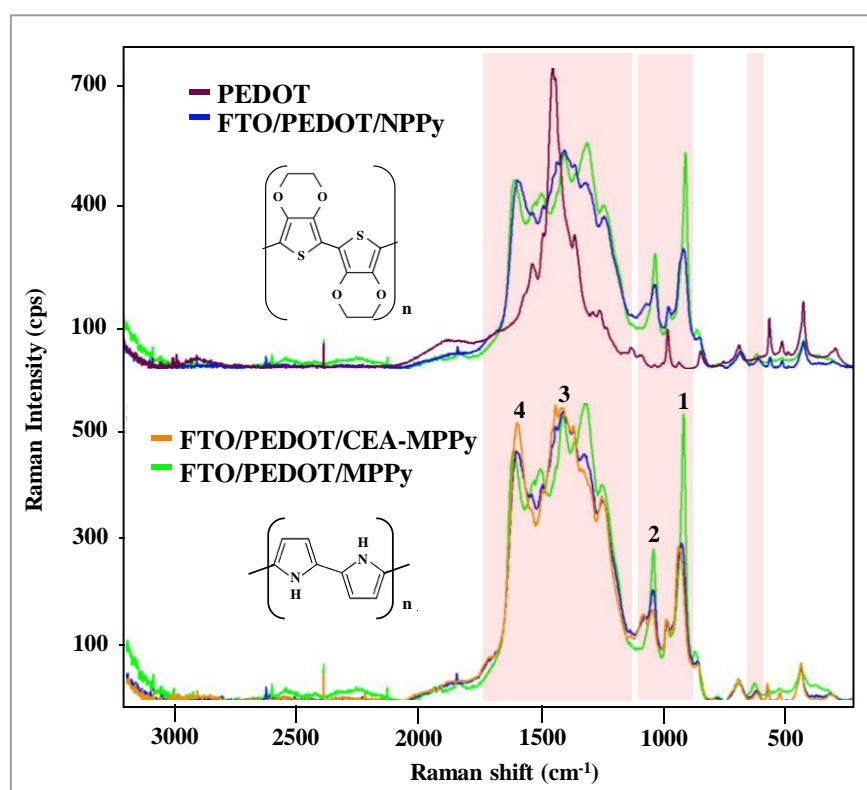


Figure 5.6 - Raman spectra of the different materials followed along the assembly of the biosensing

The addition of a polymeric network of Py to the PEDOT film was recognized by additional Raman peaks. In brief, the NPPy layer yielded typical peaks, at 624.08 cm^{-1} (C-C, ring torsional), 924.4 cm^{-1} (C-C, ring deformation vibration), 1039.6 cm^{-1} and 1073.8 cm^{-1} (C-H in-plane deformation vibration), 1326.2 cm^{-1} (C-C, ring stretching vibration), 1408.1 cm^{-1}

(C-N stretching vibration), 1492.1 cm^{-1} (C-C and C=N stretching vibration) and 1599.9 cm^{-1} (C=C in-ring of C-C inter-ring stretching vibrations), thereby confirming the presence of PPy [249-251]. The structure of the MPPy polymer may be slightly different due to presence of the protein, justifying a wavenumber shift, as confirmed in **table 5.2** [252]. Four of these peaks stand out and their intensity ratios were evaluated. Specifically, the ratio of Peak 1 and Peak 2 confirmed the exit of the protein from the CEA-MPPy film.

Table 5.2 - Raman intensity and Raman shift of typical peaks observed in the Raman spectra of different materials (Peaks 1 to 4 signalled in **Figure 5.6**).

Material	Raman intensity				Raman Shift				Peak ratio	
	1	2	3	4	1	2	3	4	I1/I2	I3/I4
NPPy	292.47	204.73	538.84	463.44	924.37	1039.63	1408.09	1599.94	1.43	1.16
MPPy	532.20	281.00	530.05	464.60	916.55	1039.49	1411.12	1607.75	1.89	1.14
CEA-MPPy	286.53	168.44	543.75	516.17	938.16	1044.01	1409.52	1596.12	1.70	1.05

5.3.2.4. CEA Rebinding features

The rebinding features of the biosensor were evaluated by calibration curves with CEA standard solutions. In this, the biosensing film was incubated in each standard solution to evaluate its response in terms of EIS. Calibration curves were recorded for (Glass-FTO/PEDOT/MPPy) and (Glass-FTO/PEDOT/NPPy) (**Figure 5.7**). The calibrations plotted current R_{ct} (in EIS) against CEA concentration, ranging from 0.1 ng/mL to 100 $\mu\text{g/mL}$.

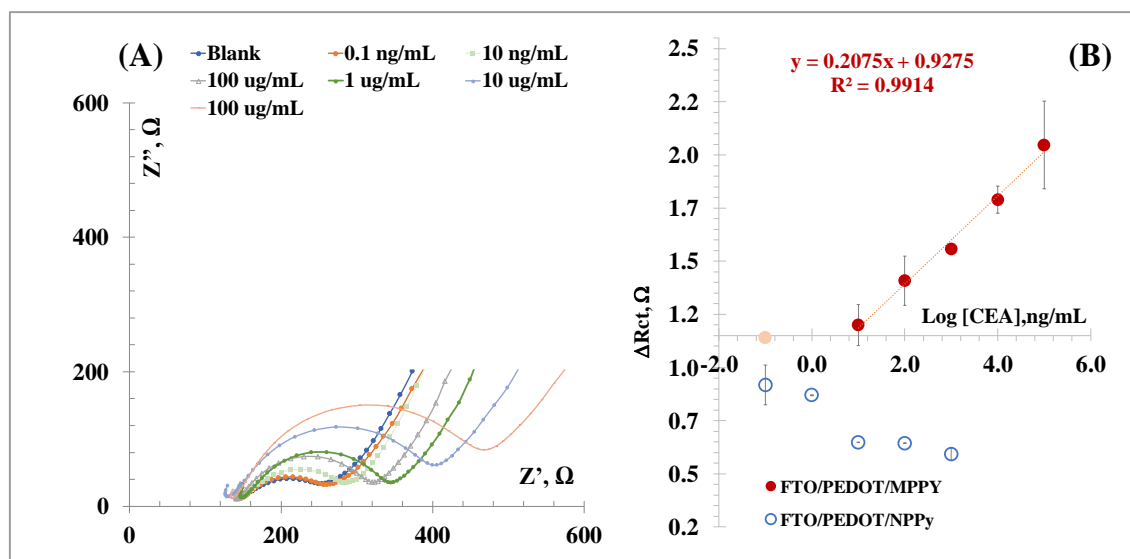


Figure 5.7 - Typical Nyquist plots (A) of the MPPy film after consecutive incubations in increasing concentrations of CEA standard solution, and the corresponding calibration curves (B), also compared to the typical behaviour of the NIP.

Overall, the Nyquits plots evidenced linear behaviour for ΔR_{ct} (which $\Delta R_{ct} = R_{ct}(\text{sample})/R_{ct}(\text{blank})$) against $\log(\text{concentration})$ from 10 ng/mL to 100 $\mu\text{g/mL}$ of CEA standard solutions prepared in buffer. The linear trend observed among different units was in good agreement when relative data was used (signal ration to the blank value), showing an anionic slope of -0.21 per decade concentration and the squared correlation coefficient > 0.99 , presenting an average of relative standard derivation below 6% for all over the concentration range tested ($n = 3$). Interestingly, the NPPy sensor showed a random behaviour with a predominance response for decreasing R_{ct} values. Overall, these results supported that the rebinding mechanism of CEA in the MPPy film was different from that in the NPPy film, being mainly governed by specific interactions at the imprinted sites.

5.3.3. Self-powered device

The self-powered device consisted in the hybrid DSSC/biosensor set-up (Figure 5.1-B), using the biosensing film as the CE of the DSSC. In this approach, the biosensing CE was previously incubated in sample for a given time, washed and interfaced in the DSSC to monitor the resulting photovoltaic performance.

5.3.3.1. Impact of the biosensing film on the DSSC operation

This impact upon the photovoltaic performance of each stage of the sensing film assembly was evaluated first, in order to understand its impact upon the DSSC operation. For this purpose, the J - V curves were followed (**Figure 5.4-C**) and the corresponding photovoltaic parameters (V_{oc} , FF , J_{sc} and η) extracted (**table 5.3**).

Table 5.3 - Photovoltaic data obtained with the hybrid DSSC/biosensor device, at the different stages of the biosensing film assembly, obtained for a photoanode area of 0.7 cm².

Counter electrodes	V_{oc} (mV)	J_{sc} (mA/cm ²)	FF (%)	η (%)
FTO/PEDOT	791.86 ± 0.01	8.125 ± 0.003	64.97 ± 0.01	4.180 ± 0.084
FTO/PEDOT/NPPy	750.99 ± 0.01	0.816 ± 0.094	39.11 ± 0.01	0.240 ± 0.029
FTO/PEDOT/CEA-MPPy	749.83 ± 0.001	0.289 ± 0.017	40.15 ± 0.01	0.097 ± 0.007
FTO/PEDOT/MPPy	727.06 ± 0.01	0.509 ± 0.040	38.65 ± 0.05	0.151 ± 0.006

V_{oc} : open-circuit voltage; J_{sc} : short-circuit current density; FF : fill factor; η : power conversion efficiency.

The use of the FTO/PEDOT as CE yielded a similar behaviour to the control DSSC with the PEDOT-based CE, showing 4.18% η , 791.9 mV V_{oc} , 8.12 mA/cm² J_{sc} and 65.0% FF . The addition of the CEA-MPPy film (FTO/PEDOT/CEA-MPPy) promoted ~97.7% decrease in η , ~5.3% decrease in V_{oc} , and ~96.4% decrease in J_{sc} , leading to a FF value that was 1.6× lower than the bare DSSC with the FTO/PEDOT CE. This was indeed consistent with the small CV current generated by the MPPy film (**Figure 5.8**). As expected, the removal of CEA from the CE (FTO/PEDOT/MPPy) promoted the opposite effect, increasing the overall η in ~36%. The J_{sc} also increased (0.51 mA/cm²), but the V_{oc} decreased (22.8 mV), leading to similar FF when compared to the previous stage.

The non-imprinted material (FTO/PEDOT/NPPy) was also tested as CE of the DSSC, leading to a higher η value ($\eta = 0.24$ %) when compared to that of the corresponding MPPy ($\eta = 0.15$ %). This was explained by absence of the protein in the control sensor and was also consistent with the higher currents observed in the CV data (**Figure 5.8**).

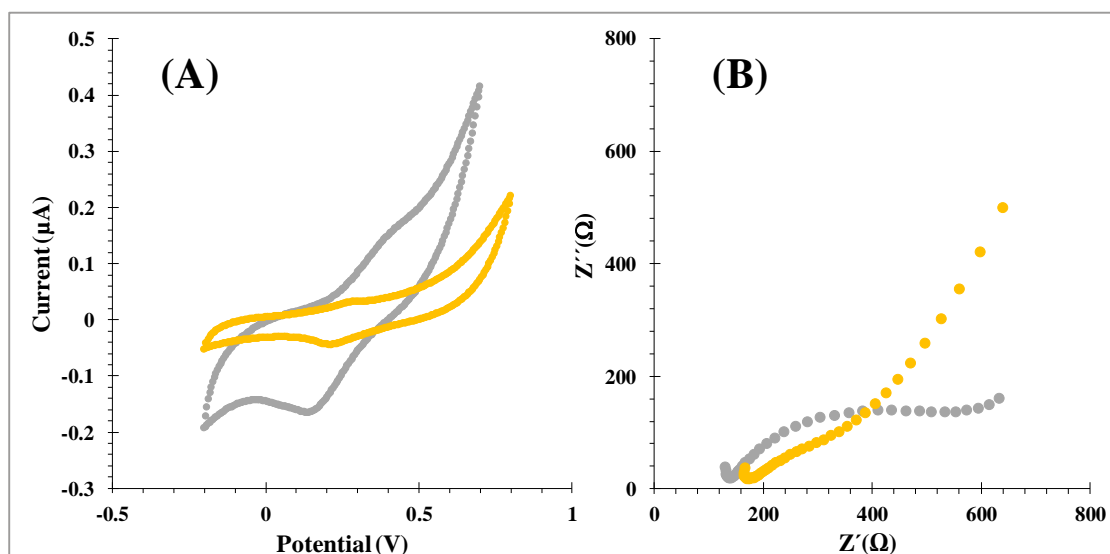


Figure 5.8 - Electrochemical CV (A) and EIS (B) data of the Mppy and NPPy materials after proteinase K treatment. Data obtained with a 5.00×10^{-3} mol/L $[\text{Fe}(\text{CN})_6]^{3-/4-}$ standard redox probe, prepared in PBS buffer, pH 7.40.

5.3.3.2. CEA Rebinding features of the hybrid DSSC/Biosensor

The analytical behaviour of this new set-up was followed by calibrating it with CEA standard solutions of increasing concentrations. Assays were made with standard solutions prepared, first, in acetate buffer (**Figure 5.9-A**) and, after, in human urine from healthy individuals, 100× diluted in buffer (**Figure 5.9-B**). The levels of CEA spiked into this blank urine solution ranged from 0.10 ng/mL to 100.0 µg/mL, and the electrochemical behaviour was evaluated by J - V measurements, using an I^-/I_3^- redox electrolyte prepared in ACN. In general, the presence of CEA decreased η values (**Figure 5.9**) in a concentration dependent manner. A linear response was observed for $\Delta\eta$ against \log of CEA concentration, both in acetate buffer conditions and in real urine samples.

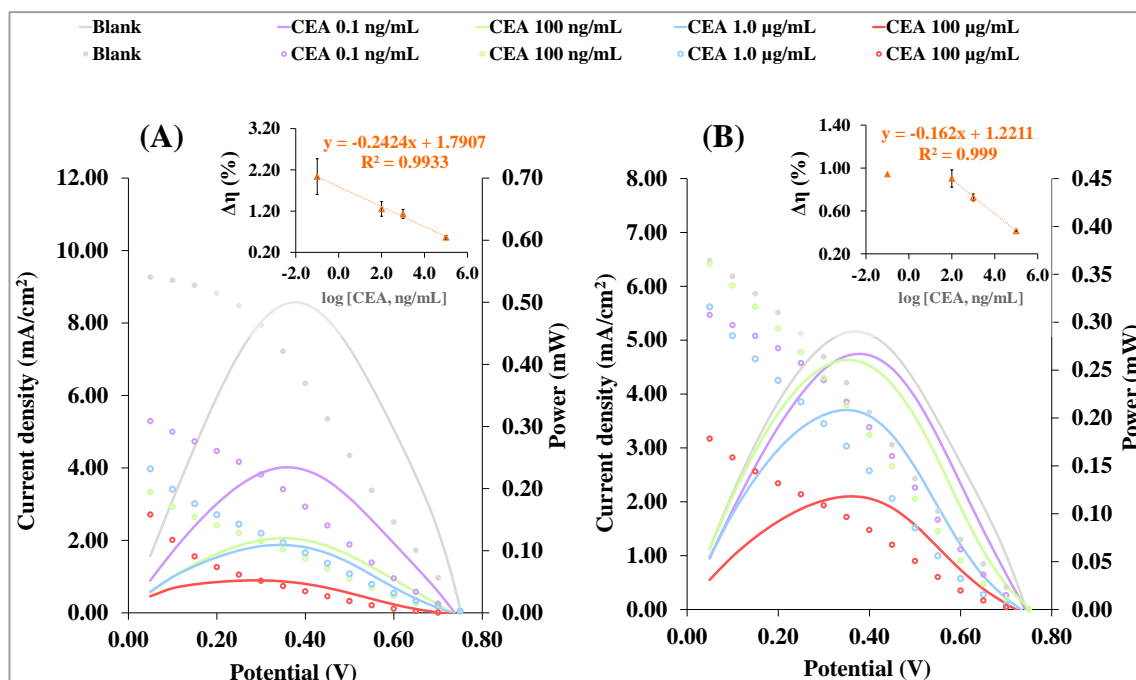


Figure 5.9 - Typical J - V and power conversion efficiency curves of the hybrid DSSC/Biosensing set-up against CEA increasing concentrations in ranging from 0.10 ng/mL to 100.0 μ g/mL, prepared in acetate buffer solution **(A)** or in human urine from healthy individual, diluted 100 \times **(B)**, and in the presence of an I^-/I_3^- redox electrolyte. Inset: typical calibration curves plotting the power conversion efficiency against log CEA increasing concentrations

After successive incubations (20 min each) with increasing CEA concentrations, the η decreased from 0.31 % to 0.09 % along the concentration range tested. The typical data so obtained was represented in **Figure 5.9-A**, displaying a linear behaviour for $\Delta\eta$ against log of CEA concentration, being $\Delta\eta$ equal to $\eta_{(\text{sample})}/\eta_{(\text{blank})}$. The anionic slope obtained was -0.24 per decade CEA concentration and the squared correlation coefficients were >0.99 . The overall change observed for V_{oc} and FF was to decrease with the increasing CEA concentrations, and J_{sc} was the single photovoltaic parameter increasing.

The typical J - V and η -based calibration plots obtained in blank human urine samples are shown in **Figure 5.9-B**. The higher η value ($\eta = 0.453$ %) was evidenced after stabilizing the hybrid device in blank urine (100 \times diluted). Comparing this blank with the blank obtained in acetate buffer, a decrease of η was observed. The $\Delta\eta$ calibration had a linear response from 100 ng/mL until 100 μ g/mL, with a slope of -0.16 per decade CEA concentration. The resulting LOD was 0.14 ng/mL, and the squared correlation coefficients were >0.99 . Moreover,

repeated calibrations ($n=3$) indicated that the response was stable and precise, with standard deviations below 9 % all over the concentration range tested. Regarding to V_{OC} , J_{SC} and FF parameters, an overall tendency to decrease with the increasing of \log of CEA concentrations was evidenced.

Overall, the response of the hybrid device using the biosensing film as CE of the DSSC was found suitable and its response was CEA concentration dependent. The CEA concentration range to which the hybrid device was providing quantitative information was also of clinical value: < 2.5 ng/mL corresponds to a normal condition and >10 ng/mL suggests the presence of cancer disease [47].

5.3.4. Self-powered and self-signalled device

As the power generated by the hybrid DSSC/biosensor (**Figure 5.1-B**) was being concentration dependent and the power reaching a given EC is expected to lead to different colour intensities, it was reasonable to infer that different concentrations of CEA would lead to different colour intensities in the EC. Thus, a fully autonomous system would be reached, in which the single requirement was light. This possibility was explored first by improving the colours generated by a PEDOT-based EM and later by interfacing the resulting EC in the external electrical circuit of the DSSC/biosensing device (**Figure 5.1-C**).

5.3.4.1. Electrochromic features of the electrochromic material

While the PEDOT holds traditional electrochromic features, it may be modified to improve colour diversity and optical contrast. To this end, SNS-NH₂ was added into it, as suggested in the literature ([180, 187]). The colour changes promoted by this cell were checked under potentiostatic control and in a 3-electrodes cell. As the potential of a conventional DSSC in blank buffer was never above 0.80 V, the working potential range selected for this test was from 0.00 to 0.80 V.

The pictures obtained after this are shown in **Appendix III.3** and the resulting colours shown in **Figure 5.10-A**, varying from purple to green and blue. In general, these colours reflected the different oxidation states of the materials at each applied potential [180]. The contrast observed herein was higher than the one generated by an EC having only PEDOT as EM.

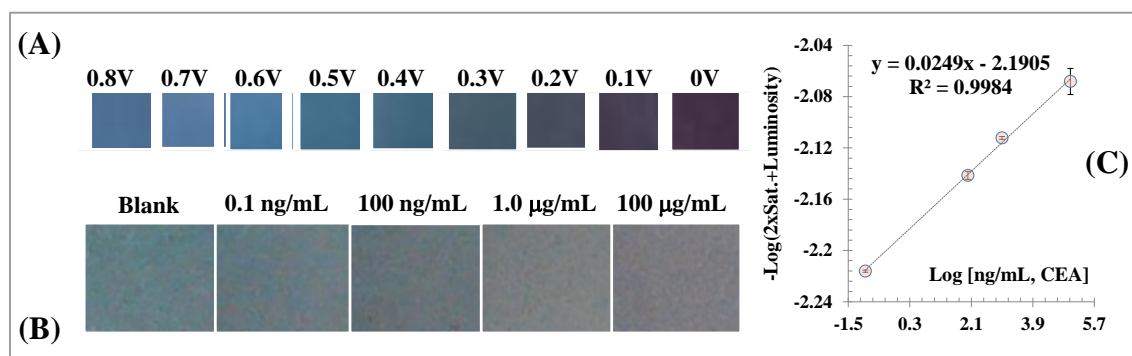


Figure 5.10 - Coloured behaviour of the electrochromic material when evaluated under a working potential in the 3-electrodes system (A) and when interfaced in the external circuit of the hybrid device DSSC/biosensor (B), with the corresponding calibration (C), generated by plotting the colour coordinates of the HSL coloured space against the logarithm CEA concentration.

5.3.4.2. Hybrid DSSC/Biosensor interfaced with the electrochromic cell

This newly developed set-up was tested first in a blank solution and after in increasing CEA concentrations, of 0.1 ng/mL, 100 ng/mL, 1µg/mL, and 100 µg/mL. This was done by using the same biosensing CE, opening, cleaning and closing it for each subsequent incubation. Time to reach a stable colour in the EC was always the same, set to 12 min.

The pictures obtained of the electrochemical cell are shown in **Appendix III.4** and the colours related to each condition shown in **Figure 5.10-B**. In detail, the control signal was generated by the biosensor incubated in the blank, corresponding to the highest power produced by the hybrid DSSC/Biosensor device and crossing the EC. This blank showed a typical blue colour (**Figure 5.10-B**). Increasing CEA concentrations incubated in the CE biosensing film yielded a hybrid device with decreasing currents and, thereby, a purple colour formation of increasing intensity. Overall, it was clear that there was a gradient of colour change that was visually perceptible for increasing CEA concentrations. Moreover, the observed gradient suggested the possibility of obtaining semi-quantitative data by simple visual inspection against a given standard colour *pallette*.

The possibility of extracting quantitative data from the obtained colours was also tested herein, in a similar way to the approach reported by [253]. To this end, the colour coordinates

of the HSL colour system were extracted by the Paint program of Windows and mathematically treated. The best mathematical fit found was represented by the y-axis as $-\log(2 \times \text{Saturation} + \text{Luminance})$ against the log CEA concentration. In this, a linear trend was observed with $y = 0.025 \log [\text{CEA}] - 2.19$, corresponding to a squared correlation coefficient of 0.99 (**Figure 5.10-C**) with RSD less than 1.02 % for all over the concentration range tested.

From this study, it was clear that the visual inspection of the colour gradient provided semi-quantitative data and this data could be further refined to generate quantitative information of clinical relevance by handling the colour coordinates.

5.3.5. Comparison to previously reported CEA sensors

The several MIP materials produced for CEA detection published throughout the years are listed in **table 5.4**. Comparing all transduced signals, the optical detection leads to a linear response within higher concentration ranges, while electrical readings allow a response among lower concentration ranges (sometimes as low as pg/mL in some cases). Overall, the MI with optical transducers seems to be unable to achieve concentrations of clinical interest. These reasons may have contributed for a greater number of electrochemical biosensors developed with MIP for CEA sensing, when compared with optical biosensors.

Table 5.4 - Previous works reporting MIP materials for CEA detection in the literature.

Transducer	MIP		LOD	Linear response	Ref
	Material	Technique			
Electrochemical	Pyrrole	Electropolymerization	–	0.05 – 1.25 pg/mL	[113]
Electrochemical	Dopamine	Electropolymerization	<0.26 pg/mL	0.001 – 1000 ng/mL	[132]
Electrochemical	Aminophenol	Electropolymerization	3.00 ng/mL	2.5 ng/mL – 1.5 µg/mL	[131]
Optical	Poly(allylamine hydrochloride) and ethylene glycol diglycidyl	Hydrogel-based protein imprinting	–	0.0005 – 0.125 mg/mL	[67]

The devices employing electrical detection systems used the electropolymerization technique to obtain the CEA biorecognition element and their results demonstrated a wider linear response and lower LOD. However, these methods were based in conventional electrical dependent biosensing devices and, additionally, different nanomaterials were used to achieve the desired electrochemical features.

Despite the LOD of this work are not as low as other electrochemical-based works previously reported, the biosensor presented herein showed useful responses for CEA concentration ranges within the values of clinical interest. Moreover, the present work involved an innovative a self-power device that provides semi-quantitative data through visual inspection and quantitative data through a suitable mathematical handling of the colour coordinated.

5.4. Conclusions

This work reported a self-powered and self-signalled biosensing device, with sensitivity to very low concentrations, which is a completely novel and disruptive approach. This required merging technology from biosensing, photovoltaic and ECs. The biosensing device was a low-cost MIP material for a cancer biomarker, produced *in situ* and acting as CE of the PV. The PV was a DSSC, inspired in nature and offering advantages in terms of costs. The EC was also a low cost PEDOT-based system produced *in situ*, with significant colour change and low power requirements.

The optimized device yielded a gradient of colour change for increasing CEA concentrations. In general, these varied from blue to purple, with higher concentrations of CEA in the FTO/PEDOT/MPPy CE leading to a more intense purple colour (signalling the lower power generated by the hybrid DSSC/Biosensor when the CEA concentrations increased). It was clear that the visual inspection of the colour gradient provided semi-quantitative data and this data could be further refined to generate quantitative information of clinical relevance by handling the colour coordinates. The mathematical manipulation of the colour coordinates may be explored in the future, by taking a picture of the observed colour by a smartphone and using a suitable App to generate quantitative data.

Overall, the novel set-up is equipment free and particularly suitable for POC, being able to screen CEA in real samples and differentiating critical concentrations for establishing a diagnosis. It holds the potential to provide clinical relevant data anywhere, in a fully independent manner. Further improvements could be achieved by operating in a DSSC format of higher power, suggesting a wider concentration range of response and a higher sensitivity. This may be achieved, for instance, by introducing plasmonic nanostructure on the photoanode of the DSSC.

6. Photovoltaics, plasmonics, plastic antibodies and electrochromism combined for a novel generation of self-powered and self-signaled electrochemical biosensors

6.1. Introduction

The previous work confirmed the possibility of having a self-powered and self-signalled device by tailoring a MIP material on the CE of a PV and linking these to an EC. In general, the electrical energy generated was biomarker concentration dependent, meaning that the coloured readout of the EC was also concentration dependent. However, several features may be evolved in this DSSC/biosensing device.

One approach to increase the sensitivity could be tailoring the biorecognition element with a material that improved the electrocatalytic features to the CE of the PV. This may be achieved by using PEDOT in the assembly of the MIP material, which shows good conductivity, excellent stability, and low cost [235, 237].

In another perspective, changes in the photoanode of the DSSC may also contribute to produce a more efficient hybrid device. According to the literature, a DSSC with plasmonic nanostructures on the photoanode allows the dye molecules to increase the photon absorption from sunlight [254-256]. Consequently, this approach shall enhance an electron flow from the dye towards the surface of the semiconductor (TiO_2), thereby increasing the photocurrent generation inside of DSSC and its η .

Thus, the current work describes the preparation of a more efficient DSSC/hybrid device, monitoring the impact of an increased power generation on the rebinding abilities of its self-powered and the self-signalled versions, by calibrating the system and retrieving both electrical and coloured data. To allow a suitable comparison to previous works, the self-

powered and self-signalled device was designed to determine CEA, an important cancer biomarker in colorectal cancer [29, 30]. The biorecognition element is the MIP material, assembled in a copolymer that also contains PEDOT. The photoanode is produced by doping the TiO₂ with gold nanoparticles (AuNPs) in order to explore their plasmonic effect. Critical variables in this context are optimized and the final system is evaluated in both buffered solutions and urine human samples, with regard to the electrical and optical output signal.

6.2. Experimental section

6.2.1. Apparatus and materials

The general electrochemical assays were conducted in a potentiostat/galvanostat, Autolab PGSTAT302N, from Metrohm, with a FRA module and interfaced in a computer by means of NOVA 1.9. EIS was performed in a frequency range 0.1-100000 Hz. The DSSC assays in particular also used the Autolab potentiostat, coupled to a LED driver operating with 450 mA output of a warm white LED. The photoanode was sintered in a Nabertherm GmbH P330 oven.

Solid materials were characterized by a DXR Raman spectroscope from Thermo-scientific; spectra were collected with a 785 nm excitation laser, from 47 to 3000 cm⁻¹, for 1 mW power, with a confocal aperture was set to 50 μm slit. The morphology of the films was followed by SEM. The digital image of the EMs was acquired by a smartphone Cink peax 2. The colour coordinates of the images belonged to the HSL colour system and were collected by using the ImageJ.

The conductive glass substrates used throughout had a conductive film of fluoride-doped tin oxide (FTO, sheet resistance 13.0 Ω/sq), and were acquired to Sigma-Aldrich. The electrolyte used in EC was a commercial Nafion solution, 20 wt% (contains alcohols) from QUINTECH.

6.2.2. Reagents and solutions

Ultrapure Milli-Q water was used throughout. This work required several reagents, namely $K_3[Fe(CN)_6]$ (Riedel-de-Haën); $K_4[Fe(CN)_6]$ (Riedel-de-Haën); PBS tablets (Amresco); Na_2HPO_4 (Riedel-de-Haën); sodium dihydrogen phosphate dihydrate, (NaH_2PO_4 , Scharlau); EDOT (Alfa Aesar); KCl (Merck), CEA (EastCoast Bio); proteinase k (Sigma); TiO_2 (IV) nanopowder anatase phase (Sigma-Aldrich); hydrogen tetrachloroaurate (III) trihydrate ($HAuCl_4 \cdot 3H_2O$, Sigma-Aldrich); N719 dye (Sigma-Aldrich); Lil (Sigma-Aldrich); EtOH absolute (EtOH, Sigma-Aldrich); I2 (Riedel-de-Haën); Sodium borohydride ($NaBH_4$, Riedel-de-Haën); toluene (TCI); 3-Mercaptopropylmethyldimethoxysilane (Si-SH, TCI); ACN (Carlo Erba); acetone (Sigma Aldrich); Py (Sigma Aldrich); and AA (Analar Normapur).

The iron redox probe solution contained 5.00×10^{-3} mol/L $K_3[Fe(CN)_6]$ and 5.00×10^{-3} mol/L $K_4[Fe(CN)_6]$, and was prepared in phosphate buffer (PB). This PB contained 0.030 mol/L of Na_2HPO_4 and 0.020 mol/L of NaH_2PO_4 (pH of 7.0). A stock standard solution of 100 μ g/mL CEA was prepared in PB buffer and the less concentrated CEA standard solutions were prepared by dilution of the stock standard solution in the same buffer. The samples used herein were urine from healthy individual, with 1000 \times dilution in PB buffer and spiked with CEA for concentrations ranging from 0.1 ng/mL to 100 μ g/mL.

6.2.3. Assembly of the counter electrode

The FTO glass was successively washed with acetone, EtOH and water. Then, it was immersed in a thiol solution of Si-SH, 0.01 mol/L, prepared in toluene) to improve the adhesion of the PEDOT film to the metal oxide layer [257]. This was made for 30 min, at 50°C, washing after the FTO glass with ACN [258].

The next stage was the formation of a poly(EDOT) film on top (**Figure 6.1-C**), made by applying 1.10 V, for 15 s, in a 3-electrodes cell dipped in a solution of 0.01 mol/L EDOT, prepared in 0.1 mol/L KCl. The final electrode (FTO/PEDOT) was also washed with ACN, to remove unreacted reagents and small oligomers.

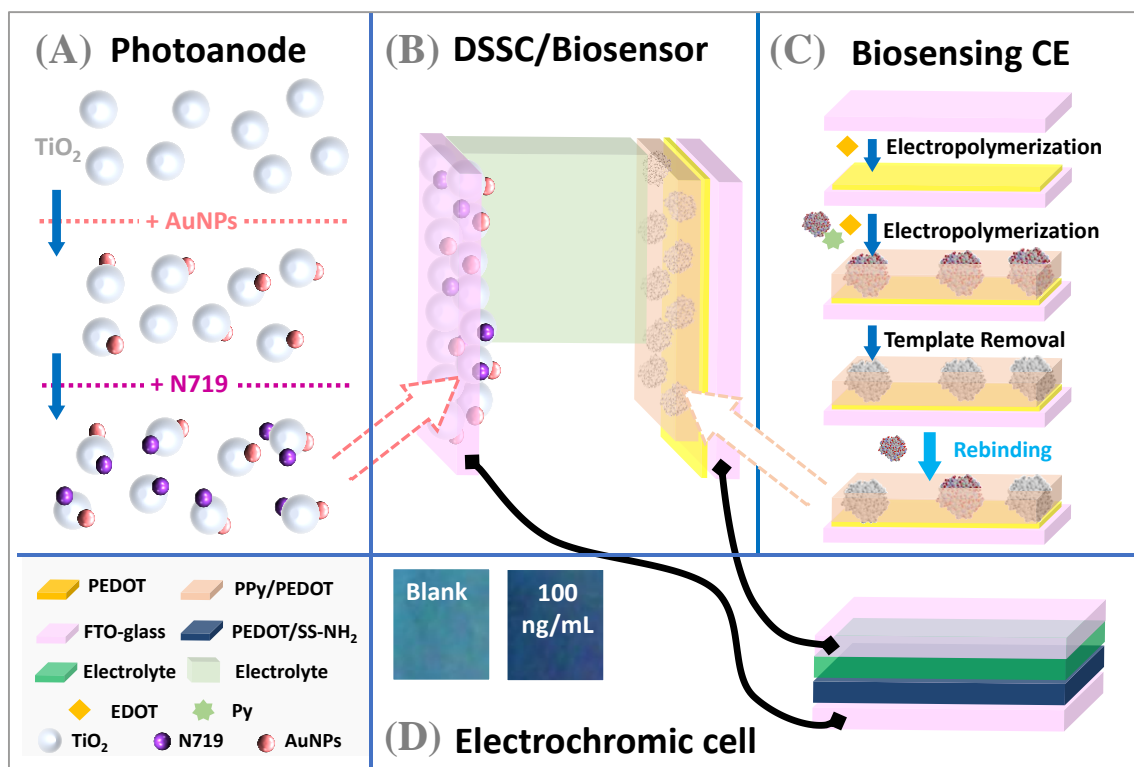


Figure 6.1 - Schematic representation of the several stages of the hybrid/DSSC biosensor set-up with optical detection, namely the photoanode with plasmonic enhancement **(A)** and the biosensing counter electrode **(C)** combined in the DSSC cell **(B)**, and their interface of the electrochromic cell **(D)**.

6.2.4. Assembly of the imprinted film on the counter electrode.

The imprinted polymer film (**Figure 6.1-C**) was assembled on top of the FTO/PEDOT glass by co-polymerizing a solution containing EDOT (0.01 mol/L) and Py (0.002 mol/L), and also 2 $\mu\text{g/mL}$ CEA, prepared in PBS (pH 7.40), by cyclic voltammetry (CV), from -0.30 to 0.95V, with a scan-rate of 50 mV/s, and for 10 cycles. This was done in a 3-electrodes cell, yielding an electrode that was assigned as FTO/PEDOT/MIP-CEA. After this, the CEA was extracted from the polymer using a solution of Proteinase k (500 $\mu\text{g/mL}$) overnight (FTO/PEDOT/MIP). The non-imprinted film was prepared the same way, but without CEA in the polymerizing solution (FTO/PEDOT/NIP).

6.2.5. Rebinding assays on the imprinted film.

The rebinding of CEA (**Figure 6.1-C**) was tested in MIP or NIP films on the FTO/PEDOT electrodes. It was done by incubating buffer, standard solutions or samples in the MIP/NIP area for 20 minutes. Calibrations started by incubating the CEA standard solution of lower concentration in the surface of the material, followed by a washing step with buffer. CEA concentrations ranged from 0.1 ng/mL to 100 µg/mL, and were prepared in PB buffer, pH 7.00, or in diluted urine.

After each rebinding stage, the electrode was combined in a 3-electrodes cell to monitor the EIS data changes of a standard iron redox probe, or in a DSSC set-up to monitor the resulting photovoltaic performance. The data reported herein corresponded to a minimum of three independent evaluations.

6.2.6. Assembly of the photoanode electrode

The first step for preparing the photoanode electrode consisted in applying a homogeneous suspension of 6.0 g of TiO₂ anatase nanopowder in 10 mL of EtOH:AA:H₂O (8:1:1), on a circular area of 0.64 cm², placed in a clean FTO glass, via doctor blade method. The electrode was then annealed at 450 °C for 30 min. After down to 80°C, the electrode was immersed in a dye solution of 5.0×10⁻⁴ mol/L N719 prepared in EtOH) for 18 h, at room temperature, in the dark [162, 235, 239-241]. Non-adsorbed dye was removed by successive washes with EtOH. The electrode was finally dried at room temperature.

Another photoanode was prepared in parallel to evaluate the plasmonic effect of AuNPs in the DSSCs (**Figure 6.1-A**). The procedure followed for this purpose was the same, but a weight ratio of 23.9 % of a colloidal AuNPs was added into the TiO₂ suspension. The AuNPs solution was prepared by the Martin method, for which 30 mL of a 2.00×10⁻³ mol/L NaBH₄ solution were added to 10 mL of an aqueous solutions containing 1.00×10⁻³ mol/L HAuCl₄.3H₂O solution, under stirring and in an ice bath [238]. The TiO₂ with AuNPs were isolated from the exceeding reagents by annealing at 450 °C for 30 min, cooled down to 80 °C and immersed in a N719 dye solution.

6.2.7. Assembly of the DSSC

The DSSC was set-up by placing photoanode (with or without AuNPs) and CE (with or without MIP/NIP films) face-to-face, in a sandwich configuration, with a spacer in-between made from scotch magic tape (double-sided, 0.06 mm thickness). The electrical circuit was closed by placing an I^-/I_3^- electrolyte in the middle (**Figure 6.1-B**). The electrolyte solution contained 0.05 mol/L of I_2 , 0.1 mol/L of LiI, 0.6 mol/L of HMII and 0.5 mol/L of TBP, dispersed in ACN.

6.2.8. Assembly of the electrochromic cell

The EM was a PEDOT-based film, produced in-situ by electropolymerization of EDOT of an FTO-glass support in a 3-electrodes set-up. To improve the colour change features of the final EM, SNS-NH₂ was added to the EDOT solution. SNS-NH₂ synthesis was made as described in [259], which consisted of an adaptation of the procedure made by [242].

The EC was set-up by placing face-to-face the FTO-glass with the EM and a second FTO-glass, with a polymeric electrolyte (Nafion[®]) in-between (**Figure 6.1-D**). It was further interfaced in the external circuit of the DSSC/biosensor set-up (**Figure 6.1-D**), after ensuring that the EM was as at 0.0 V. Under working operation, the light hit the DSSC/biosensor and the current generated flowed through this EC and promoted a colour change.

6.2.9. Electrochemical assays

The 3-electrodes cell set-up used the previously described CEs (modified or not) as WE, a Pt wire as AE and an Ag/AgCl electrode (3.4 mol/L) as RE. The electrochemical measurements monitored the EIS response for the redox probe $[Fe(CN)_6]^{3-/4-}$, under a standard potential of 0.22 V (\pm 0.01 V), with 50 scans of frequencies, and a sinusoidal potential peak-to-peak with amplitude 0.01 V in the 0.01 Hz–10000 Hz frequency range. This was done to follow-up the subsequent modifications made in the FTO glass and evaluate the impact of CEA binding on the imprinted films.

In the DSSC set-up, the $J-V$ features of the cells were recorded in the potentiostat/galvanostat and used to calculate relevant photovoltaic data (overall η ; V_{oc} ; J_{sc} ; and FF).

The chromatic features of the EM were evaluated in a 3-electrode set-up, using 0.1 mol/L of KCl as supporting electrolyte and applying specific external potentials ranging from 0.00 to +0.80 V.

6.3. Results and Discussion

6.3.1. Assembly of biosensing element on the counter electrode

6.3.1.1. Design of the imprinted film

The biosensing film was prepared as shown in **Figure 6.1-C**. First, the FTO glass was covered by a PEDOT layer (FTO/EDOT), produced by electropolymerization at a fixed potential (1.10 V). This PEDOT layer is a suitable material to act as a CE in a conventional DSSC [260-262], and thereby shall help the interface between the PV and the biosensing film. The imprinted film was assembled next, in a mixed solution containing EDOT, Py and CEA. The presence of EDOT in this stage is a novel approach and aim to improve the electrocatalytic features of the final electrode. As the copolymer was being formed (PEDOT and PPy), the protein was entrapped within the polymeric network, yielding the formation of polymeric cavities of complementary size and shape to the template. These cavities were made accessible for rebinding of other CEA proteins, after removal of the protein template. This was successfully achieved by incubating the film in proteinase k overnight.

In order to monitor the non-specific binding ability of the polymeric network, NIP was prepared the same way, but without CEA. Such polymeric layer shall play a non-specific interaction with CEA, as there are no rebinding sites. Thus, it allows evaluating the degree of non-specific interaction established between the polymeric network and the protein itself, thereby monitoring its contribution to the overall electrochemical response.

6.3.1.2. SEM and Raman analysis

The modification of the CE in its several stages was followed by SEM (**Figure 6.2**), addressing the morphological changes occurring at the surface. The presence of the PEDOT layer in the FTO/PEDOT electrode was evident, when compared with the electrode with only FTO. The overall structure seemed less rough, with denser areas of PEDOT located in the deepest sites of the FTO structure.

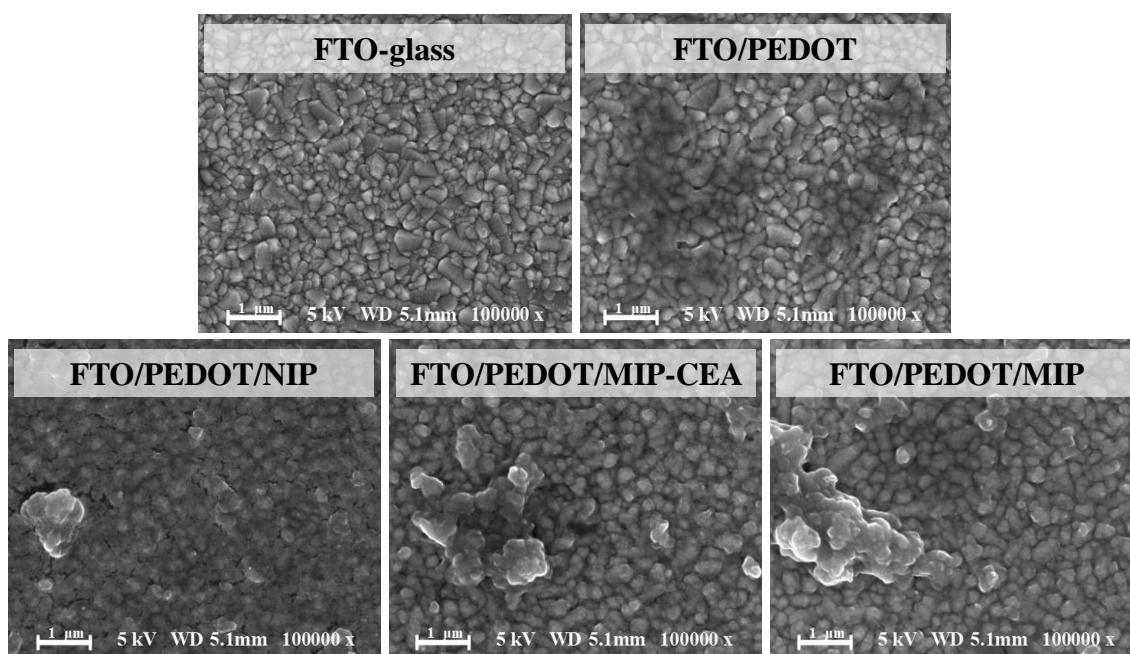


Figure 6.2 - SEM images of FTO conductive glasses according to the different stages of their modification.

This was also confirmed by Raman spectra, made to both materials (**Figure 6.3**). The spectra of FTO/PEDOT material evidenced an obvious chemical modification, signalled by three additional peaks when compared to the FTO surface: **(1)** 1367.9, **(2)** 1437.86 and **(3)** 1506.8 cm^{-1} . These peaks are typical from PEDOT and signal their presence [228]; **(1)** was assigned to the $\text{C}_\beta\text{-C}_\beta$ stretching, **(2)** was assigned to $\text{C}_\alpha\text{=C}_\beta$ (-O) symmetric stretching vibration; and **(3)** was assigned to the C=C asymmetric stretching of the polymeric network. Moreover, the peaks signalling the FTO surface at 559.9 cm^{-1} (Sn-O stretching vibration) and 1094.5 cm^{-1} (Si-O-Si stretching vibration and C-F stretching vibration) seemed less intense in the FTO/PEDOT material [162, 263].

The presence of additional polymer in both MIP- or NIP-based materials was also clear from the SEM images (**Figure 6.2**). Their overall surface seemed flatter, accounting the formation of these additional polymeric layers, made of PEDOT/PPy. This was especially evident in the NIP layer, which suggested that the amount of polymer formed in the NIP structure was higher than in the MIP. This was observed before, as the presence of the protein seemed to hinder the progress of the polymerization, including when electropolymerization is employed [213]. In the particular case of the MIP-based structures, a globular shape was also observed, which could signal the presence of the protein (several molecules) entrapped within the polymeric network. There are no differences evidenced between MIP after or before CEA removal, but this was likely to happen, as the magnification of the images is too little to identify the exit of the protein. In some studies, CEA has been visualized by electron microscopy and it seems like a rod shaped macromolecule with dimensions of 9 nm ×40 nm [264-266].

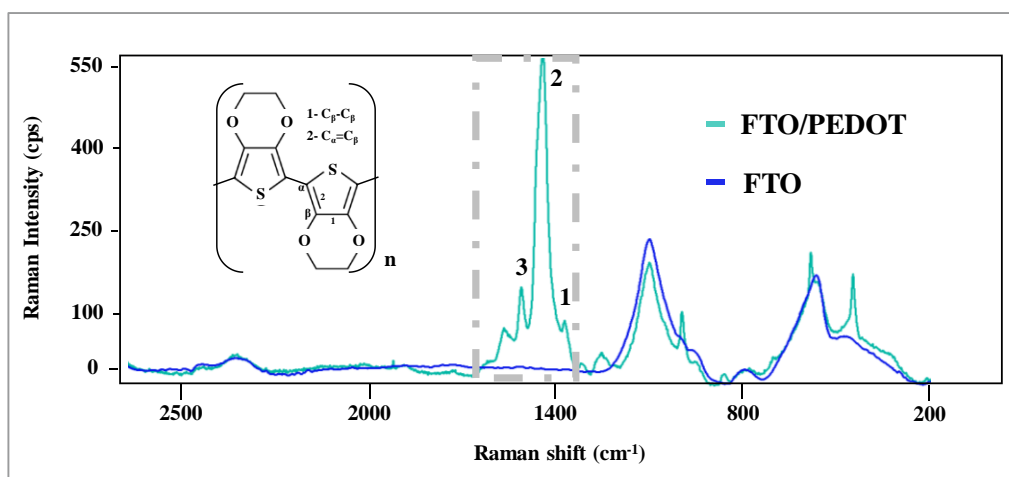


Figure 6.3 - Raman spectra of modification of counter electrode after electropolymerization of PEDOT on the FTO glass.

6.3.1.3. Electrochemical follow-up

The modification of the CEs for the hybrid device was followed by monitoring the R_{ct} of an iron redox probe in a -electrodes cell. The best electrical fit along the different stages of electrode modification was obtained for an equivalent *Randles* circuit $R(RQ)$, in which all elements showed < 5% errors. This circuit combined the R_s between WE (biosensor) and RE

and the R_{ct} in parallel with a constant phase element (Q , related with double layer). This constant phase element behaved as a pseudo-capacitance, because the value of Q exponent was higher than 0.50 [121, 124].

In general, the FTO/PEDOT glass was a highly conductive surface, but the co-polymerization of EDOT and Py on top of it led to a less conductive material, with a much higher R_{ct} value. This was particularly evident for the NIP material (FTO/PEDOT/NIP), as shown in **Figure 6.4-A**. In turn, the R_{ct} value of the MIP material obtained after finishing the polymerization (FTO/PEDOT/MIP-CEA) also increased when compared to the FTO/PEDOT surface, but it was lower than that of the NIP in absolute values. As the copolymer of PEDOT/PPy had poor conductivity features and the protein CEA is a non-conductive material, it became clear that the lower R_{ct} from the MIP film was justified by the lower amount of polymer formed, which was also consistent with the SEM images obtained (**Figure 6.2**). After template removal, an increase in R_{ct} was observed for the MIP, which was not expected (**Figure 6.4-B**). There is no explanation for this observation, but it was a consistent behaviour, also reproducible in several assays. Remotely, this could be an outcome of the charge of the surface in the different stages; the presence of CEA on the polymeric network may have generated some positively charged locations that would attract the negatively charged iron redox probe. Upon removal of CEA, these charges would no longer exist and the redox probe would have no opposite charge interaction with the polymeric network. This increase was also partially linked to the treatment with proteinase K, as the NIP surface had the same tendency, but is a smaller extent (**Figure 6.4-C**).

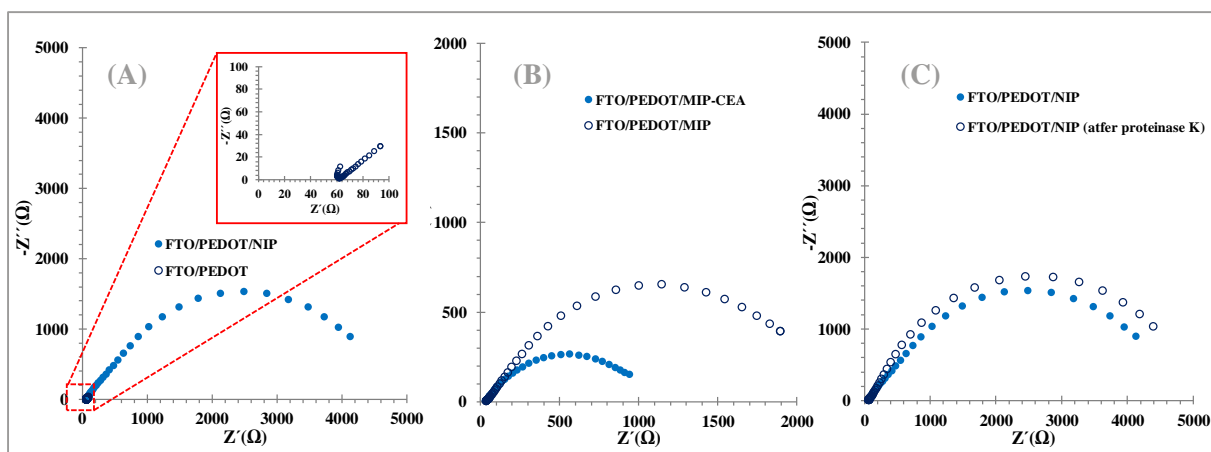


Figure 6.4 - Electrochemical EIS data of different steps involved in the construction of the different electrodes. **(A)** FTO glass with or without PEDOT. **(B)** MIP electrodes with or without CEA. **(C)** NIP electrodes with or without proteinase K treatment. Data corresponding to $5.00 \times 10^{-3} [\text{Fe}(\text{CN})_6]^{4/3-}$ readings in PB buffer, pH 7.00.

6.3.2. Rebinding features of the imprinted film

The rebinding features of the imprinted film were assessed by incubating first a blank solution and CEA standard solutions of increasing concentrations on the FTO/PEDOT/MIP surface. Each incubation was made for the same time. After this, the surface was washed with PBS buffer, and incubated in the iron redox probe to check the electrochemical features on the 3-electrodes cell. As different electrodes could be used along a single calibration, the R_{ct} signals were considered after this point as relative values (R_{ct}') to the blank, calculated as $R_{ct}' = R_{ct}(\text{CEA sample}) / R_{ct}(\text{blank})$. This approach was taken in assays made in a background medium of buffer or diluted urine.

The results obtained in buffer are shown in **Figure 6.5-A**, evidencing that the increasing of CEA concentration yielded an increase in the R_{ct} value of the iron redox probe and that this increase was CEA concentration dependent (against $\log [\text{CEA}]$). It is likely that the overall negatively charged species of CEA standing at the imprinted surface, as expected for a pH of 7.00 [67], in an increasing amount, could be increasingly avoiding the presence of the negatively charged redox probe, $[\text{Fe}(\text{CN})_6]^{3-/4-}$.

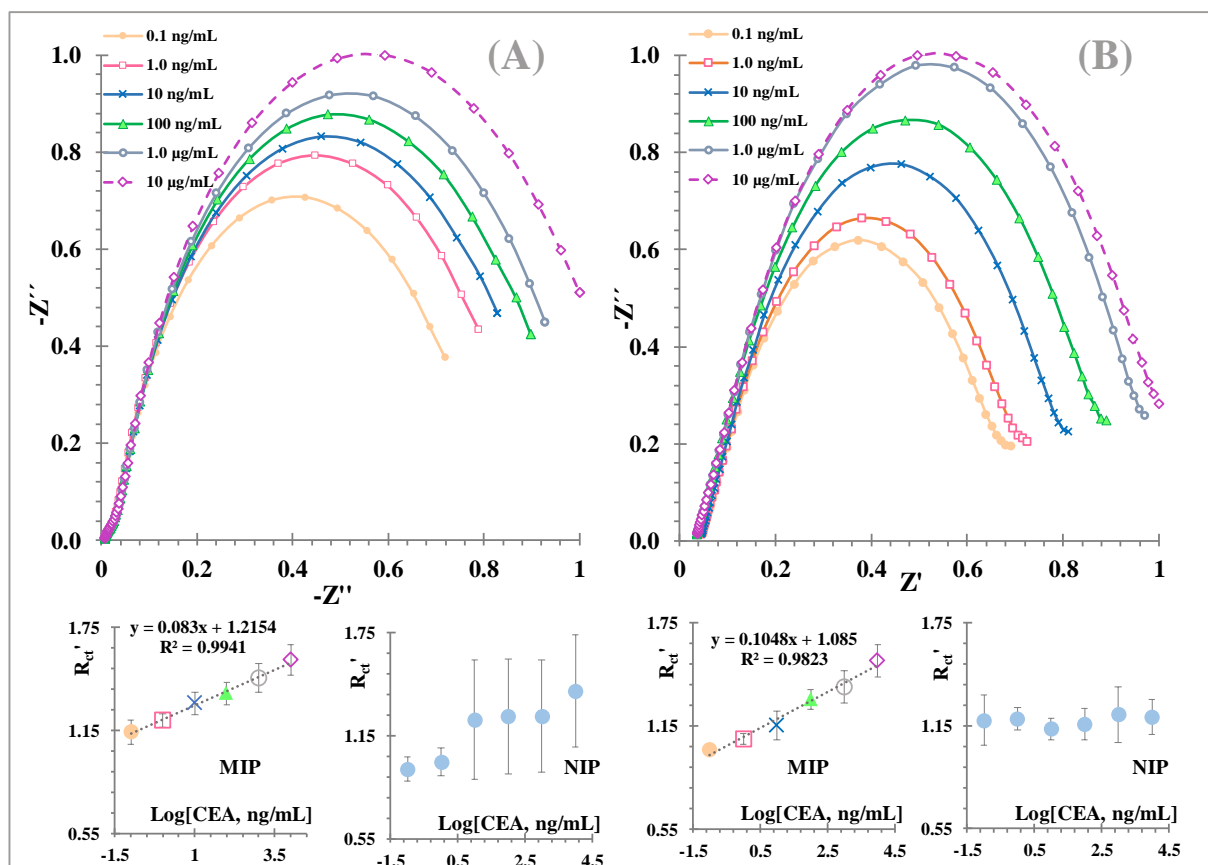


Figure 6.5 - Nyquist plots and the corresponding calibration curves (inset, as relative R_{ct} versus $\log[\text{CEA}]$) of the FTO/PEDOT/MIP electrode in a 3-electrodes cell, with a $5.00 \times 10^{-3} [\text{Fe}(\text{CN})_6]^{3-/4-}$ redox probe, prepared in PB buffer, pH 7.00, after incubation of increasing concentrations of CEA solutions prepared in buffer **(A)** or in diluted sample solution **(B)**.

In terms of analytical performance, it was clear that the MIP film was able to quantify very low CEA concentrations in buffered medium. The FTO/PEDOT/MIP electrode responded with a linear trend from 100 pg/mL to 10 µg/mL, showing a typical linear regression of $R_{ct}' = 0.083 \times \log[\text{CEA, ng/mL}] + 1.22$ and a squared correlation coefficient of 0.9941; the LOD was ~ 10 pg/mL. In contrast, the response of the corresponding NIP in the same concentration range presented a small tendency to increase, but in an uncontrolled behaviour. As shown in **Figure 6.6** the average data obtained corresponded to a slope of 0.017 per decade concentration and a squared correlation coefficient of 0.88. Moreover, the imprinted material showed very reproducible calibration curves evaluated from independent MIP units, with the corresponding data leading to standard deviations $< 7\%$. Consistently, the NIP showed lower reproducibility, in comparison with the MIP (also as shown in **Figure 6.6**).

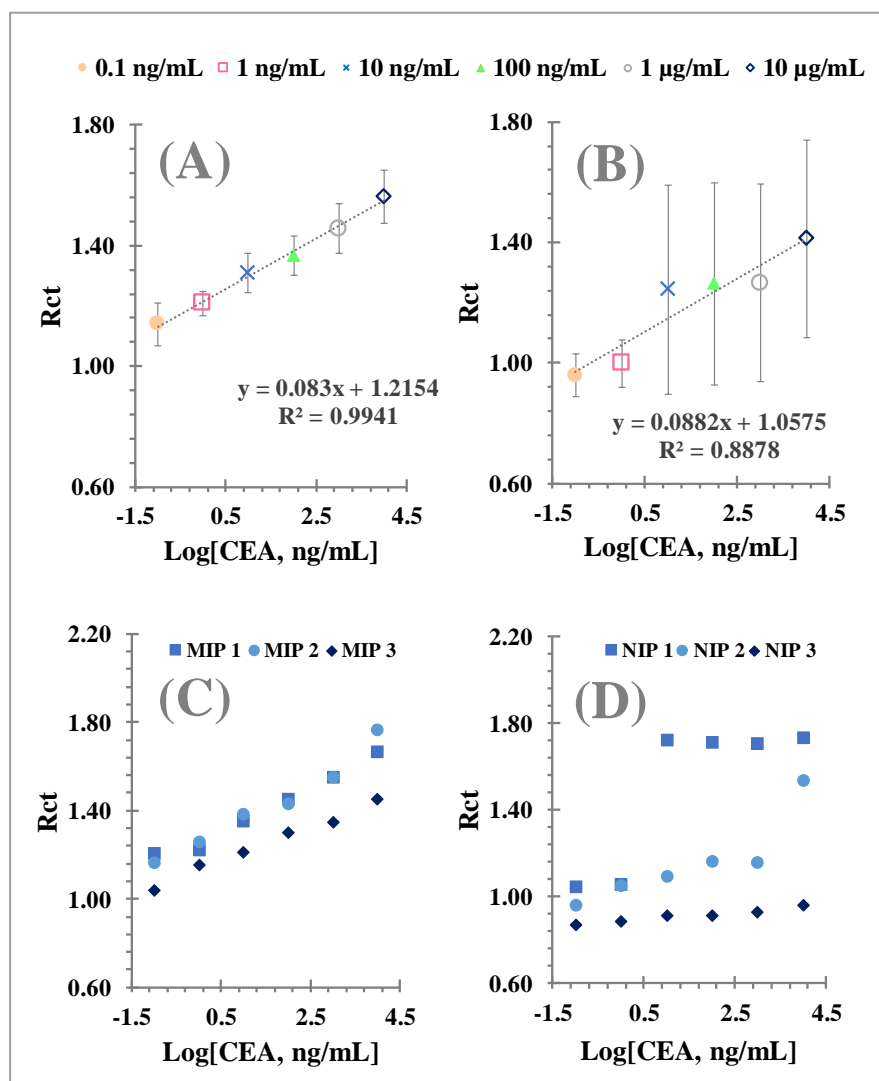


Figure 6.6 - Calibration curves corresponding to analytical performance of **(A)** FTO/PEDOT/MIP or **(B)** FTO/PEDOT/NIP electrodes, operating in a 3-electrodes cell, incubated previously in increasing concentrations of CEA standard solutions, prepared in PBS, in the presence of a 5.00×10^{-3} M $[\text{Fe}(\text{CN})_6]^{3-/4-}$ redox probe, prepared in PB buffer, pH 7.00.

Calibrations were also made in a background of diluted urine human sample, aiming to evaluate the impact of a real (complex) sample upon the electrochemical response. The typical *Nyquist* plots obtained under this condition are shown in **Figure 6.6-B**, and confirm a similar behaviour to that obtained in buffered solutions. The concentration of linear response was the same (0.10 ng/mL-10 µg/mL) and the slope was slightly higher, 0.1048 per decade concentration, than that of the buffer medium, which has been a typical behaviour in these

kind of biosensing systems [163, 267]. Most likely, this reflects the higher ionic content of urine samples.

Overall, the sensitivity of the MIP response was much greater than that of the NIP, for which the response was typically random. This suggested that the rebinding of CEA was controlled by the rebinding sites and that the non-specific adsorption of protein by the polymer had little impact upon the electrochemical response. Moreover, the concentration response range was within the physiological levels of interest for CEA (2.5 and 10 ng/mL) [47, 49, 70].

6.3.3. Integrating the imprinted film on the DSSC

6.3.3.1. The set-up

The impact of the imprinted film upon the DSSC was monitored by evaluating the photovoltaic features of DSSCs assembled with CEs of FTO/PEDOT, FTO/PEDOT/MIP-CEA and FTO/PEDOT/MIP (Figure 6.7-A).

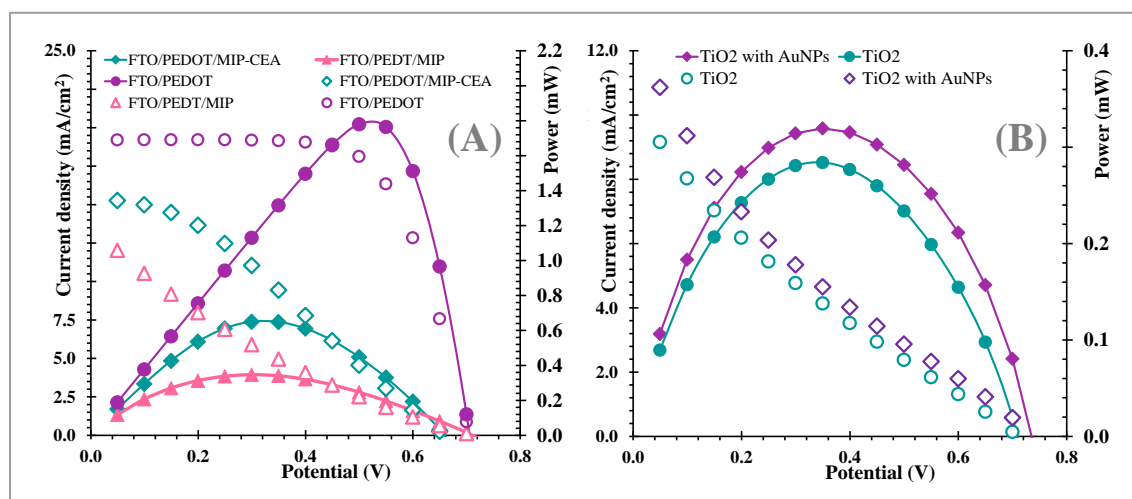


Figure 6.7 -Photocurrent density-photovoltage ($J-V$) and power conversion efficiency characteristic curves of DSSCs assembled (A) with different CEs (FTO/PEDOT, FTO/PEDOT/MIP-CEA or FTO/PEDOT/MIP) and a photoanode of TiO₂ sensitized with N719; or assembled (B) with different photoanodes, with or without AuNPs, and a CE of FTO/PEDOT/MIP. Studies made with an electrolyte of I⁻/I₃⁻.

The main features of the DSSC operating with a conventional FTO/PEDOT CE included η of 2.80 %, a J_{SC} of 5.93 mA/cm² and a FF value of 66.90 %. The preparation of the imprinted material on top of this electrode, also including the CEA protein within the polymeric network, was responsible for a ~63% decrease in the overall efficiency of the DSSC cell down to 1.02% η , which was also consistent with the data in **Figure 6.4-B**. The other photovoltaic parameters, J_{SC} , FF and P_{max} also decreased to 4.79, 32.40 and 0.65, respectively. After template removal (FOT/PEDOT/MIP), the efficiency decreased again, down to 0.55 %, a behaviour that was also consistent with the results shown in **Figure 6.4-B**, in which the exit of the protein almost doubled the R_{ct} value obtained. Yet, the overall output of the cell was however better than that obtained with a CE having only PPy and MIP material. This fact can be proved by slightly lower LOD presented herein (0.11 ng/mL) comparing with LOD of MIP PPy (0.14 ng/mL). Moreover, a wide linear range is observed in this work, 0.1 ng/mL until 100, against to the linear range of MIP PPy (100 ng/mL to 100 μ g/mL) [259]

6.3.3.2. *Rebinding features on the hybrid set-up*

A MIP electrode for CEA operating as the CE of a DSSC gets in contact with an I⁻/I₃⁻ redox probe prepared in ACN, which is quite different from the typical iron redox probe prepared buffer, used in the 3-electrodes cell evaluation. The impact of this new electrolyte in the rebinding of CEA in terms of photovoltaic operation should therefore be monitored. As in previous studies, these rebinding studies were made in both buffered solutions and diluted urine samples, for CEA concentrations ranging from 0.1 ng/mL to 100 μ g/mL.

The power curves obtained for each incubated concentration level are shown in **Figure 6.8**, and revealed a decreased performance of the PV for increasing amounts of CEA adsorbed to the MIP film. This was consistent with the data shown in **Figure 6.5**, in which the R_{ct} increased for increasing concentrations of CEA. Moreover, the DSSC set-up was also sensitive to CEA within the same concentration range as the MIP film, evaluated in the 3-electrodes cell. In buffered solutions (**Figure 6.8-A**), the linear behaviour observed for relative η ($\eta' = \eta_{(sample)} / \eta_{(blank)}$) against log [CEA] showed a typical anionic slope of 0.0757 per decade concentration and a square correlation coefficient >0.995. Other photovoltaic parameters of this system (as V_{oc} , J_{sc} and FF) were also plotted against the log [CEA], but a lower quality linear trend was obtained. The LOD of this system was 0.11 ng/mL. In diluted urine solutions

(Figure 6.8-B), the photovoltaic parameters presented similar changes when compared to the assays in buffer. The typical anionic slope for η' against $\log [CEA]$ was 0.0548 per decade concentration and the square correlation coefficients were >0.992 .

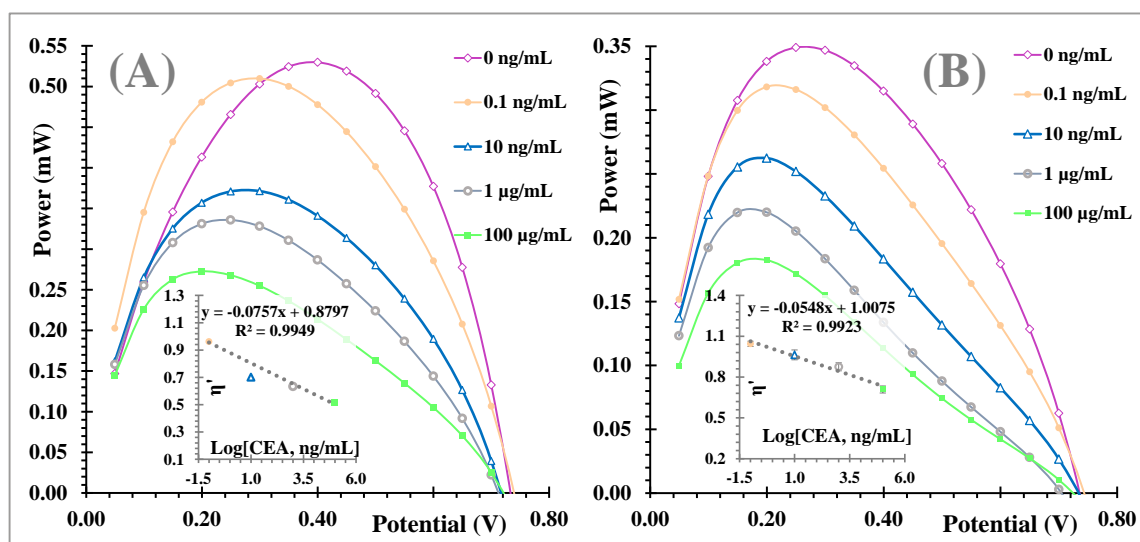


Figure 6.8 -Power curves and the corresponding calibration curves (inset, as relative η' versus $\log[CEA]$) of the FTO/PEDOT/MIP electrode in the DSSC set-up, after incubating increasing concentrations of CEA solutions, prepared in buffer **(A)** or in diluted sample solution **(B)**. DSSC with a photoanode of TiO_2 and an electrolyte of I^-/I_3^- .

Overall, the analytical response of the MIP film inside the DSSC was observed from 0.1 ng/mL to 100 $\mu\text{g/mL}$, the same concentration range of linear response in the 3-electrodes cell and using a different redox probe. In general, the system responded with a reasonable sensitivity. The slope generated by CEA solutions in urine was however slightly smaller than the one observed in buffered solutions. This was an outcome of the decreased absolute power promoted by the blank urine samples. Although not questioning the analytical usefulness of this set-up, this decreased sensitivity revealed the great impact generated by the absolute efficiency of the cell when in the blank solution. This value was interfering with the overall sensitivity of the analytical system, being therefore important to identify a strategy that would increase such efficiency value.

6.3.4. Enhancing the DSSC/biosensor efficiency

The addition of plasmonic nanomaterials to the photoanode has been identified as a way to improve the energy generated by DSSCs [238, 254-256]. For this purpose, a novel photoanode was prepared by adding metal AuNPs into the conventional semiconductor (TiO_2) support, while keeping the same active area of the photoactive layer in the previous electrodes (0.64 cm^2). The presence of Au in the TiO_2 photoanode was confirmed by SEM analysis (**Appendix IV.1**), with a backscattered electron detector, ensuring different intensities and contrasts according to the atomic number of Ti and Au [268], and by the EDS analysis. The set-up made to evaluate this feature used the FTO/PEDOT/MIP material as CE.

The J - V measurements made are shown in **Figure 6.7-B** and were used to calculate the corresponding photovoltaic performance, expressed as J_{sc} , V_{oc} , FF , and η . This data is summarized in **table 6.1**. An increase in J_{sc} from 3.10 to 3.80 mA/cm^2 was observed, when DSSC was assembled with photoanode of TiO_2 and AuNPs, which corresponded to a 22.3 % increase. Moreover, the photoanode with AuNPs displayed a better efficiency ($\eta = 0.504 \%$) than the photoanode with only semiconductor. Overall, it was possible to observe that the performance of DSSCs improved when the Au nanoparticles were introduced in the TiO_2 paste. This derived from the plasmonic effect of such NPs, which enhance the light absorption that hits the cell according to [254-256]

Table 6.1 - Photovoltaic features of DSSCs assembled with photoanodes containing or not AuNPs and a CE of FTO/PEDOT/MIP.

Photoanode	V_{oc} (mV)	J_{sc} (mA/cm^2)	FF (%)	P_{max} (mW/cm^2)	η (%)
TiO_2	708.40 \pm 0.001	3.10 \pm 0.110	20.45 \pm 0.014	0.29 \pm 0.049	0.449 \pm 0.076
TiO_2 + AuNPs	736.20 \pm 7.780	3.80 \pm 0.430	18.25 \pm 0.780	0.32 \pm 0.026	0.505 \pm 0.047

The impact of this power increase on the analytical features of the DSSC/biosensor hybrid device was also monitored by re-evaluating the rebinding features in diluted urine samples, using this set-up. The J - V measurements obtained under this condition are shown in

Figure 6.9-A. Overall, the average anionic slope obtained by using a photoanode with AuNPs was 0.0631 per decade concentration, corresponding to a 12 % higher value than that without AuNPs (**Figure 6.9-B**). The calibrations made were also linked to a wider η' change; it varied from 0.9 to 0.5, from the lowest to the highest concentration, meaning that the range of the operational useful analytical signal was also amplified by using a photoanode with AuNPs. Similar to previous experiences, the photovoltaic parameters also decreased when the concentration of CEA increased along the calibration procedure, but their linear fit with the $\log[\text{CEA}]$ was not as evident as the η' .

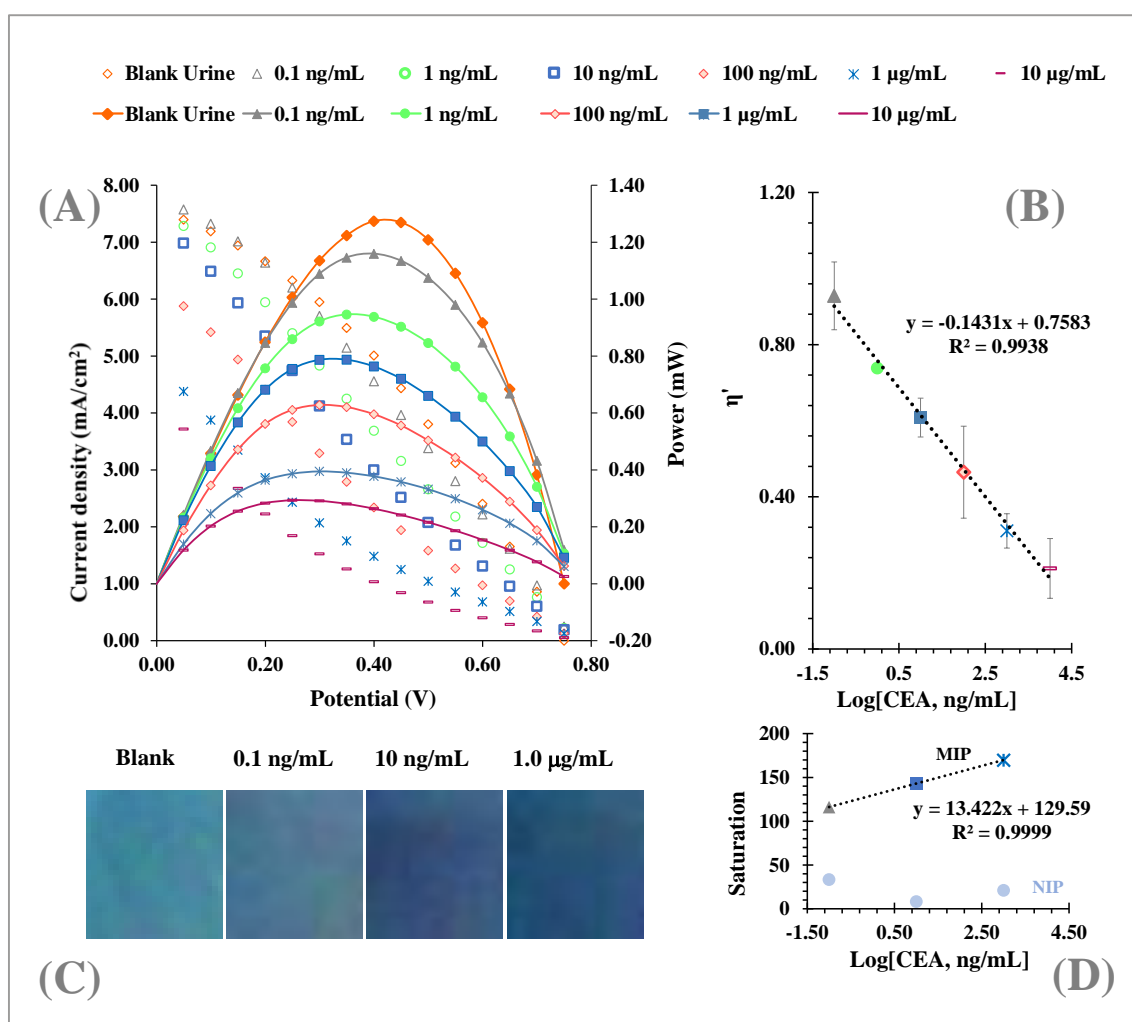


Figure 6.9 - Power curves (A) of the FTO/PEDOT/MIP electrode in the DSSC set-up containing a photoanode with AuNPs, after incubation in increasing concentrations of CEA solutions, prepared in diluted urine sample solution, (B) the corresponding calibration plots as η' versus $\log[\text{CEA}]$, along with the colour generated by the electrochromic cell (C) and the corresponding saturation coordinate of the HSL colour system against $\log[\text{CEA}]$.

A control material was also evaluated against CEA concentration in DSSC/sensor hybrid device using a photoanode with AuNPs. It showed decreasing η' values along the calibration procedure, when exposed to the same conditions as the MIP. Yet, the sensitivity of the NIP was lower than that of the MIP, evidencing an anionic slope of 0.0689, with a correlation coefficient of 0.9287 (Figure 6.10).

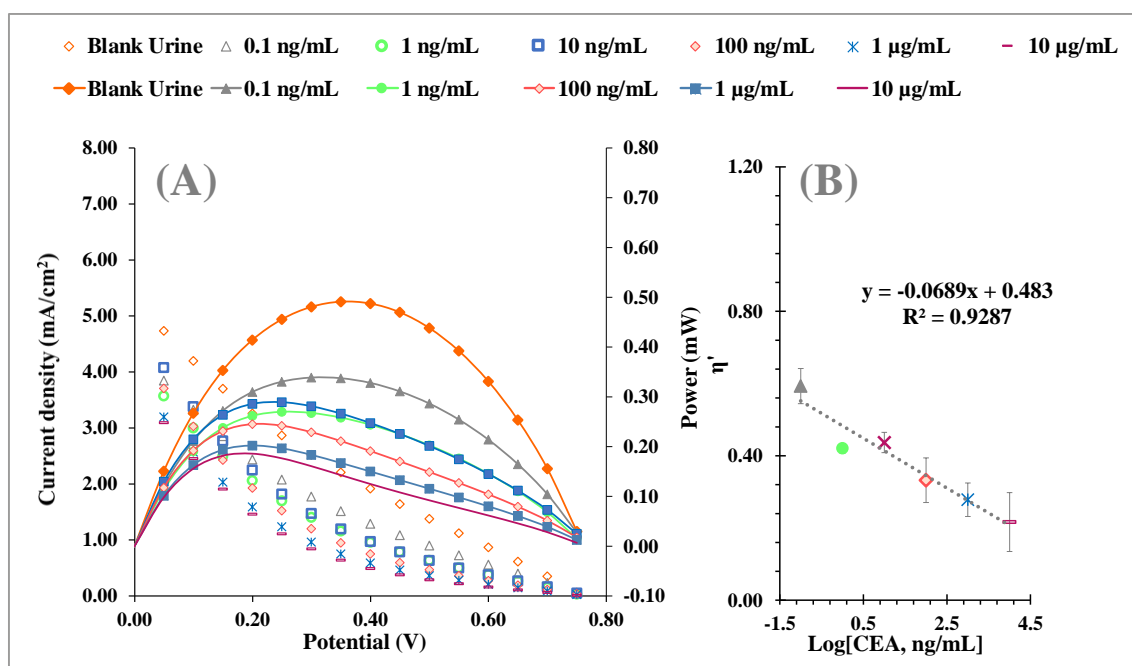


Figure 6.10 - Power curves (A) of the FTO/PEDOT/NIP electrode in the DSSC set-up containing a photoanode with AuNPs, after incubation in increasing concentrations of CEA solutions and (B) the corresponding calibration plots as η' versus $\log[\text{CEA}]$, prepared in diluted sample solution.

Overall, the DSSC/biosensor hybrid system operating with a plasmonic effect from AuNPs favoured the sensitivity of response against CEA concentration. First, the power of the blank signal increased and, second, the value of η' before saturation was lower than that with photoanodes without plasmonic nanostructures. This wider range of electrical response would most certainly favour the response of the signalling element, another aspect presented next.

6.3.5. Selectivity of DSSC/biosensor

The selectivity test evaluated the effect of chemical compounds that could be potential interfering compounds in biological fluids. This was achieved by a competing test between CEA (in 50 ng/mL) and other interfering species selected for this propose. Herein, the tumour biomarkers, Carbohydrate Antigen 15.3 (CA 15.3) and Carbohydrate Antigen 15.3 (CA 125) and urea, the most abundant compound in urine, were selected. The concentrations used for this purpose were 1.6 U/mL, 2.5 U/mL, and 1.2 mg/mL respectively, considering a possible 10 × dilution of an original serum sample.

Selectivity studies were evaluated in two different conditions, using binary (CEA + interfering species) or single component (only interfering species) solutions. Each solution was incubated in the sensing layer (CE) for 20 min, the same period used in the calibration procedure. The results obtained with the binary solutions were compared to those of a single component CEA solution. The data obtained is shown in **Figure 6.11**, evidencing that the tested compounds did not interfere significantly with the CEA readings, changing the signal from 4.1 to 15.5% (**Figure 6.11**).

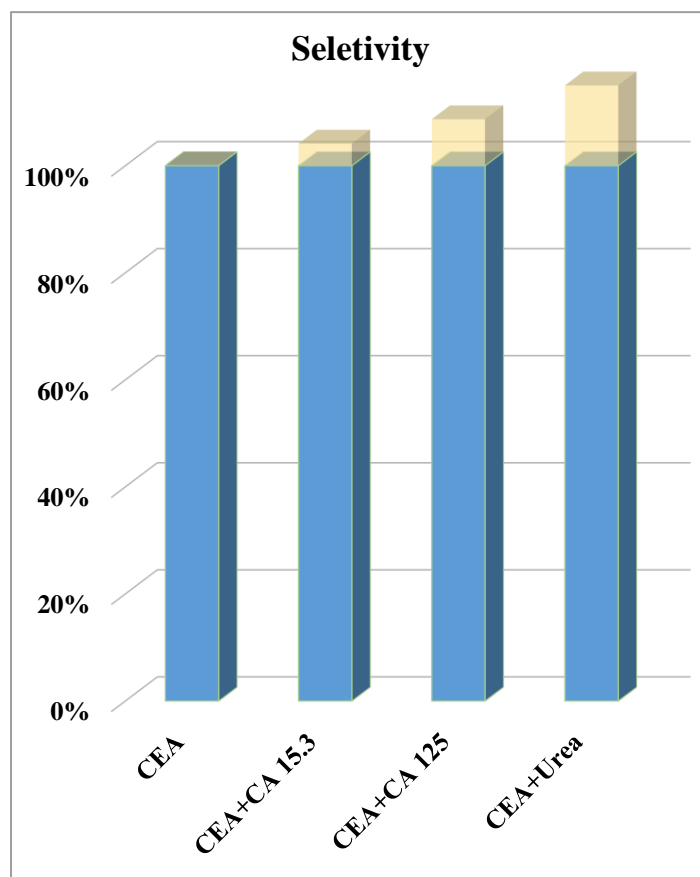


Figure 6.11 - Percentage signal change when binary solutions are incubated in the sensing layer of the electrode and tested after in the DSSC/biosensor configuration. CEA 50 ng/mL; CA 125, 2.5 U/mL; CA 15.3, 1.6 U/mL; and urea 1.2 mg/mL.

Using single component solutions, each compound was incubated separately and the results indicated a low rebinding ability for CA 15.3 (15.3 %), CA 125 (3.4 %) or urea (23 %), when compared to CEA (**Figures 6.12** and **Figure 6.13**). These values are corresponding to the worst scenario, because there was no other ion competing for the sensing layer with the interfering compound, which may allow a significant non-specific rebinding response.

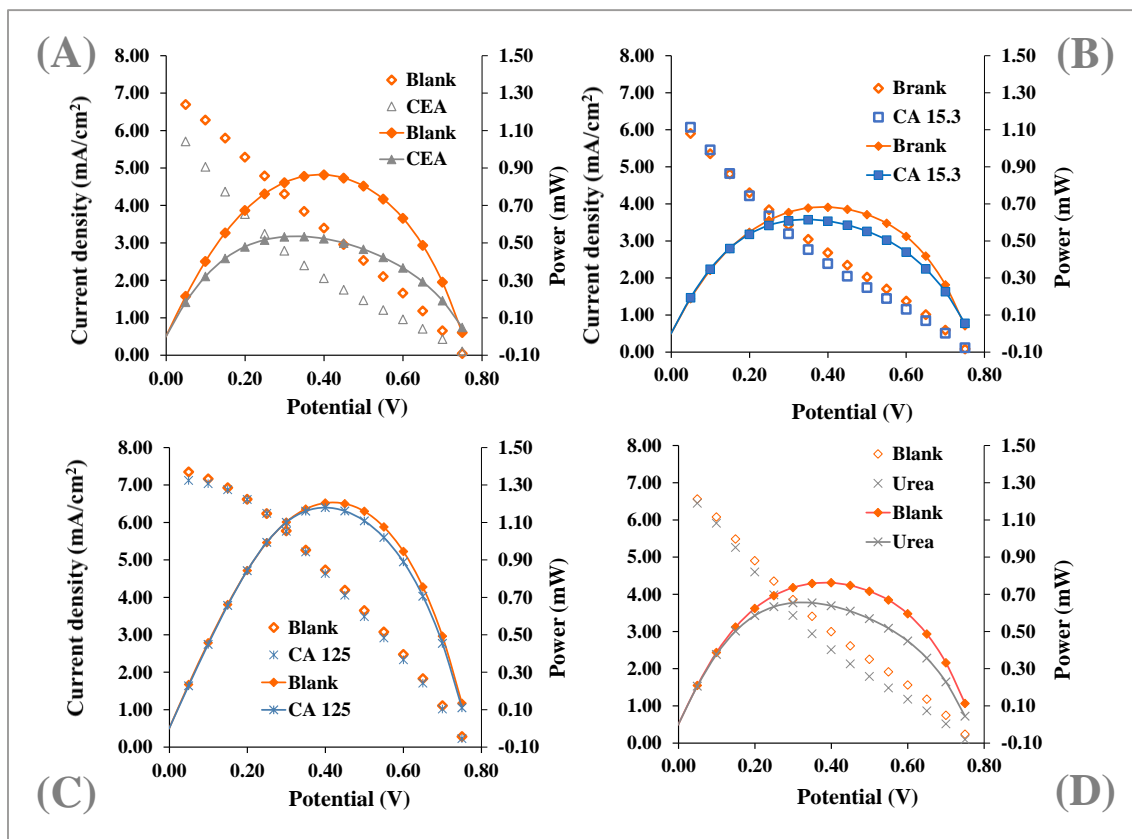


Figure 6.12 - Power curves of the FTO/PEDOT/MIP electrode in the DSSC set-up containing a photoanode with AuNPs, after incubation with **(A)** CEA; **(B)** CA 15.3 and **(C)** CA 125, prepared in buffer solution. **(D)**

Selectivity study of DSSC/biosensor with single solutions of CEA and interfering species. CEA 50 ng/mL; CA 125, 2.5 U/mL; CA 15.3, 1.6 U/mL; and urea 1.2 mg/mL.

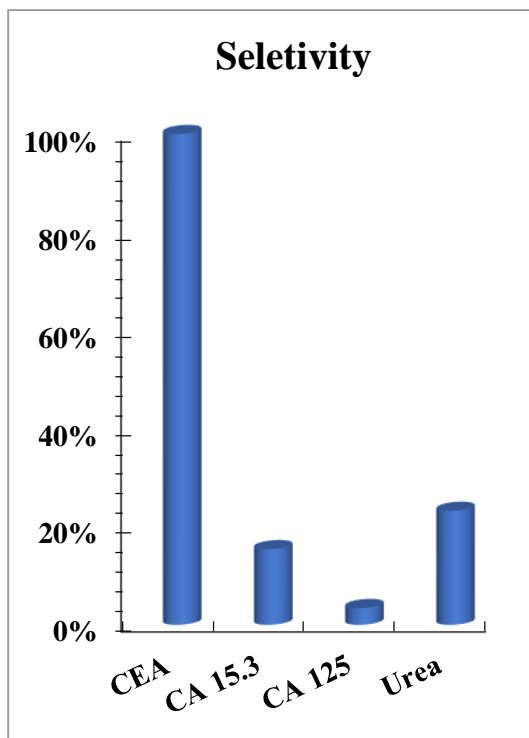


Figure 6.13 - Selectivity study of DSSC/biosensor with single solutions of CEA and interfering species. CEA 50 ng/mL; CA 125, 2.5 U/mL; CA 15.3, 1.6 U/mL; and urea 1.2 mg/mL.

Overall, the results obtained evidenced the very good selectivity features of the MIP sensing layer, confirming that the biosensor had a high affinity for the target molecule.

6.3.6. Inclusion of the self-signaling element

6.3.6.1. Interface with the electrochromic cell

The self-signalling element consisted of an EC (**Figure 6.1-D**) linked to the external circuit of the DSSC/Biosensor. This cell was set-up according to [269] with an organic EM of PEDOT and SNS-NH₂, and changed its colour in agreement with the energy arriving from the hybrid device. As the energy produced by the hybrid PV was CEA concentration dependent, it was reasonable to assume that the EM would yield colour differences under increasing CEA concentrations.

For this purpose, rebinding studies were made as previously on the FTO/PEDOT/MIP electrode, which was handled after as the CE of a DSSC cell equipped with a photoanode

containing AuNPs. The concentrations selected for this purpose were 0.10 ng/mL, 10 ng/mL, 1.0 µg/mL and 100 µg/mL, the same concentration range tested before. After rebinding, each MIP electrode was combined with the photoanode and the necessary electrolyte to generate a given current that should be in agreement with the CEA concentration. This current flowed through the EC (**Figure 6.1**), and a total of 12 min was given to reach a stable colour.

The colours obtained for the different concentrations in urine sample solutions are shown in **Figure 6.9-C**. The blank signal correspond to the incubation of diluted urine sample with no CEA, and yielded the highest power produced by the hybrid device and feeding the EC. The corresponding colour was typical light blue. Increasing CEA concentrations incubated in the MIP CE up to 1.0 µg/mL yielded decreasing currents, which were linked to the formation of a darker blue colour in the EC. The highest concentration of all, 100 µg/mL, led to no colour variation, meaning that the current arriving at this point at the EC was insignificant and unable to promote additional colour changes. Overall, the colours observed for increasing CEA concentrations were in a clear gradient change, which was visually perceptible.

The direct impact of using a more efficient hybrid device upon the colour change was also assessed, by carrying out the same assays in a DSSC with a photoanode without AuNPs. The colours produced were less intense and tended to purple instead of a dark blue colour (**Appendix IV.2**). The saturation was not reached in the complete concentration range, probably because in this configuration the power decrease for CEA increasing concentrations was less intense, thereby reaching less quickly a near close-to-zero power condition. Overall, this data confirmed the great relevance of using a more efficient cell in the coloured transduction of the rebinding event.

The gradient observed was also used to extract quantitative data, in a similar way to the approach reported by [253, 269]. To this end, the colour coordinates of the HSL colour system were extracted by the Paint program of Windows and mathematically treated. The best mathematical fit plotted y-axis as saturation, against the log of CEA concentration, yielding the linear trend observed in **Figure 6.9-D**.

Overall, it was evidenced that the visual inspection of the colour changes in the EC provided semi-quantitative data (**Figure 6.9-C** and **Appendix IV.2**) and that this data could be further refined to generate quantitative evidence. In general, all data produced was clinically relevant,

but the use of the DSSC with AuNPs may clearly benefit the generation of more accurate data, as the colour change was more intense.

6.4. Conclusions

This work confirmed the possibility of producing an effective self-powered and self-signalled biosensing device for CEA, by merging different technologies. PVs, plastic antibodies (or MIP technology), plasmonic nanomaterials and ECs were combined to target an electrochemical detection system that retrieves a coloured response. In this, the PV was responsible to generate power to the electrochemical device and acted in a concentration dependent manner, when one of its electrodes was modified with plastic antibodies. This power was driven towards an EC that converted the energy into a coloured event, enabling visual detection. The plasmonic nanomaterials were tested herein as an additional element into this system that could improve the performance of the PV and contributed to an increased sensitivity, interestingly revealed by an improved coloured detection.

From a practical perspective, the hybrid device was able to respond to CEA concentrations between 0.1 ng/mL-10 μ g/mL, which is an important range for disease screening, diagnosis or progression, and the use of plasmonic AuNPs yielded an improved sensitivity. It generated semi-quantitative data by simple visual inspection of the colour gradient, but the colour coordinates could be used to generate quantitative information. Moreover, the current device has a single light requirement and offers the potential to generate relevant data for clinical decision, in a fully independent manner, everywhere. In principle, the concept behind this hybrid device may eventually be extended to any other target biomolecule.

This device may be further evolved to eliminate the need for electrical cables connecting biosensor and EC. Micro/nanofabrication approaches could solve this and lead the final biosensor set-up to proper POC conditions. Another simplification approach could be achieved by tailoring the MIP material outside the PV, thereby simplifying the procedures involved in sample incubation and signalling.

7. Biosensors and photovoltaics merged in self-powered and self-signaled cable-free set-up

7.1. Introduction

While the possibility of developing a novel biosensor that combines MIP materials, PV cells and EC for cancer biomarker detection, with or without plasmonic nanomaterials, has been established, its use in POC context requires a smoother interface for the user. In this context, miniaturization has simplified many technical approaches throughout the years and could be implemented herein for this purpose.

Moreover, advances in micro and nanofabrication techniques have led to a reduction in the biosensors' manufacturing costs, when mass production, and consequently in the final clinical analysis cost. In addition, miniaturizing technologies provide other benefits to medical diagnosis, such as reducing sample volumes and response times and allowing multi-analyte detection [270, 271]. Thus, micro and nanotechnologies have become a key tool in the development of biosensors, combining several areas as biotechnology, electronics, chemistry and bioengineering. Biosensors that result from the combination of these technologies have demonstrated a great potential to enhance detection methods (sensitivity and LODs) and may result in alternative portable devices, easier to use as analytical tools for POC procedures [270, 272-274].

Thus, the present work reports an alternative design to the previous interface in chapter 6, aiming to produce a single unit device that contains all elements together (MIP materials, PV and EC), while being self-powered, self-signalled, and wire-free. In this novel hybrid device, the MIP biosensing element and the EC (Biosensing system) are designed on the backside of the CE of the DSSC (DSSC/CE), made in-situ by gold conductive tracks fabricated by physical

vapour deposition (PVD), using sputtering [275, 276]. The necessary electrical connections between the CE and the PV are made by an electrical connector, made for this purpose.

7.2. Experimental section

7.2.1. Apparatus

Electrochemical assays were performed in a potentiostat/galvanostatic from Metrohm Autolab, controlled by dedicated NOVA software. DSSC measurements were made in the potentiostat, coupled to a LED driver accessory from Methrom. The performance of the PV was monitored under 100 mW/cm^2 , by a LED driver, supplying 450 mA from a warm white LED.

PVD Sputtering was used for gold and ITO deposition. The ITO transmittance measurements was obtained using a spectrophotometric setup comprised by: a 200 W quartz/tungsten/halogen lamp (Newport NRC-6334NS) as a light source; a monochromator (Newport 74125); an optical fibre (Newport Standard Grade FS Fiber Optic), used to direct the light from the light source through the sample to a commercial photodiode (Hamamatsu S1336-5BQ); and a picoammeter (Keithley 487) to measure the photodiode current. The monochromator as well as the picoammeter were connected to a computer through a GPIB interface to control and collect the data.

7.2.2. Reagents and Solutions

All chemicals were of analytical grade and ultrapure Mili-Q laboratory grade water (conductivity $\leq 0.1 \mu\text{S}\cdot\text{cm}^{-1}$) was employed. The reagents employed throughout this work were obtained from different sources: $\text{K}_3[\text{Fe}(\text{CN})_6]$, $\text{K}_4[\text{Fe}(\text{CN})_6]$ and Na_2HPO_4 were obtained from Riedel-de-Häen; TBP was from TCI; NaH_2PO_4 was from Scharlau; EDOT and HMII were from Alfa Aesar; EtOH and ACN were from Carlo Erba; Py, TiO_2 anatase, N719 dye; Lil; EtOH; proteinase k; H_2SO_4 ITO glass and FTO glass were from Sigma; KCl and Pt were from Merck; PBS was obtained from Amresco and CEA from human fluids was from EastCoast Bio.

Electrochemical studies in 3 - electrodes systems were performed with the redox standard probe $[\text{Fe}(\text{CN})_6]^{3-/4-}$, with concentrations of 5.00×10^{-3} mol/L and prepared in an aqueous solution of 0.10 mol/L KCl. Electrochemical measurements of the DSSC and DSSC/Biosensor were obtained with an electrolyte containing 0.05 M of I_2 , 0.10 M of LiI, 0.60 M of HMII and 0.50 M of TBP well dispersed in ACN.

The PB contained 0.03 mol/L of Na_2HPO_4 and 0.02 mol/L of NaH_2PO_4 (pH of 7.00) was dissolved in ultrapure water. A stock standard solution of 100 $\mu\text{g}/\text{mL}$ CEA was prepared in PB buffer and the less concentrated CEA standard solutions were prepared by dilution of the stock standard solution in the same buffer for concentrations ranging from 0.1 ng/mL to 100 $\mu\text{g}/\text{mL}$.

7.2.3. Set-up of DSSC

The overall set-up of the final device is represented in **Figure 7.1-C** and its integral parts are described separately, next.

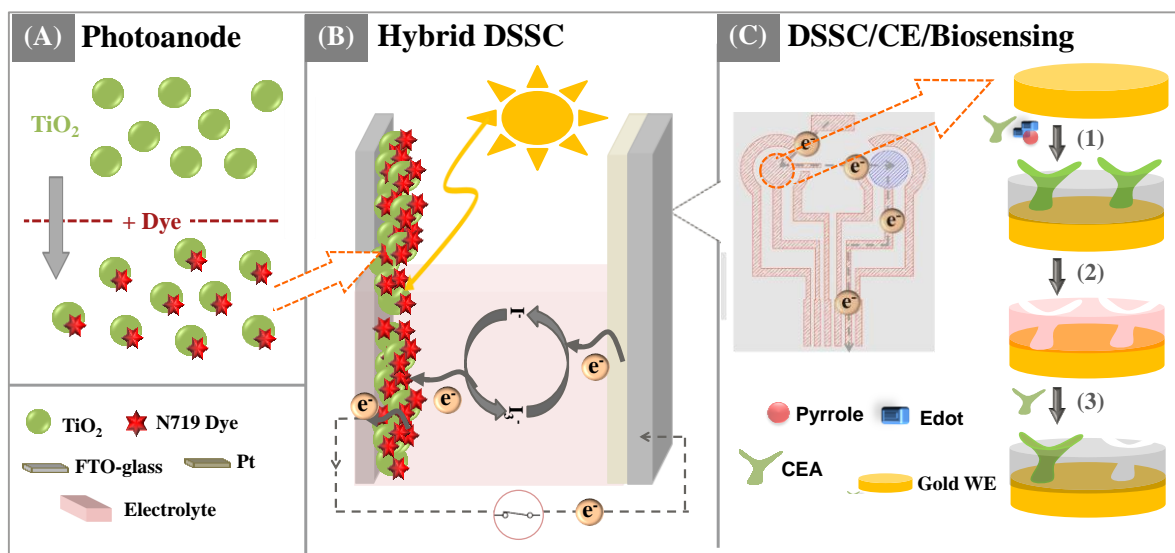


Figure 7.1 - Schematic representation of the several stages of the Hybrid DSSC set-up **(B)** with the photoanode **(A)** and biosensing film assembly back-side of DSSC/CE **(C)**: eletropolymerization **(1)**; Template Removal **(2)** and rebinding **(3)**; combined in DSSC cell.

7.2.3.1. Photoanode preparation

The photoanode was based on the TiO₂ paste, having 6.00 g of TiO₂ anatase nanopowder in 8.00 mL of EtOH, 1.00 mL of AA and in 1.0 mL of ultrapure water. The resulting paste was stirred for 1 h, at room temperature and employed as thin-films on the FTO coated glass (sheet resistance 13.0 Ω/sq, Sigma-Aldrich) via *Doctor Blade* method in circular forms with area of 0.20 cm². Afterwards, the photoanode was annealed at 450 °C for 30 min, cooled down to 80 °C and immersed in a dye bath solution for 18 h, at room temperature, in the dark. The dye bath solution was composed by 5.00×10⁻⁴ mol/L of N715 dye in EtOH. After dye adsorption, the photoanode was washed with EtOH to remove non-adsorbed dye and dried at room temperature.

7.2.3.2. Counter electrode preparation

The DSSC was assembled in a conventional configuration (**Figure 7.1-B**), for which two different TCO glass were used for the CE preparation. These were FTO (FTO/CE) or ITO (ITO/CE) glass, always assembled with Pt. The FTO and ITO glasses were previously cleaned by ultrasonication in EtOH, acetone and water for 15 minutes, followed by 15 minutes in deionized water at room temperature. The next step for preparing the CE consisted in applying an ethanolic solution of 5.00×10⁻³ mol/L Pt on a rectangular area of 7.50 cm², placed in a clean glass, via spin coating method at 3000 rotations per minute (rpm) for 20s. Afterwards, this glass was annealed in the oven at 450°C for 15 min. The CE was subsequently cleaned with acetone and dried under nitrogen flux. The same process of cleaning was used in the two masks, which served as a model for the deposition of the sensing system on back-side of DSSC/CE (DSSC/CE/Sensing).

7.2.3.3. Preparation of the DSSC/CE/Sensing

The sensors that are printed outside the DSSC were drawn by a computing aided design software, to create two different stainless steel masks (**Figure 7.2**). These masks were fabricated through laser cutting, which contained the design intended to be transferred to the sensor. The final geometry is shown in **Figure 7.1-C** and was inspired in the previously employed electrochemical sensors, with a 3-electrodes system, combining WE (4 mm of diameter), AE and RE. The area of the 3-electrodes system exposed to liquid solutions was defined by a glue.

The conductive paths and the 3-electrodes system were fabricated in Au, except the WE, which should be transparent to allow the perception of a colour change upon the response of the EM. They were obtained by PVD, using a homemade sputtering equipment. In this technique, a solid coating material with high purity (usually about 99.99%) is evaporated by bombardment with ions, under vacuum conditions. PVD was chosen to prepare the electrical connections, because it allows the production of uniform and reproducible thin films, with good adhesion of the material to the substrate [277]. Before the Au sputtering process, the glasses and the masks were cleaned with isopropyl alcohol and acetone. The thickness of all the deposited films were measured using a profilometer (Veeco Dektak 150 Surface Profiler), with an accuracy of 1Å.max.

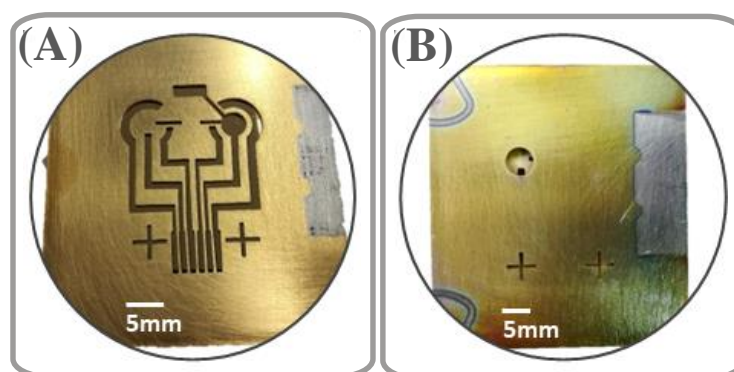


Figure 7.2 - Photograph of the masks used during the deposition of **(A)** the Au and Cr films and **(B)** the ITO film on DSSC/CE.

Before the deposition steps, the masks were previously fixed on the backside of DSSC/CE, using kapton tape, and heated in the oven at 60 °C for 2h. The chromium (Cr) film was produced as the first layer on the DSSC/CE/Sensing to improve the adhesion of the Au material to the glass. The Cr film was the first material to be deposited on DSSC/CE, at 1 nm/s and a pressure of 0.36 Pa, by using the shown in **Figure 7.2-A**. This mask was also used for the subsequent Au deposition on the Cr layer. The Au film was obtained with a rate of 2.2 nm/s and a pressure of 0.38 Pa. After that, the mask in **Figure 7.2-B** was used to deposit the ITO material to complete the Sensing/CE set-up. The ITO deposition was performed with a rate of 0.06 nm/s and a pressure of 0.39 Pa.

All electrical connections, including the 3-electrode system, were deposited on the backside of DSSC/CE and the conductivity of all films (Au or ITO) was measured by the Van der Pauw method, using 4 electrical contacts at the edge of the sample.

7.2.4. Hybrid DSSC

The set-up of the hybrid device was similar to the regular DSSC, but the biosensing electrode was positioned on the backside of the DSSC/CE. The hybrid DSSC was made using a photoanode of TiO₂ and CE of Pt (FTO/CE or ITO/CE), sealing the cell with a scotch magic tape (thickness of 0.06 mm) that acts as a spacer layer between the two electrodes with electrolyte in the middle to close the electrical circuit. The electrical connections between DSSC/CE/Sensing and the PV was interfaced in the external circuit by a special purpose electrical connector.

7.2.4.1. CEA Biosensing film assembly

An imprinted polymer for CEA was produced on the WE/Gold of the DSSC/CE/Sensing by co-electropolymerizing a solution containing EDOT (0.01 mol/L) and Py (0.002 mol/L), and also 2 µg/mL CEA, prepared in PBS (pH 7.4), by applying 10 successive cycles from -0.3 to 0.95 V, with a scan-rate of 50 mV/s. This was done in a 3-electrodes system, yielding an electrode that was assigned as WE/Gold/MIP-CEA. After this, CEA was removed by incubating the WE/Gold in a solution of Proteinase k (500 µg/mL) overnight (WE/Gold/MIP).

7.2.4.2. Rebinding assay on the Biosensing film

The rebinding of CEA was made by incubating standard solutions in the WE/Gold/MIP area for a given period. Calibrations started by incubating the CEA standard solution of lower concentration in the sensory surface of the electrode, for 20 minutes, followed by a washing step with buffer. CEA concentrations ranged from 0.1 ng/mL to 100 µg/mL, prepared in PB, pH 7.00.

7.2.4.3. Electrochromic cell assembly

The EM was a PEDOT-based film, produced by electropolymerization on the WE/ITO. CV was used for this purpose, applying a 2 scan in the potential range of 0.0 to 1.0 V, at a scan

rate of 0.50 V/s. The polymerization occurred in the presence of 2.50×10^{-4} M SNS-NH₂ and 0.10 mol/L EDOT, dissolved in electrolyte containing ACN as solvent and 0.10 M LiClO₄/0.10 mol/L NaClO₄. SNS-NH₂ synthesis was made as described in [269], which consisted of an adaptation of the procedure made by [242].

The EC was set-up by covering the area of the WE/ITO and its respective AE with KCl electrolyte of 0.10 mol/L concentration. It was still interfaced in WE/Gold, after placing pathway silver ink between both electrodes (WE/Gold and WE/ITO).

7.2.5. Electrochemical assays

The electroactive area of the WE/Gold was calculated by means of equation 4 in section 2.3.2. For this purpose, a 90 μ l volume of sample of the redox probe was placed on top of the electrode surface, covering the three electrodes (WE, CE and RE). CV experiments were conducted in a 5.00×10^{-3} mol/L [Fe(CN)₆]^{3-/4-} solution prepared in the electrolyte KCl. The potential was scanned from -0.40 to 0.50 V, at several scan-rates (0.20, 0.15, 0.10, 0.050 and 0.025 V/s), and for 20 crossing points (10 successive cycles).

The assembly of the biosensor on the WE/Gold was also followed by CV measurements in the same redox probe, but was prepared in a different medium, composed of PB with a pH of 7.00. CV assays were scanned in the same potential range, from -0.40 to 0.50 V, at a fixed scan rate of 0.05 V/s, along 2 successive CV cycles.

The performance of the hybrid DSSC was monitored by determining V_{OC} , J_{SC} , P_{max} , FF and η , from the data obtained by the J - V plot using a PV measurement system. The EIS data was collected in a frequency range of 0.1-100 kHz. The biosensor performance and rebinding stage of CEA on the DSSC/CE/biosensing were also evaluated by PV parameters. Herein, two different approaches of the hybrid DSSC configuration were considered to evaluate these stages: the biosensor on the WE/Gold was directly connected to the DSSC/CE (DSSC/CE-WE) and an electrolyte was used as pathway to ensure the current flow between the biosensor on the WE/Gold and its respective AE that was connected to the DSSC/CE (DSSC/CE-AE). This last one involved a KCl electrolyte (3.00 mol/L).

The electrochromic features of the EM were evaluated in the same electrolyte used for its synthesis, in which a potential was applied under potentiostatic control, from -0.30 V to 0.60 V, using a 3-electrode system (WE/ITO, AE and RE).

7.3. Results and Discussion

7.3.1. Cr/Au films characterization

The Cr film deposited on the glass substrate had 15 nm thickness. Afterwards, an Au film was deposited on this Cr layer, showing a final thickness of 120 nm (**Figure 7.3-B**). The configuration of the DSSC/CE/Sensing was concluded by the deposition of the ITO film. For this purpose, it was necessary to align the mask B demonstrated in **Figure 7.2-B** with the Au connections (**Figure 7.3-A**), in order to introduce the ITO material only on the specified areas of the glass, without connecting with the other electrical connections. The thickness of the ITO film was 140 nm.

The average resistivity of the Cr/Au and the ITO films was 3.95×10^{-8} and 3.647×10^{-6} $\Omega \cdot m$, respectively, as obtained by the Van der Pauw method. In general, these values were higher than those expected in the literature. The average resistivity listed for Au, at 20°C, is 2.44×10^{-8} $\Omega \cdot m$ [278], but this corresponds to pure Au and the material prepared herein corresponds to a thin Au layer on a Cr support. Regarding the ITO film, the resistivity obtained was enough to assemble in-situ the EM, as shown in section 7.3.4, while the necessary transparency features were ensured. In general, the electrical features of these materials met the necessary targets.

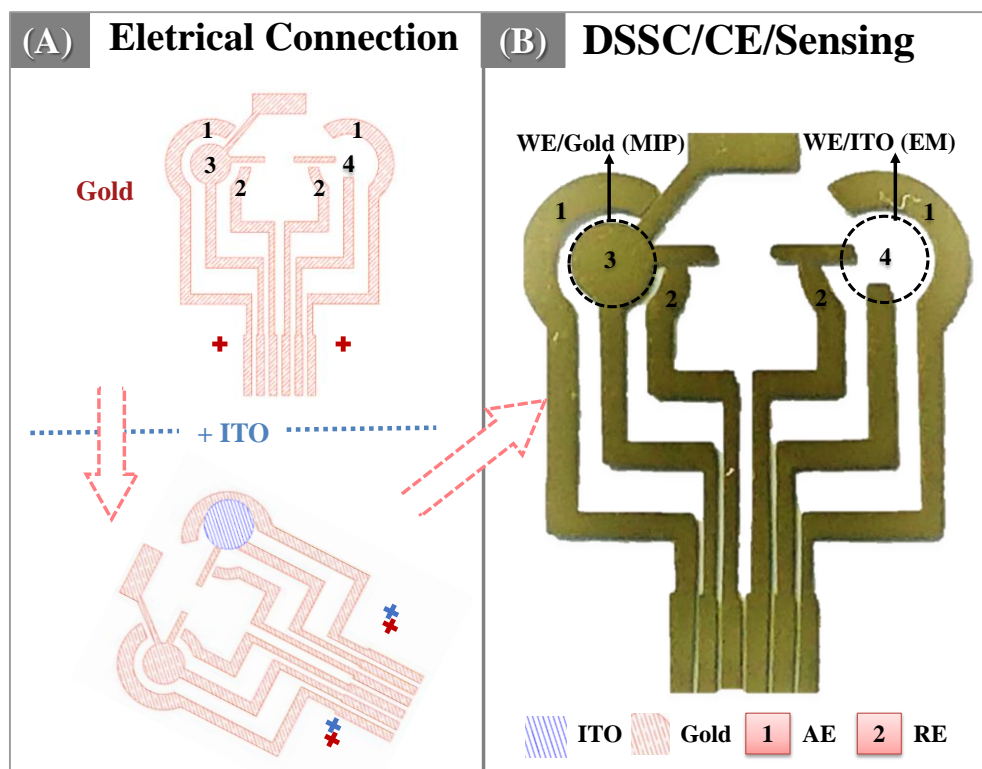


Figure 7.3 - Schematic representation of the design of the sensing system for the deposition process of (A) Au and ITO materials on DSSC/CE, and a (B) picture of the system after deposition on the back-side of DSSC/CE, indicating the location for MIP and EM deposition.

7.3.2. Analytical performance of the WE/Gold

7.3.2.1. Electrochemical study

The DSSC/CE/Sensing material for the biosensor assembly was inspired on the typical design of an SPE, using 3-electrode systems. All electrodes were made in gold, which is not common in the case of the RE [279]. As measurements of each step of construction and analytical performance of MIP are evaluated by electrochemical technique, this new system produced herein needs to be characterized electrochemically. Overall, the evaluation of these data allowed understanding the chemical phenomena involved in the WE-Gold interface [121].

The electrochemical study used several potential scan rates with a negatively charged redox couple, $[\text{Fe}(\text{CN})_6]^{3-/4-}$ with a concentration of 5.00×10^{-3} mol/L. It was possible to observe that an increment of the scan rate increased the I_p of the redox peaks (**Figure 7.4**). The I_{pa} ranged from 192.5 μA to 399.7 μA , while the I_{pc} ranged from 188.5 to 348.0 μA . The same behaviour

was observed in the E_{pa} and the E_{pc} , in which the values of both peaks increased with increasing ν . The E_{pa} increased from 40.28 mV to 110.78 mV and E_{pc} ranged between 55.39 mV and 140.90 mV. These variations of E_{pa} and E_{pc} with different ν caused the shift of ΔE_p , presenting values between 95.67 mV and 251.68 mV. Moreover, the ratio of I_{pa} and I_{pc} is near 1 (1.09 ± 0.05) in different ν . These results indicated that the system was quasi-reversible, considering that the ΔE_p for reversible processes should be constant with the ν variation [121, 122].

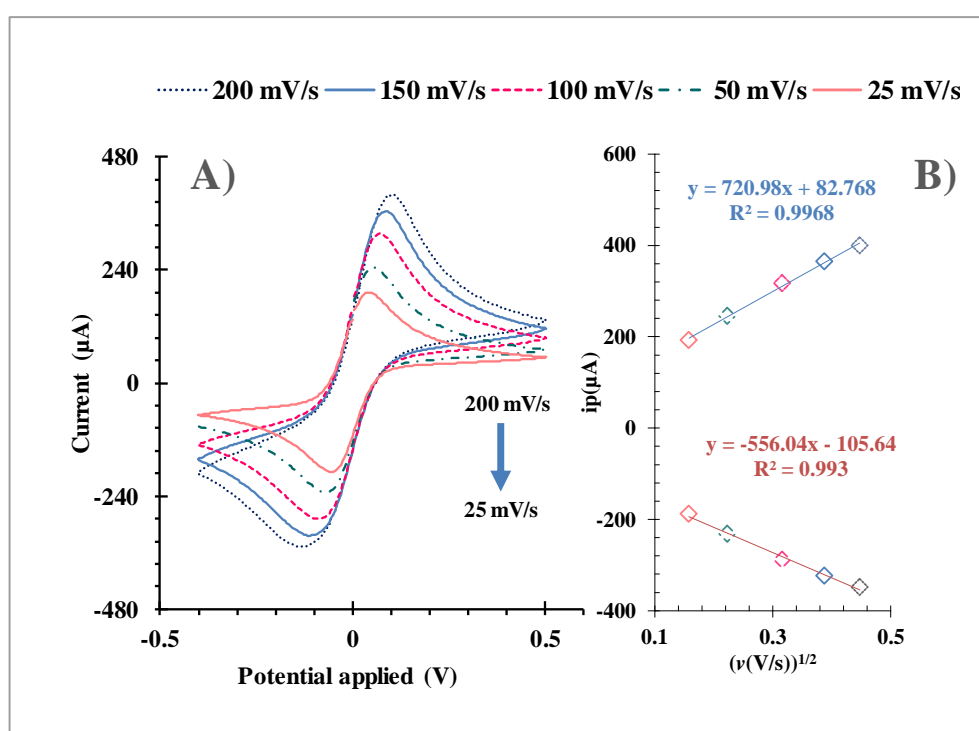


Figure 7.4 - A) Cyclic voltammogram of 3-electrode system with WE/Gold recorded of a solution of 5.00 mmol/L $[\text{Fe}(\text{CN})_6]^{3-/4-}$ prepared in an aqueous solution of KCl, at different scan rates, and **B)** the corresponding plots of the anodic/cathodic peak currents against the square root of the scan-rate.

According to the *Randles-Sevcik* equation (**equation 3**), there was a linear behaviour between the peak current and the square root of the scan rate for the studied redox species. Anodic peaks presented a slope of $721.0 \mu\text{A}/(\text{V/s})^{1/2}$ and cathodic peaks a slope of $-556.0 \mu\text{A}/(\text{V/s})^{1/2}$, both with correlation coefficient >0.99 . These results demonstrated that

the electrochemical processes had a reaction controlled by the diffusion of the electroactive species at the solution/electrode interface [121].

The *Randles–Sevcik* equation was also employed to calculate the active area of the WE in the oxidation/reduction reactions of the redox probe. The active area in this electrode was 88.1 mm², meaning that the electron transfer rate occurred in a total area of 88.1 mm² of the electrode surface. According to the literature [280, 281], the ratio between active and geometric surface areas is known as the roughness factor. In this electrochemical study, the active area of the WE/Gold is much larger than the geometric area, which is 12.6 mm². These results showed that the WE/Gold presented many active sites for electrochemical reaction at the electrode surface. Furthermore, the roughness factor was 7.0, which constitutes a strong evidence that the WE/Gold had a rough surface.

Overall, the Au electrodes showed a good electrochemical behaviour, demonstrating high ability to catalyse the oxidation or reduction of the redox probe, as reflected in CV assays of the previous study.

7.3.2.2. Modifying the WE/Gold

The assembly of the biosensor film was made on the gold surface of the WE by MI, which consisted in the electropolymerization of the EDOT and Py in the presence of the target analyte, CEA. The presence of the MIP-CEA film on the gold surface was suggested by a significant decrease of the I_{pa} and I_{pc} (**Figure 7.5**), resulting in the completely disappearance of the faradaic currents in the defined range of potential. It is likely that the polymeric film limited the charge transfer across the solution/electrode interface [120, 121].

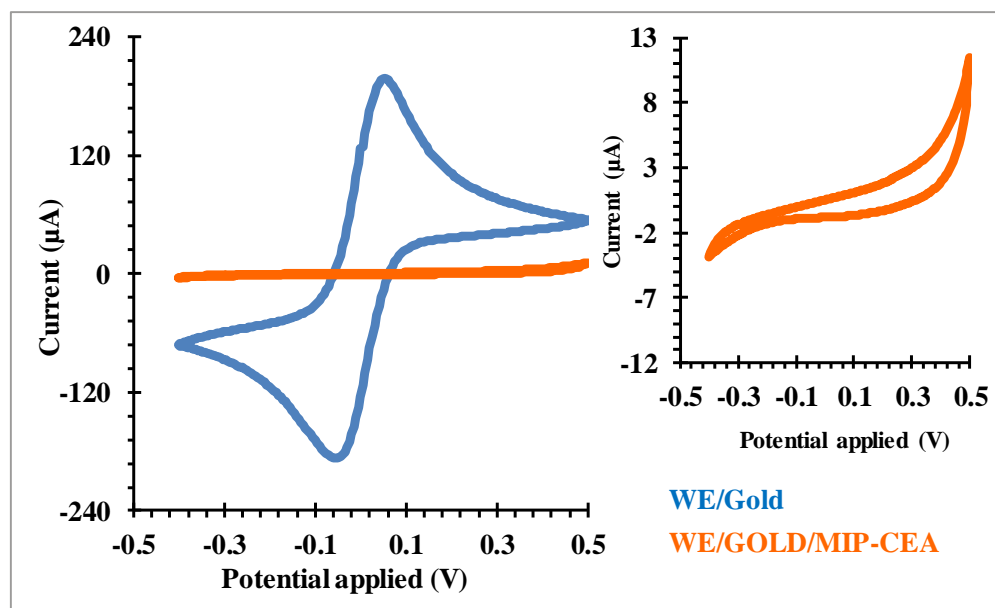


Figure 7.5 - Cyclic voltammogram data of the different steps involved in the assembly of MIP-CEA, using the 3-electrode system with a WE of Gold. Data corresponding to 5.00 mmol/L [Fe(CN)₆]^{3-/4-} readings in PB buffer, pH=7.00

In general, the polymerization in presence of CEA was successfully obtained on WE/Gold, which means that the selected monomers were oxidized onto electrode during anodic potential. The removal of the imprinted template was later evaluated by PV parameters.

7.3.2.3. Raman spectroscopy analysis

To be sure that the polymerization stage of WE/Gold modification was effective, the MIP film assembly was analysed by Raman spectroscopy (**Figure 7.6**). The presence of MIP based on PEDOT/PPY was clearly evidenced by the strongest Raman intensity peak, centred at 1442.8 cm⁻¹, probably assigned to the C_α=C_β (-O) symmetric stretching vibration from PEDOT [247, 248]. Others typical peaks of PEDOT were also found when compared to the WE/Gold surface: 991.1, 1367.5, and 1506.5 cm⁻¹, assigning the oxyethylene ring deformation, C_β-C_β stretching and asymmetric C=C stretching of the polymeric network, respectively [228].

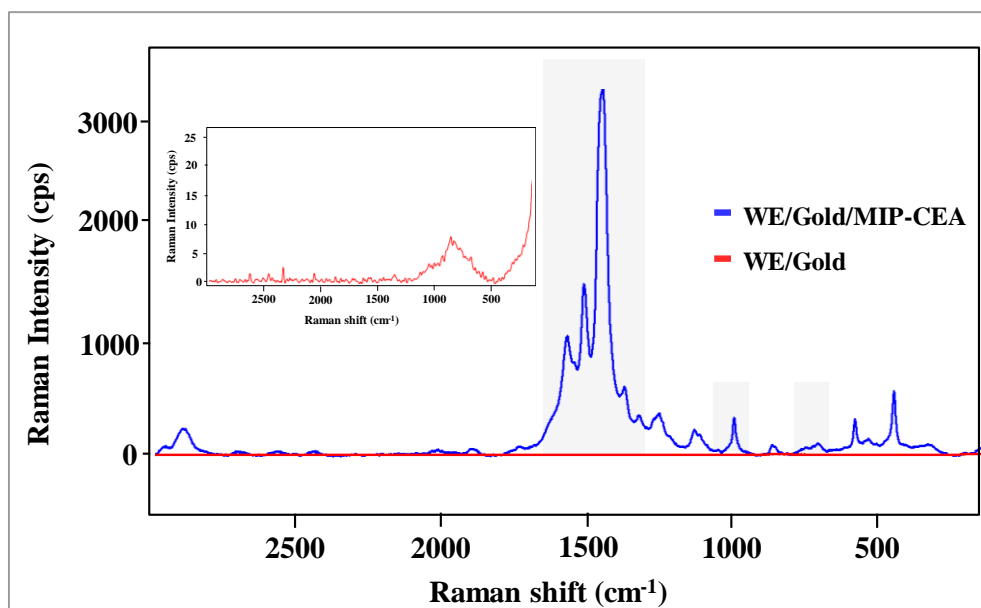


Figure 7. 6 - Raman spectra of the different materials followed along the assembly of the biosensing

The peaks at 703.8 cm^{-1} (symmetric Py), 1317.9 cm^{-1} (C-C, ring stretching vibration) and 1563.4 cm^{-1} (C=C in-ring of C-C inter-ring stretching vibrations) appear after WE/Gold modification with MIP, thereby confirming the presence of PPy [249-251]. As the concentration of Py monomer was 5 times less than EDOT in polymerizing solution, probably the peaks associated to PPy in the WE/Gold/MIP film were less evident when compared to those of PEDOT. As opposed to MIP surface, the peaks of WE/Gold obtained showed lower Raman intensity and appeared within a band at 600 and 1100 cm^{-1} . Overall, the Raman spectra confirmed that the polymeric network of PEDOT/PPy was successfully assembled on top of the WE/Gold by electrochemical technique.

7.3.3. Characterization of the WE/ITO electrode

The EC was also designed as a planar structure with a 3-electrode configuration to produce EM on a WE made of ITO. Therefore, the transmittance of the ITO film was an important optical parameter to evaluate herein, in order to maximize contrast of the EM during colour switch. Transmittance measurements of the ITO electrode film were performed by spectrophotometry. The results obtained are shown in **Figure 7.7** and demonstrated that the

transmittance values of the ITO film were higher than about 80% in the visible region of the electromagnetic spectrum.

Despite its good transparency, the ITO WE had a heterogeneous conductive film. This heterogeneity was perceptible after growing the EM film on the ITO support, in which it was possible to observe different colour intensities within the same electrode. Thus, it is possible to conclude that this parameter was important because a bad perception of colours can lead a false interpretation of diagnosis result.

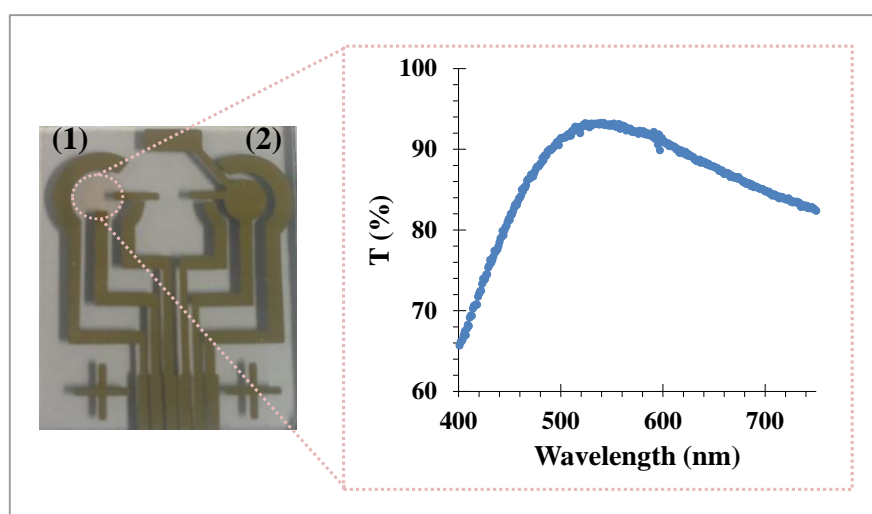


Figure 7.7 – Picture (left) picture of 3 electrode system for EM (1) and MIP (2) deposition on the back-side of DSSC/CE and visible spectra (right) of the ITO film in glass.

7.3.4. Electrochromic features of the EM

PEDOT contains typical electrochromic features, changing colours through a potential range variation. Yet, it is important to enhance colour diversity and optical contrast features PEDOT alone, in order to improve the optical signalling element of the hybrid sensing device. To this end, SNS-NH₂ was added into it, following the work developed by Rukiye Ayranc et al.[242].

The pictures obtained after deposition of the EM combining EDOT and SNS-NH₂ on the WE/ITO are shown in **Figure 7.8**. Overall, the images obtained revealed the transparency of the film due to the intensive colour produced by the material. Different coloured states were obtained by the application of a potential from -0.30 to 0.60 V, using

potentiostatic/galvanostatic equipment with the same electrolyte of its synthesis. The results demonstrated a great colour gradient, presenting a colour change from purple to blue, when the applied potential is few volts between each colour change. Thus, the EM exhibited a good colour variation and also allowed distinguishing the colour changes associated with each potential.

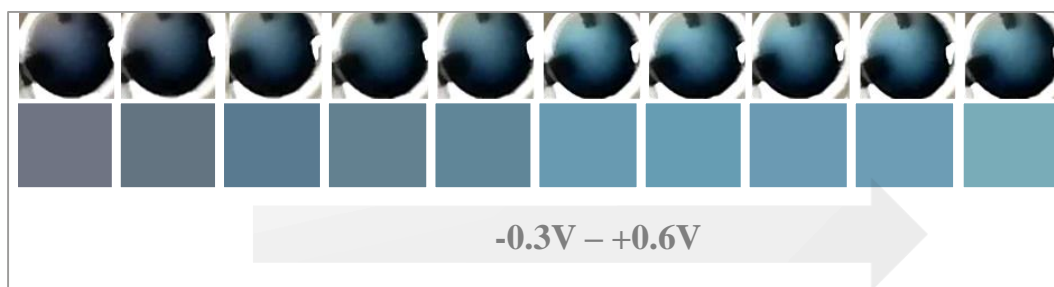


Figure 7.8 - Performance of the EM in electrochemical system with 3-electrode system.

7.3.5. Assembly of hybrid DSSC

A typical DSSC combines CE and photoanode, in electrical contact through a liquid redox electrolyte solution. The photoanode contains a semiconductor based on TiO_2 and a sensitizer dye adsorbed into it. The dye absorbs sun light and the excited electrons are injected into the conduction band of TiO_2 . The CE received electrons arriving from the photoanode through the external circuit and used these to reduce the electrolyte, which in turn would give these back to the dye, regenerating it. In previous chapters a hybrid DSSC was presented, which used a CE modified with biosensor that acted as the CE of a conventional DSSC. The analytical behavior of this hybrid DSSC was followed by calibrating the same biosensing CE with CEA standard solution, which required opening, cleaning and closing it for each subsequent incubation. As nano/microfabrication could combine several areas, it was critical to use this tool to create a biosensing system on the backside of DSSC/CE to simplify the rebinding process (**Figure 7.9**).

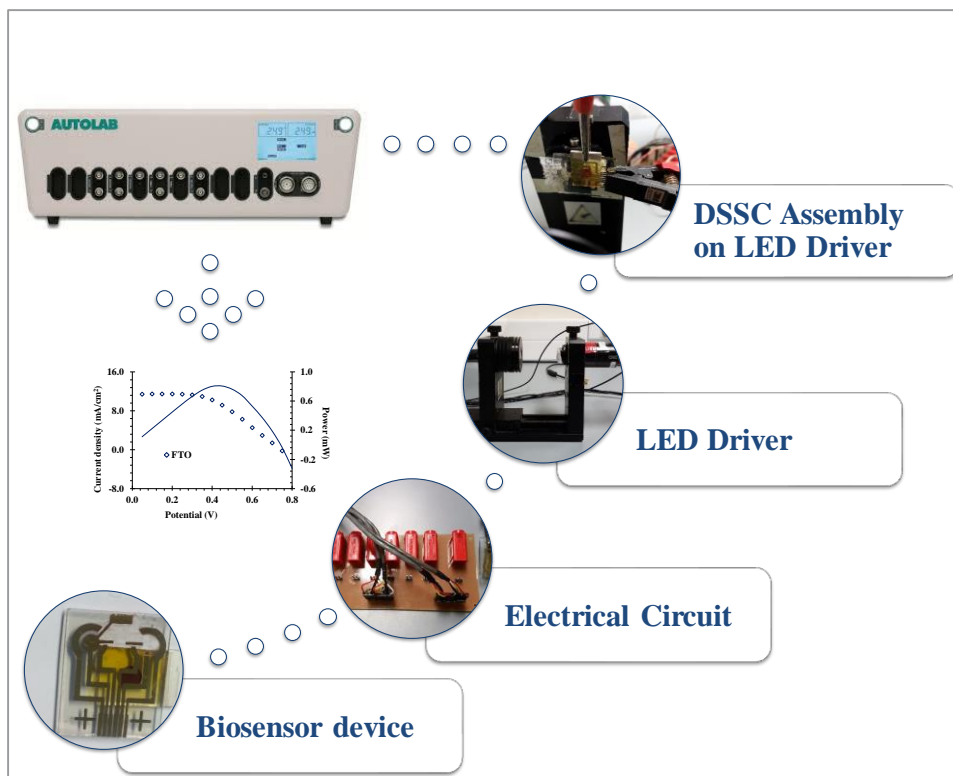


Figure 7.9 - Biosensing device integrated outside of DSSC produced by nano/microfabrication techniques, using PV measurement system. The resulting signal (J - V and power conversion efficiency characteristic curves) is obtained from potentiostatic.

7.3.5.1. Counter electrode

Two glass supports coated with different commercial TCO films were prepared and compared herein: ITO/CE and FTO/CE. These were both employed to prepare DSSC/CE modified with Pt, acting as catalytic material. This was obtained by spin coating deposition, followed by reduction of the Pt salt at high temperature to obtain the metal support.

First, the electrochemical performance was monitored for a DSSC prepared with ITO/CE, by means of J - V studies. **Figure 7.10-A** shows J - V and PCE characteristic curves so obtained, which allowed calculating the corresponding photovoltaic performance data (J_{sc} , V_{oc} , FF and η). This data was summarized in **table 7.1**, evidencing η values less than 1%. Such results were probably related to the heating stage of the Pt synthesis. According to the literature [282], the resistance of the ITO may increase when exposed to high temperature, 300 °C or higher, by more than three times. To check this possibility, the ITO glass resistance was monitored before

and after heat treatment. The measurements showed that the ITO resistance of a bare ITO glass shifted from 100-200 Ω to more than 1 k Ω after thermal treatment. This was solved next by replacing ITO by FTO due to its greater thermal stability.

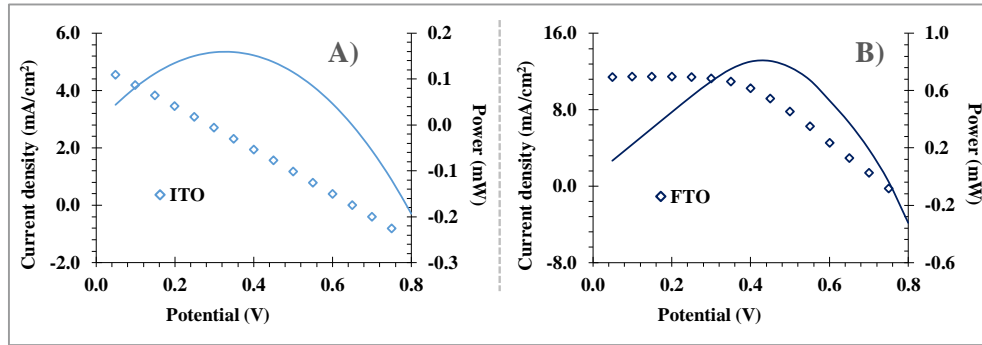


Figure 7. 10 - Photocurrent density-photovoltage (J - V) and power conversion efficiency characteristic curves of the DSSC with **A)** ITO glass and **B)** FTO glass on cathode.

When compared to an ITO based cell, the η values of a DSSC assembled with an FTO CE shifted from 0.811% to 4.124%. Moreover, all other photovoltaic parameters also improved when compared to the ITO-based DSSC. The V_{OC} shifted from 649.7 to 692.8 mV; J_{SC} increased from 4.90 to 11.44 mA/cm²; FF increased from 22.5 to 52.1%; and P_{max} from 0.159 to 0.808 mW. It is possible that the PV parameters values have not been better in this DSSC, due to the length of the electric cables that connect the electric circuit to the solar cell. The electrical resistance is defined according to equation 15 [283],

$$R = \rho \times \frac{L}{A} \quad \text{equation (15)}$$

where R is the resistance of the conductor, L is the conductor's length, A is the area of its cross section, and ρ is the resistivity.

Table 7.1 - Photovoltaic-parameters of DSSCs based on different CEs.

CE	V_{oc} (mV)	J_{sc} (mA/cm ²)	FF (%)	P_{max} (mW)	η
ITO	649.7	4.895	22.5	0.159	0.811
FTO	692.8	11.44	52.1	0.808	4.124

Overall, the DSSC assembled with an FTO-based CE showed better PV parameters than that with an ITO CE, due to the better conductivity and stability of the material after Pt deposition onto it. Thereby, the FTO/CE was selected in subsequent studies.

7.3.5.2. *Biosensing film production on DSSC/CE*

The impact of the imprinted film assembled on the backside of the DSSC/CE was also monitored by evaluating the PV parameters of the DSSC, including in the template removal stage. These studies were made without the biosensor being connected to the WE/ITO, in order to validate only its influence in the hybrid DSSC. Yet, as the biosensor would be further integrated in the DSSC circuitry, it was important to understand its sensitivity and LOD in this hybrid set-up. Thus, the main electrical features of the biosensing film on the DSSC/CE were tested in two different ways: with or without electrolyte on surface of WE/Gold. For this purpose, one of these used a pathway created by Au material to allow current flowing from the WE/Gold to the DSSC/CE (DSSC/CE-WE) (**Figure 7.11-A**), while the other used an electrolyte covering WE and AE (DSSC/CE-AE) (**Figure 7.11-B**) during biosensor reading.

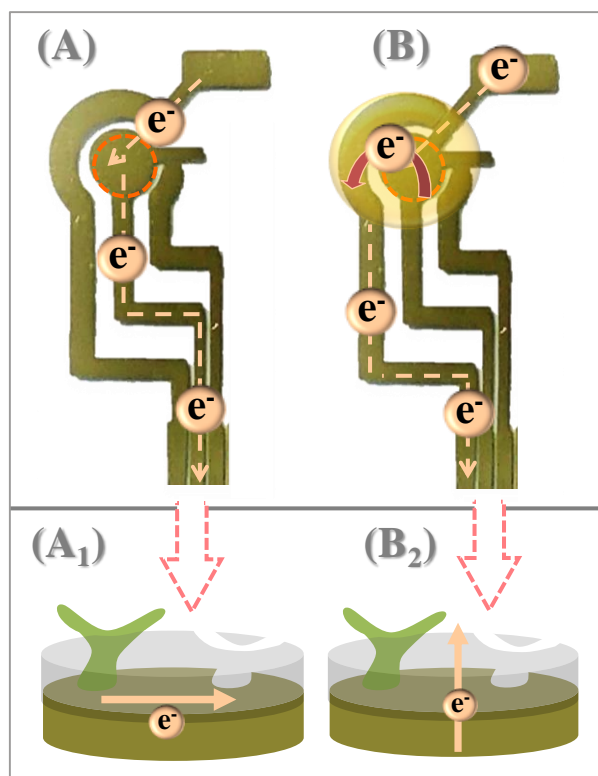


Figure 7.11 - Schematic representation **A**) DSSC/CE-WE, which the current flow across WE/Gold surface or **B**) DSSC/CE-AE, using an electrolyte as interfacial region between WE/Gold and AE. Current flow on Biosensor without **A**₁) or with **B**₂ electrolyte.

The biosensor assembly was evaluated first by direct reading without electrolyte on the WE/Gold area, in order to understand its impact upon the DSSC operation. For this purpose, the J - V curves were followed (**Figure 7.12-A**) and the corresponding parameters (V_{oc} , FF , J_{sc} and η) extracted (**table 7.2**). The main features of the hybrid DSSC operating with WE/Gold showed a η of 9.08%, a J - V of 22.00 mA/cm², FF of 54.30% and P_{max} value of 1.64 mW. This was already expected, because the length of the pathway presented between the WE/Gold and the DSSC/CE was much smaller than in the conventional set-up, and consequently the hybrid DSSC was able to generate more power and current, increasing its efficiency.

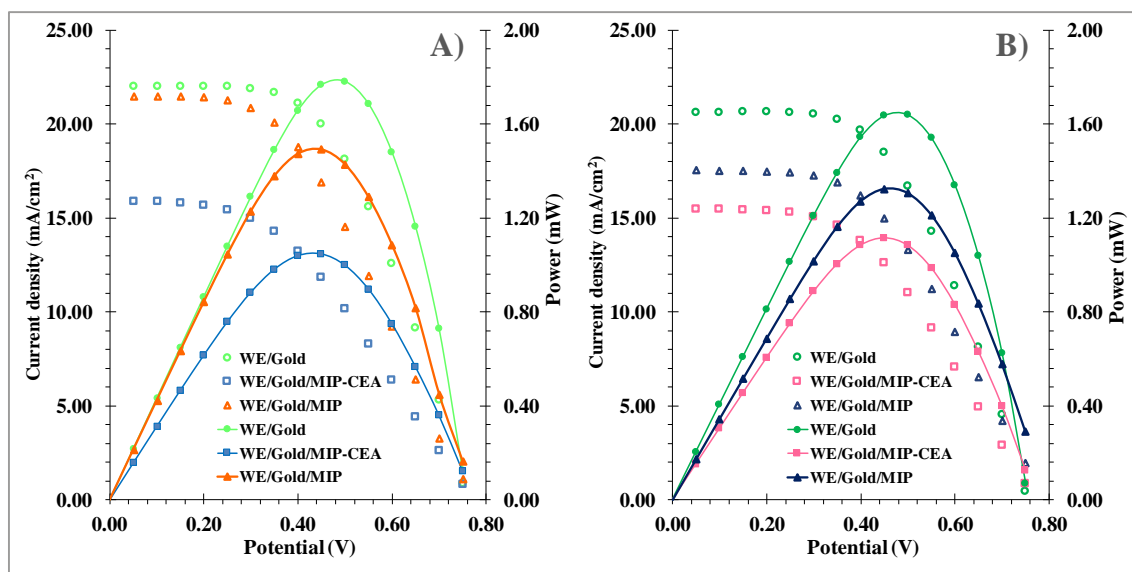


Figure 7.12 - J - V and power conversion efficiency characteristic curves of hybrid DSSC assembled: WE/Gold; WE/Gold/MIP-CEA and WE/Gold/MIP using Biosensor reading: **A)** without or **B)** with electrolyte of 3.00 mol/L KCl on its surface.

The assembly of the imprinted material on top of WE/Gold, including the CEA protein within the polymeric network, was responsible for 41 % decrease in the overall efficiency of the hybrid DSSC down to 5.36 % η . The other PV parameters, J_{sc} , FF and P_{max} also decreased to 15.92, 43.70 and 1.05, respectively. On the other hand, the V_{oc} had an increase to 773.80 mV after polymerization step. After protein removal (WE/Gold/MIP), the efficiency increased to 7.63 %, meaning that the removal process was efficient for partially recovering the efficiency of the cell.

Table 7.2 - Photovoltaic-data obtained with the hybrid DSSC, at the different states of biosensing film assembly on DSSC/CE/biosensing, obtained with reading of DSSC/CE-WE.

DSSC/CE/biosensing	V_{oc} (mV)	J_{sc} (mA/cm ²)	FF (%)	P_{max} (mW)	η (%)
WE/Gold	760.50 ±0.001	22.00 ±0.33	54.30 ±0.02	1.78 ±0.06	9.08±0.30
WE/Gold/MIP-CEA	773.80±0.01	15.92±0.48	43.70±0.06	1.05±0.10	5.36±0.49

WE/Gold/MIP	771.70 ±0.01	21.48±0.49	46.10 ±0.03	1.50 ±0.1	7.63±0.49
-------------	--------------	------------	-------------	-----------	-----------

The use of the electrolyte in the readings of the hybrid DSSC/CE/Biosensing (**Figure 7.12-B**), made in each stage of biosensor production, yielded a similar behaviour when compared to the biosensor reading directly on DSSC/CE-WE. However, the efficiency of hybrid DSSC was lower than the readings made without electrolyte, showing 8.36 % η . Consequently, other PV parameters also decreased in the presence of electrolyte, presenting 756.00 mV $J-V$, 20.62 mA/cm² V_{OC} , 53.6 % FF and 1.64 mW P_{max} . The addition of MIP-CEA on WE/Gold surface, promoted 32 % decrease in η , 25% decrease in $J-V$, 11% decrease in FF and 32% in P_{max} . As expected, the protein removal from the polymeric network promoted the opposite effect, increasing η from 5.68 to 6.74 %. Thus, it seemed that presence of electrolyte on DSSC/CE/Biosensing promoted an additional resistance to the electrical flow within the hybrid DSSC system.

Table 7.3 - Photovoltaic-data obtained with the hybrid DSSC, at the different states of biosensing film assembly on DSSC/CE/biosensing, obtained with reading of DSSC/CE-AE.

DSSC/CE/biosensing	V_{oc} (mV)	J_{sc} (mA/cm ²)	FF (%)	P_{max} (mW/cm ²)	η (%)
WE/Gold	756.00 ±0.010	20.62 ±0.58	53.60 ±0.01	1.64 ±0.03	8.36±0.13
WE/Gold/MIP-CEA	770.99±0.004	15.52±0.22	47.50±0.01	1.15±0.01	5.68±0.04
WE/Gold/MIP	794.70 ±0.01	15.56±0.11	48.30 ±0.02	1.32 ±0.0.04	6.74±0.19

The EIS assay was also involved in the impact of the electrolyte upon the biosensor and results obtained are shown in **Figure 7.13**. A variation in the R_s values was evidenced upon the addition of electrolyte to the DSSC/CE/Biosensing, which corresponded to an increment of 36% when compared to the reading of Biosensor without electrolyte on WE/Gold. This may be explained by the presence of interfacial region (electrolyte) over which the electron transfer occurs. As electrolyte is located between the photoanode and the CE, and its

resistivity can affect the current flow within the DSSC. Afterwards, the EIS data in **Figure 13** showed an increase of the R_{ct1} from 13.0 to 17.7 Ω . The other R_{ct} kept similar ($\sim 10 \Omega$) their when the electrolyte was introduced on the WE/Gold. This could mean that the rate of electron transfer produced in backside of DSSC/CE/Biosensing did not interfere with the remaining components of the DSSC. Thereby, it was clear that the presence of electrolyte affected the performance of hybrid DSSC, and it could also influence the sensitivity and LOD of the device.

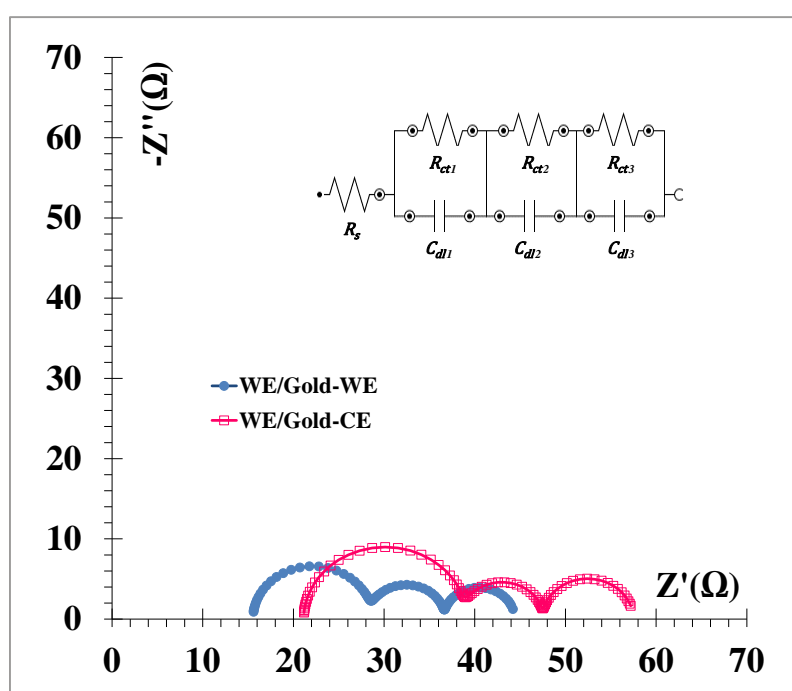


Figure 7. 13 - EIS data of hybrid DSSC using WE/Gold reading: **(Blue colour)** without or **(Pink colour)** with electrolyte of 3.00 mol/L KCl on its surface.

7.3.5.3. CEA rebinding features of hybrid DSSC

The analytical behaviour of this biosensor assembled outside hybrid DSSC was followed by calibrating the system with CEA standard solutions of increasing concentration. The WE/Gold/MIP was incubated in each standard solution (20 min each) to evaluate its response in terms of the PV parameters generated by the hybrid DSSC. Calibration curves were recorded for the biosensor with either WE/Gold-WE or WE/Gold-CE reading approaches. These

calibrations curves plotted η (in $J-V$) against CEA concentration (in \log [CEA, ng/mL]), ranging from 0.1 to 100 ng/mL.

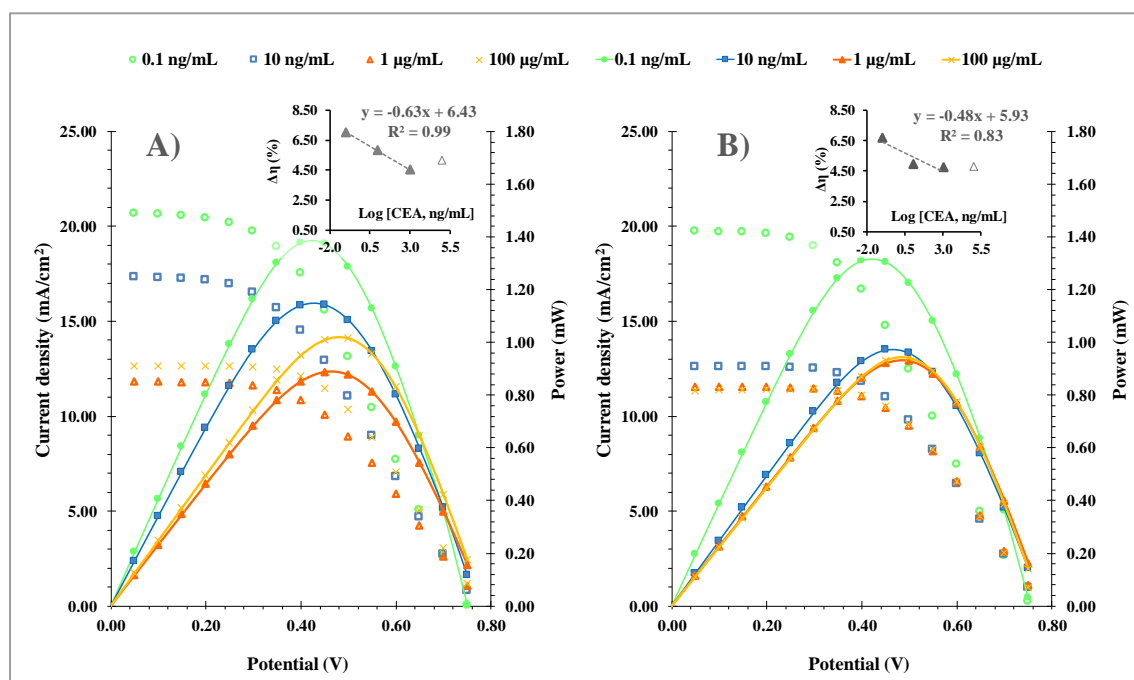


Figure 7.14 – $J-V$ and power conversion efficiency characteristic curves of hybrid DSSC with corresponding calibration curves (inset, as relative η . Versus \log [CEA]) of the WE/Gold/MIP on hybrid DSSC, after incubation of increasing concentrations of CEA standard solutions, prepared in PB buffer. Biosensor reading: **A)** without or **B)** with electrolyte of 3.00 mol/L KCl on its surface.

Overall, successive incubations of the CEA on Biosensor caused a decrease in $J-V$ and power conversion efficiency of hybrid DSSC, as demonstrated in **Figure 7.14**. This could be explained by the presence of CEA selectively adsorbed onto the WE/Gold/MIP.

The typical $J-V$ obtained without electrolyte is shown in **Figure 7.14-A**. It displayed a linear response between 0.10 ng/mL and 1.0 μ g/mL, with an anionic slope of 0.63 % per decade CEA concentration, presenting a square correlation coefficient > 0.99 . The overall J_{SC} , FF and P_{max} values decreased with increasing CEA concentrations, and the V_{OC} was the single PV parameter that increased.

The hybrid DSSC using electrolyte showed an overall similar behaviour. The results so obtained are shown in **Figure 7.14-B** and evidenced however a worst squared correlation

coefficient (0.83) than the MIP on WE/Gold-WE with increasing CEA concentration for the same concentration range.

In general, the results obtained without electrolyte supported that the reading mechanism of CEA in the hybrid-MIP device was successfully obtained. Moreover, the CEA response concentration range of the biosensor integrated on backside of DSSC/CE is lying within the concentrations of clinical interest.

7.4. Conclusions

Overall, the presented work describes the integration of electrical connections designed outside the DSSC and dedicated to the fabrication of an electrical reading box for a cancer biomarker biosensor. In detail, the Au sensor displayed suitable electrochemical features, when compared to the theoretical values.

ITO sensors showed reasonable transmittance values, but lacked homogeneity in WE-ITO. This heterogeneity in ITO surface was visible after deposition of EM. Despite this, EM presented a good colour change on electrode. The DSSC connected to the electrical system created by Au and ITO electrodes operated with acceptable values for photovoltaic parameters, presenting a performance with efficiency around 4%.

Thus, a proof of concept device was successfully obtained by assembling a DSSC with electrical connections behind the CE. Moreover, the biosensor integrated on the backside of the DSSC showed promising results, which CEA response concentration range of the MIP is lying within the concentrations of clinical interest (2.5 ng/mL and 10 ng/mL). It was also demonstrated that the connection of the biosensor to the DSSC can be done by directly reading (DSSC-CE-WE) along its performance, so, without the use of an electrolyte between its surface and AE, making the device operation simpler. An advantage of this hybrid DSSC developed herein is to allow incubating the CEA standard solutions or samples in the biosensing film without opening cell, unlike to hybrid DSSCs described in previous chapters.

The future perspectives for the integration of this biosensor to EC systems outside the DSSC are marvellous. It is expected that the performance of the biosensor depends on the concentration of the protein and its presence opposes the electrical current flow, leading to different colours in the EM. It is still intended to evaluate the colour of the EM by spectroscopy, to complement the optical detection from the presence of protein.

8. Conclusion and Future Work

8.1. Conclusions

This work reported new approaches for biosensing materials and platforms, to be applied as non-invasive methods for the early diagnosis and monitoring colorectal and ovarian cancer diseases at clinical context. In general, new artificial receptors for cancer biomarker were tested and showed to be capable of monitoring the target analyte with good sensitivity, selectivity and response at low concentration, using an electrochemical transducer. Nanomaterials were inserted on top of transducer to increase sensitivity and limit of detection of biosensor based on MIP. Biosensor was also introduced successfully into a DSSC combined with electrochromic cell working as autonomous device.

Biosensors developed in herein, demonstrated that biorecognition element based on MIP materials with polymers that are also used in PV yielded sensing device with appropriate responses to the monitoring of a given target biomolecule, mainly regarding to sensitivity and linear range of action being suitable for application in POC. Regarding the transduction, it seems that EIS and SWV are suitable electrochemical approaches. A low detection limits were achieved with these electrochemical techniques, presenting LOD below to normal physiologic level referenced for the detection of cancer biomarkers. In some conditions, EIS may lead to a better stability of the biosensor, because conductive polymers as PEDOT and PPy presented an unstable electrochemical behaviour when submitted to a wide range of potentials.

The first biosensor developed mainly focused on MIP material assembled on supports as paper using carbon material on transducers, which bring some advantages as simple production and low cost, as well as good physical and chemical stability in the detection of potential cancer biomarkers (as CRT). PEDOT widely used as catalytic material in DSSC, herein it also demonstrated to be a good artificial receptor for biomolecule screening applications in

POC. This biosensor with electrochemical transducer demonstrated a good sensitivity and selectivity for rebinding CRT. Moreover, the low LOD obtained allows its practical application to the analysis of biological fluids.

An increment in the sensitivity of the biosensor was achieved by introducing materials on the transducer that display excellent electrical properties. Comparing the use of biosensor with carbon material or conductive polymer, PEDOT, even for model protein as BSA, it seemed evident that the highly conductive supports seemed the most suitable arrangement.

The Integration of the biosensor inside the DSSC, as an electrical reading box, on one hand, resolved some limitations, such as, the dependency of an electric power source, and, on the other hand, makes a biosensor accessible anywhere in the world. For this purpose, the MIP was assembled on the CE of DSSC, containing PEDOT as catalytic material. Then, this hybrid DSSC is coupled to the electrochromic cell and the analytical response is evaluated by the observation of its colour in presence/absence of the cancer's biomarker. The CEA was template selected as cancer biomarker for producing MIP. Once again, synthetic receptors showed good affinity for cancer biomarker (CEA), which are capable of resisting to extremer conditions such as pressure and organic solvents. The determining factor for this success was the usage of the same materials already employed in DSSCs to assemble the biomimetic materials. Implementing the electrochromic cell in this biosensing device allowed giving the biosensor a complete autonomy, in which the analytical response was improved after introducing plasmonic materials in the photoanode of the DSSC. Overall, a gradient of colour change was visually perceptible for increasing CEA concentrations in electrochromic cell. Moreover, the observed gradient allowed the possibility of obtaining semi-quantitative data by simple visual inspection against a given standard colour palette.

A new strategy was proposed to simplify the configuration of hybrid devices and the handling of the biosensor in screening applications in POC. Thus, techniques of micro and nanofabrication were used to deposit electrical connections of Au material on the backside of the CE. The final geometry was inspired by the screen printed electrode with 3 electrode systems, combining WE, AE and RE. The electrochemical sensors were previously electrochemically characterized, before the production of the MIP on the WE/Gold surface. Au electrodes showed a good analytical performance, presenting acceptable results for

parameters related to electrochemistry. Comparing the overall output of the cell with different MIP materials, assembled on CE of DSSC (chapter 5 and chapter 6), PEDOT/PPy had a better analytical performance than the one obtained with a CE having only PPy. For this reason MIP based on PEDOT/PPy was selected to detect cancer biomarkers, CEA in this new approach. PV performance along with the CEA rebinding process demonstrated that the biosensors integrated on the back-side of DSSC are promising devices for CEA detection. The CEA response concentration range of the MIP was lying within the concentrations of clinical interest (2.5 ng/mL and 10 ng/mL). Additionally, the procedures involved in sample incubation were simplified by this new strategy.

Summing up, this work introduced new approaches to create biosensing devices for cancer biomarkers everywhere, monitored in a fully independent manner. From a practical perspective, the hybrid device was able to respond to low concentrations of cancer biomarkers (lower than the normal physiologic level), which is important for the disease's screening, diagnosis or progression. Moreover, the concept behind the hybrid DSSC device may eventually be extended to any other cancer biomarkers.

8.2.Future Work

In a near future, biosensors based on PEDOT/PPy outside of DSSCs could be developed and optimized with regard to the different concentration ranges of CEA. After this, the biosensor could be evaluated against biological samples, by monitoring the main photovoltaic parameters. Further studies, should be also made, including optimization procedures based on the fabrication of ITO material to obtain higher homogeneity. Besides, the colouration obtained by the EC could be further explored for quantitative purposes, by monitoring the colour coordinates (as the HSL system) from the digital images and extracting parametric data from these coordinates.

In a longer perspective, it is considered feasible to replace the glass substrate of the DSSC cathode by paper substrates, since these are cheaper and environmentally friendly materials. For this purpose, the cellulose paper coated with a carbon ink developed herein could be further tested as cathode materials in the hybrid device.

References

- [1] G.c.O. 2018, Estimated number of new cases in 2018, worldwide, all cancers, both sexes, all ages, 2018. (Accessed March 2019).
- [2] C. Wang, Z. Wang, T. Zhao, Y. Li, G. Huang, B.D. Sumer, J. Gao, Optical molecular imaging for tumor detection and image-guided surgery, *Biomaterials* 157 (2018) 62-75.
- [3] S.H. Jafari, Z. Saadatpour, A. Salmaninejad, F. Momeni, M. Mokhtari, J.S. Nahand, M. Rahmati, H. Mirzaei, M. Kianmehr, Breast cancer diagnosis: Imaging techniques and biochemical markers, *Journal of Cellular Physiology* 233(7) (2018) 5200-5213.
- [4] L. Fass, Imaging and cancer: A review, *Molecular Oncology* 2(2) (2008) 115-152.
- [5] R. Weissleder, M.J. Pittet, Imaging in the era of molecular oncology, *Nature* 452(7187) (2008) 580-589.
- [6] V.S.P.K.Sankara A. Jayanthi, A.B. Das, U. Saxena, Recent advances in biosensor development for the detection of cancer biomarkers, *Biosensors and Bioelectronics* 91 (2017) 15-23.
- [7] E. Schleicher, The clinical chemistry laboratory: current status, problems and diagnostic prospects, *Analytical and Bioanalytical Chemistry* 384(1) (2006) 124-131.
- [8] C.D.C. Chin, Sau Yin. Laksanasopin, Tassaneewan. and Sia, Samuel K., Low-Cost Microdevices for Point-of-Care Testing, in: W. Issadore D, RM (Ed.), *Point-of-care Diagnostics on a chip*, Springer, Verlag Berlin Heidelberg 2013.
- [9] J. Wang, Electrochemical biosensors: Towards point-of-care cancer diagnostics, *Biosensors and Bioelectronics* 21(10) (2006) 1887-1892.
- [10] S.K. Vashist, P.B. Lippa, L.Y. Yeo, A. Ozcan, J.H.T. Luong, Emerging Technologies for Next-Generation Point-of-Care Testing, *Trends in Biotechnology* 33(11) (2015) 692-705.
- [11] P. Mehrotra, Biosensors and their applications – A review, *Journal of Oral Biology and Craniofacial Research* 6(2) (2016) 153-159.
- [12] H.A. Alhadrami, Biosensors: Classifications, medical applications, and future prospective, *Biotechnology and Applied Biochemistry* 65(3) (2018) 497-508.
- [13] N.S. Fracchiolla, S. Artuso, A. Cortelezzi, Biosensors in clinical practice: focus on oncohematology, *Sensors (Basel, Switzerland)* 13(5) (2013) 6423-6447.
- [14] L. Wu, X.G. Qu, Cancer biomarker detection: recent achievements and challenges, *Chemical Society Reviews* 44(10) (2015) 2963-2997.

- [15] K. Baryeh, S. Takalkar, M. Lund, G. Liu, 1 - Introduction to medical biosensors for point of care applications, in: R.J. Narayan (Ed.), *Medical Biosensors for Point of Care (POC) Applications*, Woodhead Publishing 2017, pp. 3-25.
- [16] F.S. Felix, L. Angnes, Electrochemical immunosensors – A powerful tool for analytical applications, *Biosensors and Bioelectronics* 102 (2018) 470-478.
- [17] K.K. Mistry, K. Layek, A. Mahapatra, C. RoyChaudhuri, H. Saha, A review on amperometric-type immunosensors based on screen-printed electrodes, *Analyst* 139(10) (2014) 2289-2311.
- [18] R.C.B. Marques, E. Costa-Rama, S. Viswanathan, H.P.A. Nouws, A. Costa-García, C. Delerue-Matos, M.B. González-García, Voltammetric immunosensor for the simultaneous analysis of the breast cancer biomarkers CA 15-3 and HER2-ECD, *Sensors and Actuators B: Chemical* 255 (2018) 918-925.
- [19] P.B. Lippa, L.J. Sokoll, D.W. Chan, Immunosenors - principles and applications to clinical chemistry, *Clinica Chimica Acta* 314(1-2) (2001) 1-26.
- [20] K.G. Yang, L.H. Zhang, Z. Liang, Y.K. Zhang, Protein-imprinted materials: rational design, application and challenges, *Analytical and Bioanalytical Chemistry* 403(8) (2012) 2173-2183.
- [21] W.H. Organization, Cancer, 2018. (Accessed March 2019).
- [22] F. Bray, J. Ferlay, I. Soerjomataram, R.L. Siegel, L.A. Torre, A. Jemal, Global cancer statistics 2018: GLOBOCAN estimates of incidence and mortality worldwide for 36 cancers in 185 countries, *Ca-a Cancer Journal for Clinicians* 68(6) (2018) 394-424.
- [23] A.B. Hashkavayi, J.B. Raoof, R. Ojani, S. Kavosian, Ultrasensitive electrochemical aptasensor based on sandwich architecture for selective label-free detection of colorectal cancer (CT26) cells, *Biosensors and Bioelectronics* 92 (2017) 630-637.
- [24] A. Hadjipetrou, D. Anyfantakis, C.G. Galanakis, M. Kastanakis, S. Kastanakis, Colorectal cancer, screening and primary care: a mini literature review, *World Journal of Gastroenterology* 23(33) (2017) 6049-6058.
- [25] H.S. Gandomani, S.M. Yousefi, M. Aghajani, A. Mohammadian-Hafshejani, A.A. Tarazoj, V. Pouyesh, H. Salehiniya, Colorectal cancer in the world: incidence, mortality and risk factors, *Biomedical Research and Therapy* 4(10) (2017) 1656-1675.
- [26] S. Wu, S. Powers, W. Zhu, Y.A. Hannun, Substantial contribution of extrinsic risk factors to cancer development, *Nature* 529(7584) (2016) 43-47.
- [27] D. Gingras, R. Béliveau, Colorectal Cancer Prevention Through Dietary and Lifestyle Modifications, *Cancer Microenvironment* 4(2) (2011) 133-139.
- [28] N. Khan, F. Afaq, H. Mukhtar, LIFESTYLE AS RISK FACTOR FOR CANCER: EVIDENCE FROM HUMAN STUDIES, *Cancer letters* 293(2) (2010) 133-143.
- [29] N. Hauptman, D. Glavač, Colorectal Cancer Blood-Based Biomarkers, *Gastroenterology research and practice* 2017 (2017) 2195361-2195361.

- [30] X. Miao, S. Zou, H. Zhang, L. Ling, Highly sensitive carcinoembryonic antigen detection using Ag@Au core-shell nanoparticles and dynamic light scattering, *Sensors and Actuators B: Chemical* 191 (2014) 396-400.
- [31] C. Aggarwal, N.J. Meropol, C.J. Punt, N. Iannotti, B.H. Saidman, K.D. Sabbath, N.Y. Gabrail, J. Picus, M.A. Morse, E. Mitchell, M.C. Miller, S.J. Cohen, Relationship among circulating tumor cells, CEA and overall survival in patients with metastatic colorectal cancer, *Annals of Oncology* 24(2) (2012) 420-428.
- [32] W.H. Organization, *Cancer*, 2018. 2019).
- [33] M.Y. Fong, J. McDunn, S.S. Kakar, Identification of Metabolites in the Normal Ovary and Their Transformation in Primary and Metastatic Ovarian Cancer, *Plos One* 6(5) (2011).
- [34] S.I. Ferlay J, Ervik M, Dikshit R, Eser S, Mathers C, Rebelo M, Parkin DM, Forman D, Bray, F., *Cancer Incidence and Mortality Worldwide: IARC CancerBase, 2013*. <http://globocan.iarc.fr>. (Accessed May 2019).
- [35] T. Chen, G. Xie, X. Wang, J. Fan, Y. Qui, X. Zheng, X. Qi, Y. Cao, M. Su, X. Wang, L.X. Xu, Y. Yen, P. Liu, W. Jia, Serum and Urine Metabolite Profiling Reveals Potential Biomarkers of Human Hepatocellular Carcinoma (vol 10, pg 1, 2011), *Molecular & Cellular Proteomics* 10(11) (2011).
- [36] E.G. Armitage, C. Barbas, Metabolomics in cancer biomarker discovery: Current trends and future perspectives, *Journal of Pharmaceutical and Biomedical Analysis* 87 (2014) 1-11.
- [37] N. Cheng, D. Du, X. Wang, D. Liu, W. Xu, Y. Luo, Y. Lin, Recent Advances in Biosensors for Detecting Cancer-Derived Exosomes, *Trends in Biotechnology* (2019).
- [38] J.L. Connolly., S.J. Schnitt., H.H. Wang., J.A. Longtine., A. Dvorak., H.F. Dvorak., *Role of the Surgical Pathologist in the Diagnosis and Management of the Cancer Patient*, Holland-Frei Cancer Medicine, BC Decker 2003.
- [39] A. Srivastava, D.J. Creek, Discovery and Validation of Clinical Biomarkers of Cancer: A Review Combining Metabolomics and Proteomics, *Proteomics* 19(10) (2019) e1700448.
- [40] N. Goossens, S. Nakagawa, X. Sun, Y. Hoshida, Cancer biomarker discovery and validation, *Translational cancer research* 4(3) (2015) 256-269.
- [41] M.J. Selleck, M. Senthil, N.R. Wall, Making Meaningful Clinical Use of Biomarkers, *Biomark Insights* 12 (2017) 1177271917715236.
- [42] N.L. Henry, D.F. Hayes, Cancer biomarkers, *Molecular Oncology* 6(2) (2012) 140-146.
- [43] M. Ong, K.D. Mandl, Trends in prostate-specific antigen screening and prostate cancer interventions 3 years after the u.s. preventive services task force recommendation, *Annals of Internal Medicine* 166(6) (2017) 451-452.
- [44] A. Black, C.D. Berg, Prostate-Specific Antigen Screening for Prostate Cancer in Older Men in the United States of America, *Gerontology* 58(4) (2012) 331-336.

- [45] T.J. Wilt, P.T. Scardino, S.V. Carlsson, E. Basch, Prostate-Specific Antigen Screening in Prostate Cancer: Perspectives on the Evidence, *JNCI: Journal of the National Cancer Institute* 106(3) (2014) dju010-dju010.
- [46] *N.C. Institute*, Prostate-Specific Antigen (PSA) Test, 2017. <https://www.cancer.gov/types/prostate/psa-fact-sheet>. (Accessed May 2019).
- [47] M.J. Duffy, Carcinoembryonic antigen as a marker for colorectal cancer: Is it clinically useful?, *Clinical Chemistry* 47(4) (2001) 624-630.
- [48] M.J. Goldstein, E.P. Mitchell, Carcinoembryonic Antigen in the Staging and Follow-up of Patients with Colorectal Cancer, *Cancer Investigation* 23(4) (2005) 338-351.
- [49] B.D. Nicholson, B. Shinkins, D. Mant, Blood measurement of carcinoembryonic antigen level for detecting recurrence of colorectal cancer, *JAMA* 316(12) (2016) 1310-1311.
- [50] Y. Wang, T.-X. Wei, Surface plasmon resonance sensor chips for the recognition of bovine serum albumin via electropolymerized molecularly imprinted polymers, *Chinese Chemical Letters* 24(9) (2013) 813-816.
- [51] S.E. Whitmore, G.J. Anhalt, T.T. Provost, H.A. Zacur, U.M. Hamper, K.J. Helzlsouer, N.B. Rosenshein, Serum CA-125 Screening for Ovarian Cancer in Patients with Dermatomyositis, *Gynecologic Oncology* 65(2) (1997) 241-244.
- [52] K.M. Esselen, A.M. Cronin, K. Bixel, et al., Use of ca-125 tests and computed tomographic scans for surveillance in ovarian cancer, *JAMA Oncology* 2(11) (2016) 1427-1433.
- [53] S.J. Skates, M.H. Greene, S.S. Buys, P.L. Mai, P. Brown, M. Piedmonte, G. Rodriguez, J.O. Schorge, M. Sherman, M.B. Daly, T. Rutherford, W.R. Brewster, D.M. O'Malley, E. Partridge, J. Boggess, C.W. Drescher, C. Isaacs, A. Berchuck, S. Domchek, S.A. Davidson, R. Edwards, S.A. Elg, K. Wakeley, K.A. Phillips, D. Armstrong, I. Horowitz, C.J. Fabian, J. Walker, P.M. Sluss, W. Welch, L. Minasian, N.K. Horick, C.H. Kasten, S. Nayfield, D. Alberts, D.M. Finkelstein, K.H. Lu, Early Detection of Ovarian Cancer using the Risk of Ovarian Cancer Algorithm with Frequent CA125 Testing in Women at Increased Familial Risk - Combined Results from Two Screening Trials, *Clin Cancer Res* 23(14) (2017) 3628-3637.
- [54] U.K. Ballehaninna, R.S. Chamberlain, The clinical utility of serum CA 19-9 in the diagnosis, prognosis and management of pancreatic adenocarcinoma: An evidence based appraisal, *Journal of Gastrointestinal Oncology* 3(2) (2012) 105-119.
- [55] R. Zubarik, S.R. Gordon, S.D. Lidofsky, S.R. Anderson, J.M. Pipas, G. Badger, E. Ganguly, J. Vecchio, Screening for pancreatic cancer in a high-risk population with serum CA 19-9 and targeted EUS: a feasibility study, *Gastrointestinal Endoscopy* 74(1) (2011) 87-95.
- [56] J.S. Kim, J.w. Choe, H.J. Kim, M.K. Joo, J.-J. Park, Y.-T. Bak, Effectiveness of CA 19-9 as a screening test for pancreatic cancer in new onset diabetic patients, *Pancreatology* 14(3) (2014) S46.
- [57] U.K. Ballehaninna, R.S. Chamberlain, Serum CA 19-9 as a Biomarker for Pancreatic Cancer-A Comprehensive Review, *Indian journal of surgical oncology* 2(2) (2011) 88-100.

- [58] E.J. Kumpulainen, R.J. Kesikuru, R.T. Johansson, Serum Tumor Marker CA 15.3 and Stage are the Two Most Powerful Predictors of Survival in Primary Breast Cancer, *Breast Cancer Research and Treatment* 76(2) (2002) 95-102.
- [59] S. Chourin, D. Georgescu, C. Gray, C. Guillemet, A. Loeb, C. Veyret, J.P. Basuyau, Value of CA 15-3 determination in the initial management of breast cancer patients, *Annals of Oncology* 20(5) (2009) 962-964.
- [60] B. Nisman, O. Maimon, T. Allweis, L. Kadouri, B. Maly, T. Hamburger, T. Peretz, The prognostic significance of LIAISON(R) CA15-3 assay in primary breast cancer, *Anticancer Res* 33(1) (2013) 293-9.
- [61] A. Steiber, J. Kerner, C.L. Hoppel, Carnitine: a nutritional, biosynthetic, and functional perspective, *Molecular aspects of medicine* 25(5-6) (2004) 455-73.
- [62] L.A. Calo, E. Pagnin, P.A. Davis, A. Semplicini, R. Nicolai, M. Calvani, A.C. Pessina, Antioxidant effect of L-carnitine and its short chain esters - Relevance for the protection from oxidative stress related cardiovascular damage, *International Journal of Cardiology* 107(1) (2006) 54-60.
- [63] J.L. Flanagan, P.A. Simmons, J. Vehige, M.D.P. Willcox, Q. Garrett, Role of carnitine in disease, *Nutrition & Metabolism* 7 (2010).
- [64] S. Savitha, J. Tamilselvan, M. Anusuyadevi, C. Panneerselvam, Oxidative stress on mitochondrial antioxidant defense system in the aging process: Role of DL-alpha-lipoic acid and L-carnitine, *Clinica Chimica Acta* 355(1-2) (2005) 173-180.
- [65] D.B. Engle, J.A. Belisle, J.A.A. Gubbels, S.E. Petrie, P.R. Hutson, D.M. Kushner, M.S. Patankar, Effect of acetyl-L-carnitine on ovarian cancer cells' proliferation, nerve growth factor receptor (Trk-A and p75) expression, and the cytotoxic potential of paclitaxel and carboplatin, *Gynecologic Oncology* 112(3) (2009) 631-636.
- [66] F.N.U. Asad-Ur-Rahman, M.W. Saif, Elevated Level of Serum Carcinoembryonic Antigen (CEA) and Search for a Malignancy: A Case Report, *Cureus* 8(6) (2016) e648.
- [67] B.J. Casey, P. Kofinas, Selective binding of carcinoembryonic antigen using imprinted polymeric hydrogels, *Journal of Biomedical Materials Research Part A* 87A(2) (2008) 359-363.
- [68] E.-Y. Huang, J.-C. Chang, H.-H. Chen, C.-Y. Hsu, H.-C. Hsu, K.-L. Wu, Carcinoembryonic antigen as a marker of radioresistance in colorectal cancer: a potential role of macrophages, *BMC Cancer* 18(1) (2018) 321.
- [69] D.M. Nazato, L.L. Matos, D.R. Waisberg, J.R. Souza, L.C. Martins, J. Waisberg, Prognostic value of carcinoembryonic antigen distribution in tumor tissue of colorectal carcinoma, *Arq Gastroenterol* 46(1) (2009) 26-31.
- [70] O. Margalit, R. Mamtani, Y.-X. Yang, K.A. Reiss, T. Golan, N. Halpern, D. Aderka, B. Giantonio, E. Shacham-Shmueli, B. Boursi, Assessing the prognostic value of carcinoembryonic antigen levels in stage I and II colon cancer, *European Journal of Cancer* 94 (2018) 1-5.

- [71] J. Marrugo-Ramírez, M. Mir, J. Samitier, Blood-Based Cancer Biomarkers in Liquid Biopsy: A Promising Non-Invasive Alternative to Tissue Biopsy, *International journal of molecular sciences* 19(10) (2018) 2877.
- [72] S. Patel, R. Nanda, S. Sahoo, E. Mohapatra, Biosensors in Health Care: The Milestones Achieved in Their Development towards Lab-on-Chip-Analysis, *Biochemistry Research International* (2016).
- [73] S.K. Metkar, K. Girigoswami, Diagnostic biosensors in medicine – A review, *Biocatalysis and Agricultural Biotechnology* 17 (2019) 271-283.
- [74] L. Wang, Q. Xiong, F. Xiao, H. Duan, 2D nanomaterials based electrochemical biosensors for cancer diagnosis, *Biosensors and Bioelectronics* 89 (2017) 136-151.
- [75] R. Ranjan, E.N. Esimbekova, V.A. Kratasyuk, Rapid biosensing tools for cancer biomarkers, *Biosensors and Bioelectronics* 87 (2017) 918-930.
- [76] S. Andreescu, J.-L. Marty, Twenty years research in cholinesterase biosensors: From basic research to practical applications, *Biomolecular Engineering* 23(1) (2006) 1-15.
- [77] D.R. Thevenot, K. Toth, R.A. Durst, G.S. Wilson, Electrochemical biosensors: Recommended definitions and classification, *Analytical Letters* 34(5) (2001) 635-659.
- [78] M. Asal, Ö. Özen, M. Şahinler, İ. Polatoğlu, Recent Developments in Enzyme, DNA and Immuno-Based Biosensors, *Sensors (Basel, Switzerland)* 18(6) (2018) 1924.
- [79] B. Rafique, M. Iqbal, T. Mehmood, M.A. Shaheen, Electrochemical DNA biosensors: a review, *Sensor Review* 39(1) (2019) 34-50.
- [80] F. Arduini, L. Micheli, D. Moscone, G. Palleschi, S. Piermarini, F. Ricci, G. Volpe, Electrochemical biosensors based on nanomodified screen-printed electrodes: Recent applications in clinical analysis, *TrAC Trends in Analytical Chemistry* 79 (2016) 114-126.
- [81] J. Kavita V, DNA Biosensors-A Review, *Journal of Bioengineering & Biomedical Science* 7(2) (2017).
- [82] J.A. Garrido-Cardenas, F. Garcia-Maroto, J.A. Alvarez-Bermejo, F. Manzano-Agugliaro, DNA Sequencing Sensors: An Overview, *Sensors* 17(3) (2017).
- [83] H.H. Nguyen, S.H. Lee, U.J. Lee, C.D. Fermin, M. Kim, Immobilized Enzymes in Biosensor Applications, *Materials (Basel, Switzerland)* 12(1) (2019) 121.
- [84] J.A.C. Pérez, J.E. Sosa-Hernández, S.M. Hussain, M. Bilal, R. Parra-Saldivar, H.M.N. Iqbal, Bioinspired biomaterials and enzyme-based biosensors for point-of-care applications with reference to cancer and bio-imaging, *Biocatalysis and Agricultural Biotechnology* 17 (2019) 168-176.
- [85] Y. Huang, J. Xu, J. Liu, X. Wang, B. Chen, Disease-Related Detection with Electrochemical Biosensors: A Review, *Sensors (Basel, Switzerland)* 17(10) (2017) 2375.
- [86] S.S. Zhang, W. Cao, J. Li, M.M. Su, MCE enzyme immunoassay for carcinoembryonic antigen and alpha-fetoprotein using electrochemical detection, *Electrophoresis* 30(19) (2009) 3427-3435.

- [87] W.J. Li, R. Yuan, Y.Q. Chai, S.H. Chen, Reagent less amperometric cancer antigen 15-3 immunosensor based on enzyme-mediated direct electrochemistry, *Biosensors & Bioelectronics* 25(11) (2010) 2548-2552.
- [88] D.P. Tang, R. Yuan, Y.Q. Chal, Ultrasensitive electrochemical immunosensor for clinical immunoassay using thionine-doped magnetic gold nanospheres as labels and horseradish peroxidase as enhancer, *Analytical Chemistry* 80(5) (2008) 1582-1588.
- [89] B. Zhang, X. Zhang, H.H. Yan, S.J. Xu, D.H. Tang, W.L. Fu, A novel multi-array immunoassay device for tumor markers based on insert-plug model of piezoelectric immunosensor, *Biosensors & Bioelectronics* 23(1) (2007) 19-25.
- [90] G.-Y. Shen, H. Wang, T. Deng, G.-L. Shen, R.-Q. Yu, A novel piezoelectric immunosensor for detection of carcinoembryonic antigen, *Talanta* 67(1) (2005) 217-220.
- [91] A.B. Ganganboina, R.-A. Doong, Graphene Quantum Dots Decorated Gold-Polyaniline Nanowire for Impedimetric Detection of Carcinoembryonic Antigen, *Scientific Reports* 9(1) (2019) 7214.
- [92] G. Yang, Y. Lai, Z. Xiao, C. Tang, Y. Deng, Ultrasensitive electrochemical immunosensor of carcinoembryonic antigen based on gold-label silver-stain signal amplification, *Chinese Chemical Letters* 29(12) (2018) 1857-1860.
- [93] W.T. Li, Y. Wang, F.F. Deng, L.L. Liu, H.J. Nan, H. Li, Electrochemical Immunosensor for Carcinoembryonic Antigen Detection Based on Mo-Mn₃O₄/MWCNTs/Chits Nanocomposite Modified ITO Electrode, *Nano* 10(8) (2015).
- [94] I.H. Cho, J. Lee, J. Kim, M.S. Kang, J.K. Paik, S. Ku, H.M. Cho, J. Irudayaraj, D.H. Kim, Current Technologies of Electrochemical Immunosensors: Perspective on Signal Amplification, *Sensors (Basel)* 18(1) (2018).
- [95] H. Chen, J. Tang, B. Su, G. Chen, J. Huang, D. Tang, Nanogold-actuated biomimetic peroxidase for sensitized electrochemical immunoassay of carcinoembryonic antigen in human serum, *Analytica Chimica Acta* 678(2) (2010) 169-175.
- [96] T.-S. Xu, X.-Y. Li, Z.-H. Xie, X.-G. Li, H.-Y. Zhang, Poly(o-phenylenediamine) nanosphere-conjugated capture antibody immobilized on a glassy carbon electrode for electrochemical immunoassay of carcinoembryonic antigen, *Microchimica Acta* 182(15) (2015) 2541-2549.
- [97] J. Miao, X. Wang, L. Lu, P. Zhu, C. Mao, H. Zhao, Y. Song, J. Shen, Electrochemical immunosensor based on hyperbranched structure for carcinoembryonic antigen detection, *Biosens Bioelectron* 58 (2014) 9-16.
- [98] X. Yang, Y. Guo, A. Wang, Luminol/antibody labeled gold nanoparticles for chemiluminescence immunoassay of carcinoembryonic antigen, *Analytica Chimica Acta* 666(1) (2010) 91-96.
- [99] J. Wu, F. Yan, J.H. Tang, C. Zhai, H.X. Ju, A disposable multianalyte electrochemical immunosensor array for automated simultaneous determination of tumor markers, *Clinical Chemistry* 53(8) (2007) 1495-1502.

- [100] N. Laboria, A. Fragoso, W. Kemmner, D. Latta, O. Nilsson, M. Luz Botero, K. Drese, C.K. O'Sullivan, Amperometric Immunosensor for Carcinoembryonic Antigen in Colon Cancer Samples Based on Monolayers of Dendritic Bipodal Scaffolds, *Analytical Chemistry* 82(5) (2010) 1712-1719.
- [101] A.A.N.A.T.a.M.G.F.S. Liliana, Sol-Gel Chemistry in Biosensing Devices of Electrical Transduction: Application to CEA Cancer Biomarker, *Current Topics in Medicinal Chemistry* 15(3) (2015) 256-261.
- [102] Z. Altintas, Y. Uludag, Y. Gurbuz, I.E. Tohill, Surface plasmon resonance based immunosensor for the detection of the cancer biomarker carcinoembryonic antigen, *Talanta* 86 (2011) 377-383.
- [103] D.P. Tang, J.J. Ren, In Situ Amplified Electrochemical Immunoassay for Carcinoembryonic Antigen Using Horseradish Peroxidase-Encapsulated Nanogold Hollow Microspheres as Labels, *Analytical Chemistry* 80(21) (2008) 8064-8070.
- [104] T.J. Li, P.Y. Chen, P.C. Nien, C.Y. Lin, R. Vittal, T.R. Ling, K.C. Ho, Preparation of a novel molecularly imprinted polymer by the sol-gel process for sensing creatinine, *Analytica Chimica Acta* 711 (2012) 83-90.
- [105] C. Zhong, B. Yang, X. Jiang, J. Li, Current Progress of Nanomaterials in Molecularly Imprinted Electrochemical Sensing, *Critical Reviews in Analytical Chemistry* 48(1) (2018) 15-32.
- [106] G. Vasapollo, R. Del Sole, L. Mergola, M.R. Lazzoi, A. Scardino, S. Scorrano, G. Mele, Molecularly Imprinted Polymers: Present and Future Prospective, *International Journal of Molecular Sciences* 12(9) (2011) 5908-5945.
- [107] J. Erdossy, V. Horvath, A. Yarman, F.W. Scheller, R.E. Gyurcsanyi, Electrosynthesized molecularly imprinted polymers for protein recognition, *Trac-Trends in Analytical Chemistry* 79 (2016) 179-190.
- [108] S. Li., Y. Ge., S.A. Piletsky., J. Lunec., *Molecularly Imprinted Sensors: Overview and Applications*, First ed., Elsevier 2012.
- [109] M.L. Yola, T. Eren, N. Atar, Molecularly imprinted electrochemical biosensor based on Fe@Au nanoparticles involved in 2-aminoethanethiol functionalized multi-walled carbon nanotubes for sensitive determination of cefexime in human plasma, *Biosensors & Bioelectronics* 60 (2014) 277-285.
- [110] J. Ji, Z. Zhou, X. Zhao, J. Sun, X. Sun, Electrochemical sensor based on molecularly imprinted film at Au nanoparticles-carbon nanotubes modified electrode for determination of cholesterol, *Biosensors & bioelectronics* 66 (2015) 590-5.
- [111] Z.Y. Li, H.J. Quan, C.B. Gong, Y.Z. Yang, Q. Tang, Y.B. Wei, X.B. Ma, H.W. Lam, Photocontrolled solid-phase extraction of guanine from complex samples using a novel photoresponsive molecularly imprinted polymer, *Food Chemistry* 172 (2015) 56-62.
- [112] R.D. Crapnell, A. Hudson, C.W. Foster, K. Eersels, B.V. Grinsven, T.J. Cleij, C.E. Banks, M. Peeters, Recent Advances in Electrosynthesized Molecularly Imprinted Polymer Sensing Platforms for Bioanalyte Detection, *Sensors (Basel)* 19(5) (2019).

- [113] F.T.C. Moreira, M.J.M.S. Ferreira, J.R.T. Puga, M.G.F. Sales, Screen-printed electrode produced by printed-circuit board technology. Application to cancer biomarker detection by means of plastic antibody as sensing material, *Sensors and Actuators B: Chemical* 223 (2016) 927-935.
- [114] J.A. Ribeiro, C.M. Pereira, A.F. Silva, M.G.F. Sales, Disposable electrochemical detection of breast cancer tumour marker CA 15-3 using poly(Toluidine Blue) as imprinted polymer receptor, *Biosensors and Bioelectronics* 109 (2018) 246-254.
- [115] P. Damborský, J. Švitel, J. Katrlík, Optical biosensors, *Essays in biochemistry* 60(1) (2016) 91-100.
- [116] H.A. Abdulbari, E.A.M. Basheer, Electrochemical Biosensors: Electrode Development, Materials, Design, and Fabrication, *Chembioeng Reviews* 4(2) (2017) 92-105.
- [117] R. Gui, H. Jin, H. Guo, Z. Wang, Recent advances and future prospects in molecularly imprinted polymers-based electrochemical biosensors, *Biosensors and Bioelectronics* 100 (2018) 56-70.
- [118] S.P. Mohanty, E. Kougianos, Biosensors: a tutorial review, *IEEE Potentials* 25(2) (2006) 35-40.
- [119] H.J. Chen, Z.H. Zhang, D. Xie, R. Cai, X. Chen, Y.N. Liu, S.Z. Yao, Surface-Imprinting Sensor Based on Carbon Nanotubes/Graphene Composite for Determination of Bovine Serum Albumin, *Electroanalysis* 24(11) (2012) 2109-2116.
- [120] A.C. Fisher, *Electrode Dynamics* Oxford University Press, New York, United States, 2009.
- [121] C.M.A.B. Ana Maria Oliveira Brett, *Electrochemistry: Principles, Methods, and Applications*, Oxford science Publications, Oxford University, 1993.
- [122] A. Bard, L. Faulkner, *Electrochemical methods: fundamentals and applications*, (1980).
- [123] F. Lisdat, D. Schafer, The use of electrochemical impedance spectroscopy for biosensing, *Analytical and Bioanalytical Chemistry* 391(5) (2008) 1555-1567.
- [124] U. Piratoba Morales, E. Vera Lopez, C. Ortiz Otorala, BASIC ASPECTS IN THE INTERPRETATION OF THE DIAGRAMS OF ELECTOCHEMICAL IMPEDANCE, *Dyna-Colombia* 77(162) (2010) 13-19.
- [125] F. Lisdat, D. Schäfer, The use of electrochemical impedance spectroscopy for biosensing, *Analytical and Bioanalytical Chemistry* 391(5) (2008) 1555.
- [126] Y.X. Wang, Z.Z. Ye, Y.B. Ying, New Trends in Impedimetric Biosensors for the Detection of Foodborne Pathogenic Bacteria, *Sensors* 12(3) (2012) 3449-3471.
- [127] J.L. Hammond, N. Formisano, P. Estrela, S. Carrara, J. Tkac, Electrochemical biosensors and nanobiosensors, *Biosensor Technologies for Detection of Biomolecules* 60(1) (2016) 69-80.
- [128] R.S. Gomes, F.T.C. Moreira, R. Fernandes, M.G.F. Sales, Sensing CA 15-3 in point-of-care by electropolymerizing O-phenylenediamine (oPDA) on Au-screen printed electrodes, *PLOS ONE* 13(5) (2018) e0196656.
- [129] S.N. Topkaya, M. Azimzadeh, M. Ozsoz, Electrochemical Biosensors for Cancer Biomarkers Detection: Recent Advances and Challenges, *Electroanalysis* 28(7) (2016) 1402-1419.

- [130] G. Selvolini, G. Marrazza, MIP-Based Sensors: Promising New Tools for Cancer Biomarker Determination, *Sensors* 17(4) (2017).
- [131] L.A.A.N.A. Truta, M.G.F. Sales, Carcinoembryonic antigen imprinting by electropolymerization on a common conductive glass support and its determination in serum samples, *Sensors and Actuators B: Chemical* 287 (2019) 53-63.
- [132] Y. Lai, Y. Deng, G. Yang, S. Li, C. Zhang, X. Liu, Molecular Imprinting Polymers Electrochemical Sensor Based on AuNPs/PTh Modified GCE for Highly Sensitive Detection of Carcinomaembryonic Antigen, *J Biomed Nanotechnol* 14(10) (2018) 1688-1694.
- [133] T.S.C.R. Rebelo, C. Santos, J. Costa-Rodrigues, M.H. Fernandes, J.P. Noronha, M.G.F. Sales, Novel Prostate Specific Antigen plastic antibody designed with charged binding sites for an improved protein binding and its application in a biosensor of potentiometric transduction, *Electrochimica Acta* 132(0) (2014) 142-150.
- [134] J. Moret, F.T.C. Moreira, S.A.A. Almeida, M.G.F. Sales, New molecularly-imprinted polymer for carnitine and its application as ionophore in potentiometric selective membranes, *Materials Science and Engineering: C* 43 (2014) 481-487.
- [135] L.A.A.N.A. Truta, N.S. Ferreira, M.G.F. Sales, Graphene-based biomimetic materials targeting urine metabolite as potential cancer biomarker: application over different conductive materials for potentiometric transduction, *Electrochimica acta* 150 (2014) 99-107.
- [136] A.P.M. Tavares, N.S. Ferreira, L.A.A.N.A. Truta, M.G.F. Sales, Conductive Paper with Antibody-Like Film for Electrical Readings of Biomolecules, *Scientific reports* 6 (2016) 26132-26132.
- [137] S. Chander, A. Purohit, A. Sharma, Arvind, S.P. Nehra, M.S. Dhaka, A study on photovoltaic parameters of mono-crystalline silicon solar cell with cell temperature, *Energy Reports* 1 (2015) 104-109.
- [138] A.A.F. Husain, W.Z.W. Hasan, S. Shafie, M.N. Hamidon, S.S. Pandey, A review of transparent solar photovoltaic technologies, *Renewable and Sustainable Energy Reviews* 94 (2018) 779-791.
- [139] L. Andrade, J. Sousa, H. Aguilar Ribeiro, A. Mendes, Phenomenological modeling of dye-sensitized solar cells under transient conditions, *Solar Energy* 85(5) (2011) 781-793.
- [140] M. Gratzel, Photoelectrochemical cells, *Nature* 414(6861) (2001) 338-344.
- [141] B. Oregan, M. Gratzel, A low-cost, high-efficiency solar-cell based on dye-sensitized colloidal TiO_2 films, *Nature* 353(6346) (1991) 737-740.
- [142] C. Sima, C. Grigoriu, S. Antohe, Comparison of the dye-sensitized solar cells performances based on transparent conductive ITO and FTO, *Thin Solid Films* 519(2) (2010) 595-597.
- [143] P. Guo, M.A. Aegerter, Ru(II) sensitized Nb_2O_5 solar cell made by the sol-gel process, *Thin Solid Films* 351(1-2) (1999) 290-294.
- [144] M. Saito, S. Fujihara, Large photocurrent generation in dye-sensitized ZnO solar cells, *Energy & Environmental Science* 1(2) (2008) 280-283.

- [145] B. Onwona-Agyeman, S. Kaneko, A. Kumara, M. Okuya, K. Murakami, A. Konno, K. Tennakone, Sensitization of nanocrystalline SnO₂ films with indoline dyes, *Japanese Journal of Applied Physics Part 2-Letters & Express Letters* 44(20-23) (2005) L731-L733.
- [146] M. Fitra, I. Daut, M. Irwanto, N. Gomesh, Y.M. Irwan, TiO₂ Dye Sensitized Solar Cells Cathode Using Recycle Battery, *Terragreen 13 International Conference 2013 - Advancements in Renewable Energy and Clean Environment* 36 (2013) 333-340.
- [147] S. Ahmadi, N. Asim, M.A. Alghoul, F.Y. Hammadi, K. Saeedfar, N.A. Ludin, S.H. Zaidi, K. Sopian, The Role of Physical Techniques on the Preparation of Photoanodes for Dye Sensitized Solar Cells, *International Journal of Photoenergy* (2014).
- [148] D. Martineau, *Dye Solar Cells for Real*, Solaronix SA, Switzerland, 2012.
- [149] H. Chang, C.-H. Chen, M.-J. Kao, S.-H. Chien, C.-Y. Chou, Photoelectrode thin film of dye-sensitized solar cell fabricated by anodizing method and spin coating and electrochemical impedance properties of DSSC, *Applied Surface Science* 275 (2013) 252-257.
- [150] H. Wang, H. Li, J. Wang, J. Wu, M. Liu, Influence of Applied Voltage on Anodized TiO₂ Nanotube Arrays and Their Performance on Dye Sensitized Solar Cells, *Journal of Nanoscience and Nanotechnology* 13(6) (2013) 4183-4188.
- [151] M. Adachi, R. Tanino, J. Adachi, Y. Mori, K. Tsuchiya, S. Isoda, F. Uchida, Verification of necessity of one-dimensional titania nanoscale materials for dye-sensitized solar cells, *Journal of Power Sources* 226(0) (2013) 94-100.
- [152] M. Zhu, X. Li, W. Liu, Y. Cui, An investigation on the photoelectrochemical properties of dye-sensitized solar cells based on graphene TiO₂-composite photoanodes, *Journal of Power Sources* 262 (2014) 349-355.
- [153] M.-Y. Yen, C.-Y. Yen, S.-H. Liao, M.-C. Hsiao, C.-C. Weng, Y.-F. Lin, C.-C.M. Ma, M.-C. Tsai, A. Su, K.-K. Ho, P.-L. Liu, A novel carbon-based nanocomposite plate as a counter electrode for dye-sensitized solar cells, *Composites Science and Technology* 69(13) (2009) 2193-2197.
- [154] S.B. Bon, L. Valentini, J.M. Kenny, L. Peponi, R. Verdejo, M.A. Lopez-Manchado, Electrodeposition of transparent and conducting graphene/carbon nanotube thin films, *Physica Status Solidi a-Applications and Materials Science* 207(11) (2010) 2461-2466.
- [155] B. Gholamkhash, S. Holdcroft, Enhancing the durability of polymer solar cells using gold nanodots, *Solar Energy Materials and Solar Cells* 95(11) (2011) 3106-3113.
- [156] C. Quiñones, W. Vallejo, F. Mesa, Physical and electrochemical study of platinum thin films deposited by sputtering and electrochemical methods, *Applied Surface Science* 257(17) (2011) 7545-7550.
- [157] C.H. Yoon, R. Vittal, J. Lee, W.-S. Chae, K.-J. Kim, Enhanced performance of a dye-sensitized solar cell with an electrodeposited-platinum counter electrode, *Electrochimica Acta* 53(6) (2008) 2890-2896.

- [158] R. Săndulescu., M. Tertîş., C. Cristea., E. Bodoki., New Materials for the Construction of Electrochemical Biosensors, *Biosensors - Micro and Nanoscale Applications*, InTech2015.
- [159] A. Listorti, B. O'Regan, J.R. Durrant, Electron Transfer Dynamics in Dye-Sensitized Solar Cells, *Chemistry of Materials* 23(15) (2011) 3381-3399.
- [160] S. Mukherjee, C. Liu, E. Jakubikova, Comparison of Interfacial Electron Transfer Efficiency in [Fe(ctpy)₂]²⁺-TiO₂ and [Fe(cCNC)₂]²⁺-TiO₂ Assemblies: Importance of Conformational Sampling, *The Journal of Physical Chemistry A* 122(7) (2018) 1821-1830.
- [161] K. Fan, J.G. Yu, W.K. Ho, Improving photoanodes to obtain highly efficient dye-sensitized solar cells: a brief review, *Materials Horizons* 4(3) (2017) 319-344.
- [162] L.A.A.N.A. Truta, F.T.C. Moreira, M.G.F. Sales, A dye-sensitized solar cell acting as the electrical reading box of an immunosensor: Application to CEA determination, *Biosensors and Bioelectronics* 107 (2018) 94-102.
- [163] F.T.C. Moreira, L.A.A.N.A. Truta, M.G.F. Sales, Biomimetic materials assembled on a photovoltaic cell as a novel biosensing approach to cancer biomarker detection, *Scientific Reports* 8(1) (2018) 10205.
- [164] P.R. Somani, S. Radhakrishnan, Electrochromic materials and devices: present and future, *Materials Chemistry and Physics* 77(1) (2003) 117-133.
- [165] P. Yang, P. Sun, W. Mai, Electrochromic energy storage devices, *Materials Today* 19(7) (2016) 394-402.
- [166] P.F. Tavares, A.R. Gaspar, A.G. Martins, F. Frontini, Evaluation of electrochromic windows impact in the energy performance of buildings in Mediterranean climates, *Energy Policy* 67 (2014) 68-81.
- [167] S. Yamazaki, H. Ishida, D. Shimizu, K. Adachi, Photochromic Properties of Tungsten Oxide/Methylcellulose Composite Film Containing Dispersing Agents, *ACS Applied Materials & Interfaces* 7(47) (2015) 26326-26332.
- [168] S. Jockusch, N.J. Turro, F.R. Blackburn, Photochromism of 2H-Naphtho[1,2-b]pyrans: A Spectroscopic Investigation, *The Journal of Physical Chemistry A* 106(40) (2002) 9236-9241.
- [169] F.P. Lang, H. Wang, S.J. Zhang, J.B. Liu, H. Yan, Review on Variable Emissivity Materials and Devices Based on Smart Chromism, *International Journal of Thermophysics* 39(1) (2018).
- [170] I. Tsuyumoto, K. Nawa, Thermochromism of vanadium-titanium oxide prepared from peroxovanadate and peroxotitanate, *Journal of Materials Science* 43(3) (2008) 985-988.
- [171] L. Tu, C. Jia, X. Weng, L. Deng, Study on poly-O-anisidine film with the properties of electrochromism and infrared emissivity modulation, *Synthetic Metals* 161(17) (2011) 2045-2048.
- [172] B.C. Thompson, P. Schottland, K. Zong, J.R. Reynolds, In Situ Colorimetric Analysis of Electrochromic Polymers and Devices, *Chemistry of Materials* 12(6) (2000) 1563-1571.
- [173] T. Niwa, O. Takai, All-solid-state reflectance-type electrochromic devices using iridium tin oxide film as counter electrode, *Thin Solid Films* 518(18) (2010) 5340-5344.

- [174] V.K. Thakur, G.Q. Ding, J. Ma, P.S. Lee, X.H. Lu, Hybrid Materials and Polymer Electrolytes for Electrochromic Device Applications, *Advanced Materials* 24(30) (2012) 4071-4096.
- [175] P.-W. Chen, C.-T. Chang, M.M. Ali, J.-Y. Wu, Y.-C. Li, M.-H. Chen, D.-J. Jan, C.-T. Yuan, Tantalum oxide film deposited by vacuum cathodic arc plasma with improved electrochromic performance, *Solar Energy Materials and Solar Cells* 182 (2018) 188-195.
- [176] A.L.S. Eh, A.W.M. Tan, X. Cheng, S. Magdassi, P.S. Lee, Recent Advances in Flexible Electrochromic Devices: Prerequisites, Challenges, and Prospects, *Energy Technology* 6(1) (2018) 33-45.
- [177] C.G. Granqvist, *Handbook of inorganic electrochromic materials*, Elsevier, 1995.
- [178] D. Choi, M. Lee, H. Kim, W.-s. Chu, D.-m. Chun, S.-H. Ahn, C.S. Lee, Investigation of dry-deposited ion storage layers using various oxide particles to enhance electrochromic performance, *Solar Energy Materials and Solar Cells* 174 (2018) 599-606.
- [179] I. Yagmur, M. Ak, A. Bayrakceken, Fabricating multicolored electrochromic devices using conducting copolymers, *Smart Materials and Structures* 22(11) (2013).
- [180] P.M. Beaujuge, J.R. Reynolds, Color Control in π -Conjugated Organic Polymers for Use in Electrochromic Devices, *Chemical Reviews* 110(1) (2010) 268-320.
- [181] R.J. Mortimer, Organic electrochromic materials, *Electrochimica Acta* 44(18) (1999) 2971-2981.
- [182] F. Lang, H. Wang, S. Zhang, J. Liu, H. Yan, Review on Variable Emissivity Materials and Devices Based on Smart Chromism, *International Journal of Thermophysics* 39(1) (2017) 6.
- [183] M. Rakibuddin, H. Kim, Fabrication of MoS₂/WO₃ nanocomposite films for enhanced electrochromic performance, *New Journal of Chemistry* 41(24) (2017) 15327-15333.
- [184] J. Bae, D.G. Seo, S.M. Park, K.T. Park, H. Kim, H.C. Moon, S.H. Kim, Optimized low-temperature fabrication of WO₃ films for electrochromic devices, *Journal of Physics D-Applied Physics* 50(46) (2017) 8.
- [185] G.Z. Yuan, C.Z. Hua, L. Huang, C. Defranoux, P. Basa, Y. Liu, C.L. Song, G.R. Han, Optical characterization of the coloration process in electrochromic amorphous and crystalline WO₃ films by spectroscopic ellipsometry, *Applied Surface Science* 421 (2017) 630-635.
- [186] G. Sonmez, H. Meng, F. Wudl, Organic polymeric electrochromic devices: Polychromism with very high coloration efficiency, *Chemistry of Materials* 16(4) (2004) 574-580.
- [187] X. Lv, W. Li, M. Ouyang, Y. Zhang, D.S. Wright, C. Zhang, Polymeric electrochromic materials with donor-acceptor structures, *Journal of Materials Chemistry C* 5(1) (2017) 12-28.
- [188] R.J. Mortimer, A.L. Dyer, J.R. Reynolds, Electrochromic organic and polymeric materials for display applications, *Displays* 27(1) (2006) 2-18.
- [189] M.U. Ahmed, M.M. Hossain, M. Safavieh, Y.L. Wong, I.A. Rahman, M. Zourob, E. Tamiya, Toward the development of smart and low cost point-of-care biosensors based on screen printed electrodes, *Critical reviews in biotechnology* 36(3) (2016) 495-505.

- [190] P.E. Minkler, M.S. Stoll, S.T. Ingalls, J. Kerner, C.L. Hoppel, Validated method for the quantification of free and total carnitine, butyrobetaine, and acylcarnitines in biological samples, *Anal Chem* 87(17) (2015) 8994-9001.
- [191] M. Moder, A. Kiessling, H. Loster, Current methods for determination of L-carnitine and acylcarnitines, *Monatshefte Fur Chemie* 136(8) (2005) 1279-1291.
- [192] K.-G. Seline, H. Johein, The determination of L-carnitine in several food samples, *Food Chemistry* 105(2) (2007) 793-804.
- [193] M. Dabrowska, M. Starek, Analytical approaches to determination of carnitine in biological materials, foods and dietary supplements, *Food Chemistry* 142 (2014) 220-232.
- [194] Dropsens, Screen-Printed Electrodes, 2016. (Accessed April 2016).
- [195] O. Hitech, Nanostructured screen printed electrodes, 2015. (Accessed April 2016).
- [196] A. Hayat, J.L. Marty, Disposable Screen Printed Electrochemical Sensors: Tools for Environmental Monitoring, *Sensors* 14(6) (2014) 10432-10453.
- [197] P. Samyn, Wetting and hydrophobic modification of cellulose surfaces for paper applications, *Journal of Materials Science* 48(19) (2013) 6455-6498.
- [198] S. Khan, J.K. Singh, Wetting transition of nanodroplets of water on textured surfaces: a molecular dynamics study, *Molecular Simulation* 40(6) (2014) 458-468.
- [199] M. Andrew, B. Bijeljic, M.J. Blunt, Pore-scale contact angle measurements at reservoir conditions using X-ray microtomography, *Advances in Water Resources* 68 (2014) 24-31.
- [200] K.K. Sadasivuni, D. Ponnamma, S. Thomas, Y. Grohens, Evolution from graphite to graphene elastomer composites, *Progress in Polymer Science* 39(4) (2014) 749-780.
- [201] A.C. Ferrari, Raman spectroscopy of graphene and graphite: Disorder, electron-phonon coupling, doping and nonadiabatic effects, *Solid State Communications* 143(1-2) (2007) 47-57.
- [202] Z. Luo, T. Yu, Z. Ni, S. Lim, H. Hu, J. Shang, L. Liu, Z. Shen, J. Lin, Electronic Structures and Structural Evolution of Hydrogenated Graphene Probed by Raman Spectroscopy, *Journal of Physical Chemistry C* 115(5) (2011) 1422-1427.
- [203] T. Lin, F. Huang, J. Liang, Y. Wang, A facile preparation route for boron-doped graphene, and its CdTe solar cell application, *Energy & Environmental Science* 4(3) (2011) 862-865.
- [204] S.K. Vashist, J.H.T. Luong, Recent advances in electrochemical biosensing schemes using graphene and graphene-based nanocomposites, *Carbon* 84 (2015) 519-550.
- [205] W. Wang, G. Xu, X.T. Cui, G. Sheng, X. Luo, Enhanced catalytic and dopamine sensing properties of electrochemically reduced conducting polymer nanocomposite doped with pure graphene oxide, *Biosensors & bioelectronics* 58 (2014) 153-6.
- [206] V. Castagnola, C. Bayon, E. Descamps, C. Bergaud, Morphology and conductivity of PEDOT layers produced by different electrochemical routes, *Synthetic Metals* 189 (2014) 7-16.
- [207] M. Omastova, M. Trchova, J. Kovarova, J. Stejskal, Synthesis and structural study of polypyrroles prepared in the presence of surfactants, *Synthetic Metals* 138(3) (2003) 447-455.

- [208] A. Bello, M. Giannetto, G. Mori, R. Seeber, F. Terzi, C. Zanardi, Optimization of the DPV potential waveform for determination of ascorbic acid on PEDOT-modified electrodes, *Sensors and Actuators B-Chemical* 121(2) (2007) 430-435.
- [209] M. Gao, Y. Xu, Y. Bai, S. Jin, Effect of electropolymerization time on the performance of poly(3,4-ethylenedioxythiophene) counter electrode for dye-sensitized solar cells, *Applied Surface Science* 289 (2014) 145-149.
- [210] A. Menaker, V. Syritski, J. Reut, A. Öpik, V. Horváth, R.E. Gyurcsányi, Electrosynthesized Surface-Imprinted Conducting Polymer Microrods for Selective Protein Recognition, *Advanced Materials* 21(22) (2009) 2271-2275.
- [211] A. Ramanavicius, A. Ramanaviciene, A. Malinauskas, Electrochemical sensors based on conducting polymer- polypyrrole, *Electrochimica Acta* 51(27) (2006) 6025-6037.
- [212] P.S. Sharma, A. Pietrzyk-Le, F. D'Souza, W. Kutner, Electrochemically synthesized polymers in molecular imprinting for chemical sensing, *Analytical and Bioanalytical Chemistry* 402(10) (2012) 3177-3204.
- [213] F.T.C. Moreira, S. Sharma, R.A.F. Dutra, J.P.C. Noronha, A.E.G. Cass, M.G.F. Sales, Protein-responsive polymers for point-of-care detection of cardiac biomarker, *Sensors and Actuators B-Chemical* 196 (2014) 123-132.
- [214] X.D. Wang, J. Dong, H.M. Ming, S.Y. Ai, Sensing of glycoprotein via a biomimetic sensor based on molecularly imprinted polymers and graphene-Au nanoparticles, *Analyst* 138(4) (2013) 1219-1225.
- [215] S.Q. Liu, L. Bakovic, A.C. Chen, Specific binding of glycoproteins with poly(aniline boronic acid) thin film, *Journal of Electroanalytical Chemistry* 591(2) (2006) 210-216.
- [216] N.S. Ferreira, A.P.T. Moreira, M.H.M. de Sá, M.G.F. Sales, New electrochemically-derived plastic antibody on a simple conductive paper support for protein detection: Application to BSA, *Sensors and Actuators B: Chemical* 243 (2017) 1127-1136.
- [217] T.S.C.R. Rebelo, C.M. Pereira, M.G.F. Sales, J.P. Noronha, F. Silva, Protein Imprinted Material electrochemical sensor for determination of Annexin A3 in biological samples, *Electrochimica Acta* 190 (2016) 887-893.
- [218] H. Yao, Y.Y. Sun, X.H. Lin, Y.H. Tang, L.Y. Huang, Electrochemical characterization of poly(eriochrome black T) modified glassy carbon electrode and its application to simultaneous determination of dopamine, ascorbic acid and uric acid, *Electrochimica Acta* 52(20) (2007) 6165-6171.
- [219] H. Yao, Y.Y. Sun, X.H. Lin, Y.H. Tang, A.L. Liu, L. Guangwen, L. Wei, S.B. Zhang, Selective determination of epinephrine in the presence of ascorbic acid and uric acid by electrocatalytic oxidation at poly(eriochrome black T) film-modified glassy carbon electrode, *Analytical Sciences* 23(6) (2007) 677-682.
- [220] L.H. Wang, X.L. Liao, Y.T. Ding, F. Gao, Q.X. Wang, DNA biosensor based on a glassy carbon electrode modified with electropolymerized Eriochrome Black T, *Microchimica Acta* 181(1-2) (2014) 155-162.

- [221] X. Li, G. Wang, D. Chen, Y. Lu, β -Carotene and astaxanthin with human and bovine serum albumins, *Food Chemistry* 179(0) (2015) 213-221.
- [222] E.L. Gelamo, C.H.T.P. Silva, H. Imasato, M. Tabak, Interaction of bovine (BSA) and human (HSA) serum albumins with ionic surfactants: spectroscopy and modelling, *Biochimica et Biophysica Acta (BBA) - Protein Structure and Molecular Enzymology* 1594(1) (2002) 84-99.
- [223] Y. Inoue, A. Kuwahara, K. Ohmori, H. Sunayama, T. Ooya, T. Takeuchi, Fluorescent molecularly imprinted polymer thin films for specific protein detection prepared with dansyl ethylenediamine-conjugated O-acryloyl L-hydroxyproline, *Biosensors & Bioelectronics* 48 (2013) 113-119.
- [224] J. Anguizola, R. Matsuda, O.S. Barnaby, K.S. Hoy, C. Wa, E. DeBolt, M. Koke, D.S. Hage, Review: Glycation of human serum albumin, *Clinica Chimica Acta* 425(0) (2013) 64-76.
- [225] W. Wang, G. Xu, X.T. Cui, G. Sheng, X. Luo, Enhanced catalytic and dopamine sensing properties of electrochemically reduced conducting polymer nanocomposite doped with pure graphene oxide, *Biosensors & bioelectronics* 58 (2014) 153-6.
- [226] Q. Zhao, R. Jamal, L. Zhang, M.C. Wang, T. Abdiryim, The structure and properties of PEDOT synthesized by template-free solution method, *Nanoscale Research Letters* 9 (2014).
- [227] F. Withers, S. Russo, M. Dubois, M.F. Craciun, Tuning the electronic transport properties of graphene through functionalisation with fluorine, *Nanoscale Research Letters* 6 (2011).
- [228] S. Garreau, G. Louarn, J.P. Buisson, G. Froyer, S. Lefrant, In situ spectroelectrochemical Raman studies of poly(3,4-ethylenedioxythiophene) (PEDT), *Macromolecules* 32(20) (1999) 6807-6812.
- [229] H.-S. Park, S.-J. Ko, J.-S. Park, J.Y. Kim, H.-K. Song, Redox-active charge carriers of conducting polymers as a tuner of conductivity and its potential window, *Scientific Reports* 3 (2013) 2454.
- [230] X.J. Li, J.J. Zhou, L. Tian, W. Li, B.L. Zhang, H.P. Zhang, Q.Y. Zhang, Bovine serum albumin surface imprinted polymer fabricated by surface grafting copolymerization on zinc oxide rods and its application for protein recognition, *Journal of Separation Science* 38(19) (2015) 3477-3486.
- [231] H.F. El-Sharif, H. Yapati, S. Kalluru, S.M. Reddy, Highly selective BSA imprinted polyacrylamide hydrogels facilitated by a metal-coding MIP approach, *Acta Biomaterialia* 28(Supplement C) (2015) 121-127.
- [232] N.V.H. Phan, H.F. Sussitz, P.A. Lieberzeit, Polymerization Parameters Influencing the QCM Response Characteristics of BSA MIP, *Biosensors* 4(2) (2014) 161-171.
- [233] H.-J. Chen, Z.-H. Zhang, L.-J. Luo, S.-Z. Yao, Surface-imprinted chitosan-coated magnetic nanoparticles modified multi-walled carbon nanotubes biosensor for detection of bovine serum albumin, *Sensors and Actuators B: Chemical* 163(1) (2012) 76-83.
- [234] D. Grieshaber, R. MacKenzie, J. Voros, E. Reimhult, Electrochemical biosensors - Sensor principles and architectures, *Sensors* 8(3) (2008) 1400-1458.
- [235] C.K. Hong, H.S. Ko, E.M. Han, K.H. Park, Electrochemical Properties of Electrodeposited PEDOT Counter Electrode for Dye-sensitized Solar Cells, *International Journal of Electrochemical Science* 10(7) (2015) 5521-5529.

- [236] R. Chen, C.J. Yang, W.Z. Cai, H.Y. Wang, J.W. Miao, L.P. Zhang, S.L. Chen, B. Liu, Use of Platinum as the Counter Electrode to Study the Activity of Nonprecious Metal Catalysts for the Hydrogen Evolution Reaction, *Acs Energy Letters* 2(5) (2017) 1070-1075.
- [237] D. Yoo, J. Kim, J.H. Kim, Direct synthesis of highly conductive poly(3,4-ethylenedioxythiophene):poly(4-styrenesulfonate) (PEDOT:PSS)/graphene composites and their applications in energy harvesting systems, *Nano Research* 7(5) (2014) 717-730.
- [238] L.A.A.N.A. Truta, S. Pereira, C. Hora, T. Trindade, M.G.F. Sales, Coupling gold nanoparticles to Dye-Sensitized Solar Cells for an increased efficiency, *Electrochimica Acta* 300 (2019) 102-112.
- [239] K.T. Dembele, R. Nechache, L. Nikolova, A. Vomiero, C. Santato, S. Licoccia, F. Rosei, Effect of multi-walled carbon nanotubes on the stability of dye sensitized solar cells, *Journal of Power Sources* 233 (2013) 93-97.
- [240] N. Chander, A.F. Khan, E. Thouti, S.K. Sardana, P.S. Chandrasekhar, V. Dutta, V.K. Komarala, Size and concentration effects of gold nanoparticles on optical and electrical properties of plasmonic dye sensitized solar cells, *Solar Energy* 109 (2014) 11-23.
- [241] U. Mehmood, Rahman, S., Harrabi, K., Hussein, I., B.V. Reddy, Recent Advances in Dye Sensitized Solar Cells, (2014) 1-12.
- [242] R. Ayranci, D.O. Demirkol, M. Ak, S. Timur, Ferrocene-Functionalized 4-(2,5-Di(thiophen-2-yl)-1H-pyrrol-1-yl)aniline: A Novel Design in Conducting Polymer-Based Electrochemical Biosensors, *Sensors* 15(1) (2015) 1389-1403.
- [243] P.R.T. Gordon G. Wallace, Geoffrey M. Spinks, Leon A. P. Kane-Maguire, *Conductive Electroactive Polymers: Intelligent Polymer Systems*, Third Edition ed., CRC Press, TAYLOR & FRANCIS Group 2008.
- [244] D. Gupta, M. Bag, K.S. Narayan, Area dependent efficiency of organic solar cells, *Applied Physics Letters* 93(16) (2008).
- [245] B. Qi, J. Wang, Fill factor in organic solar cells, *Physical Chemistry Chemical Physics* 15(23) (2013) 8972-8982.
- [246] C.S. Xiao-Zi Yuan, Haijiang Wang, Jiujuun Zhang, *Electrochemical Impedance Spectroscopy in PEM Fuel Cells. Fundamentals and Applications.*, Springer-Verlag London 2010.
- [247] B.R. Moraes, N.S. Campos, C.M.S. Izumi, Surface-enhanced Raman scattering of EDOT and PEDOT on silver and gold nanoparticles, *Vibrational Spectroscopy* 96 (2018) 137-142.
- [248] W.W. Chiu, J. Travaš-Sejdić, R.P. Cooney, G.A. Bowmaker, Spectroscopic and conductivity studies of doping in chemically synthesized poly(3,4-ethylenedioxythiophene), *Synthetic Metals* 155(1) (2005) 80-88.
- [249] S. Gupta, Hydrogen bubble-assisted syntheses of polypyrrole micro/nanostructures using electrochemistry: structural and physical property characterization, *Journal of Raman Spectroscopy* 39(10) (2008) 1343-1355.

- [250] S.Y. Lee, B.H. Boo, Molecular structures and vibrational spectra of pyrrole and carbazole by density functional theory and conventional ab initio calculations, *Journal of Physical Chemistry* 100(37) (1996) 15073-15078.
- [251] J. Stejskal, M. Trchova, P. Bober, Z. Moravkova, D. Kopecky, M. Vrnata, J. Prokes, M. Varga, E. Watzlova, Polypyrrole salts and bases: superior conductivity of nanotubes and their stability towards the loss of conductivity by deprotonation, *Rsc Advances* 6(91) (2016) 88382-88391.
- [252] D. McStay, A.H. Al-Obaidi, R. Hoskins, P.J. Quinn, Raman spectroscopy of molecular imprinted polymers, *Journal of Optics a-Pure and Applied Optics* 7(6) (2005) S340-S345.
- [253] H.I.A.S. Gomes, M.G.F. Sales, Development of paper-based color test-strip for drug detection in aquatic environment: Application to oxytetracycline, *Biosensors and Bioelectronics* 65 (2015) 54-61.
- [254] W.-Y. Rho, D.H. Song, H.-Y. Yang, H.-S. Kim, B.S. Son, J.S. Suh, B.-H. Jun, Recent advances in plasmonic dye-sensitized solar cells, *Journal of Solid State Chemistry* 258 (2018) 271-282.
- [255] M.D. Brown, T. Suteewong, R.S.S. Kumar, V. D’Innocenzo, A. Petrozza, M.M. Lee, U. Wiesner, H.J. Snaith, Plasmonic Dye-Sensitized Solar Cells Using Core–Shell Metal–Insulator Nanoparticles, *Nano Letters* 11(2) (2011) 438-445.
- [256] S. Guldin, S. Hüttner, M. Kolle, M.E. Welland, P. Müller-Buschbaum, R.H. Friend, U. Steiner, N. Tétreault, Dye-Sensitized Solar Cell Based on a Three-Dimensional Photonic Crystal, *Nano Letters* 10(7) (2010) 2303-2309.
- [257] L. Ouyang, B. Wei, C.-c. Kuo, S. Pathak, B. Farrell, D.C. Martin, Enhanced PEDOT adhesion on solid substrates with electrografted P(EDOT-NH(2)), *Science Advances* 3(3) (2017) e1600448.
- [258] S. Carli, L. Casarin, G. Bergamini, S. Caramori, C.A. Bignozzi, Conductive PEDOT Covalently Bound to Transparent FTO Electrodes, *The Journal of Physical Chemistry C* 118(30) (2014) 16782-16790.
- [259] A.P.M. Tavares, L.A.A.N.A. Truta, F.T.C. Moreira, G. Minas, M.G.F. Sales, Photovoltaics, plasmonics, plastic antibodies and electrochromism combined for a novel generation of self-powered and self-signalled electrochemical biomimetic sensors, *Biosensors and Bioelectronics* 137 (2019) 72-81.
- [260] J.-G. Chen, H.-Y. Wei, K.-C. Ho, Using modified poly(3,4-ethylene dioxythiophene): Poly(styrene sulfonate) film as a counter electrode in dye-sensitized solar cells, *Solar Energy Materials and Solar Cells* 91(15–16) (2007) 1472-1477.
- [261] D. Song, M. Li, T. Wang, P. Fu, Y. Li, B. Jiang, Y. Jiang, X. Zhao, Dye-sensitized solar cells using nanomaterial/PEDOT–PSS composite counter electrodes: Effect of the electronic and structural properties of nanomaterials, *Journal of Photochemistry and Photobiology A: Chemistry* 293 (2014) 26-31.
- [262] Y.-C. Li, S.-R. Jia, Z.-Y. Liu, X.-Q. Liu, Y. Wang, Y. Cao, X.-Q. Hu, C.-L. Peng, Z. Li, Fabrication of PEDOT films via a facile method and their application in Pt-free dye-sensitized solar cells, *Journal of Materials Chemistry A* 5(17) (2017) 7862-7868.

- [263] V. Kumar, A. Govind, R. Nagarajan, Optical and Photocatalytic Properties of Heavily F--Doped SnO₂ Nanocrystals by a Novel Single-Source Precursor Approach, *Inorganic Chemistry* 50(12) (2011) 5637-5645.
- [264] M.K. Boehm, M.O. Mayans, J.D. Thornton, R.H. Begent, P.A. Keep, S.J. Perkins, Extended glycoprotein structure of the seven domains in human carcinoembryonic antigen by X-ray and neutron solution scattering and an automated curve fitting procedure: implications for cellular adhesion, *J Mol Biol* 259(4) (1996) 718-36.
- [265] D. Schumann, J. Huang, P.E. Clarke, J. Kirshner, S.W. Tsai, V.N. Schumaker, J.E. Shively, Characterization of recombinant soluble carcinoembryonic antigen cell adhesion molecule 1, *Biochem Biophys Res Commun* 318(1) (2004) 227-33.
- [266] H.S. Slayter, J.E. Coligan, Electron microscopy and physical characterization of the carcinoembryonic antigen, *Biochemistry* 14(11) (1975) 2323-30.
- [267] F.T.C. Moreira, S. Sharma, R.A.F. Dutra, J.P.C. Noronha, A.E.G. Cass, M.G.F. Sales, Detection of cardiac biomarker proteins using a disposable based on a molecularly imprinted polymer grafted onto graphite, *Microchimica Acta* 182(5) (2015) 975-983.
- [268] G.E. Lloyd, Atomic-number and crystallographic contrast images with the sem - a review of backscattered electron techniques, *Mineralogical Magazine* 51(359) (1987) 3-19.
- [269] A.P.M. Tavares, L.A.A.N.A. Truta, F.T.C. Moreira, L.P.T. Carneiro, M.G.F. Sales, Self-powered and self-signalled autonomous electrochemical biosensor applied to carcinoembryonic antigen determination, *Biosensors and Bioelectronics* 140 (2019) 111320.
- [270] B. Derkus, Applying the miniaturization technologies for biosensor design, *Biosensors and Bioelectronics* 79 (2016) 901-913.
- [271] L. Soleymani, F. Li, Mechanistic Challenges and Advantages of Biosensor Miniaturization into the Nanoscale, *ACS Sens* 2(4) (2017) 458-467.
- [272] A.J. Baeumner, Chapter 6 Bioanalytical microsystems: technology and applications, *Comprehensive Analytical Chemistry*, Elsevier2005, pp. 251-284.
- [273] X. Zhang, Q. Guo, D. Cui, Recent advances in nanotechnology applied to biosensors, *Sensors (Basel)* 9(2) (2009) 1033-53.
- [274] Y.-C. Kuo, C.-K. Lee, C.-T. Lin, Improving sensitivity of a miniaturized label-free electrochemical biosensor using zigzag electrodes, *Biosensors and Bioelectronics* 103 (2018) 130-137.
- [275] V.F. Cardoso, P. Martins, G. Botelho, L. Rebouta, S. Lanceros-Méndez, G. Minas, Degradation studies of transparent conductive electrodes on electroactive poly(vinylidene fluoride) for uric acid measurements, *Science and technology of advanced materials* 11(4) (2010) 045006-045006.
- [276] T.S. Monteiro, P. Kastytis, L.M. Goncalves, G. Minas, S. Cardoso, Dynamic Wet Etching of Silicon through Isopropanol Alcohol Evaporation, *Micromachines* 6(10) (2015) 1534-1545.

- [277] U. Helmersson, M. Lattemann, J. Bohlmark, A.P. Ehasarian, J.T. Gudmundsson, Ionized physical vapor deposition (IPVD): A review of technology and applications, *Thin Solid Films* 513(1) (2006) 1-24.
- [278] J. Baptiste, *Resistivity Of Gold*, 2004.
<https://hypertextbook.com/facts/2004/JennelleBaptiste.shtml>. (Accessed June 2019).
- [279] M.C.C.G. Carneiro, F.T.C. Moreira, R.A.F. Dutra, R. Fernandes, M.G.F. Sales, Homemade 3-carbon electrode system for electrochemical sensing: Application to microRNA detection, *Microchemical Journal* 138 (2018) 35-44.
- [280] V. Fragkou, Y. Ge, G. Steiner, D. Freeman, N. Bartetzko, A.P.F. Turner, Determination of the Real Surface Area of a Screen-Printed Electrode by Chronocoulometry, *International Journal of Electrochemical Science* 7(7) (2012) 6214-6220.
- [281] M. Lukaszewski, M. Soszko, A. Czerwinski, Electrochemical Methods of Real Surface Area Determination of Noble Metal Electrodes - an Overview, *International Journal of Electrochemical Science* 11(6) (2016) 4442-4469.
- [282] T. Kawashima, T. Ezure, K. Okada, H. Matsui, K. Goto, N. Tanabe, FTO/ITO double-layered transparent conductive oxide for dye-sensitized solar cells, *Journal of Photochemistry and Photobiology A: Chemistry* 164(1) (2004) 199-202.
- [283] N. Kipnis, A Law of Physics in the Classroom: The Case of Ohm's Law, *Science & Education* 18(3) (2009) 349.
- [284] J. Wu, T. Chen, X. Luo, D. Han, Z. Wang, J. Wu, TG/FTIR analysis on co-pyrolysis behavior of PE, PVC and PS, *Waste Management* 34(3) (2014) 676-682.
- [285] A. Castaneda-Facio, R. Benavides, M.E. Martinez-Pardo, Thermal stability of PVC formulations gamma irradiated at different dose rates, *Radiation Physics and Chemistry* 97 (2014) 75-80.

I. Conductive Paper with Antibody-Like Film for Electrical Readings of Biomolecules

I.1 TG features of the carbon-ink.

TG analysis allowed studying the thermal decomposition behavior of the different ink compounds, as depicted in **Figure 3.4** (main paper). The differential gravimetric data of the conductive ink (**Figure 3.4-B**, in main paper) showed little mass loss up to 201.0 °C, of ~ 1.06 %. The significant mass loss occurred in a two-stage behavior, from 201.0 to 360.1 °C and after that up to 488.6 °C, corresponding to two endothermic peaks centered at 273.2 °C and 441.1 °C, respectively. Considering that the first mass loss corresponded to 8.92 % and the second one to 3.81 %, this overall mass loss (12.73 %) was assigned to the degradation of PVC-COOH. A 15% theoretical mass loss could be achieved if all PVC-COOH was degraded, which compared well with an experimental mass decrease of 12.73%. Moreover, a third mass loss was evident between 488.6 °C and 1000° C. This mass loss was small (3.37 %) and occurred over a large temperature range (~511.4 ° C). It was probably related to a small thermal decomposition of the graphite powder along this high temperature range, as evidenced by the thermogram of pure graphite powder presented in **Figure 3.4-A** (main paper).

The thermal assay of pure PVC-COOH (**Figure 3.4-C**, in main paper) also presented two mass losses at temperatures very close to those observed in the conductive ink: 218.6 °C to 371.7 °C (corresponding to 60.96 % mass); and 371.7 °C to 519.5 °C (corresponding to 26.89 % mass). Both ranges corresponded to endothermic events, centered at 274.9 °C and 432.3 °C, respectively. The mass loss in the first temperature range was assigned to the evolution of HCl to form polyenes, leading to the competition of two reactions: decomposition for producing volatiles, mainly benzene, or intermediate cross-linked material decomposing at higher temperatures to produce pyrolysis and more volatile products (aromatics)[284, 285]. The

mass loss in the second temperature range was attributed to the evolution of toluene and methylated aromatics, coming from the decomposition of polyenes and meaning that a substantial quantity of hydrogen chloride and aromatic groups could be present [284, 285].

Compared to the pure PCV-COOH, the temperature ranges of decomposition of the conductive ink shifted negatively in 17.6/11.6 °C for the first significant mass loss, and 11.6/30.9 °C for the second mass loss. The maximums peaks of degradation corresponding to these ranges occurred at about the same temperatures, with maximum shift of 8.8 °C. These results revealed the presence of PVC-COOH within the conductive ink and that the presence of graphite powder yielded little effect upon the thermal degradation of this polymer. Moreover, the conductive ink offered high thermal stability, remaining stable up to 201 °C.

1.2 Electrical changes caused by the redox probe concentration.

The electrochemical behavior in terms of response of these conductive paper was evaluated by EIS measurements of different concentrations solutions of $K_3[Fe(CN)_6]$ and $K_4[Fe(CN)_6]$ in 1.0×10^{-2} mol/L PBS. For this study the same electrode was used in the measurement in different concentrations of redox probe. The corresponding *Nyquist* plots are shown in **Figure I.1**.

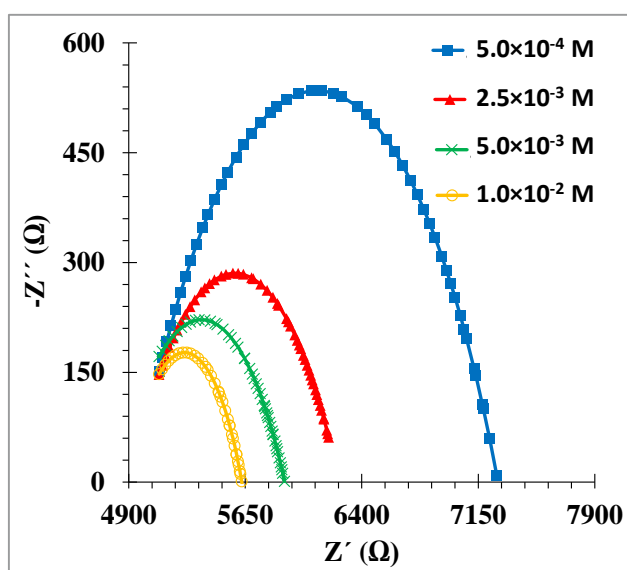


Figure I.1 - EIS data for different iron redox probe concentrations prepared in HEPES buffer.

In general, the Ohmic resistance increased when the concentration of $K_3[Fe(CN)_6]$ and $K_4[Fe(CN)_6]$ decreased. An intermediate concentration was selected in this study, 2.50×10^{-3} mol/L $K_3[Fe(CN)_6]$ and $K_4[Fe(CN)_6]$, as a compromise between having high electrical transfer rates for a low concentration of iron redox probe.

1.3 Gran's Method of multiple standard addition.

This method allows determining the unknown concentration and minimizing matrix effects, such as varying ionic strength or the presence of interfering ions. The plot of $10^{R_{ct}/S}$ versus the concentration of CRT added gave a straight line where the x axis intercept indicated directly the concentration of the unknown on the analysed sample (CRT already present in the urine real sample before spiking with different standard levels) (Figure I.2).

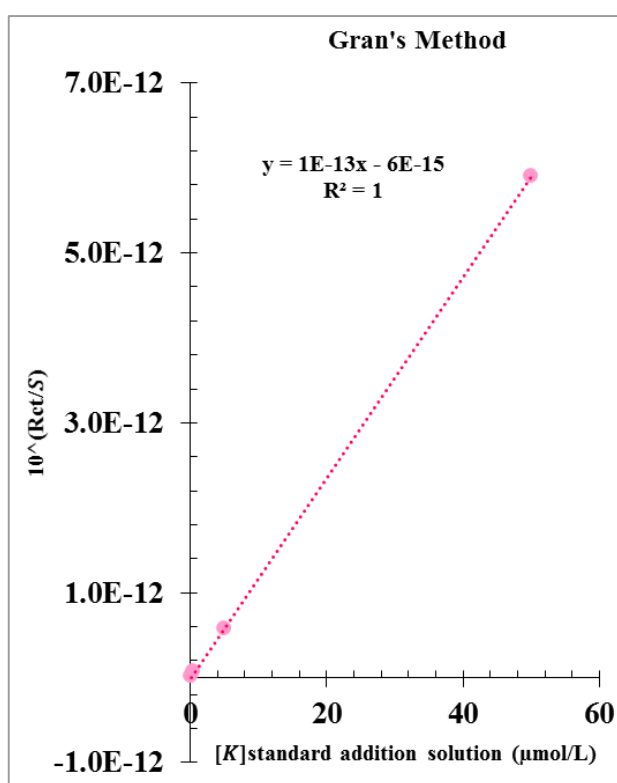


Figure I.2 - Calibration curve obtained for a CRT sample. S corresponds to the slope of the experimental calibration; R_{ct} the charge transfer resistance of each spiked level; and $[k]$ the known concentration of carnitine present in the each level of spiked sample.

The data points seem superimposed for lower values, but this results from the use of a wide concentration range using a *log* scale in the normal calibration and using this data to have a Gran's plot. The estimated CRT concentration in urine was 0.06 $\mu\text{mol/L}$ (or 9.67 ng/mL), a value that lies within the concentration range of healthy individuals.

1.4 Synthetic urine

The selectivity of the sensory layers for CRT was also tested by calibrating the paper-based sensors in synthetic urine with the overall composition: 5.00×10^{-6} mol/L urea, 5.30×10^{-6} mol/L Crea, 9.8×10^{-7} mol/L magnesium chloride, 6.80×10^{-7} M calcium chloride, 3.20×10^{-6} mol/L NaH_2PO_4 , 3.30×10^{-6} mol/L ammonium chloride, 3.90×10^{-6} mol/L potassium sulphate, 6.50×10^{-6} mol/L sodium chloride and 3.00×10^{-8} mol/L BSA. The calibration of the sensors under synthetic urine is presented in **Figure I.3** and indicates a similar behaviour to that under real urine. Thus, negligible interference from a controlled urine composition, where BSA was added as protein source, is unexpected.

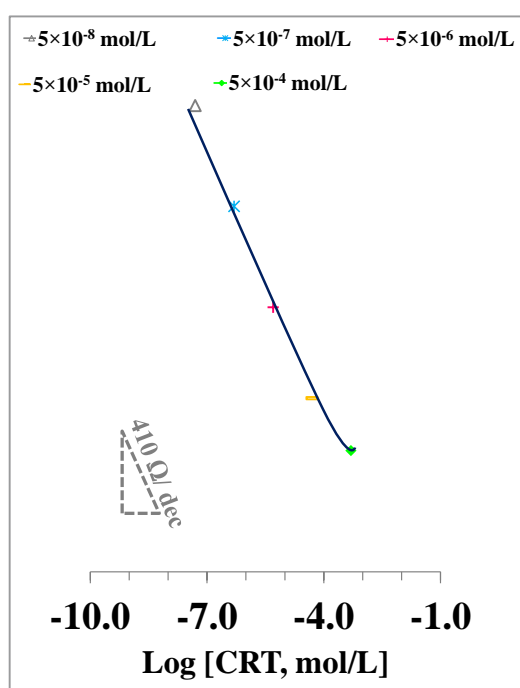


Figure I.3 - Calibration curve obtained for CRT in synthetic urine.

1.5 Analytical Parameters

Table I.1 - Further bioanalytical Parameters.

Material	Monomer	Limits		Precision		%CV	Reproducibility	
		LOD (mol/L)	LOQ (mol/L)	Linearity (mol/L)	Intra-day N=3	Inter-day N=3	Intraday N=3	Fabrication N=4
Antibody-like	EDOT	2.25×10^{-8}	7.51×10^{-8}	1.0×10^{-7} – 5×10^{-3}	1.29 ± 0.09	1.45 ± 0.29	7.34%	1.04 ± 0.05
Antibody-like	DBS	1.93×10^{-9}	6.42×10^{-9}	1×10^{-8} – 5×10^{-4}	1.85 ± 0.05	1.93 ± 0.12	3.09%	0.51 ± 0.18

II. Novel electro-polymerized protein-imprinted materials using Eriochrome Black T: application to BSA sensing

II.1 *The CV features of the components of interest*

The CV data of individual components is shown in **Figure II.1**. It is possible to see in **Figure II.1-A** the eletropolymerization of EBT on the carbon surface, showing two anodic peaks (**1,2**) and one cathodic peak (**3**). During to polymerization, the first anodic peak (**1**) appears at 0.15 V and the second one (**2**) at 0.32, corresponding to the oxidation of EBT, forming a benzoquinone diime structure [218]. Both peaks tend to decrease with the increasing number of cycles, as well as cathodic peak (**3**) at -0.33 V. It was also clear that consecutive cycles yielded current decreases, signaling that the growing polymer hold non-conductive properties. Both PBS buffer and BSA solutions have no peak within the same potential range tested.

The formation of a PEBT film in the presence of BSA is similar to that of a NIP, as shown in **Figure II.1-B**. The oxidation peak potentials of EBT in the presence of BSA shifted to more positive potentials (from +0.15 to +0.16 V in first peak, and from +0.32 to +0.34 V in the second one). The cathodic peak did not present a significant displacement, but it demonstrated a decrease of the current with the presence of the protein. These results indicated the presence of the template and that it was becoming part of the polymeric matrix.

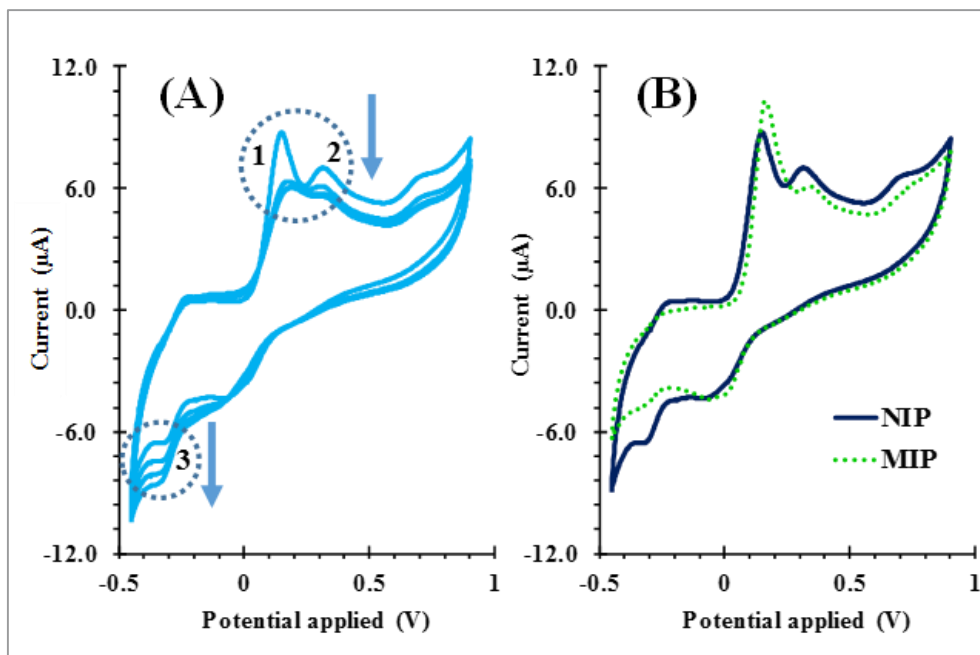


Figure II.1 - Electropolymerization graph of EBT by CV in PBS buffer pH 7. **(A)** The electropolymerization graph of EBT at 100 mV/s, indicating anodic peaks (1 and 2) and cathodic peak (3); **(B)** Influence of protein presence during electropolymerization process.

II.2 BSA concentration

EBT was polymerized in the presence of different concentrations of BSA (**Figure II.2**). The Nyquist plots obtained indicated the changes in the resistance of the polymeric surface along each modification carried out onto the substrate. These changes are monitored in terms of R_{ct} at the electrode surface, given by the diameter of the semicircle [209].

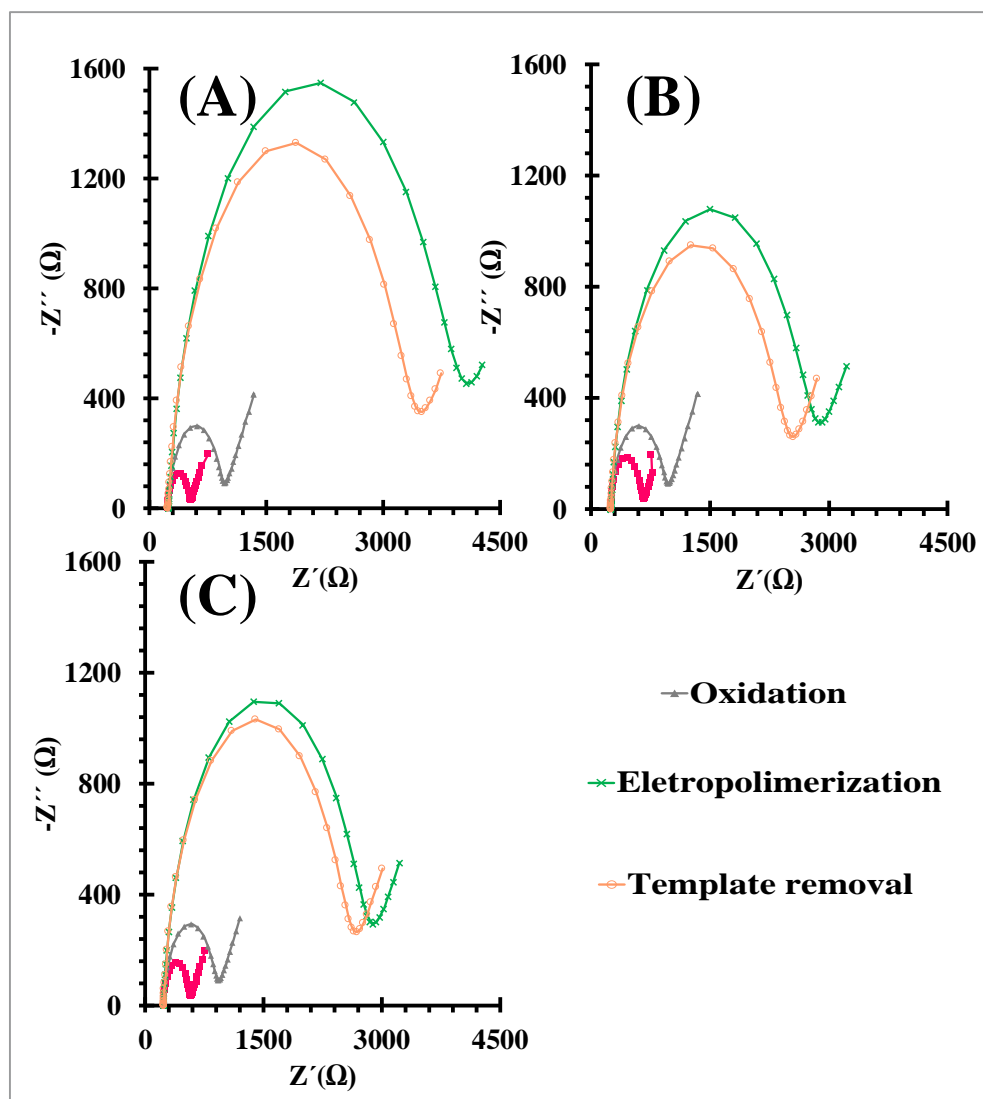


Figure II.2 - Nyquist plots for polymeric systems formed with different BSA concentrations, evaluated in $[\text{Fe}(\text{CN})_6]^{3-/4-}$ in PBS buffer pH 7. **(A)** 1.00×10^{-5} mol/L; **(B)** 1.00×10^{-6} mol/L; **(C)** 1.00×10^{-7} mol/L.

As shown, the R_{ct} increased with BSA increasing concentrations, thereby indicating that more BSA molecules were entrapped within the polymer. In turn, the R_{ct} decreased upon the template removal, to generate BSA rebinding sites. Being this R_{ct} decrease more evident for the higher concentrations, it was clear that high BSA concentrations favoured the creation more rebinding sites.

II.3 Incubation time of BSA in the biosensor

As in immunosensors, the time given for BSA to interact with the plastic antibody is very important. Herein, calibration curves were recorded for different time of incubation, from 15 to 30 minutes. Overall, the longest period shows a higher sensitivity (Figure II.3).

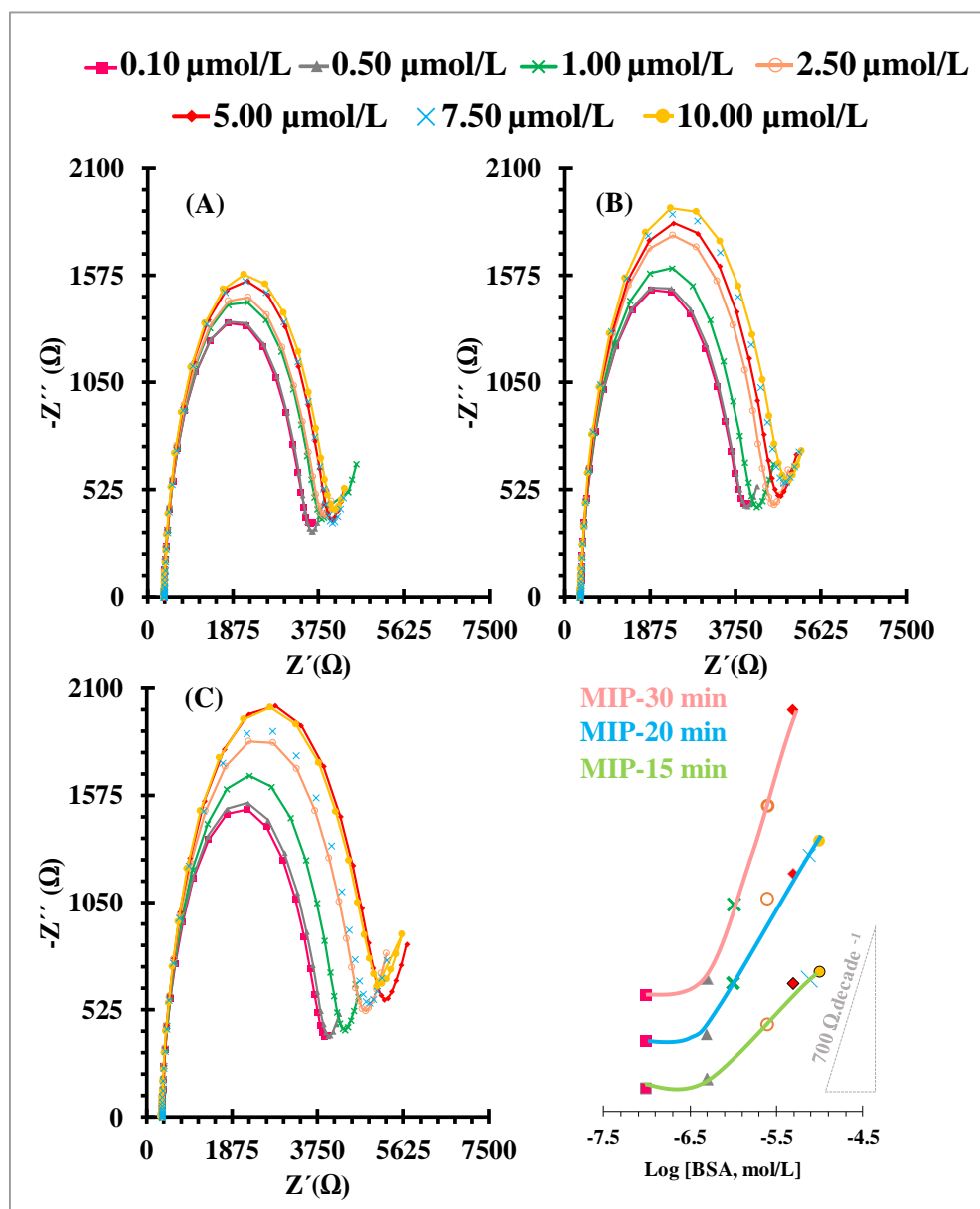


Figure II.3 - Nyquist plots of the same MIP film in $[\text{Fe}(\text{CN})_6]^{3-/4-}$ in PBS buffer pH 7.00, read after BSA incubation periods of (A) 15 min, (B) 20 min, or (C) 30 min, and the corresponding calibration curves (D).

II.4 Analytical performance by Bode diagram

Overall, the impedance is the proportion factor between voltage and current. The generated current can change in terms of amplitude which may be linked to a phase shift, according to the duration of the applied voltage. Thereby, EIS measurements can be illustrated in two different ways: **(a)** a *Bode* plot (**Figure II.4**), plotting $\log(Z/\Omega)$ and ϕ as a function of $\log(f/\text{Hz})$; **(b)** and a *Nyquist* plot, plotting Z_R and Z_I where Z_R is a real part and Z_I is the imaginary part of the impedance.

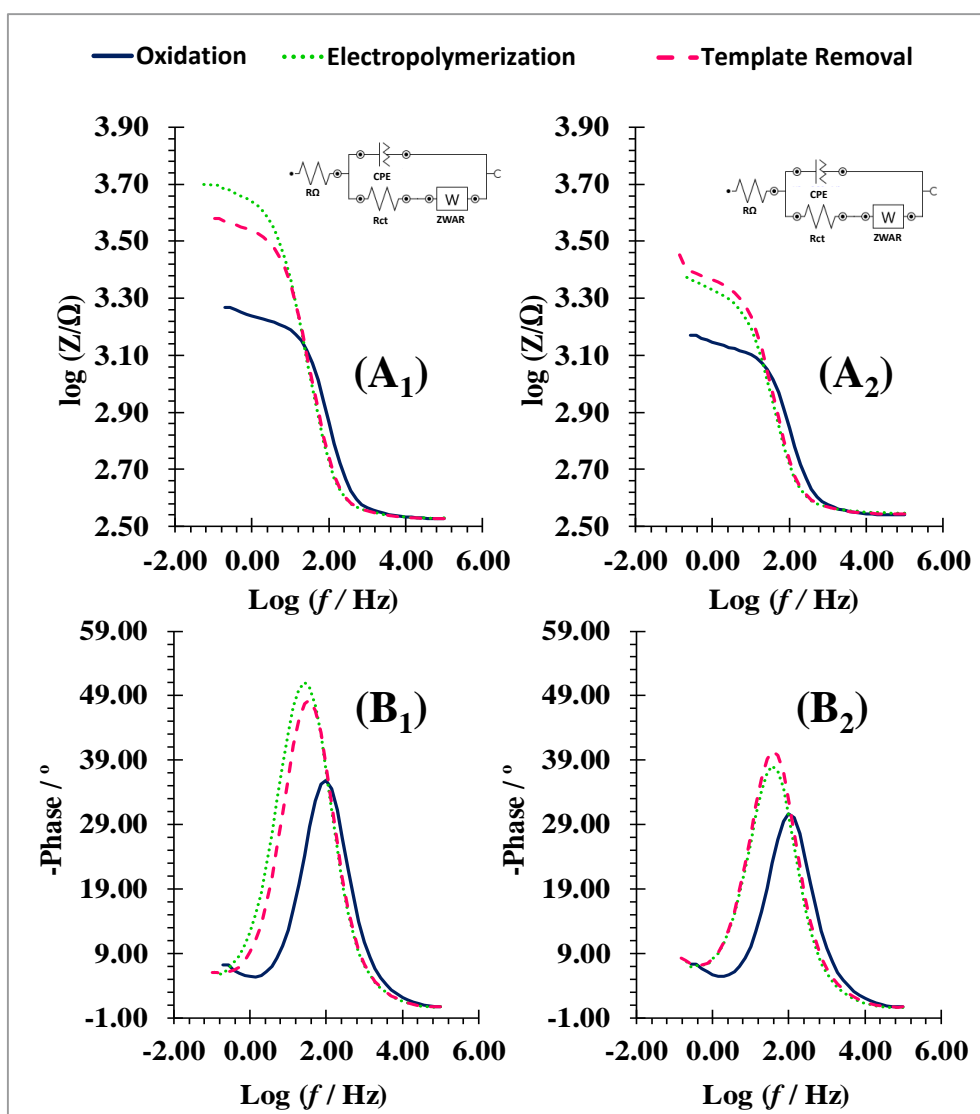


Figure II.4 - Bode diagrams obtained at the assembly of MIP **(1)** and NIP **(2)** films on carbon supports, corresponding to readings in $[\text{Fe}(\text{CN})_6]^{3-/4-}$ solution, prepared in PBS buffer, pH 7.00.

Table II.1 - Circuit report of plot fitted to experimental data using equivalent circuit.

Element	Parameter	Value	Estimated Error (%)
R1	R	341.07	0.366
Q1	Y0	9.6502×10^{-6}	1.980
	N	0.88445	0.411
R2	R	4178.5	0.700
W1	Y0	0.0021998	6.869
	χ^2	0.0092814	

II.5 Selectivity of the sensor

The interfering species tested were selected among those that may be found in the biological fluids: Crea, Glu, and Myo. The results are shown in **Figure II.5** and indicate low rebinding ability for Crea (4.45%), Glu (3.82%), Myo (7.64%), Hb (11.4%) and IgG (-2.62%) meaning that the sensor has affinity for the target molecule.

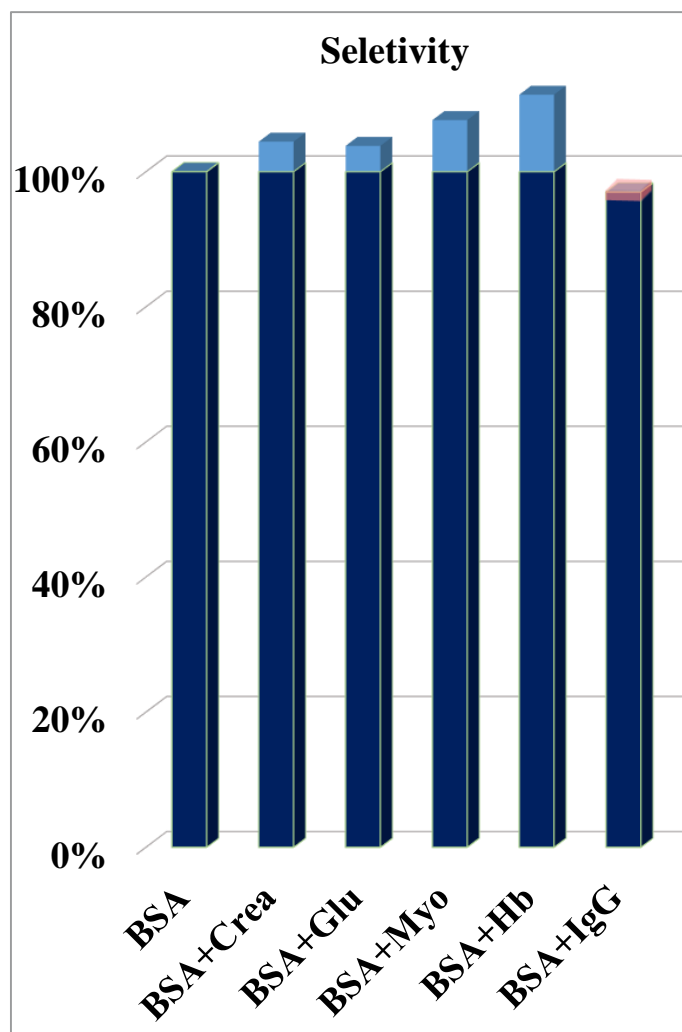


Figure II.5 - Selectivity study of the BSA sensor.

II.7 Comparison of MIP and MIP-PEDOT sensors

A PEDOT layer was produced above the carbon electrode and before growing the MIP and NIP films, with the purpose of improving the sensitivity of the final biosensor. This was indeed observed, as may be seen in **Figure II.6**, which compares the calibration curves of MIP and MIP-PEDOT sensors, considering the relative R_{ct} data obtained, calculated as $[R_{ct}(\text{standard}) / R_{ct}(\text{blank})]$.

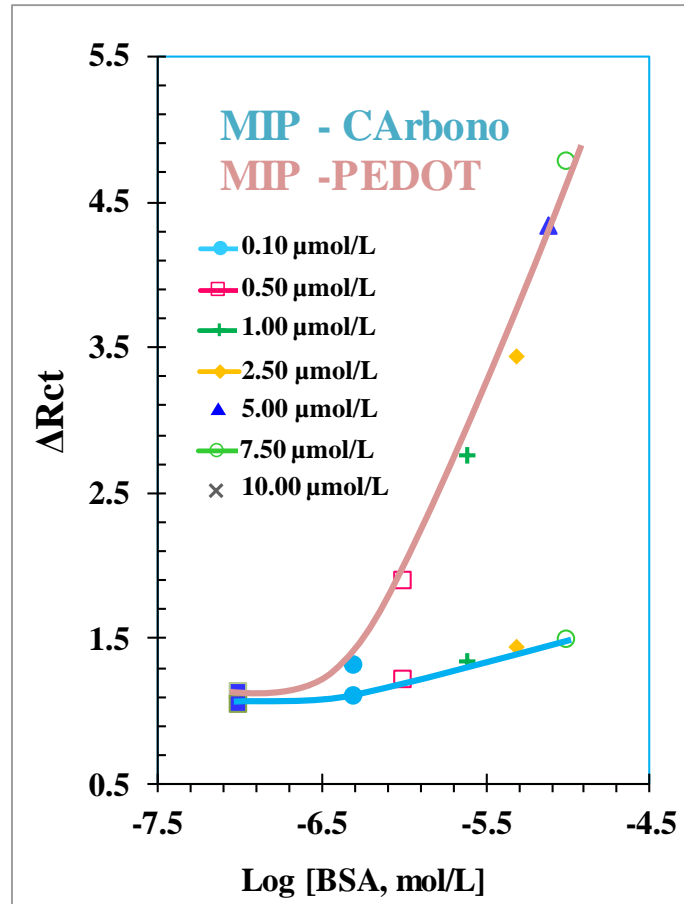


Figure II.6 - Calibration curves of the MIP BSA sensor assembled directly on the carbon support or on a PEDOT film, prepared in simulated serum.

III. Self-powered and self-signaled autonomous electrochemical biosensor applied to carcinoembryonic antigen determination.

III.1 Synthesis of electrochromic derivative, SNS-NH₂

The synthesized monomer (**Figure III.1**) was characterized by ¹H- NMR (300 MHz, CDCl₃), and the obtained spectrum was represented in **Figure III.2**. The NMR results are consistent with the structure of SNS-NH₂.

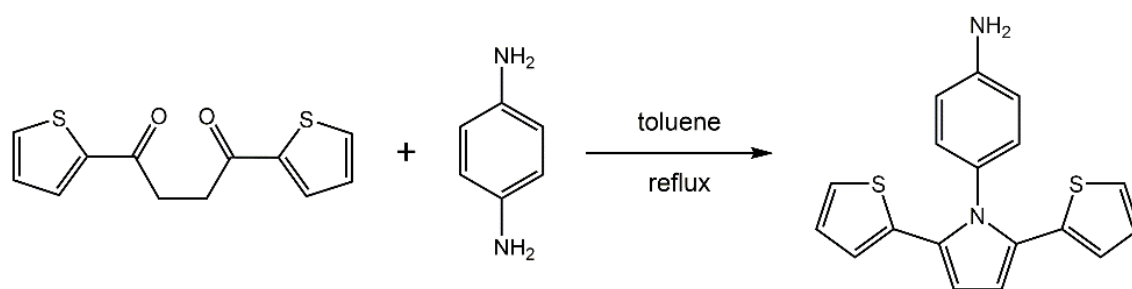


Figure III.1 - Scheme of Synthesis of SNS-NH₂.

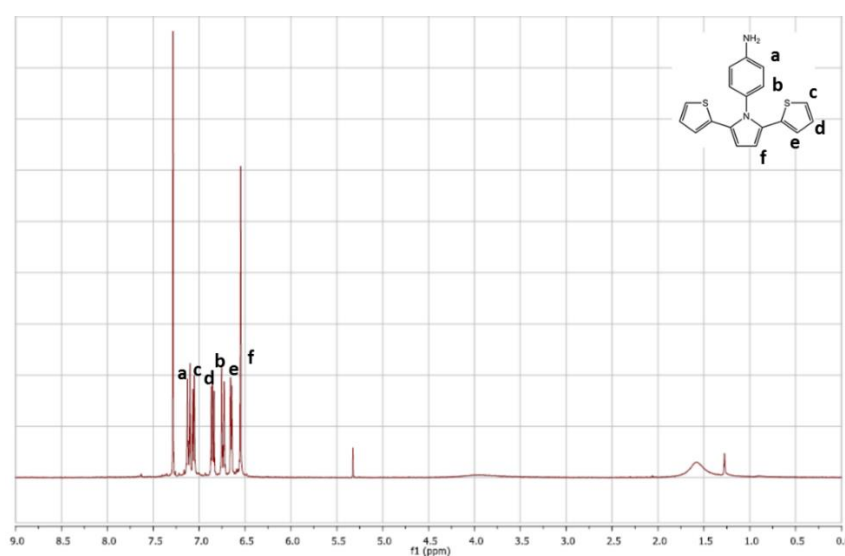


Figure III.2 - ¹H- NMR spectrum of SNS-NH₂ in CDCl₃.

III.2 Colour change of the electrochromic material under within the potential working range

Figure III.3 showed coloration of electrochromic material after application different potential in electrochemical system with 3 electrodes (Working potential).



Figure III.3 - Performance of electrochromic material in electrochemical system with 3-electrodes and under the indicated working potential (against Ag/AgCl reference electrode).

III.3 Colour variations of the electrochromic cell triggered by the hybrid DSSC/biosensor device

Figure III.4 showed a performance of electrochromic material when coupled with DSSC-PEDOT (DSSC Potential).

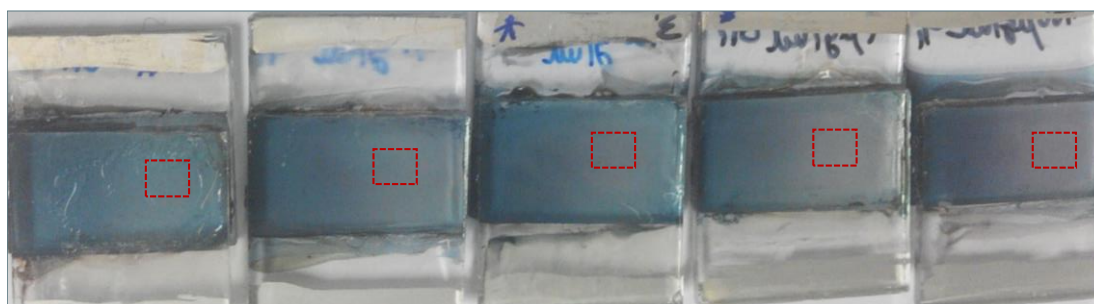


Figure III.4 - Performance of electrochromic material when coupled with DSSC-PEDOT (DSSC Potential).

IV. Photovoltaics, plasmonics, plastic antibodies and electrochromism combined for a novel generation of self-powered and self-signalled electrochemical biosensors

IV.1 Morphology of different photoanode

The morphological analysis of photoanode with TiO₂ (**Figure IV.1-A**) and TiO₂ + AuNPs (**Figure IV.1- B**) was evaluated by SEM. The presence of Au* in photoanode was proven using Backscattered electrons (BSE) detector. This detector allowed to obtain an image contains different intensities and contrast related with atomic number of each chemical element, 22 of TiO₂ against 79 of Au* [268] . Moreover, the introduction of the Au* in TiO₂ paste was also confirmed by the EDS analysis.

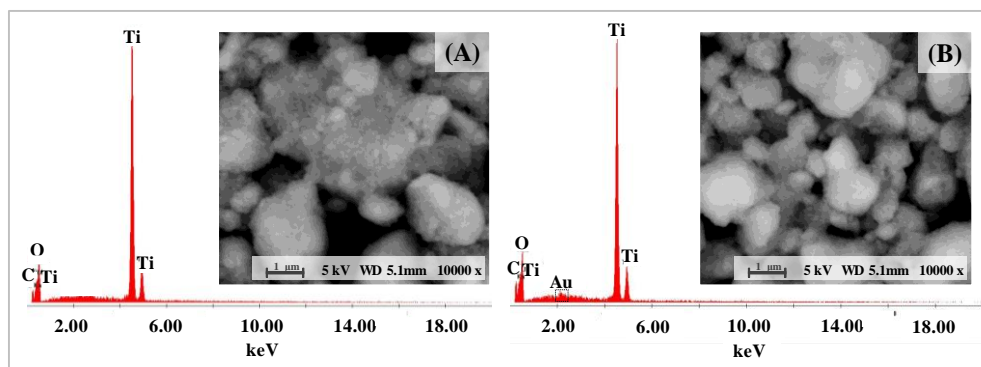


Figure IV.1 - SEM images and EDS analysis of photoanodes prepared with (A) TiO₂ or (B) TiO₂ with AuNPs, both sensitized with dye N719.

IV.2 Analytical Performance of EC

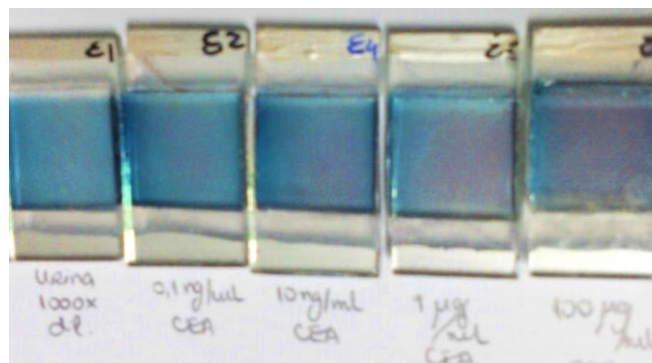


Figure IV.2 - EC performance representing MIP(TiO_2) behavior against CEA increasing concentrations in the range of 0.10 ng/mL to 100.00 µg/mL in real urine from healthy individual, diluted 1000x.

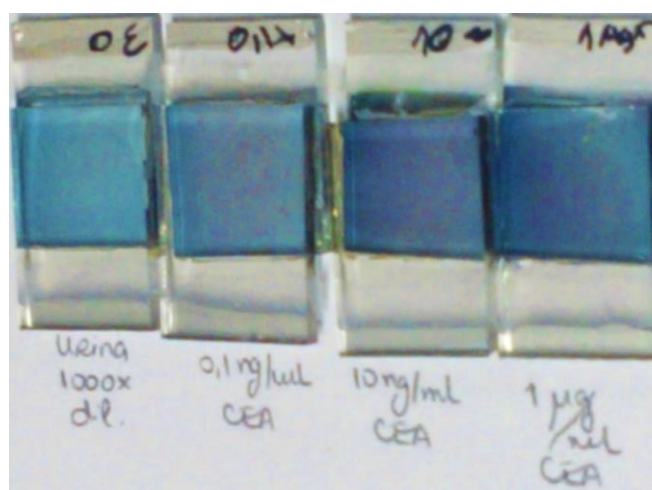


Figure IV.3 - EC performance representing MIP(TiO_2+NP_s) behavior against CEA increasing concentrations in the range of 0.10 ng/mL to 100.00 µg/mL in real urine from healthy individual, diluted 1000x.